Chain-length dependent rheology and relaxation dynamics in glass-forming polymers

Matthew Reynolds

University of Leeds

School of Physics and Astronomy

Submitted in accordance with the requirements for the degree of

Doctor of Philosophy

September 2018

Acknowledgements

I would like to express my sincere gratitude to my principle supervisor Dr. Johan Mattsson for his continued support through my PhD. His patience and guidance has helped me through the last 4 years. I would like to thank EPSRC for funding my PhD, and allowing me to carry out this research.

I would like to thank my co-supervisor Dr. Peter Hine for all the help he has provided. In particular I would also like to thank Dr. Daniel Baker for all his help with BDS and DSC, and for general lab assistance.

An additional thank you to all my co-PhD students who have had to put up with me, and to everyone in the Soft Matter Group.

Last but not least, I would like to thank my family, in particular my Mum and Dad, for their continued support throughout the last 30 years.

Abstract

Glassy materials differ greatly from crystalline solids; their lack of long range order makes it difficult to model their behaviour. While a lot of work has been done regarding the properties of glass-forming polymers, their exact nature is not well understood. This thesis primarily focuses on the chain-length dependence of glassy dynamics, in particular poly(methyl methacrylate) (PMMA), which is of interest due to its commercial and industrial applications.

Using dielectric spectroscopy, rheology, and calorimetry, the relaxation behaviour of chain-modes and the segmental, α, relaxation were determined as a function of chain-length. Time-temperature superposition adequately describes the rheology data, even though decoupling between chain-modes and segmental relaxations were observed. Changes occur in the behaviour of the glass transition temperature, T_g, at the molecular weight, M, of the "dynamic bead", M_R. Relaxation times of the α relaxation and chain-modes of PMMA and other polymer systems collapse when renormalized by T_g, suggesting universal behaviour. This occurs when the number of correlated monomers, N_a, in the α relaxation corresponds to M_R.

N_a was determined using modulated calorimetry and dielectric spectroscopy. A clear change in N_a was observed at M_R for less flexible PMMA and polystyrene, whereas this was less pronounced for the more flexible poly(dimethyl siloxane). This may relate to a change from intermolecular to mainly intramolecular behaviour. Furthermore, for PMMA the activation enthalpies of the α and β relaxations below T_g are approximately equal at M_R, suggesting these relaxations

act on similar lengthscales. The activation enthalpy of the β relaxation also becomes M invariant for $M > M_R$, suggesting M_R characterises the β relaxation.

Finally, the ionic conductivity was determined for PMMA and two poly(propylene glycol) (PPG) chain-length systems. The α relaxation and conductivity were coupled for PPG, whereas for PMMA decoupling occurred for $M > M_R$. This demonstrates that polymer behaviour leads to this decoupling in PMMA. We also show that non-polymeric systems do not exhibit this decoupling behaviour.

Contents

1 Introduction **1**

1.1 The glass transition . . . 1

1.2 Relaxation dynamics in glasses . . . 3

1.2.1 The structural (α) relaxation . . . 3

1.2.2 Models for the glass transition . . . 6

1.2.3 Secondary relaxations . . . 11

1.3 Polymers and polymer dynamics . . . 12

1.3.1 The freely jointed chain model . . . 13

1.3.2 Rouse model . . . 16

1.3.3 Entanglement and reptation models . . . 19

1.3.4 Molecular weight and microstructure . . . 22

1.4 Poly(methyl methacrylate) . . . 24

1.4.1 Molecular weight studies . . . 26

1.5 Thesis overview . . . 27

2 Experimental **29**

2.1 Rheology . . . 29

2.1.1 The complex shear modulus . . . 30

2.1.2 The Maxwell model and stretched exponential . . . 33

2.1.3 Time-temperature superposition . . . 36

2.1.4 ARES shear strain-controlled rheometer . . . 39

2.1.5 Linear viscoelastic regime tests . . . 41

2.1.6 Test of rheometer compliance effects . . . 44

2.2 Broadband Dielectric Spectroscopy . . . 48

2.2.1 Dielectric properties of materials . . . 48

2.2.2 Polarisation and relaxation of materials 49
2.2.3 DC conductivity 52
2.2.4 Novocontrol Alpha-A analyser 53
2.2.5 Dielectric response functions 54
2.3 Differential Scanning Calorimetry 59
2.3.1 Rate dependent DSC 62
2.3.2 Temperature modulated DSC 64
2.3.3 TA Instruments Q2000 DSC 68

3 Chain-length dependent rheology and relaxation dynamics of PMMA 73
3.1 Dynamic shear modulus 77
3.1.1 Dynamic shear modulus measurements 77
3.1.2 Dynamic shear modulus modelling 82
3.2 The α relaxation 88
3.2.1 Comparisons to BDS and DSC 91
3.2.2 The glass transition temperature 96
3.2.3 Dynamic fragility 98
3.3 Differential scanning calorimetry 101
3.3.1 Width and height of the glass transition 102
3.4 Chain modes 104
3.4.1 The dynamic bead size 106
3.4.2 Sub-Rouse modes 109
3.5 Validity of TTS from glass to melt 110
3.5.1 Comparisons between rheology and BDS 112
3.5.2 Other polymer systems 117
3.6 Conclusions 124

4 Molecular cooperativity in glass-forming oligomers and polymers 127
4.1 Heat capacity determination of N_a 130
4.1.1 The complex heat capacity 134
4.1.2 Heat capacity response 139
4.1.3 The size of the cooperative region 149

4.1.4 Comparisons to literature . . . 152
4.2 Susceptibility determination of $N_{corr,4}$ . . . 155
4.2.1 The complex permittivity . . . 158
4.2.2 χ_4 determination of the number of correlated units . . . 160
4.3 Comparison between N_a and $N_{corr,4}$ . . . 168
4.3.1 N_a from broadband dielectric spectroscopy . . . 171
4.4 Molecular cooperativity of the α relaxation from oligomer to polymer 173
4.4.1 Secondary relaxations . . . 176
4.4.2 Activation enthalpy of the α relaxation . . . 181
4.4.3 Correlations of cooperativity to dynamic behaviours . . . 184
4.5 Conclusions . . . 186
4.5.1 Future work . . . 188

5 Decoupling of ion conductivity and the α relaxation in polymer systems 189
5.1 Dielectric determination of τ_α and σ . . . 194
5.1.1 Complex permittivity measurements . . . 197
5.2 The α relaxation and DC conductivity . . . 198
5.2.1 The coupling of τ_α and σ . . . 201
5.2.2 Effects of ion concentration on DC conductivity . . . 207
5.2.3 Small molecular glass formers . . . 209
5.3 Conclusions . . . 211
5.3.1 Future work . . . 212

6 Conclusions 215

References 249

List of Figures

1.1 Typical behaviour of enthalpy ($H(T)$) or volume ($V(T)$) as a function of temperature for a supercooled liquid cooled at two different rates through their respective glass transition temperatures, T_g. . 2

1.2 Arrhenius plot showing τ_α, τ_β, and τ_γ as a function of $1/T$ for a typically glass forming material (PMMA n=906). 4

1.3 Angell plot showing examples of strong (large D, small m) and fragile (small D, large m) glasses. 5

1.4 Stickel plot showing the same VFT functions as figure 1.3. From equation 1.5, the slope of this depends on D (shown), and $T_0 =$ 373.15K. 6

1.5 Representation of a potential energy landscape describing a glass forming liquid. 10

1.6 Simplified time domain relaxation moduli of a liner entangled polymer. 13

1.7 Schematic of a single flexible polymer containing $n+1$ atoms with n bonds between them. 14

1.8 Schematic of a Rouse chain consisting of beads connected by springs. 16

1.9 A basic schematic showing a polymer chain (blue) constrained due to entanglements from other chains (red) to a tube with diameter a. 20

1.10 Mass fraction, W, as a function of molecular weight, M, for two different samples with $M_W = 100$kg/mol, but different PDI. . . . 23

1.11 Poly(methyl methacrylate) (PMMA) molecule, monomer molecular weight $M_0 = 100$g/mol. 25

LIST OF FIGURES

2.1 Visualisation of a shear deformation resulting from an applied a shear force. . . . 30
2.2 An applied oscillatory strain, $\gamma(t)$, resulting in a stress, $\sigma(t)$, out of phase by angle, δ. . . . 32
2.3 Maxwell model, comprised of a spring (with modulus G_0) and dashpot (with viscosity η) in series. . . . 33
2.4 Maxwell model showing log-log behaviour of $G'(\omega)$ and $G''(\omega)$ of complex shear modulus. . . . 34
2.5 KWW approximation for G'' from equation 2.16 showing the effect of stretching parameter β. . . . 36
2.6 PMMA oligomer (n=96). a) Complex shear modulus measurements performed at discrete temperatures. b) TTS master curve constructed by frequency shifting all data sets onto an arbitrary reference temperature. Circles and triangles are G' and G'' respectively. . . . 38
2.7 Schematic of strain-controlled shear rheometer, with separate actuator and transducer. . . . 39
2.8 Parallel plate sample of heigh h, and radius r. A toque, M, is applied, which shears the sample, resulting in an angular deformation, θ. . . . 40
2.9 1Hz strain sweep measurements on DC705. Linear fits of torque and strain (with a slope of 1 on this log-log scale) indicate measurements are within the LVR. Gray dashed lines indicate torque range of the transducer. . . . 42
2.10 Penta phenyl-trimethyltri-siloxane (DC705) molecule[1]. Molecular weight, $M = 546$g/mol. . . . 42
2.11 DC705 strain sweep tests. (a) 1Hz complex shear modulus as a function of strain. (b) TTS master curve with dashed lines indicating the position of these strain sweeps (shown in (a)). Alternating red, green, and blue sections indicate frequency sweeps taken as discrete temperatures, with circles and triangles representing G' and G'' respectively. . . . 43

2.12 A simple schematic showing both rheometer (K_r) and sample (K_r) contributions to the total sample stiffness. 45
2.13 TTS master curves of DC705. A comparison between different diameter parallel plates, (a) modulus shifted to distinguish between curves, and (b) actual modulus values. (c) 3mm diameter parallel plates compared to literature PSG data. 46
2.14 Small diameter (d=3mm) parallel plate tools. 47
2.15 TTS master curve of DC705, simulating the complex shear modulus if machine/tool stiffness is comparable to sample stiffness. . . 48
2.16 An electric field across a polarised material ($\boldsymbol{E}(t)$, shown by the blue line) is removed at $t = 0$. The resulting polarisation ($\boldsymbol{P}(t)$, shown by the red line) decays towards zero. 50
2.17 Debye model showing log-log behaviour of $\epsilon'(\omega)$ and $\epsilon''(\omega)$ of complex permittivity. 52
2.18 Circuit schematic setup of a broadband dielectric spectrometer. . 53
2.19 Electrode configurations used in BDS for: a) solid samples (top down view); and b) liquid samples (cross section). 54
2.20 ϵ' (a) and ϵ'' (b) for Cole-Cole (Havriliak-Negami, where $\beta = 1$) relaxation with different α parameters. 55
2.21 ϵ' (a) and ϵ'' for Cole-Davidson (Havriliak-Negami, where $\alpha = 1$) relaxation with different β parameters. 56
2.22 ϵ' (a) and ϵ'' (b) as a function of frequency for PMMA n=3 at 225K. The solid line represents fitting of the entire spectra, and dashed lines show the individual contributions to the spectra. . . 57
2.23 a) $\epsilon'(\omega)$ of PMMA n=906 at 404K. b) $\epsilon''(\omega)$ and $\epsilon''_{deriv}(\omega)$ calculated using equation 2.39 from $\epsilon'(\omega)$. The solid line represents fitting of the entire spectra, and dashed lines show the individual contributions to the spectra. 58
2.24 c_p as a function of T measured on heating for amorphous PDMS trimer (n=3). a) Entire heat capacity spectra with typical features labelled. b) Enlarged glass transition region from (a). 59

2.25 Enthalpy (H) as a function of temperature for a supercooled liquid cooled below T_g, aged in the glassy state, and subsequently reheated above T_g. 60
2.26 c_p as a function of T measured at 10K/min on cooling across T_g for PMMA (n=906). Analysis procedures used to determine T_g, Δc_p, and ΔT are also shown. 61
2.27 Enthalpy (H) as a function of temperature for a supercooled liquid cooled at two different rates through their respective glass transition temperatures, T_g. 63
2.28 Example of a TMDSC temperature profile with: An underlying heating rate of $B = 0.5$K/min (shown by the gray dotted line); a period of $P = 60$s; and an amplitude of $A = 1$K. 64
2.29 TMDSC measurements on DC705, using the same experimental parameters as outlined for figure 2.28. a) The components of the heating rate from the modulation (blue), and the underlying heating rate (red). b) Heat flow response due to both of these components. 65
2.30 $c_{p,tot}$, $c_{p,r}$, and $c_{p,nr}$ for DC705 across T_g using the same experimental parameters as outlined for figure 2.28. 67
2.31 Basic schematic of a turret style heat-flux DSC. 69
2.32 Reversing heat capacity $c_{p,r}$ measurement for sapphire for different modulation periods, P=40, 60, and 100s. Literature data for the heat capacity of sapphire is also shown[2]. 71

3.1 Chemical structure of a poly(methyl methacrylate) (PMMA) molecule. 75
3.2 PMMA dynamic shear modulus TTS master curves for samples with different degrees of polymerisation (n). Alternating red, green, and blue sections indicate frequency sweeps taken as discrete temperatures, with circles and triangles represent G' and G'' respectively. 79
3.3 PMMA Van-Gurp-Palmen (VGP) plots for the samples shown in figure 3.2. 81

3.4 TTS master curve of PMMA n=2. Gray lines are a series of Maxwell modes (with peak positions shown by the gray dashed lines) fitted to the KWW approximation of G'', shown by the black line. The orange line indicates the real component sum of Maxwell modes. 84
3.5 PMMA TTS master curves with appropriate models fitted for the samples shown in figure 3.2. 87
3.6 Arrhenius plot showing τ_α determined from the TTS master curves as a function of inverse T. The legend gives the degree of polymerisation, and solid lines are VFT fits to the data. 89
3.7 a) Angell plot, showing PMMA α relaxation timescales attained from TTS master curves as a function of T_g/T. b) Stickel plot linearising VFT behaviour. The legends give the degree of polymerisation, and solid lines are VFT fits to the data. 90
3.8 Dielectric loss at different temperatures for a) $n = 3$ and b) $n = 906$ PMMA samples. Solid line represent fitting of the entire spectra. Dashed line shows an example of individual contributions to the spectra. 92
3.9 Specific heat capacity as a function of temperature for PMMA n=906. The red dashed lines indicate the behaviours in the glass ($c_{p,g}$) and liquid ($c_{p,l}$) states. The black dashed line shows the, so called, fictive temperature. 93
3.10 Transition temperatures from standard DSC measurements performed at different cooling rates (black circles), vertically shifted using shift factor, y, to transition temperatures from TMDSC (red triangles) for PMMA a) n=2 and b) n=906. 94
3.11 PMMA α relaxation Arrhenius plots. a) BDS (triangles) and DSC (squares) for all PMMA samples, with VFT fits through BDS data. b) Rheology (circles), BDS (triangles), and DSC (squares) for common samples, with VFT fits through rheology data. The legends show the degree of polymerisation (n). 95

3.12 a) T_g vs M_W from Rheology TTS master curves, BDS, and DSC. b) Including literature data[3, 4]. Fox-Flory fits (equation 3.19) for the entire data set (red), and for data with $M_W > 10^3$g/mol (black). 96
3.13 a) T_g vs M from rheology TTS master curves, BDS, and DSC. b) Inlcuding literature data[3, 4]. Region I, II, and III represent changes in polymer behaviour with M. Solid black symbols on the top axis indicate M_K (circle), M_e (left facing triangle), and M_c (right facing triangle). 97
3.14 Dynamic fragility (m) vs M from rheology TTS master curves, and BDS. Orange dashed lines are guides to the eye, showing possible regional behaviour. Errors are calculated from errors in VFT fitting. Solid black symbols on the top axis indicate M_K (circle), M_e (left facing triangle), and M_c (right facing triangle). 99
3.15 a) High frequency TTS master curves for PMMA M_W series, scaled on to the high frequency crossover point. Circles and triangles are G' and G'' respectively. b) KWW stretching parameter vs M_W from Rheology TTS master curves, and BDS at $\tau_\alpha \sim 1s$. BDS Havriliak-Negami high frequency exponents at $\tau_\alpha \sim 1s$ is also shown. 100
3.16 c_p as a function T from 10K/min DSC measurement on the PMMA M series. The dashed lines are a guide to the eye, showing systematically increasing glassy and liquid state specific heat capacities. The legend shows degree of polymerisation (n). 101
3.17 a) Change in c_p between $c_{p,liquid}$ and $c_{p,glass}$ at T_g as a function of M. b) Difference in temperature between onset and offset definitions of T_g (discussed in section 2.3) as a function of M. Dash lines indicate regional boundaries. 103
3.18 The heat capacity step (Δc_P) normalised by T_g as a function of M for this PMMA chain length series. Dash lines indicate regional boundaries. 104

3.19 Comparison of entangled PMMA samples. a) Samples measured in this work (n=906, and n=1478) across the entire dynamic range from glass to melt. b) Monodisperse samples from this work and literature, focusing on low frequency entanglement and melt dynamics. 105
3.20 PS TTS master curves with a sum of glassy and Rouse models. a) $M_R = 850$g/mol. b) $M_R = 5000$g/mol. 108
3.21 PMMA TTS master curves for a) n=7 and b) n=8. A single KWW fit of the α relaxation in insufficient to describe the entire spectra, shown by the black fit. 109
3.22 Left: TTS master curves for n=19, 43, and 96 PMMA showing fitting routine of segmental and chain dynamics. Dashed gray lines indicate changes from α dominant, to intermediate, to chain dominant regimes. Right: Approximate position of single frequency sweeps (using $f = 0.5$Hz as the representative frequency) indicating the α timescale where these regimes change. BDS timescale data is also shown (which is α dominant by definition.) 111
3.23 PMMA n=4. a) Imaginary permittivity for T=251, 263, 275, and 287K. b) Imaginary dielectric modulus of the same temperatures as in the left figure. Peak positions of the imaginary permittivity are shown by dashed lines. 113
3.24 Arrhneius plot showing τ_α timescales attained from: Rheology TTS shift factors (modulus); BDS permittivity (compliance); and BDS modulus. 114
3.25 α relaxation Arrhenius plots for PMMA n=2, 19, 96, and 906. τ_α attained from rheology was shifted to BDS VFT fits across the entire τ_α range, and in the "α dominant" range, where $\tau_\alpha > 10^{-3}$s when applicable. 115

3.26 PMMA α relaxation Arrhenius plot. Timescales attained from TTS master curves (circles) are shifted across the entire τ_α range (with the expetion of n=7 and 8, which are shifted across the "α dominant" range ($10^{-3}s < \tau_\alpha$)) to timescales attained from BDS (triangles), with VFT fits. The legend indicates the degree of polymerisation (n). 116

3.27 a) TTS master curve for n=109 PS showing fitting routine of segmental and chain dynamics. Dashed gray lines indicate changes from α dominant, to intermediate, to chain dominant regimes. b) Approximate position of single frequency sweeps (using $f = 0.5Hz$ as the representative frequency) indicating the α timescale where these regimes change. 118

3.28 TTS master curves for PI n=1632. a) Low temperature data showing α relaxation, with a KWW fit. b) High temperature data showing chain modes, with a Likhtman-McLeish[5] fit. 119

3.29 PI α relaxation and chain mode Arrhenius plots for PI n=1632. Left: Chain mode and α relaxation timescales for rheology, BDS, and FFCNMR. Right: Timescales from both the α relaxation and chain modes collapsed onto BDS and FFCNMR τ_α data, with "(s)" in the legend indicating which data sets have been shifted. 120

3.30 a) T_g scaled Arrhenius plot for a variety of oligomeric/polymeric systems: PMMA, PI, PS, polycarbonate (PC), and dimethyl-ethers (DME). Data shown is: τ_α (circles for PMMA, squares for other systems); Direct measurements of τ_n (triangles) which, along with all τ_α data ("+" symbols), are collapsed onto a master curve. b) PMMA and PI (τ_n) data from (a), along with all PMMA n=2, 3, and 4, τ_α data (from figure 3.26, including high frequency BDS data) from BDS and rheology shifted to $T_g/T \sim 0.95$. 122

4.1 From left to right: PMMA, PS, and PDMS molecules. The end groups reported by the manufacturer are also shown. 128

4.2 Visualisation of a system comprised of dynamically independent subvolumes, V_a, with lengthscale $\xi_a = V_a^{1/3}$. 131

4.3 Example of the real, c_p', and imaginary, c_p'', components of the complex heat capacity for a non-polymeric glass former (DC705). T_α and δT define the peak temperature, and the half width at half maximum of c_p'' respectively. 135
4.4 a) Heating rate ($\mathrm{d}T/\mathrm{d}t$), and b) Heat flow ($\mathrm{d}Q/\mathrm{d}T$) for PMMA n=2. For each modulation period (shown in different colours), $\mathrm{d}T/\mathrm{d}t$ and $\mathrm{d}Q/\mathrm{d}t$ are approximately the same amplitude, and contain the same number of oscillations across the temperature range. 137
4.5 a) Reversing heat capacity. b) Phase angle signal, with reversing heat capacity fitting shown in black (right) for PMMA $n = 2$ sample for each period. 138
4.6 c_P'' vs T for low (left) and high (right) M PMMA, PS, and PDMS samples. The three different oscillation periods are shown for each, with Gaussian fits shown by the black lines. 141
4.7 c_P'' ($P = 60$s) vs T for all (a) PMMA, (b) PS, and (c) PDMS, samples with Gaussian fits shown in black. The legends indicate the degree of polymerisation (n). 142
4.8 τ_α vs M for PMMA, PS, and PDMS from TMDSC measurements, with regional boundaries indicated. 143
4.9 Left: c_p'' as a function of temperature normalised onto the peak position from Gaussian fitting for PMMA (a), PS (c), and PDMS (e). The legends indicate the degree of polymerisation (n). Right: The half width at half maximum from Gaussian fits to c_p'', interpreted as the mean fluctuation temperature. 145
4.10 Reversing heat capacity measurements from TMDSC for M series' of a) PMMA, b) PS, and c) PDMS. The legends indicate the degree of polymerisation (n). 146
4.11 Left: Change in reversing heat capacity between liquid and glass as a function of M for PMMA, PS, and PDMS. Right: The rate of change of entropy between liquid and glass as a function of M. 148

4.12 Size of the cooperative region for PMMA, PS, and PDMS for three modulation periods (P=40, 60, and 100s). (a), (c), and (e): Volume, calculated using equation 4.10. (b), (d), and (f): Lengthscale, calculated using equation 4.12. 150
4.13 Number of monomer units in the cooperative region calculated from TMDSC ($P = 60s$) using equation 4.13 for (a) PMMA, (b) PS, and (c) PDMS M_W series. Orange dashed lines are guides to the eye, with regional boundaries indicated. 152
4.14 Number of monomer units in the cooperative region for PS including: Data from this work is from TMDSC (P=60s); and literature data measured using standard (10K/min) DSC, which have been collapsed onto our data using a single shift factor. Regional boundaries are indicated. 153
4.15 Number of monomer units in the cooperative region for PnBMA calculated from TMDSC ($P = 60s$). Inset shows PnBMA molecule. 155
4.16 ϵ' (a) and ϵ'' (b) with HN fitting for PDMS n=2. Different colours represent different temperatures between $T = 121.5 - 128.5$K. . . 159
4.17 Normalised susceptibility (calculated using equation 4.38 from Havriliak-Negami parameters) for PDMS n=2 as a function of frequency. The different colours correspond to the same temperatures as in figure 4.16. 160
4.18 Temperature derivative of this normalised real permittivity for PDMS n=2. The different colours represent different temperature differences used in order to compute the derivatives. 161
4.19 Havriliak-Negami fitting parameters: (a) ϵ_∞, (b) $\Delta\epsilon$, (c) α, (d) β, and (e) τ_α for PDMS n=2 as a function of temperature. Polynomials are fitted to all except (e), which is fitted with a VFT expression. The different colours correspond to the same temperatures as in figure 4.16. 163
4.20 Arrhenius plots for a) PMMA, b) PS, and c) PDMS. The fitted lines are VFT expressions. The temperature where $\tau_\alpha = 100s$ (dashed line) is commonly taken as the glass transition temperature. The legend shows the degree of polymerisation (n). 164

4.21 Low (a) and high (b) M PDMS samples showing $T|\mathrm{d}\chi(\omega,T)$, with different curves representing temperatures where measurements were taken. The two methods of HN parametrisation are shown, with single data points represent TTS approximations for the peak value. 166
4.22 $N_{corr,4}$ for a) PMMA, b) PS, and c) PDMS as a function of τ_α calculated using three techniques: full HN modelling (circles), τ_α only modelling (triangles), and TTS approximation (squares). The legends indicate the degree of polymerisation (n). 167
4.23 N_a (circles) and $N_{corr,4}$ (triangles) for PMMA (a), PS (b), and PDMS (c) as a function of τ_α. The legend indicates degree of polymerisation (n). 170
4.24 BDS measurements of the ϵ'' as a function of temperature for PDMS n=2. Alternating colours are isofrequency measurements. The solid black curve is c_p'' rescaled from TMDSC ($P = 60s$) measurement. 172
4.25 Number of oligomers/polymers in the cooperative region calculated from TMDSC ($P = 60s$) for (a) PMMA, (b) PS, and (c) PDMS M series. Orange dashed lines indicate a change in behaviour, regional boundaries indicated by vertical dashed lines, and horizontal dashed line is when $N_p = 1$. The number of monomers in the cooperative region is also shown for (d) PMMA and PS. . . . 174
4.26 Arrhenius plot for PMMA showing α (triangles), β (diamonds), and γ (stars) relaxations from BDS, with VFT (α) or Arrhenius (β and γ) fits. TMDSC α relaxation data is also shown (squares). The legend indicates the degree of polymerisation (n). 177
4.27 Activation enthalpies for α (calculated at T_g, to be discussed in section 4.4.2), β, and γ relaxations as a function of M for PMMA. Regional boundaries are indicated by dashed lines. 178
4.28 K parameter determined using equation 4.50 from BDS measurements of T_g and ΔH_β for PMMA M series. Shaded area indicates the prediction from equation 4.49. Regional boundaries are also indicated. 180

4.29 a) Angell plot displaying VFT fits of τ_α data, and τ_β data with Arrhenius fits extrapolated to where the two relaxation timescales are equal ($\tau_{\alpha,\beta}$). b) $\tau_{\alpha,\beta}$ (circles) and $\tau_\beta(T_g)$ (triangles) as a function of M, with regional boundaries indicated. 181
4.30 Length of the CRR (ξ_a), ratio of α and β activation energies (n_c), and scaled ratio of ΔH_β to T_g (A/K) as a function of M for PMMA. 185

5.1 From left to right: PMMA, PPG-DME, and PPG molecules. The end groups reported by the manufacturer are also shown.. 192
5.2 Example of a Walden plot, with molar ionic conductivity, Λ, against inverse α relaxation timescale, $1/\tau_\alpha$. Superionic and subionic regimes are indicated. PEO 1k, PPG 1k, AgI-$AgPO_3$, and the H_2O+$LiClO_4$ reference point are from literature[6]. 196
5.3 PMMA Arrhenius plots: a) $\tau_\alpha(T)$, with VFT fits (from equation 5.10). The temperature where $\tau_\alpha = 100$s (dashed line) is commonly taken as the T_g. b) $\sigma(T)$, with VFT fits (from equation 5.11). The legends indicate the degree of polymerisation, n. 199
5.4 Arrhenius plots showing $\tau_\alpha(T)$ for PPG-DME (a) and PPG (b) M series (with VFT fits, from equation 5.10). The temperature where $\tau_\alpha = 100$s (dashed line) is commonly taken as the T_g. The legends indicate the degree of polymerisation, n. 200
5.5 T_g normalised Arrhenius (Angell) plots for PPG-DME (a) and PPG (b) M series. Triangles represent τ_α data (with VFT fits from equation 5.10), and squares represent τ_n data. The legends indicate the degree of polymerisation, n. 201
5.6 Un-normalised Walden plot of σ against $1/\tau_\alpha$ determined from BDS for PMMA M series. The gray dashed line represents a slope of 1, and γ_α is the decoupling exponent of each data set. The legend indicates the degree of polymerisation, n. 202
5.7 The decoupling parameter, γ_α, as a function of M for PMMA. Circles: γ_α values corresponding to figure 5.6. Squares: γ_α values corresponding to PMMA $n = 140$ with $LiBF_4$ salt (discussed in section 5.2.2). 203

5.8 The decoupling parameter between σ and τ_α, γ_α, for the PMMA M series, as a function of: (a) dynamic fragility, m; and b the glass transition temperature, T_g. 204
5.9 Un-normalised Walden plot of σ against $1/\tau_\alpha$ determined from BDS for (a) PPG-DME and (b) PPG M series. The gray dashed line represents a slope of 1. The legend indicates the degree of polymerisation, n. 205
5.10 Un-normalised Walden plot of σ against $1/\tau_n$ determined from BDS for PPG-DME M series. The gray dashed line represents a slope of 1. The legend indicates the degree of polymerisation, n. 206
5.11 The decoupling parameter, γ, as a function of M for (a) PPG-DME and (b) PPG. Circles: γ_α values corresponding to figure 5.9. Triangles: γ_n values corresponding to figure 5.10. 206
5.12 Lithium tetrafluoroborate ($LiBF_4$) salt. This dissociates into a Li cation, and BF_4 anion. 207
5.13 T=393K. 208
5.14 Molecular structures of small molecular glass formers. From left to right: Propylene carbonate (PC), Phenyl salicylate (Salol), ortho-Terphenyl (OTP), and o-Cresolphthalein dimethylether (KDE). . 210
5.15 a) Un-normalised Walden plot of σ against $1/\tau_\alpha$ determined from BDS small molecular glass formers. The gray dashed line represents a slope of 1. b) The decoupling parameter γ_α, defined as the slope in (a), as a function of molecular weight, M. 211

Abbreviations

k_B	Boltzmann's constant
T	Temperature
R	Universal gas constant
G	Shear modulus
ϵ	Relative permittivity
c_p	Isobaric specific heat capacity
σ	Ionic conductivity
τ	Relaxation timescale
ω	Angular frequency
T_g	Glass transition temperature
ΔH	Activation enthalpy
M_W	Weight-averaged molecular weight
PDI	Polydispersity index
KWW	Kohlrausch-Williams-Watts equation
β_{KWW}	KWW stretching parameter
TTS	Time-temperature superposition
BDS	Broadband dielectric spectroscopy
DSC	Differential scanning calorimetry
HN	Havriliak-Negami equation
VFT	Vogel-Fulcher-Tammann equation
D	Strength parameter
T_0	Vogel temperature
PMMA	Poly(methyl methacrylate)
PS	Polystyrene
PDMS	Poly(dimethyl siloxane)
PPG	Poly(propylene glycol)

Chapter 1

Introduction

1.1 The glass transition

From an early age we are taught that when heating or cooling a material it will transition between three equilibrium states of matter: solid, liquid, and gas. However, glasses are non-equilibrium solids, which possesses an amorphous structure, similar to that of a liquid, but behave mechanically like a solid[7]. When cooling a material, molecular motions slow down with decreasing temperature. If a liquid is cooled below its melting temperature, T_m, it will crystallise if it is thermodynamically favourable to do so. However, if the cooling rate is sufficiently large (or the molecules are not able to nucleate), crystallisation may be avoided meaning the liquid becomes supercooled. Supercooled liquids exhibit a rapid increase in viscosity with decreasing temperature and, at a particular temperature, molecular rearrangements occur so slowly that upon further cooling the molecules cannot find a new thermodynamic equilibrium on the relevant timescale. The corresponding temperature at which a supercooled liquid falls out of equilibrium is referred to as the glass transition temperature, T_g. Below this temperature, the material is referred to as a glass. T_g is generally defined as the temperature where the viscosity is $\eta = 10^{12}$Pa·s, corresponding to a characteristic relaxation time of $\tau_\alpha = 100$s[8, 9].

Figure 1.1 shows the idealised behaviour of enthalpy, $H(T)$, or free volume, $V(T)$, with decreasing temperature for a glass forming material.

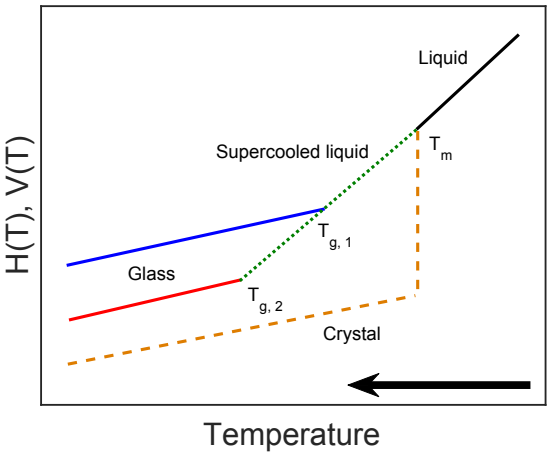

Figure 1.1: Typical behaviour of enthalpy ($H(T)$) or volume ($V(T)$) as a function of temperature for a supercooled liquid cooled at two different rates through their respective glass transition temperatures, T_g.

Commonly, a liquid cooled below T_m will crystallise. This is a first order phase transition, which leads to a discontinuity in the first derivative of free energy[10], as shown by the orange dashed line in figure 1.1. If crystallisation is avoided, the liquid becomes supercooled (green dashed line in figure 1.1). The temperature at which a material falls out of equilibrium depends on the rate of cooling: the quicker the rate, the higher the temperature that this will happen. The blue and red lines in figure 1.1 show the change in enthalpy or free volume where $T_{g,1}$ is the result of a faster cooling rate than $T_{g,2}$.

The entropy of a liquid can be expressed as a sum of two components: a vibrational entropy, S_{vib}, which is approximately equal in both the liquid and crystalline states; and a configurational entropy, S_{con}, which can be approximated as the so-called excess entropy (the measured difference in entropy between liquid and crystalline states $S_{exc} = S_{liq} - S_{cry}$)[11]. An extrapolation of S_{con} in the supercooled region falls below 0 at some finite temperature. A liquid where $S_{conf} < 0$ is unphysical, and this finding was coined the "entropy crisis" by Kauzmann[12, 13] and the temperature where this is predicted to happen is known as the Kauzmann temperature, T_K. However, experimentally, a material always falls out of equilibrium at $T > T_K$.

1.2 Relaxation dynamics in glasses

Glass forming materials exhibit multiple relaxation mechanisms, labelled α, β, γ, etc in order of decreasing relaxation timescale (or increasing frequency)[14]. The slowest relaxation mechanism (α relaxation), often referred to as the structural relaxation, is that which governs glass formation (vitrification) of a material. The so-called secondary relaxations (β, γ, etc) tend to be associated with more local molecular motions. The following section will outline the behaviours of these observed relaxation mechanisms.

1.2.1 The structural (α) relaxation

Glass forming dynamics are governed primarily by the α relaxation. At low temperatures near T_g, the mechanism for this relaxation requires long range collective (cooperative) motions of many units in order to occur. When the characteristic timescale of the α relaxation, τ_α, is large, molecular motion is slow and the material will behave as a solid. As temperature increases, τ_α increases, molecular motions become faster and the material will behave more 'liquid like'. According to Maxwell[15], the viscosity of a material, η, is related to τ_α through the following equation,

$$\eta = G_\infty \tau_\alpha \tag{1.1}$$

where G_∞ is the instantaneous shear modulus. As stated in section 1.1, the viscosity at which the glass transition is defined is $\eta = 10^{12}$Pa·s. Glassy materials may exhibit instantaneous shear moduli of $G_\infty \sim 10^{10}$Pa and therefore the value of τ_α which corresponds to the glass transition temperature with this definition is $\tau_\alpha \approx 100s$[16].

The temperature dependence of τ_α is commonly described by Vogel-Fulcher-Tammann (VFT)[17–19] function, as shown in equation 1.2.

$$\tau_\alpha(T) = \tau_0 \exp\left(\frac{DT_0}{T - T_0}\right). \tag{1.2}$$

Here, τ_0 is the timescale of molecular motion at significantly higher temperatures than the glass transition, and D is the so-called strength parameter which determines the "curvature" of $\tau_\alpha(T)$. T_0 is the temperature at which $\tau_\alpha(T)$ diverges, which has been shown to relate to the Kauzmann temperature (T_K, as described in section 1.1)[20, 21].

Figure 1.2 is an Arrhenius plot showing typical behaviour of the timescales of molecular relaxations in a glass forming material as a function of temperature. The VFT behaviour of $\tau_\alpha(T)$ is shown by the red line. T_g is defined as the temperature at which $\tau_\alpha = 100$s, indicated by the black dashed line. τ_β (blue line) and τ_γ (green line) are secondary relaxation mechanisms which exhibit Arrhenius behaviour (represented by a straight line in an Arrhenius plot). These secondary relaxations will be discussed in section 1.2.3.

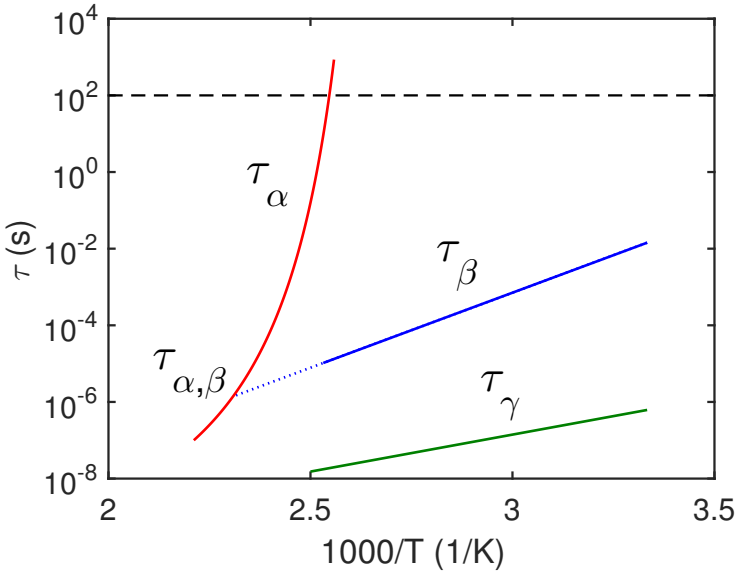

Figure 1.2: Arrhenius plot showing τ_α, τ_β, and τ_γ as a function of $1/T$ for a typically glass forming material (PMMA n=906).

As previously stated, the D parameter in equation 1.2 determines the curvature of $\tau_\alpha(T)$. Another common metric for this temperature dependence is the so-called dynamic fragility parameter, m, [22], which is defined as follows:

$$m = \left.\frac{\mathrm{d}\log\tau_\alpha}{\mathrm{d}(T_g/T)}\right|_{T=T_g}. \tag{1.3}$$

The fragility parameter, m, is a direct measure of the slope of τ_α in a T_g normalised Arrhenius, or Angell[23], plot. The effect of variations of both D and m are shown in figure 1.3.

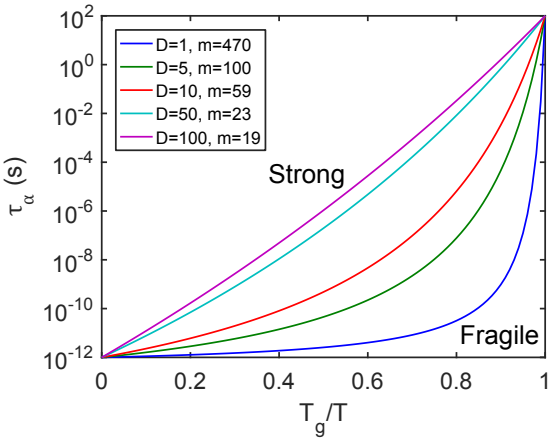

Figure 1.3: Angell plot showing examples of strong (large D, small m) and fragile (small D, large m) glasses.

The strength parameter, D, is a measure of the degree of departure from Arrhenius behaviour, whereby the smaller the value, the more "curved" the VFT expression becomes. The fragility parameter, m, is a measure of the slope at $T_g/T = 1$, and therefore describes how rapidly α relaxation dynamics slow down with decreasing temperature at T_g. These two parameters are often used to describe glass forming materials as either being "strong" or "fragile", the difference of which is apparent in figure 1.3.

In addition to this, a derivative, or Stickel[24], analysis of the temperature dependence of τ_α can be employed. This is shown in equation 1.4:

$$Z = \left(\frac{\mathrm{d}\log\tau_\alpha}{\mathrm{d}(1000/T)}\right)^{-1/2} = \left(\frac{DT_0\log e^1}{1000(T_0/T-1)^2}\right)^{-1/2}. \tag{1.4}$$

This derivative linearises the VFT behaviour, whereby the slope of the Stickel parameter, Z, is related to the VFT parameters D and T_0, as shown in equation 1.5.

$$\frac{\mathrm{d}Z}{\mathrm{d}(1000/T)} = -\left(\frac{T_0}{1000D\log e^1}\right)^{1/2}. \tag{1.5}$$

A change in the slope of Z therefore indicates a change in VFT behaviour, which is not as obvious in an Arrhenius plot. An example of this kind of derivative analysis for the same VFT curves shown in figure 1.3 is shown in figure 1.4.

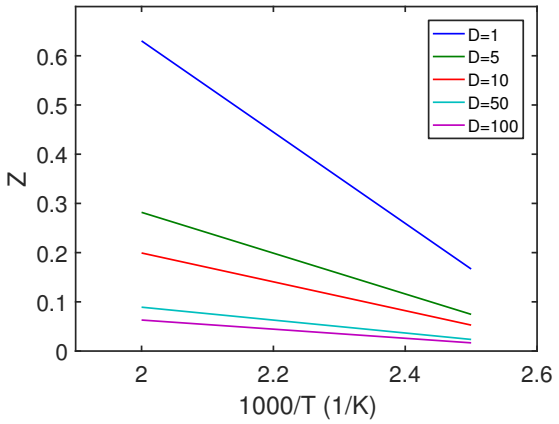

Figure 1.4: Stickel plot showing the same VFT functions as figure 1.3. From equation 1.5, the slope of this depends on D (shown), and $T_0 = 373.15$K.

It is apparent in figure 1.4 that Arrhenius behaviour will be manifested as a horizontal line (Z is invariant with temperature), and therefore the gradient is, in effect, a measure of deviations from Arrhenius behaviour. This type of analysis is often used to determine a change in VFT behaviour, which will be discussed in section 1.2.3.

1.2.2 Models for the glass transition

The glass transition is a widely studied phenomenon. As such, many different models exists which describe glassy dynamics with varying degrees of accuracy and scale. The following reviews and books provide much more detail of these models, amongst others [7, 9–11, 25–27]. However, this section will briefly outline a few models which are commonly used to describe the glass transition and are relevant to the work presented in this thesis.

Entropy models

Many models are based on the role of entropy in glass formation. In this section, two will be briefly outlined. These are: the Adam-Gibbs model[28], which applies to small molecular glass formers; and the Gibbs-DiMarzio model[29], which applies to polymeric systems.

Adam and Gibbs suggested that the rate of molecular rearrangement depends on the size of the rearranging region[28]. This so-called "cooperatively rearranging region" (CRR) is defined as the minimum size of a region which can reconfigure into another configurational state independent of its surroundings[9, 28]. The size of a CRR is assumed to be temperature dependent, increasing in size with decreasing temperature. As previously discussed in section 1.1, if a liquid was cooled in equilibrium to the Kauzmann temperature, T_K, the configurational entropy would be $S_{con} = 0$. Noting this, $S_{con}(T)$ can be defined as equation 1.6[10].

$$S_{con}(T) = a\frac{T - T_K}{T}, \tag{1.6}$$

where a is a constant. Assuming that the activation energy for the α relaxation is proportional to the volume of the CRR, the α relaxation timescales can be expressed in terms of configurational entropy[11], S_{con}:

$$\tau_\alpha(T) = \tau_0 \exp\left(\frac{C}{TS_{con}(T)}\right). \tag{1.7}$$

Here, the C is a material dependent constant, which is proportional to the volume of the CRR. By inserting equation 1.6 into equation 1.7, the VFT expression (equation 1.2) is obtained. This assumes that T_K is equal to the Vogel temperature, T_0. The fact that T_K and T_0 are often close gives validity to the Adam-Gibbs model, although this is not always the case[30].

An entropy model specifically devised for polymeric systems is that of the Gibbs-DeMarzio model[29]. This is based on the Flory-Huggins model using lattice statistics, and models polymer systems as a collection of chains where the flexibility can be set. This yields a second-order phase transition at the point where $S_{con} = 0$.

Free volume models

The notion of "free" volume comes from the assumption that the volume of a liquid can be divided into two parts: the first is the volume occupied by molecules and the second is that which is not occupied by molecules. The latter of these two is termed the "free" volume, v_f, and allows for the rearrangement of the system[31, 32]. A material has to have a large enough v_f in order to rearrange. However, as a liquid is cooled, v_f decreases due to thermal contraction. At a certain temperature, v_f is no longer large enough for the α relaxation to take place, i.e. the material becomes dynamically "stuck". Above T_g, the free volume expands according to equation 1.8

$$v_f(T) = v_c + v_g \Delta\alpha_{l,g}(T - T_g) \tag{1.8}$$

where, v_c is a constant, which is the free volume of the glass, divided by the number of particles in the system, and $\Delta\alpha_{l,g}$ is the difference in the thermal coefficients of the liquid and glass. This expression can be rewritten as equation 1.9.

$$v_f(T) = v\Delta\alpha_{l,g}(T - T_0) \tag{1.9}$$

Here, T_0 is the temperature where free volume is zero if no glass transition occurs, and v is simply defined so that at $v_f(T_g) = v_c$. The free volume is assumed to be described using Boltzmann statistics, i.e. equation 1.10 holds.

$$p(v_f) = \frac{1}{\bar{v}_f} \exp\left(\frac{-v_f}{\bar{v}_f}\right) \tag{1.10}$$

where $p(v_f)$ is the probability of finding v_f in a system of average free volume, $\bar{v}_f$. This can be expressed in terms of the α relaxation timescale, whereby the relaxation depends on finding a free volume larger than v_c, as shown in equation 1.11.

$$\tau_\alpha(T) \propto \exp\left(\frac{v_c}{\bar{v}_f(T)}\right). \tag{1.11}$$

By replacing $\bar{v}_f(T)$ with equation 1.9, then a VFT expression is obtained, shown in equation 1.12

$$\tau_\alpha(T) = \tau_0 \exp\left(\frac{B}{T - T_0}\right) \tag{1.12}$$

Where $B = 1/v\Delta\alpha_{l,g}$ is a constant, which in a VFT equation is generally written as DT_0 instead.

Specific models based on this "free" volume assumption can be problematic due to the fact that $v_f(T)$ is difficult to define[11, 33]. Furthermore, liquids under isochoric conditions also exhibit a glass transition[34, 35], suggesting that there is more to glass formation than simply the availability of "free" volume.

The coupling model

The coupling model (CM) proposed by Ngai[36, 37] is based on the notion that in order for a glass forming liquid to relax, there must be some cooperative motion of molecules. This model suggests that a glass forming liquid comprising many body interactions will exhibit a two-step relaxation, with some crossover time t_c[38] (for most systems this is of the order of $t_c \sim 10^{-12}$s[39]), whereby the motion of molecules transitions from being non-cooperative to cooperative. For $t < t_c$, the basic units relax independently via a single exponential decay:

$$\phi(T) = \phi_0 \exp(-t/\tau_0), \tag{1.13}$$

Where τ_0 is the primitive relaxation timescale of the molecules. At $t > t_c$, relaxations are said to occur via a stretched exponential decay:

$$\phi(T) = \exp((-t/\tau)^{1-n}), \tag{1.14}$$

where n is the "coupling parameter", and is related to the KWW stretching parameter (to be discussed in section 2.1.2): $n = 1-\beta$. n is said to depend on the intermolecular interactions of the system[40]. The crossover between equations 1.13 and 1.14 occurs when $t = t_c$, and the continuity of these two functions leads to the following expression:

$$\tau = (t_c^{-n}\tau_0)^{1/(1-n)}. \tag{1.15}$$

This links the cooperative relaxation time, τ, to the primitive relaxation time τ_0. This model gives no insight into microscopic interactions of the molecules. However, it has been shown to describe complex dynamics in a wide range of phenomena, such as: the glass transition, polymer viscosity, and the dynamics of ionics in glassy and crystalline conductors[40]. It has also been shown that the α relaxation, along with the KWW stretching parameter, is able to yield a primitive relaxation which is comparable to that of the β relaxation in some systems[41, 42]. This coupling suggests that the β relaxation may be a precursor to the α relaxation in these systems.

The potential energy landscape model

In 1969, Goldstein proposed a topographical model for describing viscous liquids close to T_g[43]. It was suggested that a landscape representing $3N+1$ dimensions (3 spacial coordinates per particle, plus all particles of potential energy k_BT) could describe the configurational state of a system. An representation of this potential energy landscape is shown in figure1.5.

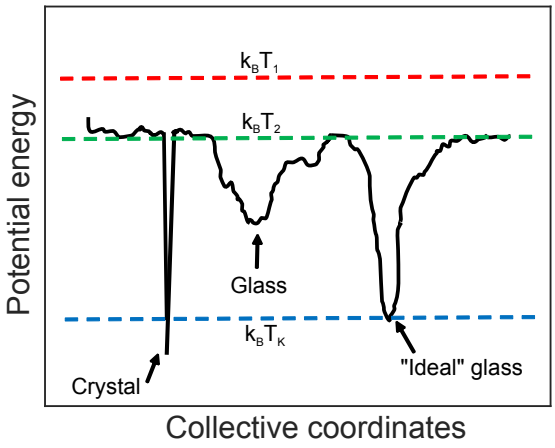

Figure 1.5: Representation of a potential energy landscape describing a glass forming liquid.

Temperature affects how the system is influenced by the landscape[7]. In figure 1.5, at T_1, the temperature is too high for a particular system to be significantly influenced by the landscape and therefore the particles can freely diffuse.

At T_2, the landscape influences the configurational state of the system: the system explores local minima which represent local relaxation mechanisms. As temperature decreases further, the system will become trapped in a deeper potential energy minima, which leads to non-exponential relaxation timescales[7]. Eventually, upon further cooling, the system will become "stuck" in a large energy minima, forming a glass. If it exists, the deepest energy minima should represent that of the "ideal" glass, which will have a potential energy minima at $k_B T_K$.

It is thought that more fragile systems have a larger density of minima in the potential energy landscape[27, 44], representing more glassy states, than stronger liquids. This model also provides an interpretation for the dynamic crossover (discussed in section 1.2.3), whereby, within a larger potential energy minimum representing a α relaxation, the system can also sample local minima representing the β relaxation[45]. This dynamic crossover will be discussed in section 1.2.3.

1.2.3 Secondary relaxations

In addition to the α relaxation, glass forming materials exhibit faster, more local, relaxation mechanisms. These are generally labelled β, γ, δ, etc in order from slowest to fastest relaxation timescales at a fixed temperature[14]. Such relaxations typically display thermally activated Arrhenius behaviour, as the straight lines show in figure 1.2[46]. This is quantified in equation 1.16.

$$\tau(T) = \tau_0 \exp\left(\frac{\Delta H}{k_B T}\right). \tag{1.16}$$

Here, τ_0 is the relaxation time at high temperatures, ΔH is the activation enthalpy, and $k_B T$ is thermal energy.

The β relaxation was orginally assumed to be intramolecular in nature, involving the reorientation or rotation of small, mobile, chemical groups[47]. However, Johari and Goldstein[48, 49] showed that small molecular systems, which lack intramolecular degrees of freedom (such as toluene), also exhibit a β relaxation. Therefore, at least for small molecular systems, the β relaxation must have an intermolecular component. This intermolecular nature of the β relaxation was also shown to be the case for polymers[50, 51], whereby the mechanisms involve motions within side groups as well as relaxation of the polymer backbone. The

heterogeneous nature of this relaxation is the topic of much discussion[52, 53]. At low temperatures close to T_g, it has been suggested that there exists "islands of mobility", whereby some regions relax, while others are relatively immobile[54]

The timescale at which the α and β relaxations merge, marked $\tau_{\alpha,\beta}$ in figure 1.2, relates to the so-called dynamic crossover. It has been observed that there there are several changes in dynamic behaviour at the $\tau_{\alpha,\beta}$ crossover, such as i) decoupling between translational and rotational diffusion[55], ii) a change in the dielectric strength ($\Delta\epsilon$) of the α relaxation[56] and iii) a distinct change in the VFT behaviour of τ_α, which has been observed in various small molecular and polymeric systems[57].

Relaxations faster than the β relaxation are typically attributed to a much more local motion, such as in PMMA, where the γ relaxation has been attributed to some reorientation within the side groups[58].

1.3 Polymers and polymer dynamics

The term polymer comes from the Greek words poly, meaning "many", and mer, meaning "part". Polymers are macromolecules which are made up of many covalently bonded repeated monomer units. A molecule containing only a few monomer units is sometimes referred to as an oligomer[59]. Polymer properties such as backbone chemistry, side groups, tacticity, and molecular weight have a huge impact on both glassy and chain dynamics. Despite this, the ability to characterise polymers using limited resolution models is key to understanding how polymer chains interact. A visualisation of the relaxation moduli for a linear entangled polymer is shown in figure 1.6.

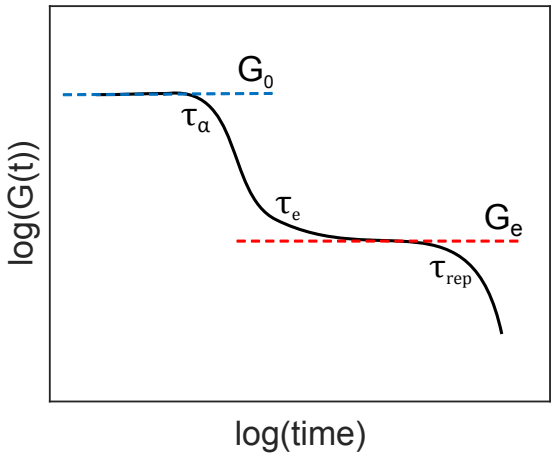

Figure 1.6: Simplified time domain relaxation moduli of a liner entangled polymer.

Figure 1.6 shows that at $t < \tau_\alpha$, glass dynamics dominate, and the material acts like an elastic solid. At $t > \tau_\alpha$, the polymer enters a viscoelastic regime, whereby the interaction of polymer chains become important. In this regime, so called Rouse modes occur, which relax the chain through a series of normal modes. At $t > \tau_e$, entanglement dynamics become applicable and polymer motion is hindered by overlapping chains. Finally, at $t > \tau_{rep}$, these chains are able to move through each other (reptate) and the polymer system is relaxed, exhibiting viscous behaviour. In this section, these polymer behaviours will be outlined. In this section, basic models of chain behaviour in these regimes will be outlined, and will closely follow well established literature[5, 60, 61].

1.3.1 The freely jointed chain model

For a flexible polymer of $n + 1$ backbone atoms, the end-to-end vector can be expressed simply using equation 1.17[60],

$$\boldsymbol{R}_n = \sum_{i=1}^{n} \boldsymbol{r}_i \tag{1.17}$$

$\boldsymbol{R}_n$ and $\boldsymbol{r}_i$ represent the end-to-end vector (as a summation of n bonds) and the i^{th} bond vector respectively. This is visualised in figure 1.7, showing a simple schematic of a flexible polymer with $n + 1$ atoms.

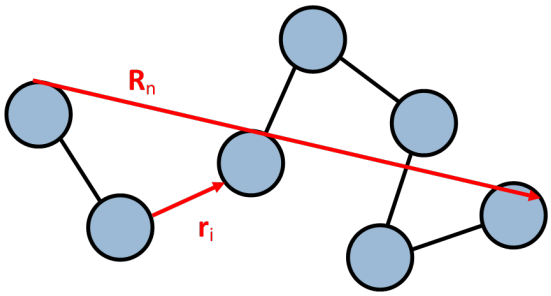

Figure 1.7: Schematic of a single flexible polymer containing $n+1$ atoms with n bonds between them.

Different chains will have different end-to-end vectors. In an isotropic polymer system, the mean end to end distance is zero, $\langle \boldsymbol{R}_n \rangle = 0$. However, the mean-square end-to-end distance is non-zero:

$$\langle \boldsymbol{R}_n^2 \rangle = \langle \boldsymbol{R}_i \cdot \boldsymbol{R}_j \rangle = \left\langle \left(\sum_{i=1}^{n} \boldsymbol{r}_i \right) \cdot \left(\sum_{j=1}^{n} \boldsymbol{r}_j \right) \right\rangle = \sum_{i=1}^{n} \sum_{j=1}^{n} \langle \boldsymbol{r}_i \cdot \boldsymbol{r}_j \rangle. \tag{1.18}$$

If all backbones bonds are of the same length, i.e. $|\boldsymbol{r}_i| = l$, the scalar product in equation 1.18 can be written in terms of l and the bond angle between $\boldsymbol{r}_i$ and $\boldsymbol{r}_j$, $\theta_{i,j}$. This is expressed as:

$$\boldsymbol{r}_i \cdot \boldsymbol{r}_j = l^2 \cos \theta_{i,j}. \tag{1.19}$$

Therefore, the mean-square end-to-end distance becomes:

$$\langle \boldsymbol{R}_n^2 \rangle = \sum_{i=1}^{n} \sum_{j=1}^{n} \langle \boldsymbol{r}_i \cdot \boldsymbol{r}_j \rangle = l^2 \sum_{i=1}^{n} \sum_{j=1}^{n} \langle \cos \theta_{i,j} \rangle. \tag{1.20}$$

The freely jointed chain model assumes constant bond length, and that there are no correlations between different bond vectors[60], i.e. $\langle \cos \theta_{i,j} \rangle = 0$ for $i \neq j$. Therefore, equation 1.20 contains n non-zero terms ($\cos \theta_{i,j} = 1$ for $i = j$) and the mean-square end-to-end distance becomes:

$$\langle \boldsymbol{R}_n^2 \rangle = nl^2. \tag{1.21}$$

In reality, there are correlations between adjacent (and nearby) bond vectors, i.e. $\langle\theta_{i,j}\rangle \neq 0$. However, bond vectors far enough apart will be uncorrelated. Therefore, for bond vector $\boldsymbol{r}_i$, the summation of all other bond vectors, $\boldsymbol{r}_{i,j}$ can be expressed as a finite number[60, 62]:

$$C_i' = \sum_{j=1}^{n} \langle \cos\theta_{i,j} \rangle. \tag{1.22}$$

Therefore, the mean-square end-to-end distance in equation 1.20 becomes:

$$\langle \boldsymbol{R}_n^2 \rangle = nl^2 \frac{1}{n} \sum_{i=1}^{n} C_i' \tag{1.23}$$

Flory's characteristic ratio, C_∞, is the average of C_i' over all backbone bonds in a polymer, expressed as:

$$C_n = \frac{1}{n} \sum_{i=1}^{n} C_i'. \tag{1.24}$$

This yields equation 1.25 as the mean-square end-to-end distance of a polymer:

$$\langle \boldsymbol{R}_n^2 \rangle = C_n n l^2. \tag{1.25}$$

For large n where this value becomes independent on chain length, the value $C_n \to C_\infty$. The value of C_∞ depends on the local flexibility of the polymer chain. For example, in a flexible polymer such as polyisoprene, $C_\infty = 4.7$, whereas for a more rigid polymer such as poly(methyl methacrylate), $C_\infty = 8.2$[60].

Rather than describing a polymer chain in terms of single monomer units, an ideal polymer can be described as a freely jointed chain with N units of length b, otherwise known as the Kuhn length[61]. This is described in terms of the contour length, R_{max}:

$$R_{max} = Nb, \tag{1.26}$$

Where the mean-square end-to-end vector is described as:

$$\langle \boldsymbol{R}_n^2 \rangle = Nb^2 = bR_{max} = C_\infty n l^2. \tag{1.27}$$

Therefore, the Kuhn monomer length can be defined as:

$$b = \frac{\langle \boldsymbol{R}_n^2 \rangle}{R_{max}} = \frac{C_\infty n l^2}{R_{max}}. \tag{1.28}$$

In effect, this definition describes real polymers as freely jointed chains with "Kuhn monomers" comprising of multiple (∼10) monomer units.

1.3.2 Rouse model

The Rouse model is often used to describe chain dynamics for unentangled polymer systems. This model describes a polymer chain as a series of independent Rouse monomers of size b attached by harmonic springs[60, 63], as shown in figure 1.8.

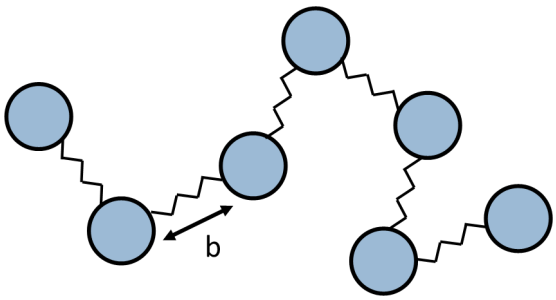

Figure 1.8: Schematic of a Rouse chain consisting of beads connected by springs.

The polymer in figure 1.8 consists of N monomers connected by springs of size b. The monomers interact with each other through the springs, each with a friction coefficient ζ. Therefore, the total friction coefficient of the Rouse chain is simply the sum of these contributions, shown in equation 1.29.

$$\zeta_R = N\zeta. \tag{1.29}$$

Here, ζ_R is the friction coefficient of the entire Rouse chain. Using the Einstein relation ($D = k_B T/\zeta$), this can be expressed in terms of a diffusion coefficient:

$$D_R = \frac{k_B T}{\zeta_R} = \frac{k_B T}{N\zeta}. \tag{1.30}$$

Where D_R is the diffusion coefficient of the Rouse chain, and k_BT is thermal energy. The time it takes for a polymer to diffuse its own distance is coined the Rouse time, τ_R:

$$\tau_R \approx \frac{R^2}{D_R} \approx \frac{R^2}{k_BT/(N\zeta)} = \frac{\zeta}{k_BT} NR^2. \tag{1.31}$$

The Rouse time is of particular importance as it represents the crossover between viscoelastic and diffusive behaviour of a polymer chain[60]. For timescales shorter than the Rouse time, $t < \tau_R$, the chain is unrelaxed (or partly relaxed) and will therefore exhibit viscoelastic properties. However, for timescales longer than the Rouse time, $t > \tau_R$, the chain is relaxed and can diffuse, exhibiting viscous properties.

The Rouse chain has $N - 1$ springs but, for long chains, this number can be approximated as N. Due to the fractal nature of polymers, the size of a polymer is related to the number of monomers by a power law, as shown in equation 1.32:

$$R \approx bN^{\nu}. \tag{1.32}$$

Here, ν is the reciprocal fractal dimension ($\nu = 1/2$ for a ideal linear polymer chain with no interactions[60]). The relaxation timescale of individual monomers can be expressed as follows:

$$\tau_0 = \frac{\zeta b^2}{k_BT}. \tag{1.33}$$

This is the relaxation time of a single Rouse bead. Inserting equation 1.33 into equation 1.31 yields the Rouse time:

$$\tau_R \approx \frac{\zeta}{k_BT} NR^2 \approx \frac{\zeta b^2}{k_BT} N^{1+2\nu}. \tag{1.34}$$

As previously stated, for ideal linear chains, $\nu = 1/2$. Therefore, the Rouse time for such chains simply becomes:

$$\tau_R \approx \tau_0 N^2. \tag{1.35}$$

Rouse derived a full expression for the relaxation time of an ideal chain[63], which differed from this derivation by a factor of $1/(6\pi^2)$. Hence, the full expression of the Rouse time is fomulated as:

$$\tau_R = \frac{\zeta b^2}{6\pi^2 k_B T} N^2. \tag{1.36}$$

This is the timescale for an entire Rouse chain to relax. τ_R and τ_0 are important quantities that determine the behaviour of a Rouse chain: when $t < \tau_0$, the beads are unable to relax, and therefore exhibit an elastic response; for $\tau_0 < t < \tau_R$, the response will be viscoelastic; and when $t > \tau_R$, the entire chain is relaxed and will exhibit a viscous response[62].

Equation 1.35 gives the relaxation time of the entire Rouse chain. Therefore the relaxation time for a N/p monomers can be expressed as:

$$\tau_p \approx \tau_0 \left(\frac{N}{p}\right)^2, \tag{1.37}$$

Where $p = 1, 2, 3, ..., N$. From this, it is clear that $p = 1$ and $p = N$ represent the longest and shortest Rouse times respectively. Breaking the chain down into N/p modes gives a spectrum of relaxation modes, each with its own relaxation timescale. Therefore, at time $t = \tau_p$, modes with a higher index than p are mostly relaxed, whereas modes with a lower index than p are mostly unrelaxed[60].

The number of unrelaxed modes at time $t = \tau_p$ is equal to p. Each unrealxed mode can contribute energy of the order of $k_B T$ to the relaxation modulus. This relaxation modulus is proportional to $k_B T$ and the number density of sections with N/p monomers:

$$G(\tau_p) \approx \frac{k_B T}{b^3} \frac{\phi}{N} p. \tag{1.38}$$

Here, ϕ is the volume fraction for the chain with N/p beads. By inserting p from equation 1.37 in to equation 1.38, this yields the relaxation modulus for intermediate timescales:

$$G(t) \approx \frac{k_B T}{b^3} \phi \left(\frac{t}{\tau_0}\right)^{1/2} \quad \text{for} \quad \tau_0 < t < \tau_R. \tag{1.39}$$

Beyond the longest Rouse time (terminal regime), the relaxation modulus will decay as a single exponential. Therefore the relaxation modulus beyond τ_R will be a product of equation 1.38 and a single exponential:

$$G(t) \approx \frac{k_B T}{b^3}\phi\left(\frac{t}{\tau_0}\right)^{1/2}\exp(-t/\tau_R) \quad \text{for} \quad \tau_R < t. \tag{1.40}$$

The relaxation modulus of the entire Rouse spectrum can be be expressed as a sum of each individual Rouse mode[60, 64]:

$$G(t) = \frac{k_B T}{N b^3}\phi\sum_{p=1}^{N}\exp(-t/\tau_p) = \frac{\rho k_B T}{M}\sum_{p=1}^{N}\exp(-t/\tau_p). \tag{1.41}$$

This is the relaxation modulus of the Rouse model. The pre factor here can also be expressed in terms of a density and polymer molecular weight. Using a Fourier transform, this can be expressed as a complex shear modulus in the frequency domain:

$$G^*(\omega) = \frac{\rho k_B T}{M}\sum_{p=1}^{N}\frac{i\omega\tau_p}{1+i\omega\tau_p}. \tag{1.42}$$

Equations 1.41 and 1.42 are the standard expressions of the Rouse model for the relaxation modulus in time and frequency domain respectively. For short chains containing a relatively small amount of Rouse beads, τ_p takes the form[47]:

$$\tau_p = \frac{\tau_1}{sin^2(p\pi/2(N+1))}. \tag{1.43}$$

In this project, the Rouse model was used in this way to describe the relaxation moduli of chain modes for unentangled polymers.

1.3.3 Entanglement and reptation models

Above a certain molecular weight, polymer chains become entangled. This is due to overlapping polymer chains imposing topological constraints on each other, i.e. hindering motion due to the fact that they cannot pass through each other. These restraints are referred to as entanglements[61]. To characterise this behaviour, the tube model is employed, which describes a single polymer chain as being contained

in an imaginary tube, the shape of which is determined by the chemistry of the particular polymer system[64, 65]. A schematic of this is shown in figure 1.9.

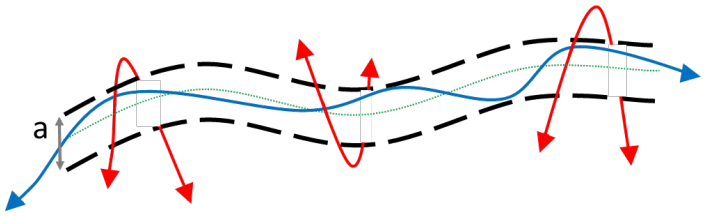

Figure 1.9: A basic schematic showing a polymer chain (blue) constrained due to entanglements from other chains (red) to a tube with diameter a.

The polymer, shown in blue in figure 1.9, can only diffuse within the tube (black dashed lines) due to it being constrained by other polymer chains (shown in red). In this model, each monomer has limited movement and will stick close to the primitive path (shown by the green dotted line) with some fluctuations due to thermal motions which define the diameter of the tube, a[60]. Long chain polymers may have many entanglements per molecule depending on its molecular weight. The molecular weight of the polymer between these entanglements is called the entanglement molecular weight, M_e, which is comprised of N_e Rouse monomers. The tube diameter is related to the end-to-end distance of the entanglement strand, shown in equation 1.44.

$$a \approx bN_e^{1/2}, \tag{1.44}$$

where b is the size of the monomers. This entanglement strand defines the modulus of the rubber plateau (G_e, visualised in figure 1.6):

$$G_e = \frac{\rho k_B T}{M_e}. \tag{1.45}$$

Here, ρ is the density and $k_B T$ is thermal energy. The role of entanglement on the mechanical response is of crucial importance in understanding the dynamics of entangled polymers[60].

The polymer can be viewed as a random walk of either entanglement strands (N/N_e strands of size a) or monomers (N monomers of size b). Thus, the total length of the polmer, R, can be expressed as:

$$R \approx a\left(\frac{N}{N_e}\right)^{1/2} \approx bN^{1/2}. \tag{1.46}$$

The average length of the primitive path, $\langle L \rangle$, is the product of a and N/N_e:

$$\langle L \rangle \approx a\frac{N}{N_e} \approx \frac{b^2 N}{a} \approx \frac{bN}{N_e^{1/2}}. \tag{1.47}$$

For polymers where the chain length is much greater than the strand length ($N >> N_e$), the modulus may be relatively constant over a long time due to entanglements[60]. The occupied volume of an entanglement strand is the product of N_e and the monomer volume, v_0:

$$v_0 N_e = \frac{M_e}{\rho} \approx v_0\frac{a^2}{b^2} \approx \frac{v_0}{b^3}a^2 b. \tag{1.48}$$

Therefore, using equation 1.45, the plateau modulus can be defined as:

$$G_e = \frac{\rho k_B T}{M_e} \approx \frac{k_B T}{v_0 N_e} \approx \frac{b^2 k_B T}{a^2 v_0}. \tag{1.49}$$

This shows that the plateau modulus depends on thermal energy, the tube diameter and the size of the monomers.

Eventually, the polymer chain is able to escape this tube in a mode of motion described by de Gennes as "reptation"[65]. This curvilinear motion along the tube is characterised by the friction coefficient, ζ[60] and the curvilinear diffusion coefficient, describing the motion of the polymer along the tube is defined as:

$$D_c = \frac{k_B T}{N\zeta}. \tag{1.50}$$

The time the chain takes to diffuse out of its original tube of length $\langle L \rangle$ is:

$$\tau_{rep} \approx \frac{\langle L \rangle^2}{D_c} \approx \frac{\zeta b^2 N^3}{N_e k_B T}. \tag{1.51}$$

Here, τ_{rep} is often referred to as the reptation time. Equation 1.51 suggests that $\tau_{rep} \propto N^3$. However, modifications to this simple model allow for (i) tube length fluctuations, whereby the size of the tube changes due to Rouse motion at the chain ends, and (ii) constraint release, whereby tubes may reorganise due

to entanglement release from the motion of the surrounding chains[64]. Taking these factors into account, one finds that $\tau_{rep} \propto N^{3.4}$[65].

These models can predict the relaxation modulus, $G(t)$, for entangled polymer systems. On length scales shorter than N_e, relaxation dynamics are still governed by Rouse dynamics. The crossover from Rouse dynamics to entanglement dynamics occurs at the timescale τ_e:

$$\tau_e \approx \tau_0 N_e^2. \tag{1.52}$$

Here, τ_e is often referred to as the entanglement time and is simply the Rouse time of an entanglement strand.

Many models exist that predict relaxation moduli of entangled polymers using the tube model[66–68]. For this project, the Likhtman-McLeish model[5] was used to describe the relaxation moduli of polymer dynamics. This is a tube model for linear, monodisperse polymers, which assumes that different contributions to the moduli can be broken down into different components: (i) constraint release, (ii) longitudinal relaxation modes along the tube and (iii) Rouse modes between entanglements.

1.3.4 Molecular weight and microstructure

The polymer chains in a sample will not contain exactly the same number of monomer units i.e. there will be some degree of polydispersity. To distinguish between grades of polymers, the number average, M_n and weight average, M_w, molecular weights are defined[61, 69]. These are shown in equation 1.53 and 1.54.

$$M_n = \sum \frac{n_i M_i}{n_i} \tag{1.53}$$

$$M_W = \sum \frac{n_i M_i^2}{n_i M_i} \tag{1.54}$$

where n_i is the number of molecules of molecular weight M_i, which are summed up over i molecular weights. M_n is simply the total weight of a sample divided by the total number of polymers in that sample whereas M_W depends on both

the number of polymers but also on the weight of each polymer. From these two quantities, the polydispersity index, PDI, can be defined as follows:

$$PDI = \frac{M_W}{M_n}. \tag{1.55}$$

Samples which contain chains of identical molecular weight are "monodisperse", which corresponds to PDI=1. Through careful polymerisation techniques, low PDI samples can be produced. However, in reality, polymeric samples will always have some degree of polydispersity.

Gel permeation chromatography (GPC) can be used to characterise the molecular weight distribution of a sample[61]. This is a form of size exclusion chromatography, which differentiates between molecules of different sizes by the speed at which they can move through a porous medium. Smaller molecules will have a larger retention time due to them being able to diffuse in and out of the pores. An example of a typical molecular weight distribution of two polymers with different PDI is shown in figure 1.10.

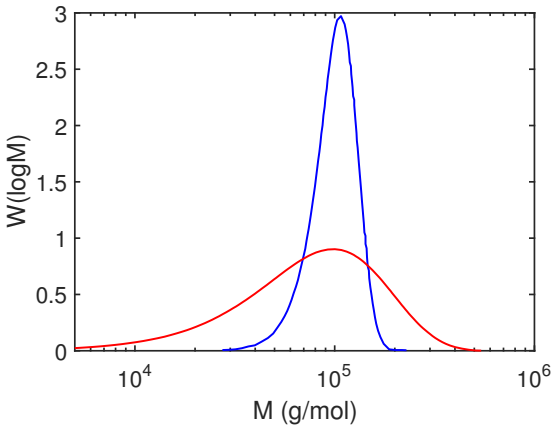

Figure 1.10: Mass fraction, W, as a function of molecular weight, M, for two different samples with $M_W = 100$kg/mol, but different PDI.

Figure 1.10 shows the mass fraction of two samples, both with $M_W = 100$kg/mol, but different PDI. The red curve has a higher PDI, and is clearly broader than the blue curve with a lower PDI. Of course, $W(\log M)$ does not necessarily have a smooth distribution, this depends entirely on polymerisation technique and this

may be tailored to suit particular needs. Multi-modal distributions can also be obtained by mixing samples of different M.

Throughout this project, we focused primarily on relatively monodisperse oligomeric/polymeric samples (PDI$<$ 1.44) to reduce the effects of polydispersity on the measured relaxation dynamics.

Tacticity

Another important property of polymer systems are the side groups attached to the main polymer backbone. The relative orientation of side groups with respect to the backbone is termed 'tacticity', which can vary due to chiral centres in the backbone[61].

Tacticity can have large effects on polymer behaviours such as viscosity, glass formation, and crystallisation. Therefore, knowledge of this is crucial when attempting to characterise any polymer system. The different types of tacticity are:

- Atactic - Side groups randomly orientated along the chain.
- Isotactic - All the side groups are orientated in a single direction along the chain.
- Syndiotactic - Side groups are in alternating positions along the chain.

This relative orientation of side groups along the chain can be tailored through particular synthesis techniques and can be determined post synthesis through experimental techniques such as NMR[70, 71]. In this project, all polymer systems are reported to be atactic by their manufacturers and therefore side groups should have no overall directional preference relative to each other.

1.4 Poly(methyl methacrylate)

A polymeric system of particular importance to this project was poly(methyl methacrylate) (PMMA). This section will provide a brief overview of literature relevant to this work.

PMMA is more commonly known as acrylic, or by its original trade name "Perspex". It has a wide variety of both commercial and industrial applications: from a high-impact glass substitute, to medicine and dentistry. The PMMA molecular structure is shown in figure 1.11.

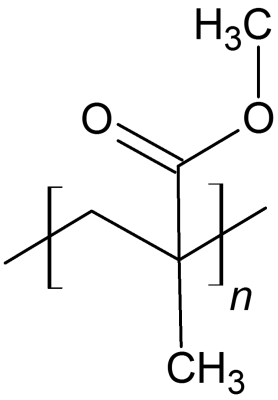

Figure 1.11: Poly(methyl methacrylate) (PMMA) molecule, monomer molecular weight $M_0 = 100$g/mol.

PMMA is a vinyl polymer with a monomer molecular weight of $M_0 = 100$g/mol. It is commonly produced via free radical polymerisation of methyl methacrylate.

The first significant study of the mechanical properties of PMMA was performed in 1940 by Alexandrov and Lazurkin in the USSR[72]. They measured the effect of frequency and temperature on deformation due to an applied sinusoidal stress. This was, in effect, a study of the structural relaxation dynamics.

Early work done in the 1950s and 60s laid the groundwork in characterising both the rheological and dielectric responses of polymeric PMMA[47]. These studies encompassed chain modes, α, β, and γ dynamics for long-chain PMMA, providing detailed relaxation behaviour over a wide dynamic range. Since then, more detailed rheology studies have been carried out, such as looking at sub-rouse dynamics using higher resolution techniques[73], finding that the onset of these relate to the merging of the α and β relaxations. It is also noted that the merging of these relaxation mechanisms appears to occur at the same temperature when measured using rheology[74] and broadband dielectric spectroscopy

(BDS)[75]. However, due to the differences in these techniques, the corresponding τ_α is different by an order of magnitude.

Other work using BDS by Casalini and Roland[76] yielded $\tau_\alpha(T)$ below T_g, which was shown to correspond to the decay in the dielectric strength of the β relaxation. This was consistent with a more direct determinations of $\tau_\alpha(T)$ below T_g for PMMA[77]. This group also performed pressure dependent dielectric and calorimetric measurements on PMMA[78], whereby they determined the number of dynamically correlated units in the α relaxation as a function of τ_α. Interestingly, they found that unlike fragility, which shows pressure dependence, the number of dynamically correlated units does not alter with pressure. This shows a disconnect between dynamic heterogeneities and fragility.

The size of the dynamically correlated region (related to the number of dynamically correlated units) has been determined for long-chain PMMA by others using differential scanning calorimetry (DSC)[79, 80]. This has been found to be between $\xi_a \sim 1.5 - 2.5$nm, which is consistent with other fragile polymeric systems.

The effects of tacticity and end-groups of both oligomeric[81] and long-chain[82] PMMA has been studied using ^{1}H and ^{13}C NMR, which allows for these properties to be determined using this technique. PMMA is also a well studied polymer in molecular dynamics simulations (MD)[83–85] with particular focus on the effects of tacticity on the T_g.

1.4.1 Molecular weight studies

In this project, the molecular weight dependence of the dynamics of PMMA was a primary focus. An early example of a systematic molecular weight, M, study on PMMA was carried out by Thompson[3] in 1966. This focused on the heat capacity response measured using differential thermal analysis (DTA) over the glass transition on a range of oligomeric and polymeric samples with varying tacticity. It was shown that within this M range, T_g exhibits Fox-Flory behaviour[86]. A more recent DSC study by O'Driscoll et. al.[4] showed that a modified Fox-Flory expression had to be employed when including small molecular weight PMMA samples.

Further DSC studies by Andreozzi et. al.[87] showed disagreement with the potential energy landscape model for PMMA whereby, with changing M, the change in heat capacity between liquid and glass and dynamic fragility, m, did not correlate as they do for small molecular glass formers. Low molecular weight PMMA samples have been studied using BDS and DSC by Casalini et. al.[88]. They determined an equation of state from PVT measurements and comment on the large T_g and m change across this low M range, attributing it to the relatively low chain flexibility in PMMA compared to other polymer systems.

Two examples of rheological measurments of PMMA, covering the large oligomer to polymer M range, looked at how both M and tacticity affect entanglement, viscosity, and T_g[89, 90]. Fuchs *et. al.* comment that these properties of PMMA within this M range exhibit no outlying behaviour with respect to other polymer systems.

In 2018, Zulli et. al.[91] measured the viscosity and the rotational diffusion (of a probe molecule) of a relatively monodisperse PMMA M series spanning from small molecular glass former to polymer. This was performed using both rheology and electron spin resonance spectroscopy. They note that a decoupling between the viscosity and rotational diffusion of the probe occurs at $M \sim 1200$g/mol, and that at this point there is a changeover between small molecular to polymer behaviour. This general finding is consistent with work done in this project.

1.5 Thesis overview

This thesis will discuss work done in characterising the rheological, dielectric, and calorimetric responses of chain length series of linear polymer systems, with particular focus on PMMA. An overview of each chapter is shown below.

Chapter 3 focuses on the rheological response of a chain-length series of PMMA spanning from small molecular glass former to fully entangled polymer. This data was analysed and modelled using standard techniques, including applying time-temperature superposition (TTS) over the dynamic range spanning from the glass to the melt. The dielectric and calorimetric responses were compared to rheology in order to determine the validity of using TTS across this

dynamic range, which may be invalid due to the decoupling of chain and segmental, α, dynamics. We show that TTS is approximately valid in describing the α relaxation, whereby τ_α values obtained from TTS and broadband dielectric spectroscopy can be superimposed over a wide dynamic range. τ_α data are compared to other polymer systems, and we note a "universal" scaling of chain dynamics, and τ_α at longer times when normalised by T_g/T. We suggest a link between this universality and the size of the correlated region of the α relaxation.

In chapter 4, the results from advanced calorimetric and dielectric techniques are presented. These measurements were performed in order to determine the number of correlated units involved in the α relaxation. This was carried out on a PMMA, PS, and PDMS chain-length series spanning from small molecular glass former to fully entangled polymer. The effect of the difference in flexibility/fragility between PMMA, PS, and PDMS was apparent in the number of cooperative units as a function of molecular weight. We surmise that rigid/fragile polymer systems such as PMMA and PS exhibit a changeover between a mostly intermolecular and a more intramolecular cooperativity as chain behaviour becomes apparent.

Lastly, chapter 5 contains work done to determine the role of chain-length on the coupling of ionic conductivity and the α relaxation. This was performed on a PMMA, PPG, and PPG-DME molecular weight series. We show that these dynamics decouple in relatively rigid/fragile PMMA series when chain behaviour becomes apparent, whereas this decoupling does not occur in the flexible/strong PPG and PPG-DME series. This is also compared to small molecular glass formers of varying fragility and T_g, which all show coupling between ionic conductivity and the α relaxation. Therefore, it is noted that any correlations between these fragility or T_g and decoupling is due to polymeric behaviour.

Chapter 2

Experimental

In this chapter, the experimental techniques used in the work will be outlined. These were: Shear rheology; Broadband Dielectric Spectroscopy (BDS); and Differential Scanning Calorimetry (DSC). These techniques provide access to relaxation dynamics over timescales spanning $10^{-8} < \tau < 10^{3}$s, each having their own advantages and disadvantages in probing different relaxation mechanisms in glass forming materials. While this chapter outlines the basic principles of these techniques and the equipment used, more specific details on the interpretation of the data will be discussed within other chapters as required.

2.1 Rheology

"We see how quickly through a colander the wines will flow; how, on the other hand, the sluggish olive-oil delays: no doubt, because 'tis wrought of elements more large, or else more crook'd and intertangled"
- On the Nature of Things, Lucretius 99-55BC[92].

The term Rheology comes from the Greek, literally meaning "the study of flow". Varying rheological properties of materials are apparent in nature: from water, which flows freely, exhibiting viscous properties, to steel, which deforms upon imparting large forces, displaying elastic properties. Material behaviour between these two extremes are coined viscoelastic properties[8]. These varying properties are a result of how the atoms or molecules within a material interact

and move, and hence measurements of these properties give information on both the microscopic structure and dynamics of these materials.

In this section, the principles needed to determine the complex shear modulus of viscoelastic liquids and polymers, both in the melt and glassy states, will be outlined. Along with this, the rheological equipment and testing methods will be discussed in the context of well established literature and procedures.

2.1.1 The complex shear modulus

The shear modulus is defined as a material's resistance to a shear deformation. Quantitatively, this is the ratio of shear stress to shear strain, as visualised in figure 2.1.

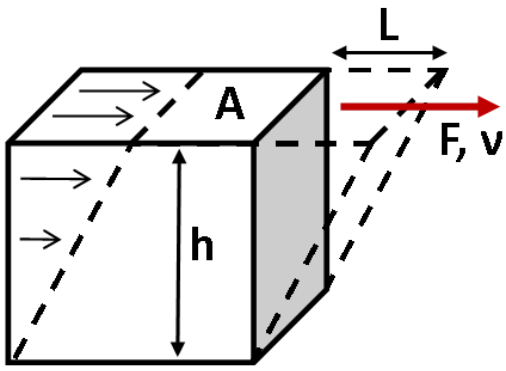

Figure 2.1: Visualisation of a shear deformation resulting from an applied a shear force.

Figure 2.1 shows a simple schematic of a shear deformation induced by an applied shear force. From this, a few basic terms are defined:

- Shear stress, $\sigma = F/A$, is the shear force, F, applied perpendicular to area A. This has the unit of $\mathrm{N/m^2}$.
- Shear strain, $\gamma = L/h$, is the normalised deformation of the material due to the applied shear stress; the strain is dimensionless.
- Shear rate, $\dot{\gamma} = \nu/h$, is the rate of change of the shear stress, which has the unit $\mathrm{s^{-1}}$.

These definitions hold for the deformation of a simple rectangular geometry. Using these quantities, both the shear modulus, G, and viscosity, η, are defined using equations 2.1 and 2.2 respectively.

$$\sigma = G\gamma \tag{2.1}$$

$$\sigma = \eta\dot{\gamma} \tag{2.2}$$

These are the basic definitions of a Hookean solid (defining G) and a Newtonian liquid (defining η), and are applicable to ideally elastic and viscous materials. If a sinusoidal strain, $\gamma = \gamma_0 \sin(\omega t)$ (where γ_0 is the amplitude of the strain), is applied, equations 2.1 and 2.2 become equations 2.3 and 2.4 respectively.

$$\sigma(t) = G\gamma(t) = G\gamma_0 \sin(\omega t) \tag{2.3}$$

$$\sigma(t) = \eta\dot{\gamma}(t) = \eta\gamma_0\omega \cos(\omega t) = \eta\gamma_0\omega \sin(\omega t + \pi/2) \tag{2.4}$$

In the case of an ideal elastic response shown in equation 2.3, $\sigma(t)$ and $\gamma(t)$ are in-phase, i.e. $\delta = 0$ (where δ is the stress-strain phase angle). Whereas, for an ideal viscous response shown in equation 2.4, $\sigma(t)$ and $\gamma(t)$ are out of phase by $\delta = \pi/2$. Generally, materials are viscoelatic and thus exhibit both elastic and viscous properties. An example of the stress-strain behaviour of a viscoelastic material is shown in figure 2.2.

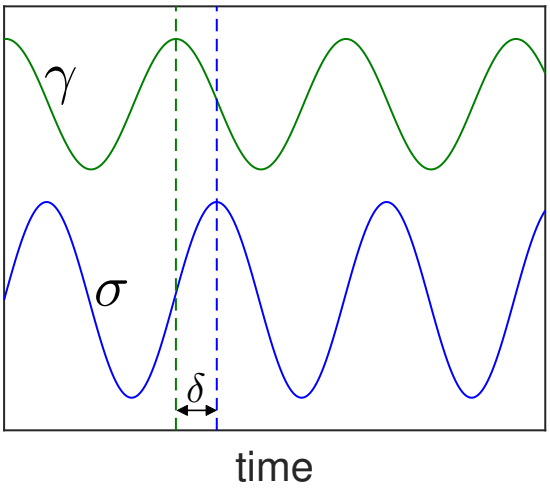

Figure 2.2: An applied oscillatory strain, $\gamma(t)$, resulting in a stress, $\sigma(t)$, out of phase by angle, δ.

Figure 2.2 shows a typical stress-strain response of a viscoelastic material, whereby upon the application of an oscillatory strain, $\gamma(t) = \gamma_0 \sin(\omega t)$, the resulting stress leads the strain by some phase angle, $\sigma(t) = \sigma_0 \sin(\omega t + \delta)$ (where σ_0 is the amplitude of the stress). This behaviour defines the complex shear modulus, as shown in equation 2.5.

$$G^* = \frac{|\sigma_0|}{|\gamma_0|} e^{i\delta} = G' + iG'' \tag{2.5}$$

Using Euler's relation ($e^{i\delta} = \cos(\delta) + i\sin(\delta)$), G' and G'' can be expressed as equations 2.6 and 2.7.

$$G' = \frac{|\sigma_0|}{|\gamma_0|} \cos(\delta) \tag{2.6}$$

$$G'' = \frac{|\sigma_0|}{|\gamma_0|} \sin(\delta) \tag{2.7}$$

These define G' and G'' as the in-phase (elastic) and out-of-phase (viscous) components of the complex shear modulus. G' is often referred to as the storage modulus, as this represents energy stored during deformation which reforms the material to its original shape once the load has been released. In contrast, G''

is often referred to as the loss modulus, as it represents the energy lost during deformation[8]. A loss factor is therefore defined as the ratio of these two components, as shown in equation 2.8.

$$\tan\delta = \frac{G''}{G'} \tag{2.8}$$

$\tan\delta$ is referred to as the loss tangent, and describes whether a material repose is more elastic (G' dominant, $\tan\delta < 1$) or more viscous (G'' dominant, $\tan\delta > 1$).

2.1.2 The Maxwell model and stretched exponential

A basic model for viscoelatic materials is that of the Maxwell model. This is comprised of a spring and dashpot in series[93], as shown in figure 2.3.

Figure 2.3: Maxwell model, comprised of a spring (with modulus G_0) and dashpot (with viscosity η) in series.

Upon an instantaneous deformation (strain), a Maxwell model will exhibit an elastic response (G_0). However, over time the addition of the dashpot will allow the system to relax through viscous flow. This gives rise to a single exponential decay function, shown in equation 2.9.

$$G_{MW}(t) = G_0 \exp(-t/\tau) \tag{2.9}$$

This is a single exponential decay with characteristic timescale $\tau = \eta/G_0$, where G_0 is the instantaneous shear modulus at $t = 0$. For an oscillatory experiment, as outlined in section 2.1.1, the can be expressed in complex form, as shown in equation 2.10.

$$G^*_{MW}(\omega) = i\omega \int_0^\infty \mathrm{e}^{i\omega t} G_{MW}(t)\mathrm{d}t = G_\infty \frac{i\omega\tau}{1 + i\omega\tau} \tag{2.10}$$

Equation 2.10 can be obtained through a Fourier transform of equation 2.9, yielding the complex shear modulus of the Maxwell model. The instantaneous shear modulus, G_∞, now occurs at infinite frequency, and is equivalent to G_0 from equation 2.9. The complex shear modulus of the Maxwell model is shown in figure 2.4.

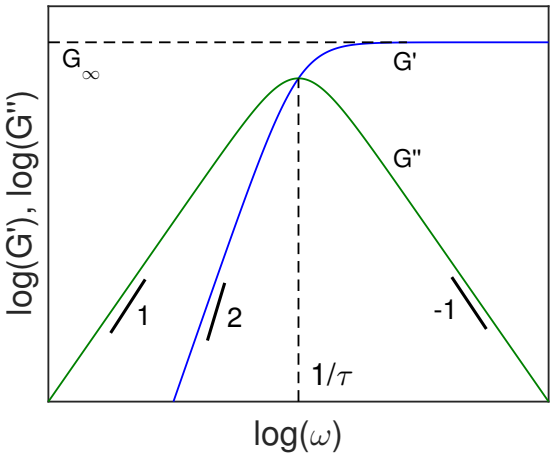

Figure 2.4: Maxwell model showing log-log behaviour of $G'(\omega)$ and $G''(\omega)$ of complex shear modulus.

The low frequency ($\omega < \tau$) behaviour for the Maxwell model shown in figure 2.4 shows power-law behaviour, with slopes of 2 and 1 for G' and G'' respectively. This is characteristic of terminal (melt) behaviour. At higher frequencies ($\omega > \tau$), G' reaches a plateau with modulus G_∞, and G'' falls off with a power-law slope of -1.

This Maxwell model is the simplest relaxation spectrum corresponding to a single relaxation mode. In reality, relaxation spectra are generally more complex, containing a distribution of relaxation modes. A common alteration of the simple Maxwell model is a stretched exponential, or Kohlrausch-Williams-Watts (KWW) expression[94]. In the time domain, this is shown in equation 2.11.

$$G_{KWW}(t) = G_0 \exp\left[-(t/\tau)^\beta\right] \tag{2.11}$$

This expression is similar to equation 2.9, with the addition of a stretching parameter β, which when constrained to $0 < \beta < 1$ leads to broadening of the

relaxation spectra. The KWW expression has no analytic expression in the frequency domain, and therefore requires a numerical Fourier transform to convert to a complex shear modulus. However, Bergman[95] produced a simple expression which approximates the imaginary response of the frequency dependent KWW expression, $G''_{KWW}(\omega)$. This is produced through a simple ansatz describing a minimum representing the inverse loss peak (originally described for the dielectric loss, but is applied here to loss modulus), $G''(\omega)$, which is characterised by low and high frequency power-law behaviour. This is shown in equation 2.12.

$$\frac{G''_p}{G''(\omega)} = A\omega^{-a} + B\omega^{b} + C \tag{2.12}$$

Here, $-a$ and b correspond to the low and high frequency power-law flanks respectively, and a C is a constant setting the bluntness of the minimum. The derivative of equation 2.12, should be zero at the minimum, occurring at ω_p, which leads to equations 2.13 and 2.14

$$A = \left(\frac{b(1-C)}{a+b}\right)\omega_p^{a} \tag{2.13}$$

$$B = \left(\frac{a(1-C)}{a+b}\right)\omega_p^{-b} \tag{2.14}$$

By inserting these expressions in equation 2.12, this yields equation 2.15.

$$G''(\omega) \approx \frac{G''_p}{\frac{(1-C)}{a+b}\left[b\left(\frac{\omega}{\omega_p}\right)^{-a} + a\left(\frac{\omega}{\omega_p}\right)^{b}\right] + C} \tag{2.15}$$

Equation 2.15 is very general response function for $G''(\omega)$, which can describe a loss peak using 5 parameters. Where, G''_p and ω_p describe the peak loss modulus and frequency respectively, a and b describe the low and high frequency power-law behaviours respectively, and C effects the bluntness of the maxima. By setting $a = 1$ and $C = 1 - b$, this has been shown to describe the loss peak of a KWW expression in the frequency domain to a very good approximation[95]. This expression is shown in figure 2.16.

$$G''_{KWW}(\omega) \approx \frac{G''_p}{1 - \beta + \frac{\beta}{1+\beta}[\beta(\omega_p/\omega) + (\omega/\omega_p)^{\beta}]} \tag{2.16}$$

In this expression, G''_p and ω_p also describe the peak modulus and frequency of G'', and therefore ω_p relates to the characteristic timescale ($\tau = 1/\omega_p$). The b parameters from equation 2.15 is now the KWW stretching parameter, β, in equation 2.16. Examples of this expression are shown in figure 2.5.

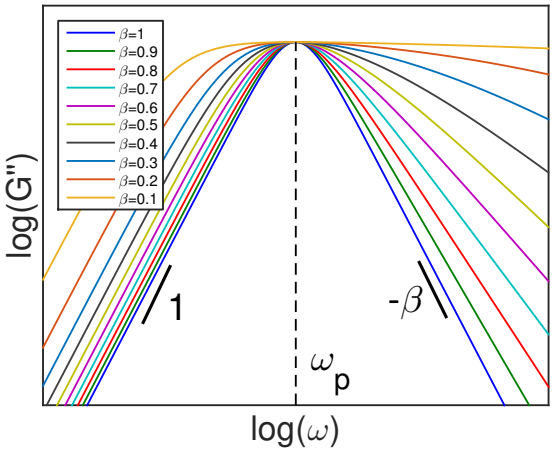

Figure 2.5: KWW approximation for G'' from equation 2.16 showing the effect of stretching parameter β.

The effect of a decrease in the stretching parameter, β, is apparent in figure 2.5. For $\beta = 1$, this simply corresponds to $G''(\omega)$ of the the Maxwell model (shown previously in figure 2.4), with high and low frequency power-law flanks of 1 and -1 respectively. As β decreases, the high frequency flank broadens, displaying a power-law behaviour with slope $-\beta$.

This analytic approximation of the KWW expression only produces $G''(\omega)$, whereas $G''(\omega)$ also has a corresponding $G'(\omega)$. G' and G'' are related through the Kramer-Kronig relation[96], and therefore G' can be obtained based on G''. A method of obtaining G' from G'' for this KWW approximation will be discussed in section 3.1.2.

2.1.3 Time-temperature superposition

The complex shear modulus response of materials can be complicated, with dynamics spanning many decades in frequency. Typically, shear rheometers are able to perform measurements over frequency ranges from $\sim 10^{-3}$rad/s to a few

hundred rad/s[97]. This limits the amount of dynamic information which can be obtained.

In order to probe dynamic behaviour over a wider frequency range, a time-temperature superposition (TTS) technique can be employed. This is achieved by performing complex shear modulus measurements at discrete temperatures, and superimposing these onto data measured at a reference temperature. Therefore, this approach yields a wider frequency response at the reference temperature.

TTS is only valid if all relaxation modes contributing to $G^*(\omega)$ at these temperatures have the same temperature dependence (also known as a thermorheologically simple reponse[98]), i.e. changing temperature will have the same effect as shifting frequency[61]. If this assumption holds, then the relaxation timescales can be described using a single frequency (horizontal) shift factor per temperature, shown in equation 2.17.

$$a_T = \frac{\tau(T)}{\tau(T_0)} = \frac{\omega(T_0)}{\omega(T)} \tag{2.17}$$

The frequency shift factor a_T is the ratio of the timescale (or frequency) of the response measured at temperature T to that measured at the reference temperature T_0.

A modulus (vertical) shift factor is also sometimes appropriate, which for chain modes (Rouse or entanglement behaviour), can be quantified using equation 2.18.

$$b_T = \frac{\rho_0 T_0}{\rho T} \tag{2.18}$$

This modulus shift factor b_T is based on density variations between temperatures, effecting the modulus in the regime where rubber elasticity is applicable[47]. For modulus contributions from the α relaxation, this is not the case. However, over typical temperature ranges which TTS is used, the modulus variations are typically small. Therefore, it is recommended that either equation 2.18 is applied when appropriate (and when $\rho(T)$ data is available), or that no modulus shift factor is applied ($b_T = 1$)[61].

In glass forming polymers, both the structural (α) relaxation and chain modes are often assumed to have the same temperature dependence[8] (at least at short α relaxation timescales, which will be discussed further in section 3.5). As such,

frequency measurement at discrete temperatures, capturing both α and chain dynamics, should collapse onto a common master curve using a single shift factor per temperature . An examples of this is shown in figure 2.6.

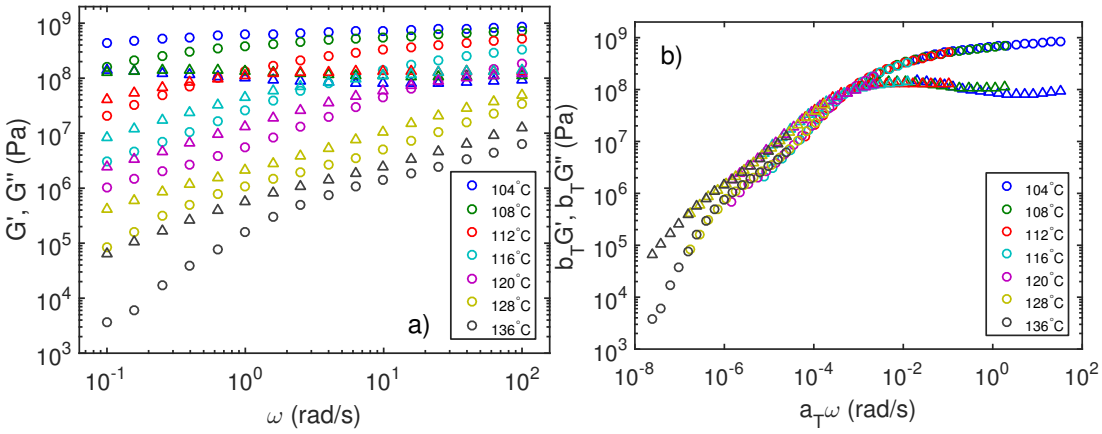

Figure 2.6: PMMA oligomer (n=96). a) Complex shear modulus measurements performed at discrete temperatures. b) TTS master curve constructed by frequency shifting all data sets onto an arbitrary reference temperature. Circles and triangles are G' and G'' respectively.

Figure 2.6 (a) shows frequency sweep data taken at discrete temperatures for a non-entangled PMMA sample. These frequency sweeps were performed in a frequency range between $\omega = 10^{-1} - 10^{2}$rad/s (three decades in frequency is generally considered the minimum required to perform TTS[98]). Figure 2.6 (b) is the same data as in (a), but superimposed by frequency shifting ($b_T = 1$, as vertical shifting was unnecessary) onto a common arbitrary reference temperature.

The frequency shift factors are often described using a Williams-Landel-Ferry (WLF) equation[99], as shown in equation 2.19.

$$\log(a_T) = \frac{-C_1(T - T_0)}{C_2 + (T - T_0)} \tag{2.19}$$

This is an alternative to the VFT equation (as discussed in section 1.2.1), which describes the frequency shift factors in terms of parameters C_1 and C_2, and the reference temperature T_0. It has been suggested that for an appropriate choice of T_0 (close to T_g), C_1 and C_2 are approximately universal for temperatures far

enough above T_g ($C_1 = 17.4$, and $C_2 = 51.6$K). This potential universality will be discussed further in section 3.5.

2.1.4 ARES shear strain-controlled rheometer

In order to measure the complex shear modulus, a Rheometrics (now TA instruments) ARES (Advanced Rheometric Expansion System) rheometer was used. This is a strain-controlled shear rheometer with a forced convection oven using either compressed air, or liquid nitrogen (LN2) to control the sample temperature between $-150 < T < 300$°C. A basic schematic of this strain-controlled operation is shown in figure 2.7.

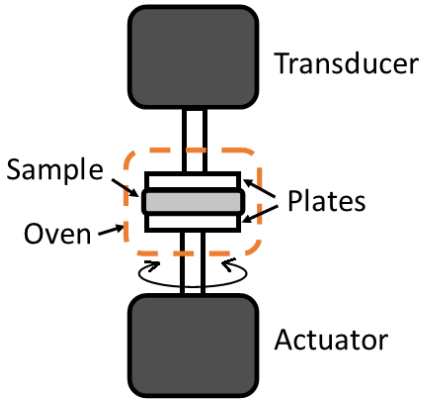

Figure 2.7: Schematic of strain-controlled shear rheometer, with separate actuator and transducer.

Rather than the deformation of simple rectangular geometry shown previously in figure 2.1, this ARES strain-controlled shear rheometer applies an angular deformation using a rotary actuator, with a frequency range of $10^{-5} < \omega < 5 \times 10^2$rad/s. The resulting torque is measured using a rotational transducer, with a torque range of $4 \times 10^{-6} < M < 2 \times 10^{-2}$Nm, on the other side of the sample.

Different sample geometries allow measurements of a wide range of viscosities and shear moduli. In this project, a parallel plate geometry was used, which consists of two circular parallel plates, with radius r, adhered to the sample

between them, with height h. A basic schematic of the sample between these plates is shown in figure 2.8.

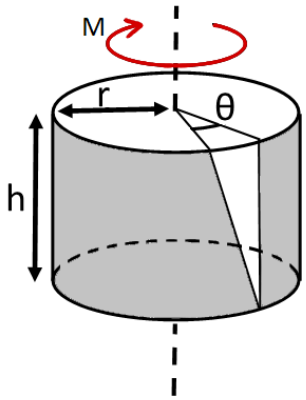

Figure 2.8: Parallel plate sample of heigh h, and radius r. A toque, M, is applied, which shears the sample, resulting in an angular deformation, θ.

This geometry was used because: (i) using small sample diameters (3mm), it allowed us to measure high shear moduli (up to $\sim$ 2x10^{9}Pa); (ii) due to these small geometries, only a small amount of sample was required; and (iii) it allowed for the adjustment of sample height when changing temperature due to thermal expansion, which is not possible when using a cone and plate geometry. For the parallel plate geometry, the resulting shear stress and applied shear strain are calculated using equations 2.20 and 2.21.

$$\sigma = \frac{2M}{\pi r^3} \tag{2.20}$$

$$\gamma = \frac{r\theta}{h} \tag{2.21}$$

Here, θ and M are the angular deformation of the rotary actuator and the resulting transducer torque respectively, and r and h are the sample radius and height respectively (shown in figure 2.8). The strain field of the parallel plate geometry is inhomogeneous, i.e. the strain is maximum at the plate radius, and zero at $r = 0$. However, this was not an issue due to the fact that measurements were performed within the linear viscoelastic region (LVR), whereby the stress-strain response does not change (this will be discussed in detail in section 2.1.5).

Using equations 2.20 and 2.21, the complex shear modulus is defined by equation 2.22.

$$G^* = \frac{\sigma^*}{\gamma^*} = \frac{2M^*h}{\pi\theta^* r^4} \tag{2.22}$$

Where M^* and θ^* are the complex torque and angular deformation. From equation 2.22, it is clear that a small error in r could lead to a larger error in G. Therefore, maintaining a fixed sample shape throughout the experiment was crucial.

2.1.5 Linear viscoelastic regime tests

The applied strain, for a given temperature, had to be chosen so that the response was both within the linear viscoelastic regime (LVR), and within the torque range of the transducer over the measured frequency window. Outside of the torque range of the rheometer, the results obtained would not be reliable, and an applied torque which is too high could cause permanent damage to the transducer. An example of transducer torque with increasing strain at different temperatures around the α relaxation is shown in figure 2.9.

Figure 2.9 shows five measurements whereby the modulus increases with decreasing temperature. A slope of 1 on this log-log of plot of torque, M, against strain, γ, indicates measurements are within the LVR, as indicated by the straight lines. The gray dashed lines indicate the transducer torque range. The measurements shown in figure 2.9 are across the α relaxation of a simple non-polymeric glass forming material (penta phenyl-trimethyltri-siloxane, or Dow Corning DC705 diffusion pump oil[1]). The chemical structure of DC705 is shown in figure 2.10.

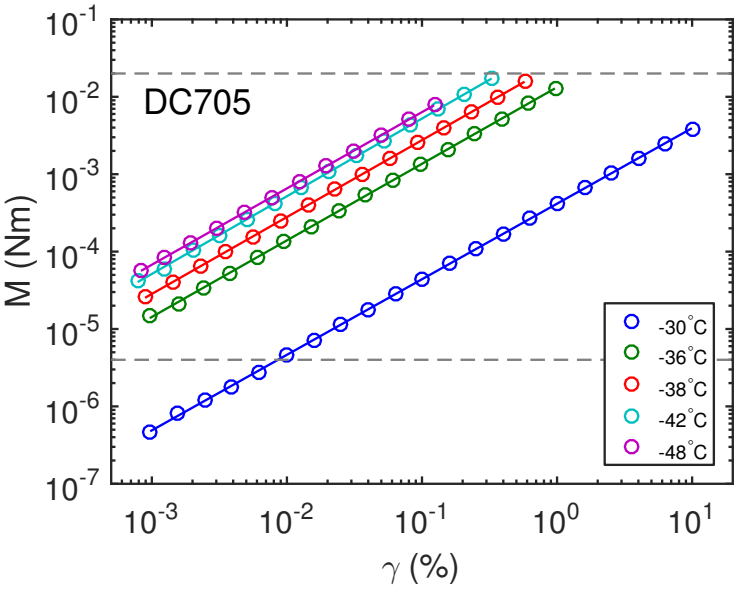

Figure 2.9: 1Hz strain sweep measurements on DC705. Linear fits of torque and strain (with a slope of 1 on this log-log scale) indicate measurements are within the LVR. Gray dashed lines indicate torque range of the transducer.

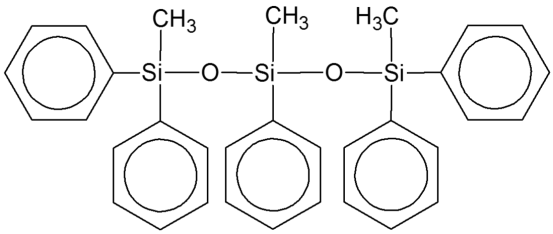

Figure 2.10: Penta phenyl-trimethyltri-siloxane (DC705) molecule[1]. Molecular weight, $M = 546$g/mol.

DC705 was used for testing α responses throughout this project because:

- It is a liquid at room temperature, which makes it easy to use in the lab.
- It readily forms a glass (easily avoiding crystallisation) at an easily accessed temperature ($T_g \sim -45$°C).
- It exhibits no clear secondary relaxations in any technique used in this project. Therefore, measurements showed an isolated, clear α relaxation

response.

- It has been measured using shear rheology previously[100] with a piezo strain gauge (PSG) technique, which measures the complex shear modulus over a wide frequency range without relying on TTS.
- It has an extremely low vapour pressure, allowing many thermal cycles without mass loss.

In figure 2.9, as the sample goes from melt to glass (higher to lower temperature), the strain had to be reduced in order to remain within the transducer torque range (shown by the gray dashed lines). While the relations between torque (proportional to stress) and applied strain appear proportional (showing a slope of 1 in this log-log plot), the complex shear modulus (G' and G'') was plotted against applied strain in order to investigate this further. An example of the shear-dependent for the same sample and temperatures as figure 2.9 is shown in figure 2.11.

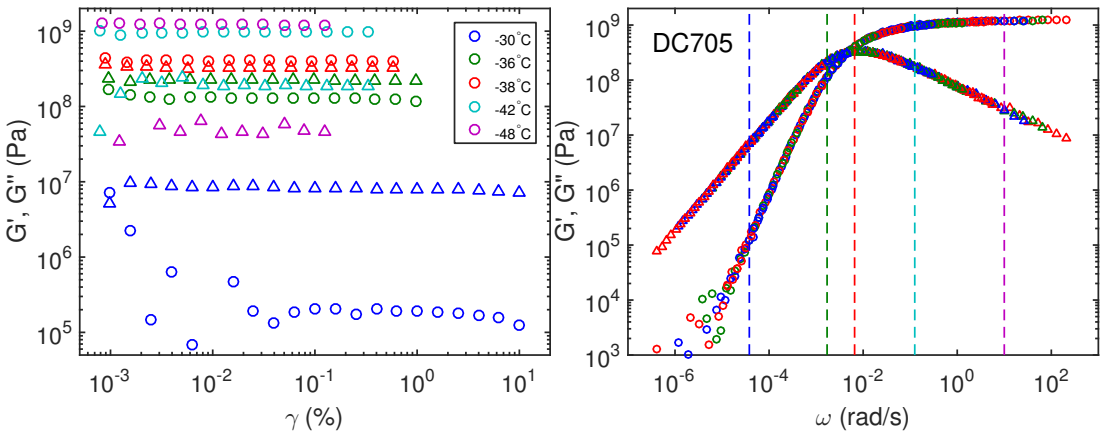

Figure 2.11: DC705 strain sweep tests. (a) 1Hz complex shear modulus as a function of strain. (b) TTS master curve with dashed lines indicating the position of these strain sweeps (shown in (a)). Alternating red, green, and blue sections indicate frequency sweeps taken as discrete temperatures, with circles and triangles representing G' and G'' respectively.

Figure 2.11 (a) shows G' and G'' at the same temperatures shown in figure 2.9 as a function of strain, γ, for DC705. This indicates that for for strains higher

than $\gamma \sim 5\%$ at $-30°C$, the response is starting to deviate from the linear regime (below $\gamma \sim 0.05\%$ is below the torque range of the transducer, which is shown in figure 2.9). The other temperatures and strains are within the LVR. A strain was chosen for each temperature so that with changing frequency, the response would remain within both the transducer torque range and the LVR. Figure 2.11 (b) shows the TTS master curve constructed from frequency measurements performed at different temperatures. The dashed lines indicate the positions of the strain sweeps from 2.11 (a).

2.1.6 Test of rheometer compliance effects

It is often assumed that the rheometer and sample tools have negligible compliance compared to that of the sample. However, for rigid samples, such as polymers approaching their glassy state, this may not be the case. Thus, if the compliance of the rheometer tools or related machinery becomes comparable to the sample compliance, then the shear stiffness (un-normalised shear modulus, $K = M/\theta$) measured by the rheometer will be false due to both the sample and machine responding to the deformation. An approximate schematic of this scenario is shown in figure 2.12.

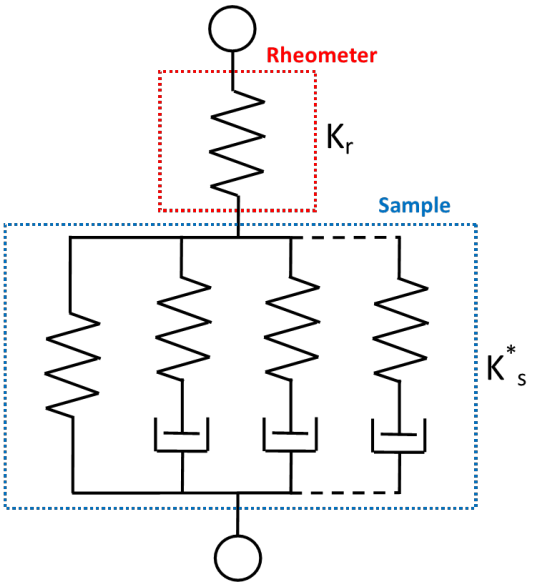

Figure 2.12: A simple schematic showing both rheometer (K_r) and sample (K_r) contributions to the total sample stiffness.

The schematic in figure 2.12 shows the total stiffness, K_T^*, measured by the rheometer as having contributions from the rheometer/tool, represented by a single elastic spring (K_r), and the sample, represented by a generalised Maxwell model (K_s^*). Quantitatively this can be described by equation 2.23.

$$\frac{1}{K_T^*} = \frac{1}{K_s^*} + \frac{1}{K_r} \tag{2.23}$$

One method to account for K_r is to directly measure it using connected parallel plates with no sample present, and subtracting this stiffness from subsequent measurements on samples[101]. However, in order to see if this was necessary, a simple test was carried out[102]. This entailed performing linear dynamic shear modulus measurements on the same simple non-polymeric glass forming material as introduced in section 2.1.5 (DC705) from the melt to the glassy state using a range of different parallel plate diameters (d=3, 5, and 8mm).

Considering that the shear stiffness scales as $K \propto d^4$ (shown in equation 2.22), by changing the sample diameter from 3 to 8mm, the stiffness increases by more than 50 times if the sample height is kept the same. If machine compliance is an issue, one would clearly observe this in the rheological response. These results

were also compared to literature data on the same sample[100], measured using a PSG method, where machine compliance was not observed. These are shown in figure 2.13.

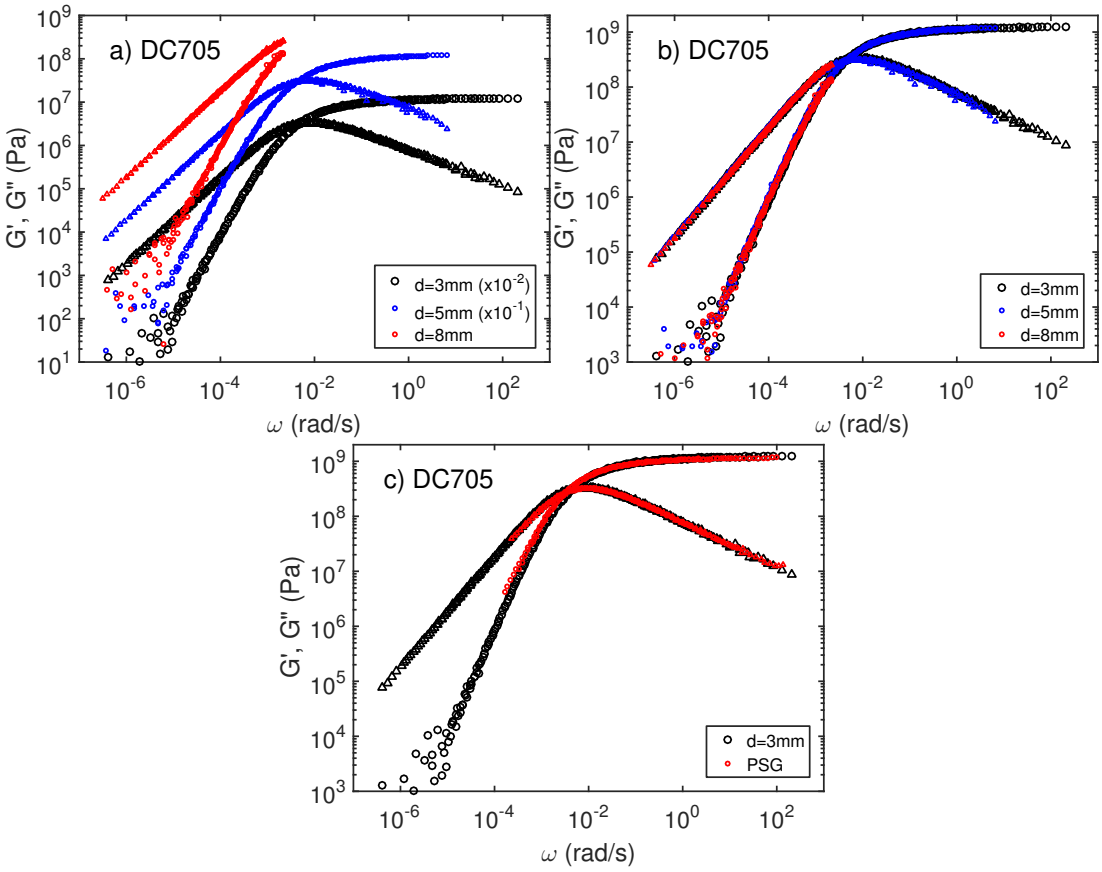

Figure 2.13: TTS master curves of DC705. A comparison between different diameter parallel plates, (a) modulus shifted to distinguish between curves, and (b) actual modulus values. (c) 3mm diameter parallel plates compared to literature PSG data.

Figure 2.13 (a) and (b) shows that for d=8mm, the high frequency data was limited due to rheometer actuator/transducer limitations, as this sample is more than 50 times stiffer than for d=3mm with the same sample height. However, d=3mm and d=5mm show very good agreement, indicating that machine compliance was not an issue. This is further indicated in figure 2.13 (c), whereby

our d=3mm data and literature data performed using the PSG, yielded the same response.

If machine compliance was an issue when measuring these glassy moduli, then the largest source would be the stainless steel tools which are in contact with the sample. A schematic of this is shown in figure 2.14.

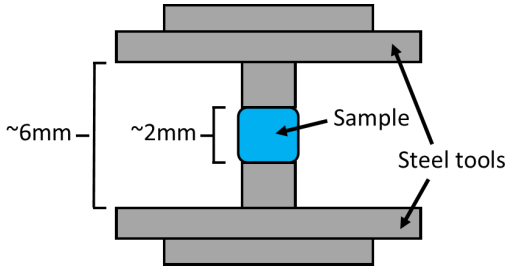

Figure 2.14: Small diameter (d=3mm) parallel plate tools.

Figure 2.14 shows a schematic of the steel tools that we designed and constructed to perform high modulus shear rheology experiments. The two nubs, in direct contact with the sample, are approximately twice the typical height of the sample, which was minimised so as to contribute as little to the machine/tool compliance as possible. Stainless steel has a shear modulus of $\sim$ 80GPa, and in the glassy regime the polymer samples have a typical modulus of $\sim$ 1GPa. Therefore, considering $K \propto h^{-1}$, the steel nubs are $\sim$ 40 times stiffer than the sample. In order to assess the potential effects of this, these compliances were simulated using the simple relation shown in equation 2.23. This is shown in figure 2.15.

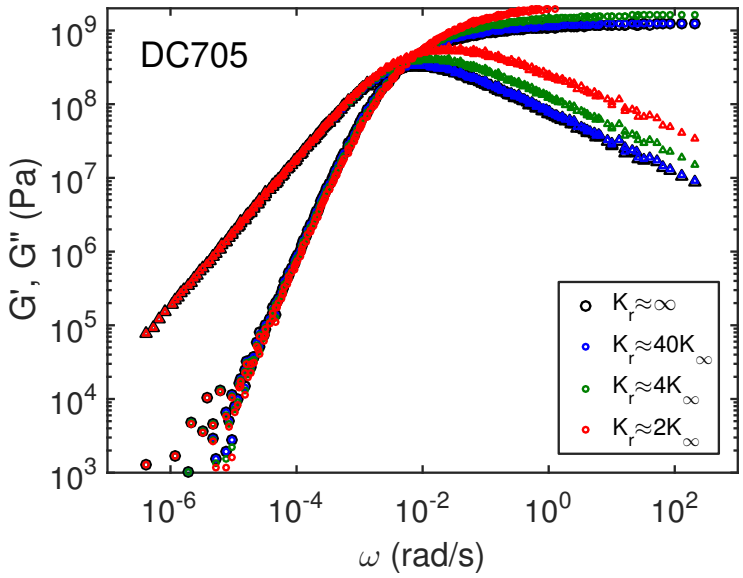

Figure 2.15: TTS master curve of DC705, simulating the complex shear modulus if machine/tool stiffness is comparable to sample stiffness.

Figure 2.15 shows what the shear modulus of the DC705 would be if the stiffness of the rheometer/tools (K_r) was comparable to the glassy shear modulus of the sample (K_∞). Where this is only 2 times stiffer than the glassy modulus (red data in figure 2.15), there is a distinct difference between what is measured and what would be the real shear modulus in the glassy regime. However, as we approach the estimate of 40 times stiffer (blue data in figure 2.15), this difference all but vanishes.

Given these comparisons between plate diameter, literature data, and simulating the effects of machine compliance, the contribution to the shear modulus from the rheometer itself was deemed not to be an issue for these measurements.

2.2 Broadband Dielectric Spectroscopy

2.2.1 Dielectric properties of materials

Many materials are dielectric, meaning that in the presence of an electric field there is only a transient displacement of charges (dipoles) rather than the migration of charges as in a conductor. The modes through which these dipoles

reorientate and relax due to an applied electric field are coupled to the molecular relaxation processes present in the material[14].

Broadband dielectric spectroscopy (BDS) is a technique which can be used to measure the frequency dependent permittivity of a sample which relates to the displacement of dipoles in the presence of an electric field. Therefore, this technique can be used to access information of the relaxation phenomena coupled to the reorientation of dipoles in a material. This section will outline the physical principles and equipment used in performing BDS measurements to access both relaxation behaviour and ion mobility in glass forming materials.

2.2.2 Polarisation and relaxation of materials

From Maxwell's equations, the relationship between an electric field applied to a material ($\boldsymbol{E}$) and the resulting dielectric displacement field ($\boldsymbol{D}$) can be defined using the following equation [14]:

$$\boldsymbol{D} = \epsilon\epsilon_0\boldsymbol{E}. \tag{2.24}$$

Here, ϵ_0 and ϵ are the permittivity of free space, and the relative permittivity of the material respectively. Assuming the electric field strength is relatively small, there is a linear relationship between $\boldsymbol{E}$ and the polarisation ($\boldsymbol{P}$):

$$\boldsymbol{P} = (\epsilon - 1)\epsilon_0\boldsymbol{E}. \tag{2.25}$$

Upon the application of an electric field, a material will polarise. If the applied electric field is removed, the polarisation will relax back to its equilibrium value due to thermal fluctuations[103–105], as shown in figure 2.16.

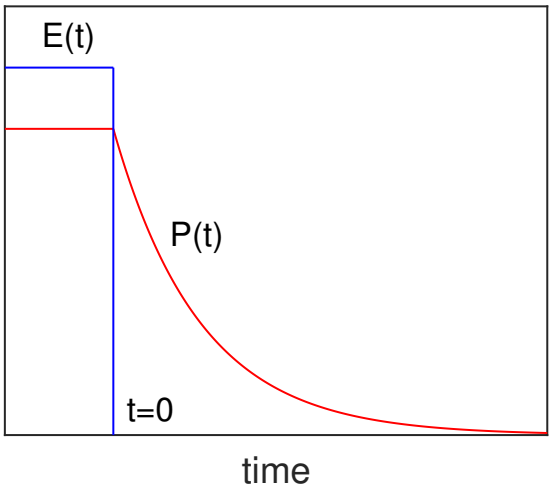

Figure 2.16: An electric field across a polarised material ($\boldsymbol{E}(t)$, shown by the blue line) is removed at $t = 0$. The resulting polarisation ($\boldsymbol{P}(t)$, shown by the red line) decays towards zero.

The general relaxation function of $\boldsymbol{P}(t)$ can be expressed as:

$$\boldsymbol{\phi}(t) = \frac{\boldsymbol{P}(t)}{\boldsymbol{P}(0)}. \tag{2.26}$$

If the applied electric field strength is small, then the perturbation of the material is limited. If this is the case, the response of the material obeys fluctuation dissipation theorem[14]. This states that the response of the sample due to external perturbation is equivalent to that caused by thermal fluctuations in equilibrium. Therefore, measurement of the polarisation of a material subjected to an electric field with appropriate strength yields a response relating to the molecular dynamics of the material.

If an oscillatory electric field, $\boldsymbol{E}^*(\omega)$, is applied, the resulting polarisation, $\boldsymbol{P}^*(\omega)$, can be expressed as follows:

$$\boldsymbol{P}^*(\omega) = (\epsilon^*(\omega) - 1)\epsilon_0 \boldsymbol{E}^*(\omega). \tag{2.27}$$

Where ϵ^* is the frequency dependent complex permittivity, defined as:

$$\epsilon^*(\omega) = |\epsilon^*|(\omega)\mathrm{e}^{-i\delta(\omega)} = \epsilon'(\omega) - i\epsilon''(\omega). \tag{2.28}$$

Here, ϵ' and ϵ'' are the real and imaginary components of the permittivity. These relate to the energy stored and energy lost as a function of frequency, analogous to the complex shear modulus (disscussed in section 2.1.1) [106]. In relation to equation 2.24, ϵ' and ϵ'' relate to the in-phase ($\delta = 0$), and out-of-phase ($\delta = \pi/2$) ratios of $\boldsymbol{D}^*$ and $\boldsymbol{E}^*$.

In the frequency domain, the relationship between $\boldsymbol{\phi}(t)$ and the complex permittivity is:

$$\frac{\epsilon^* - \epsilon_\infty}{\Delta\epsilon} = 1 - i\omega \int_0^\infty \boldsymbol{\phi}(t) \mathrm{e}^{-i\omega t} \mathrm{d}t \tag{2.29}$$

Where ϵ_∞ and $\Delta\epsilon$ are the high frequency permittivity, and the change in permittivity respectively. $\Delta\epsilon$ can be quantified via Curie's law[14, 107]:

$$\Delta\epsilon = \frac{1}{3\epsilon_0} \frac{\mu^2}{k_B T} \frac{N}{V}. \tag{2.30}$$

In this expression, μ is the strength of the dipole moment, $k_B T$ is thermal energy, and N/V is the number density of the dipoles. This describes the dielectric strength due to orientational polarisation. However, it assumes that dipoles do not interact with each other, and that that local field effects, or shielding of the electric field, are negligible[14].

In the simplest case, the decay of $\boldsymbol{\phi}(t)$ is a single exponential:

$$\boldsymbol{\phi}(t) = \mathrm{e}^{-t/\tau}, \tag{2.31}$$

where τ is the characteristic decay time. By inserting this expression into equation 2.29, this leads to an expression for the so-called Debye relaxation:

$$\epsilon^*(\omega) = \epsilon_\infty \frac{\Delta\epsilon}{1 + i\omega\tau_D}. \tag{2.32}$$

A Debye relaxation represents a simple, single relaxation mode caused by the reorientation of non-interacting dipoles. The real and imaginary components of this are shown in figure 2.17.

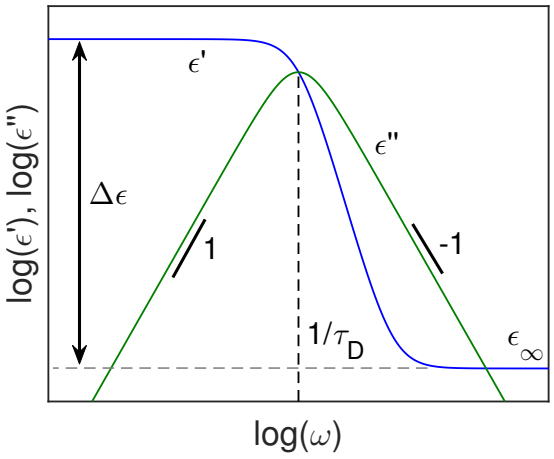

Figure 2.17: Debye model showing log-log behaviour of $\epsilon'(\omega)$ and $\epsilon''(\omega)$ of complex permittivity.

The Debye relaxation manifests itself as a step in $\epsilon'(\omega)$ and a peak in $\epsilon''(\omega)$ occurring at $\omega = 1/\tau_D$. ϵ' plateaus at ϵ_∞ and $\epsilon_\infty + \Delta\epsilon$ at high and low frequencies respectively. The response function of ϵ'' is a symmetric peak with power-law exponents of -1 and 1 for the low and high frequency flanks. This is an idealised response function and rarely represents relaxation phenomena. An empirical alternative used in this project, which can account for more complex behaviour, will be discussed in section 2.2.5.

2.2.3 DC conductivity

Migration of charged species (ions) through a material will contribute to the complex permittivity[14]. This additional response manifests as a low frequency power-law flank in ϵ'':

$$\epsilon^*_{cond}(\omega) = -i\frac{\sigma}{\epsilon_0\omega} \tag{2.33}$$

The strength of the DC conductivity (σ) relates to both the molecular diffusion and the number density of ions present. Therefore, DC conductivity may drown out the permittivity contribution from relaxation dynamics at higher temperatures if the ion content is significant. This can be reduced by cleaning the samples

to remove the ions if required[108]. At higher temperatures, an ionic contribution in ϵ' due to electrode polarisation can be observed.

2.2.4 Novocontrol Alpha-A analyser

BDS measurements in this work were performed using a Novocontrol Alpha-A dielectric analyser, through which complex permittivity measurements could be performed over a frequency range of $10^{-2} < \nu < 10^{6}$Hz. The sample cryostat was connected to a Quatro Cryosystem allowing measurements to be conducted over a temperature range of $100 < T < 700$K with an accuracy of ± 0.1K.

A BDS experiment is carried out by applying a oscillatory voltage across the sample and measuring the resulting current[38]. A basic circuit schematic of this is shown in figure 2.18.

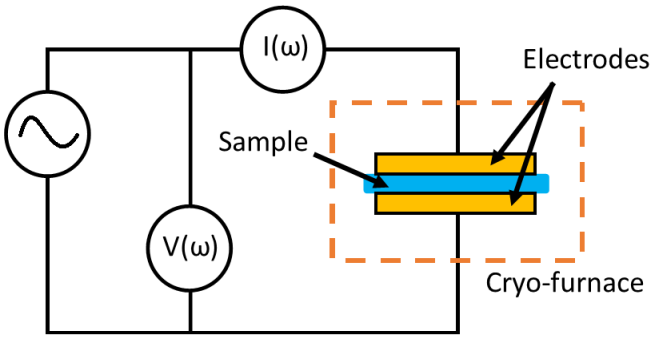

Figure 2.18: Circuit schematic setup of a broadband dielectric spectrometer.

An oscillatory voltage, $V(\omega)$, is applied across the sample sandwiched between two electrodes with known area and distance between the electrode plates. The resulting current, $I(\omega)$, across the sample is then measured. Frequency dependent measurements of voltage and current across the sample yield the impedance, as shown by equation 2.34.

$$Z^*(\omega) = \frac{|V^*|(\omega)}{|I^*|(\omega)} \mathrm{e}^{i\delta} = Z'(\omega) + iZ''(\omega) \tag{2.34}$$

Where Z' and Z'' are the in-phase (resistive, $\delta = 0$), and out-of-phase (capacitive, $\delta = \pi/2$) components of Z^*. From this, the complex permittivity can be calculated using equation 2.35.

$$\epsilon^*(\omega) = \frac{-i}{\omega Z^*(\omega) C_0} \tag{2.35}$$

Here, C_0 is the capacitance of an empty sample cell, defined as $C_0 = \epsilon_0 A/d$, where A is the electrode area (20mm diameter), and d is the sample thickness (0.1mm).

Two electrode configurations were used depending on if the sample was solid or liquid at room temperature. These two configurations are shown in figure 2.19

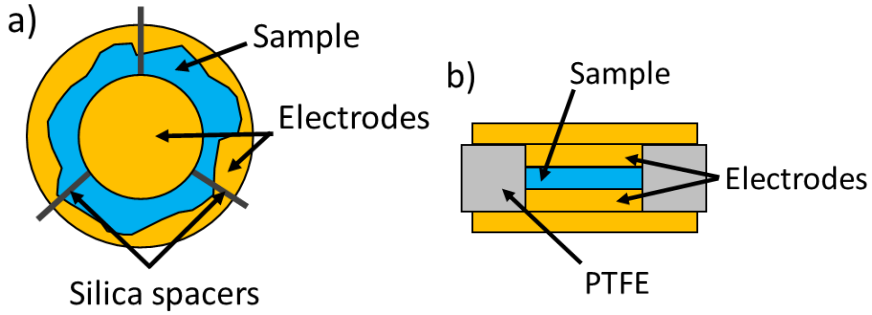

Figure 2.19: Electrode configurations used in BDS for: a) solid samples (top down view); and b) liquid samples (cross section).

For solid samples, figure 2.19 (a) shows the electrode configuration used. The sample was prepared on a 40mm diameter brass electrode, silica spacers with a thickness of 0.1mm were placed in the sample as shown, and a smaller (20mm) brass electrode was placed on top of the sample.

For liquid samples, a Novocontrol BDS 1308 liquid cell was used, as shown in figure 2.19 (b). The basic sample geometry of the cell consists of two 20mm diameter electrodes with silica spacers and the samples in between. These electrodes are contained within a Teflon ring sitting in a brass dish with a brass 30mm 'lid' electrode placed on top.

2.2.5 Dielectric response functions

In section 2.2.2, the response function of a single, simple, relation mode was described and the Debye model. However, in most cases, the step in ϵ' and the peak in ϵ'' for a particular relaxation mode are broader than those predicted by

this model. Thus, empirical modifications of equation 2.32 are commonly used to describe measured relaxation modes. One example of these is the Havriliak-Negami (HN) expression[109]:

$$\epsilon^*(\omega) = \epsilon_\infty + \frac{\Delta\epsilon}{(1 + (i\omega\tau_{HN})^\alpha)^\beta} \tag{2.36}$$

This expression contains two empirical parameters, α and β, which quantify the symmetric and anti-symmetric stretching of an observed relaxation mode: in ε'', the exponent of the low frequency flank of a dielectric loss peak is α and the exponent of the high frequency flank is $\alpha\beta$. The expression reduces to the Debye model if $\alpha = \beta = 1$.

Symmetric broadening of a relaxation mode can be described through variation of α between 0 and 1 when $\beta = 1$. In this case equation 2.36 reduces to the so-called Cole-Cole (CC) expression[110]. The effect of variation of α is shown in figure 2.20.

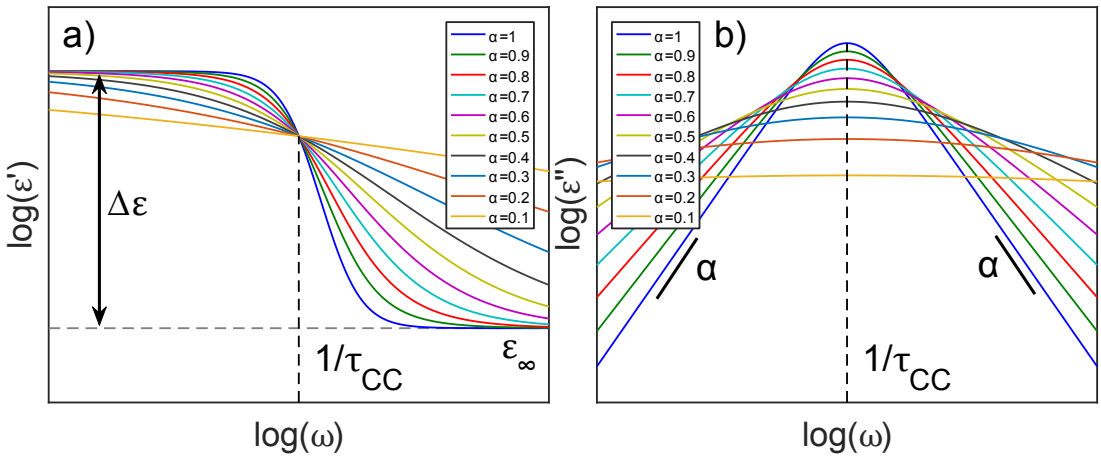

Figure 2.20: ϵ' (a) and ϵ'' (b) for Cole-Cole (Havriliak-Negami, where $\beta = 1$) relaxation with different α parameters.

Lower values of α lead to a greater degree of symmetric broadening. Secondary relaxation mechanisms are often well described using the CC expression. τ_{HN} in this case is inversely proportional to the peak frequency in ϵ'' and therefore the characteristic relaxation time ($1/\omega''_{peak} = \tau$).

Anti-symmetric broadening can be described through variation of β between 0 and 1, holding α constant: $\alpha = 1$.This is known as the Cole-Davidson (CD) expression[111]. The effect of variation of β is shown in figure 2.21.

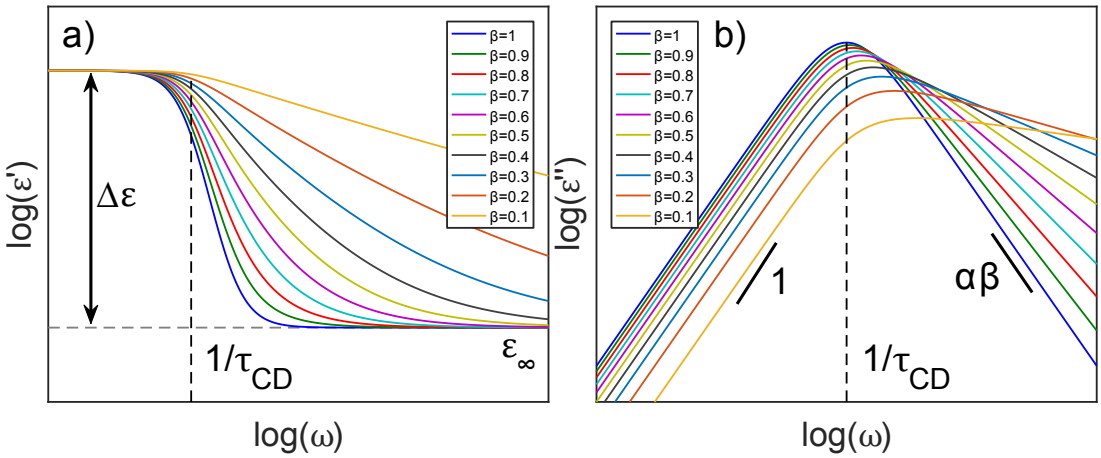

Figure 2.21: ϵ' (a) and ϵ'' for Cole-Davidson (Havriliak-Negami, where $\alpha = 1$) relaxation with different β parameters.

Once again, for $\beta = 1$ in figure 2.21, the simple Debye relaxation is obtained. Decreasing values of β, increases asymmetrical broadening. In some systems, the α relaxation can be adequately described using a CD relaxation. However, in most cases, α relaxation modes demonstrate both symmetric and asymmetric broadening and so the full HN expression is required.

In the case of asymmetric relaxations, where $\beta \neq 1$, τ_{HN} does not correspond to either the average relaxation time, or the most probable relaxation time (the peak frequency in ϵ''), i.e. $1/\omega''_{peak} \neq \tau_{HN}$. Therefore, to correct for this, the following expression is used[14].

$$\frac{1}{\tau_p} = \frac{1}{\tau_{HN}} \left[\sin \frac{\alpha\pi}{2+2\beta}\right]^{1/\alpha} \left[\sin \frac{\alpha\beta\pi}{2+2\beta}\right]^{-1/\alpha} \tag{2.37}$$

In glass forming materials, the complex permittivity measured using BDS can contain contributions from multiple different relaxation mechanisms. An example of $\epsilon^*(\omega)$ at a single temperature for a small molecular glass former (PMMA, $n = 3$) is shown in figure 2.22.

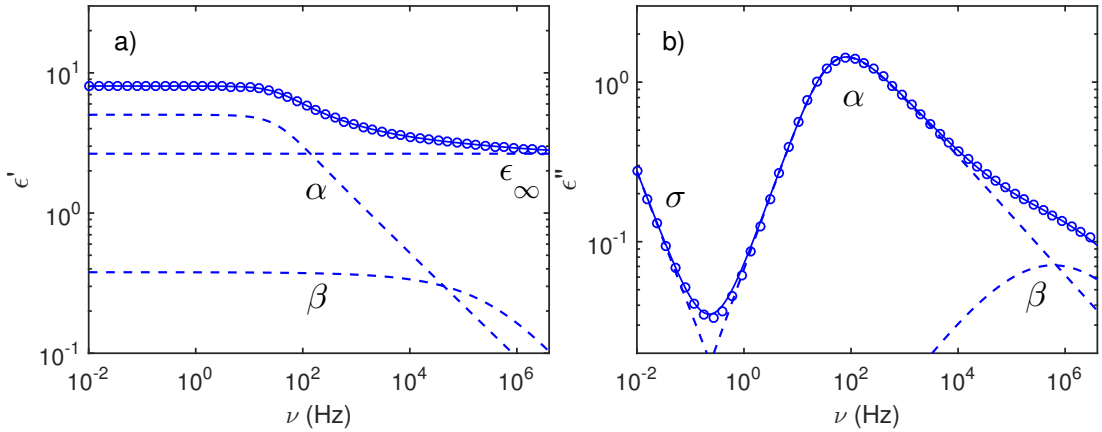

Figure 2.22: ϵ' (a) and ϵ'' (b) as a function of frequency for PMMA n=3 at 225K. The solid line represents fitting of the entire spectra, and dashed lines show the individual contributions to the spectra.

The contributions to $\epsilon^*(\omega)$ at each temperature can be described using sum of relevant terms. For example:

$$\epsilon^*(\omega) = \frac{-i\sigma}{\omega} + \sum_{j=1}^{N} \frac{\Delta\epsilon_j}{(1 + (i\omega\tau_{HN,j})^{\alpha,j})^{\beta,j}} + \epsilon_\infty \tag{2.38}$$

This is the HN equation for N relaxations (α, β, γ, etc) visible in the frequency window at a particular temperature combined with a DC-conductivity contribution (from equation 2.33). Figure 2.22 shows ϵ'' contributions from three different mechanisms. The α and β relaxations are describe using the HN and CC functions respectively and the conductivity is described by a negative power-law slope. The different contributions to ε'' are denoted by the dashed lines in figure 2.22. The combination of these relaxation functions (formulated using equation 2.38) is shown by the solid lines interpolating the data.

Typically, we fit either the full complex response, or ϵ'' spectra because: (i) the releaxation peaks are easier to paramaterise than steps, with the relaxation time being inversely proportional to the peak frequency (or related to in the case where $\beta \neq 1$); and (ii) one fewer fitting parameter is required as ϵ_∞ does not contribute to ϵ''[14].

In some cases, including that shown in figure 2.22, the DC conductivity contribution can obscure peaks in ϵ''. ϵ' and ϵ'' obey the Kramer-Kronig relations, meaning that they can be transformed between each other. Wübbenhorst and Turnhout[112] suggested an approximate form for ϵ'', formulated using the derivative of ϵ':

$$\epsilon''_{deriv}(\omega) = -\frac{\pi}{2}\frac{\partial\epsilon'(\omega)}{\partial \ln\omega} \approx \epsilon''(\omega) \tag{2.39}$$

This frequency derivative of $\epsilon'(\omega)$ adequately describes $\epsilon''(\omega)$. An example of this conversion is shown in figure 2.23.

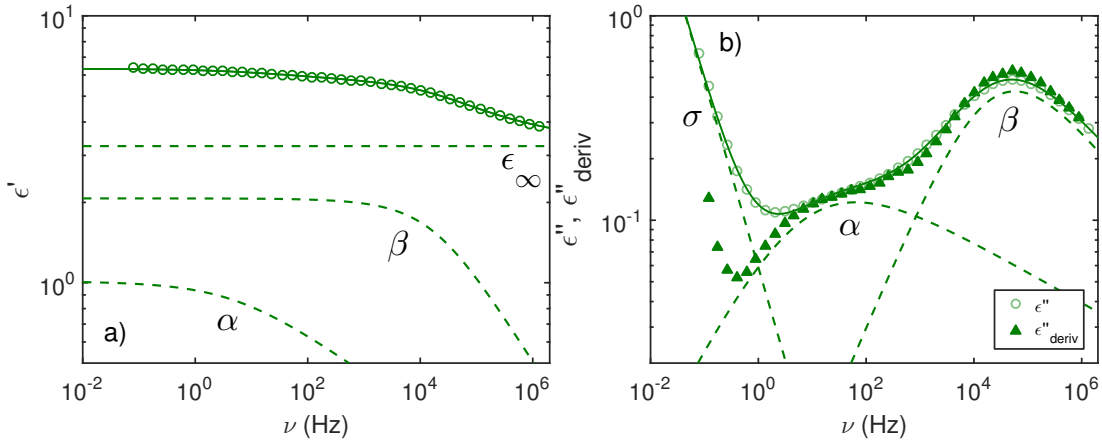

Figure 2.23: a) $\epsilon'(\omega)$ of PMMA n=906 at 404K. b) $\epsilon''(\omega)$ and $\epsilon''_{deriv}(\omega)$ calculated using equation 2.39 from $\epsilon'(\omega)$. The solid line represents fitting of the entire spectra, and dashed lines show the individual contributions to the spectra.

$\epsilon''_{deriv}(\omega)$ appears to approximately match up to $\epsilon''(\omega)$ in figure 2.23 (b), which was calculated from $\epsilon'(\omega)$, shown in figure 2.23 (a), using equation 2.39. While the shape of these two versions of ϵ'' may vary slightly, it has been shown that the peak frequency (the inverse of the characteristic relaxation time) is generally preserved. This makes it an ideal tool for obtaining relaxation times when the relaxation spectra is obscured by DC conductivity.

2.3 Differential Scanning Calorimetry

In this section, the background and application of differential scanning calorimetry (DSC) measurements in this project will be discussed. DSC is a technique which involves measurement of the difference in heat flow, $\mathrm{d}Q/\mathrm{d}T$, between a sample and a reference as a function of temperature [113]. The ratio of the heat flow and the heating/cooling rate ($\mathrm{d}T/\mathrm{d}t$) yields the heat capacity of the sample:

$$C_P = \frac{\mathrm{d}Q}{\mathrm{d}t} \Big/ \frac{\mathrm{d}T}{\mathrm{d}t}. \tag{2.40}$$

DSC measurements enable characterisation of the enthalpy changes associated with thermodynamic transitions within a sample and the temperature at which they occur. The isobaric specific heat capacity, c_p, as a function of temperature for an amorphous small molecular glass former on heating is shown in figure 2.24.

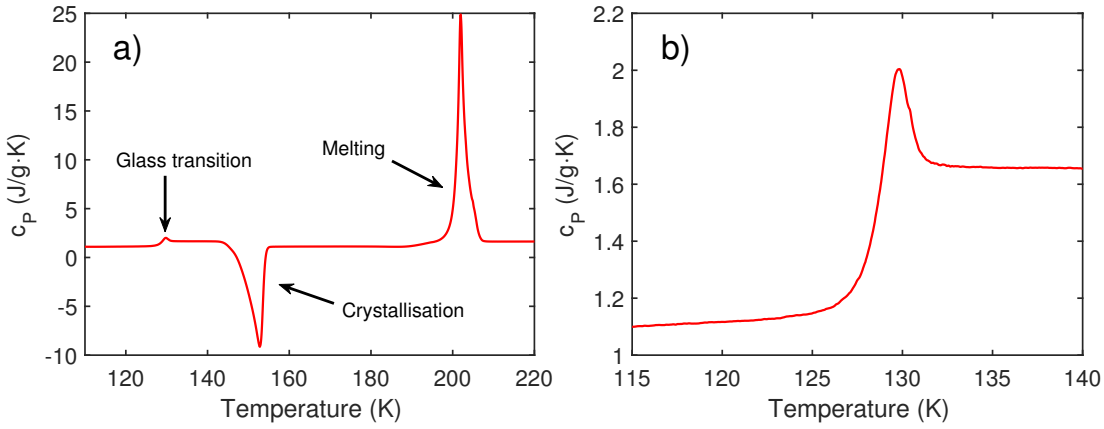

Figure 2.24: c_p as a function of T measured on heating for amorphous PDMS trimer (n=3). a) Entire heat capacity spectra with typical features labelled. b) Enlarged glass transition region from (a).

Figure 2.24 is that of a PDMS trimer (n=3) that had been quenched (to avoid crystallisation) from above its melting point, T_m, to below T_g. Once in this glass, the $c_p(T)$ was measured on heating, which is shown in figure 2.24 (a). The data has three distinct features. The first of these is the glass transition, observed as a step-like change in the heat capacity due to the difference in the available molecular degrees of freedom in the glassy and super-cooled liquid states[9]. Upon

further heating, a trough in c_p is observed indicating crystallisation. This so-called 'cold crystallisation' can occur at temperatures below the melting point, T_m, for some polymers (such as PDMS) due to the increase of molecular motions in the supercooled state. For this reason, polymers that crystallise readily below T_m must be quenched in order to analyse their glass transitions. This is done by plunging the sample into liquid nitrogen to rapidly cool it, and them placing it into the pre-cooled DSC. Finally, at T_m, the sample melts, indicated by a peak in c_p. The area under the melting peak corresponds to the enthalpy of fusion[113]. In this case, this area which should equal that of the cold crystallisation peak, under the assumption that the sample was quenched into an entirely amorphous state to begin with.

A close-up representation of the glass transition for this sample is shown in figure 2.24 (b). In such a representation, one can observe a clear overshoot of the glass transition step, occurring at $T \approx 130$K. This is due to the thermal history of the material, and is often referred to as the enthalpy relaxation[114]. This occurs due to enthalpy recovery of the sample while in the glassy state. A idealised example of the change in enthalpy as a function of temperature is shown in figure 2.25.

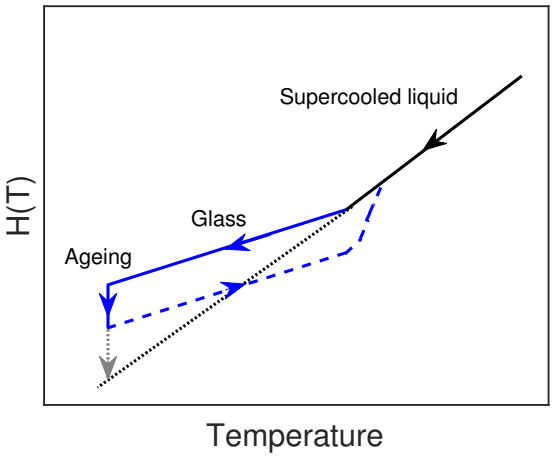

Figure 2.25: Enthalpy (H) as a function of temperature for a supercooled liquid cooled below T_g, aged in the glassy state, and subsequently reheated above T_g.

This figure shows a representation of the enthalpy behaviour of a glass forming

material which has been cooled from the supercooled liquid (equilibrium) state below T_g, aged within the glassy state, and subsequently reheated above T_g. A material in the non-equilibrium glassy state will evolve towards the equilibrium state[115, 116]. This is indicated by the gray arrow, whereby the longer the sample is aged, the lower the enthalpy becomes. Upon subsequent heating, the enthalpy is recovered, and the enthalpy of the system takes the path indicated by the blue dashed line. This recovered enthalpy is manifested as a peak in c_p.

To avoid ageing effects, DSC measurements in this project were performed on cooling instead. An example of the glass transition step in c_p observed on cooling is shown in figure 2.26.

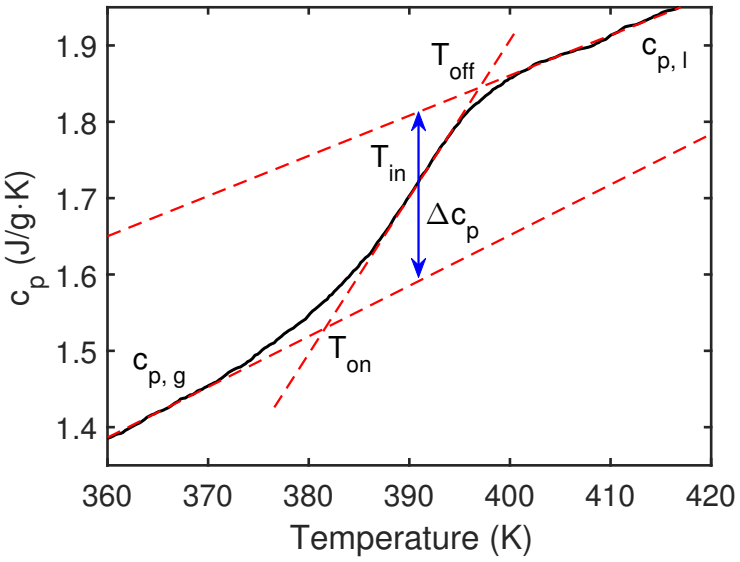

Figure 2.26: c_p as a function of T measured at 10K/min on cooling across T_g for PMMA (n=906). Analysis procedures used to determine T_g, Δc_p, and ΔT are also shown.

The red dashed lines in the figure indicate extrapolations of both the glassy and liquid state heat capacities ($c_{p,g}$ and $c_{p,l}$), and a tangent to the inflection point of c_p. Three characteristic temperatures associated with the glass transition step can be determined here: (i) the onset temperature, T_{on}, which is the intercept between $c_{p,g}$ and the tangent to the inflection point; (ii) the inflection point, T_{in};

and (iii) the offset temperature, T_{off}, which is the intercept between $c_{p,l}$ and the tangent to the inflection point.

Typically, T_{on} or T_{in} are used as definitions of T_g, and are generally repeatable within $\pm$1K[113]. An alternative to these definitions is that of the fictive temperature, which is sometimes referred to as the thermodynamic glass transition temperature[117]. This is the temperature at which the temperature dependence of the enthalpy changes, as indicated in figure 2.27. This will be discussed further in section 3.2.1.

The step height in the heat capacity, Δc_p, is defined as the the change in heat capacity between liquid and glassy states at T_g. This is shown by the blue arrow in figure 2.26, using T_{in} as the definition of T_g. The width of the heat capacity, ΔT, can also be obtained, which is defined as the difference in temperature between T_{on} and T_{off}, $\Delta T = T_{off} - T_{on}$.

2.3.1 Rate dependent DSC

A typical DSC measurement involves measurement of the heat flow through a sample whilst maintaining a constant heating/cooling rate. Typically, heating/cooling rates of $|dT/dt| = 10$K/min are used. The heating/cooling rate is inversely proportional to the characteristic timescale of the α relaxation (τ_α) of the sample [118]. Thus, measurement at slower rates will lead to higher measured values of T_g. To illustrate this, an idealised example of the enthalpy of a sample as a function of temperature close to T_g at two different cooling rates is shown in figure 2.27.

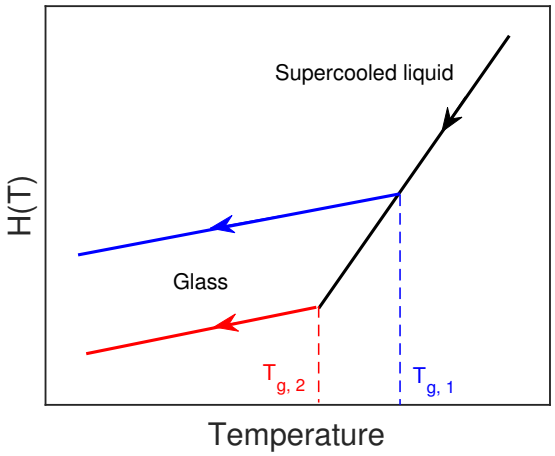

Figure 2.27: Enthalpy (H) as a function of temperature for a supercooled liquid cooled at two different rates through their respective glass transition temperatures, T_g.

In this figure, the blue line indicates a faster cooling rate leading to a higher glass transition temperature, $T_{g,1}$ and the red line indicates a slower cooling rate leading to a lower glass transition temperature, $T_{g,2}$. The inverse relationship between heating/cooling rate and τ_α can be quantified using the following equation:

$$\tau_\alpha = \frac{A}{B}, \tag{2.41}$$

where B is the heating/cooling rate and A is a system specific parameter. In this project, a rate of $B = 10$K/min was used when performing standard DSC measurements. This rate has been shown to reasonably correspond to $\tau_\alpha = 100$s for both polymeric and non polymeric glass formers. This was shown to be the case by comparing the transition temperature obtained at different heating/cooling rates with those obtained using Temperature Modulated DSC (TMDSC), where the timescale is set by the modulation period[119] (this will be discussed in section 2.3.2). Therefore this rate was used in order to obtain dynamic behaviour of the α relaxation comparable to other techniques such as dielectric spectroscopy and rheology.

2.3.2 Temperature modulated DSC

Temperature modulated DSC (TMDSC) is a more advanced DSC technique which combines two simultaneous heating profiles: a linear heating/cooling rate, similar to that of standard DSC, and a sinusoidal component[120]. When relatively slow linear heating/cooling rates are used, the addition of a sinusoidal component allows for a higher resolution determination of heat capacities than would usually be possible in more standard DSC measurements[121]. Also, TMDSC measurements allows the heat capacity to be split into so-called reversible and non-reversible components, which are affected differently by physical processes within a sample[113].

The temperature profile of a simple sinusoidal TMDSC experiment is shown in the following equation:

$$T(t) = T(0) + Bt + A\sin\left(\frac{2\pi t}{P}\right), \tag{2.42}$$

where B is the underlying heating rate, A is the modulation amplitude, and P is the oscillation, or modulation period. An example of this is shown in figure 2.28.

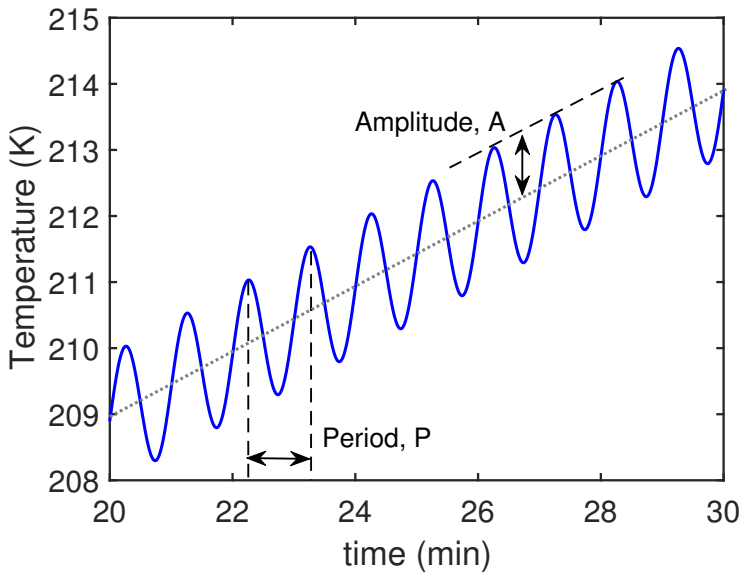

Figure 2.28: Example of a TMDSC temperature profile with: An underlying heating rate of $B = 0.5$K/min (shown by the gray dotted line); a period of $P = 60$s; and an amplitude of $A = 1$K.

Figure 2.28 shows an example of a heating-cooling mode TMDSC experiment, for which the heating rate ($\mathrm{d}T/\mathrm{d}t$) due to the modulation is large enough, compared to the underlying heating rate, that the sample undergoes both heating and cooling. This technique generally yields larger heat flows, and therefore a larger signal response, than a heating-only mode. Heating-cooling mode TMDSC was the mode used throughout this project.

A generic expression for heat flow into a sample during a DSC measurement is shown in equation 2.43:

$$q_{tot} = \frac{\mathrm{d}Q}{\mathrm{d}T} = C_p \frac{\mathrm{d}T}{\mathrm{d}t} + g(T,t), \tag{2.43}$$

where q_{tot} is the total heat flow of the sample, C_p is the heat capacity of the sample, and $g(T,t)$ is defined as the kinetic heat flow, which is the difference between the other two components[122].

q_{tot} is the quantity that is determined during typical DSC measurements, i.e. using a linear heat/cooling rate. The response from TMDSC measurements can be split into both q_{tot} and $C_p\mathrm{d}T/\mathrm{d}t$ components. q_{tot} is the heat flow due to the underlying heating rate, B, whereas, $C_p\mathrm{d}T/\mathrm{d}t$ is the heat flow due to modulation (q_m). An example of these responses from TMDSC is shown in figure 2.29.

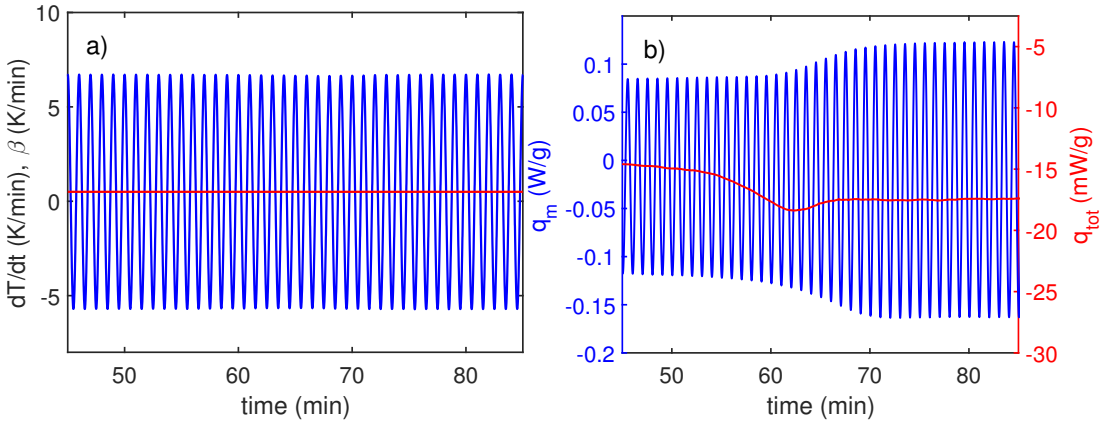

Figure 2.29: TMDSC measurements on DC705, using the same experimental parameters as outlined for figure 2.28. a) The components of the heating rate from the modulation (blue), and the underlying heating rate (red). b) Heat flow response due to both of these components.

Figure 2.29 (a) shows temperature profiles of a TMDSC experiment. The total heating rate is shown in blue, and the underlying heating rate is shown in red. Figure 2.29 (b) shows the response of a small molecular glass former (DC705) across the glass transition due to the temperature profiles in (a). The heat flow due to modulation is shown in blue, and the total heat flow due to the underlying heating rate is shown in red. From the two modulated signals shown in blue in figure 2.29, the average signal (due to the underlying heating rate) is subtracted, and is then analysed using a Fourier transform procedure in order to obtain the amplitudes (and phase difference) of these two signals[120]. Using these, the heat capacity can be calculated using the following equation:

$$C_{p,r} = \frac{A_{\mathrm{d}T/\mathrm{d}t}}{A_{q_m}}, \tag{2.44}$$

where $A_{\mathrm{d}T/\mathrm{d}t}$ and A_{q_m} are the instantaneous values (amplitudes) of the $\mathrm{d}T/\mathrm{d}t$ and q_m. $C_{p,r}$ is referred to as the reversing heat capacity. The components of the heat flow response from equation 2.43 are shown as specific heat capacities in equation 2.45.

$$c_{p,tot} = c_{p,r} + c_{p,nr} \tag{2.45}$$

$c_{p,tot}$ is the specific heat capacity due to the underlying heating rate, $c_{p,r}$ is the reversing specific heat capacity, and $c_{p,nr}$ is the non-reversing specific heat capacity. $c_{p,nr}$ is the heat capacity due to kinetic components of the heat flow ($g(T,t)$ from equation 2.43), and results from "non-reversible" events, such as enthalpy relaxations or cold crystallisation. An example of these three components is shown in figure 2.30.

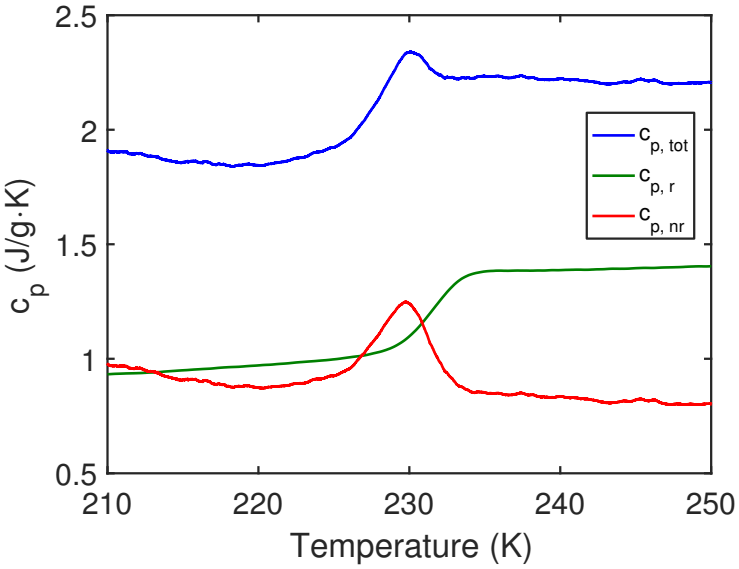

Figure 2.30: $c_{p,tot}$, $c_{p,r}$, and $c_{p,nr}$ for DC705 across T_g using the same experimental parameters as outlined for figure 2.28.

$c_{p,r}$ in figure 2.30 shows the characteristic heat capacity step change across the glass transition. $c_{p,tot}$ contains a contribution due to the enthalpy relaxation, which is shown in $c_{p,nr}$ as a peak.

It good practice in TMDSC measurements to tailor the underlying heating/cooling rate such that 4-6 modulation cycles are within the transition of interest[123]. Fewer than this leads to a lack of sufficient resolution, and information in c_p may be smeared or lost. In order to ensure enough cycles are present in the transition region, equation 2.46 is used.

$$B = 60\frac{T_{1/2}}{nP} \tag{2.46}$$

Here, B is the underlying heating/cooling rate, n is the desired number of cycles (4-6), P is the modulation period, and $T_{1/2}$ is the full width at half maximum of $c_{p,nr}$. Smaller values of β lead to a higher resolution of the data obtained. However, smaller values of β require significantly more experimental time. In addition to this, information on q_{tot} (and therefore q_{nr}) will be lost due to smaller heat flows. For this project, information contained in q_{nr} (and therefore q_{tot}) was

not required, and thus B was chosen so that an excess of 4-6 cycles was always present within the transition region.

From $c_{p,r}$ and the phase angle between dT/dt and dQ/dt, a complex heat capacity can be calculated[113]:

$$C_p^* = \frac{A_{\mathrm{d}T/\mathrm{d}t}}{A_{q_m}} \mathrm{e}^{-i\delta} = C_p' - iC_p''. \tag{2.47}$$

Here, $|C_p^*|$ is the so-called reversing heat capacity, and δ is the phase angle between $A_{\mathrm{d}T/\mathrm{d}t}$ and A_{q_m} (as defined in equation 2.44). C_p' and C_p'' are the in-phase and out-of-phase components of the heat capacity, which are often referred to as the phase-corrected reversing and kinetic heat capacities respectively[120]. Across the glass transition, C_p'' yields information about the transition width δT, and the temperature, T_α. This will be discussed further in section 4.1.1.

2.3.3 TA Instruments Q2000 DSC

The calorimetric determination of heat flow through a sample as a function of temperature can be performed in two different ways:

- Power compensated DSC - This technique involves having the sample and reference in two separate furnaces. The power difference required to change the temperature of both furnaces in order to maintain the same temperature profile is directly related to the difference in heat flow between the sample and reference.
- Heat-flux DSC - In this technique, both sample and reference are situated in the same furnace, connected by a well characterised heat conduction path. As the temperature of the furnace changes, the temperature difference between sample and reference is directly related to the heat flow.

DSC measurements were performed using a TA Instruments Q2000 with a liquid nitrogen cooling system (LNCS). This is an example of a heat-flux DSC and a basic schematic of this is shown in figure 2.31.

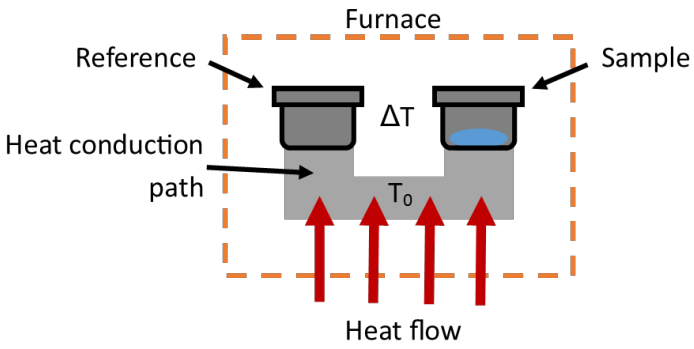

Figure 2.31: Basic schematic of a turret style heat-flux DSC.

This setup consists of a constantan base connecting two constantan turrets onto which two aluminium pans, one empty (reference) and one filled with ∼10mg of sample, are placed. This geometry is contained in a silver measurement cell which is purged with gaseous helium, used to prevent ice buildup and to ensure even temperature control throughout the cell[124].

Temperature control is achieved using a combination of a heating jacket surrounding the cell and a flange (cooled to $\sim -150°C$ using liquid nitrogen) connected to a silver plate at the base of the cell via nickel rods. Precise measurements of the temperature difference between reference and sample (ΔT), along with the temperature of the heat conduction path (T_0), allows for the precise determination of heat flow into the sample.

Steady state heat flow can be described by the Biot-Fourier equation[113, 125], shown in equation 2.48

$$\frac{q}{A} = -\Lambda \nabla \cdot T \tag{2.48}$$

where q is the heat flow, A is the cross sectional area of the conduction path between the source and the sink (therefore q/A is the heat flux), and λ is the thermal conductivity. In a DSC experiment, heat flows between the furnace and the sample and the reference, with the same length, Δl, between the sample/reference and the furnace. Therefore, equations 2.49 and 2.50 can be constructed.

$$\frac{q_{SF}}{A} = -\lambda \frac{\Delta T_{SF}}{\Delta L} \tag{2.49}$$

$$\frac{q_{RF}}{A} = -\lambda \frac{\Delta T_{RF}}{\Delta L} \tag{2.50}$$

Here, q_{SF} and q_{RF}, are the heat flows between the sample and furnace, and between the reference and furnace respectively, and ΔT_{SF} and ΔT_{RF} are the temperature differences between the sample and furnace, and between the reference and furnace respectively. From these, the differential heat flow, $q = q_{SF} - q_{RF}$, is shown in equation 2.51.

$$q = \frac{-\lambda A}{\Delta L} \Delta T_{SR} \tag{2.51}$$

The term $\lambda A/\Delta L = K$ is some value which depends on the thermal properties of the system[113]. This shows a linear relation between differential heat flow, q, and the difference in temperature between the sample and the reference, ΔT_{SR}, as shown in equation 2.52.

$$q = -K \Delta T_{SR} \tag{2.52}$$

This is the basic principle of how the heat-flux DSC calculates q from ΔT_{SR}. Other considerations, such as thermal resistances and capacitances between furnace and sample and reference are also calibrated for. It is also worth noting that the temperature of the heat conduction path (T_0, shown in figure 2.31) is also measured in the TA Q2000 DSC. This allows for more precise measurements of heat flow across the heat conduction path, and therefore a more precise q baseline can be determined.

Calibration

Initial calibration of the Q2000 involves performing an 'empty cell' measurement (i.e. with no sample or reference pan) and a measurement of two sapphire samples (with well characterised heat capacity as a function of temperature) over the temperature range of the instrument at a typical rate of 10K/min. Accurate determination of the thermal resistances and capacitances associated with the measurement cell allows for precise measurement of the heat flow through a sample by removing machine response from the resulting DSC trace [126].

Temperature and enthalpy calibrations were performed using two materials with well defined thermodynamic transitions: (i) indium, with a melting point of T_m = 156.6°C and enthalpy of fusion of 28.66J/g[127]; and (ii) adamantane, which exhibits a solid-solid transition at -65.5°C[128]. The differences between the measured transition temperatures and enthalpy changes are compared to these literature values and used to correct subsequent measurements.

Modulated DSC Calibration

TMDSC measurements require an additional calibration step. This involves the calibration of the reversing heat capacity ($c_{p,r}$), and is performed by measuring $c_{p,r}$ of a sapphire sample and comparing with well characterised literature values[2]. For different modulation periods, this is shown in figure 2.32.

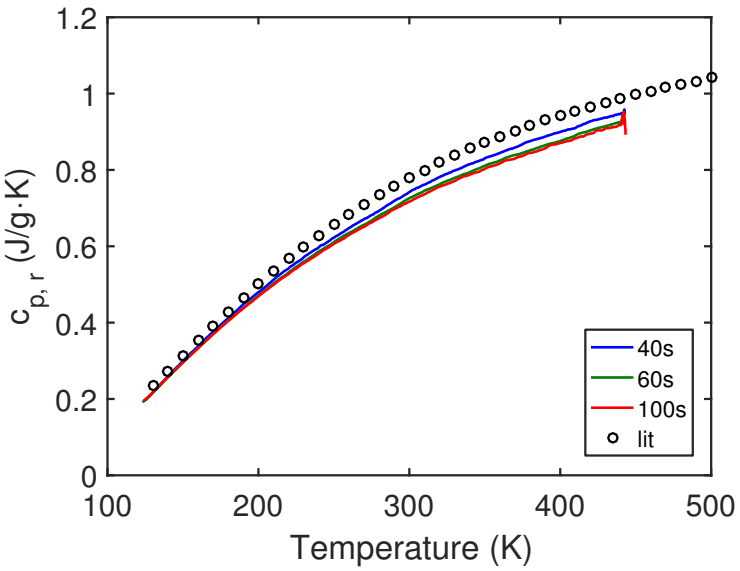

Figure 2.32: Reversing heat capacity $c_{p,r}$ measurement for sapphire for different modulation periods, P=40, 60, and 100s. Literature data for the heat capacity of sapphire is also shown[2].

It is clear from figure 2.32 that the measured $c_{p,r}$ differs for different modulation periods. In turn, these differ from well characterised literature values. A calibration value for $c_{p,r}$ was calculated by taking the average difference between

$c_{p,r}$ measured for a particular modulation period and that of the literature values across the relevant temperature range.

Correction of the heat flow phase angle (shown in equation 2.47) is required when calculating C_p^*. This will be discussed in detail in section 4.1.1.

Chapter 3

Chain-length dependent rheology and relaxation dynamics of PMMA

In this chapter, the rheological response of a chain length series of atactic, linear, poly(methyl methacrylate) (PMMA) oligomers and polymers was studied and comparisons with the behaviour on some other chosen polymers were made. The complex shear modulus was measured for PMMA samples ranging from small molecules, to oligomers and long-chain polymers, and the behaviour of each sample was determined both in the melt and glass state.

The development of the mechanical and relaxation response for chain-length series ranging from the monomer-scale to entangled polymer is poorly understood, and most studies have focused on the longer chain-length regime. PMMA is important both as a model system and as an industrially relevant polymer. However, full chain-length studies have not been performed on PMMA. Moreover:

- Atactic PMMA is a good glass-former and can thus be studied over the full chain-length range without issues with crystallization.
- It is commercially available over the full chain-length, and it is possible to purchase highly monodisperse samples.

- The ester side groups contain large dipole moments. Therefore, it exhibits a large dielectric signal for dynamics associated with these side groups (α, β, and γ relaxation dynamics) so that the full relaxation dynamics can be readily measured.

- PMMA is a relatively "stiff" polymer, characterised by a Flory characteristic ratio of $C_\infty = 9.0$[60] and this translates to a significant T_g variation with chain-length, which means that the changes with molecular weight can be investigated in detail.

- The PMMA samples used are proton capped, meaning that we do not have to take account of any bulky initiator groups.

- PMMA is a so called type-C polymer, which means that the permanent dipoles are situated within the ester side groups. Therefore, it does not have a dipole moment component directed along the backbone, which means that chain-modes will not be observed using Broadband Dielectric Spectroscopy (BDS). This is an advantage in this study since we can study both the α relaxation and chain modes using rheology, but only the α relaxation with BDS (along with secondary relaxations). Therefore, the combination of these techniques can efficiently be used to separate the observed relaxations.

- As discussed in section 1.4, a lot of other aspects of PMMA have been previously studied in literature, which allows for comparisons.

It is often assumed that at short timescales (or high temperatures), the structural (α) relaxation - which is associated with the glass transition - is coupled to chain dynamics, i.e. both α and chain relaxations have the same temperature dependence. This allows for the application of time-temperature superposition (TTS), whereby the rheological response at different temperatures can be superimposed onto a single master curve, which effectively yields the response over a wider dynamic range at a single temperature. However, it has been shown as the glass transition temperature (T_g) is approached from the melt, these relaxation mechanisms decouple[129–132].

Ding and Sokolov[133] show that the dynamic fragility (m) determines the degree of decoupling between α and chain dynamics, whereby more fragile polymers (PC, PMMA, PS, etc) decouple at shorter α relaxation timescales than stronger (less fragile) polymers (PI, PPG, PDMS, etc). Therefore, an important question in rheology arises: is TTS a valid approximation from melt to glass, especially in more fragile systems such as PMMA? To test this for a PMMA chain length series, TTS master curves spanning both short and long α relaxation timescales were constructed, and described using a simple ansatz, whereby the total response spectra was described by a sum of a chain mode contribution and a contribution from α relaxation. This rheological response was compared to the broadband dielectric spectroscopy (BDS) measurements, which is able to probe the α relaxation directly over a broad frequency range without relying on TTS.

The chemical structure of PMMA and sample specifications are shown in figure 3.1 and table 3.1.

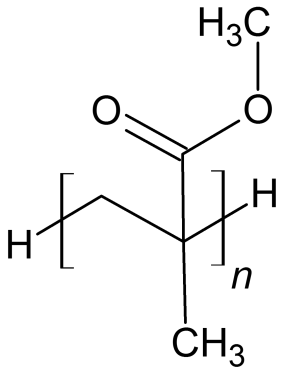

Figure 3.1: Chemical structure of a poly(methyl methacrylate) (PMMA) molecule.

n	M_W (g/mol)	PDI	Suppler
2	202	1.00	PSS
3	302	1.00	PSS
4	402	1.00	PPS
7	771	1.18	PSS
8	840	1.44	PSS
19	1900	1.10	PSS
43	4300	1.05	PSS
96	9590	1.05	PSS
906	90600	1.04	PSS
1478	147800	2.46	Goodfellow

Table 3.1: PMMA sample specifications showing: the degree of polymerisation (n), weight average molecular weight (M_W), polydisersity index (PDI=M_W/M_N), and the supplier.

The PMMA samples (monomer molecular weight, M_0=100g/mol) were purchased from Polymer Standards Service (PSS), and reported by the manufacturer to be proton capped, with no initiator side groups. The chemical structure of PMMA is shown in figure 3.1, where n represents the number of monomer units, and therefore the degree of polymerisation. Table 3.1 shows the degree of polymerisation, n, the weight average molecular weight, M_W, and the polydispersity index, PDI, as characterised by the supplier. To make sure that no low molecular weight species or solvents were present in the sample, representative samples across the molecular weight range were heated far above T_g in a vacuum oven for at least 24 hours and any changes heat capacity response were monitored using DSC. No changes were observed upon the heat treatment, except for the samples with n=7 and 8, where residual small molecular weight species were detected and these samples were thus heated far above T_g in a vacuum oven for at least 24 hours to remove any such species from the manufacturing process. In addition to this, a high molecular weight (M) sample with a higher polydispersity was obtained from Goodfellow to investigate the effects of polydispersity.

By comparing α relaxation timescales (τ_α) independently measured rheology,

BDS, and DSC, the validity of using TTS on this PMMA chain length series was investigated. Other polymeric systems of varying glassy properties were also compared, which appear to yield similar α relaxation behaviour at short relaxation times. These results yield how α relaxation properties (glass transition temperature (T_g), dynamic fragility (m), and heat capacity response) change with increasing chain connectivity in PMMA, which have have been shown to exhibit regional M behaviour in other polymeric systems[134, 135].

3.1 Dynamic shear modulus

Shear rheology measurements were performed using a Rheometrics ARES rheometer, as outlined in section 2.1.4, using 3mm parallel plate geometry in order to measure the high moduli of samples in their glassy state. Using an oscillatory strain profile, the complex shear modulus was measured, as shown in equation 3.1.

$$G^*(\omega) = |G^*|(\omega)e^{i\delta(\omega)} = G'(\omega) + iG''(\omega) \tag{3.1}$$

As discussed in section 2.1.1, the complex shear modulus consists of in-phase, elastic (G'), and out-of-phase, viscous (G'') components, where δ is the stress-strain phase angle. At low temperatures (high frequencies) in the glass, G' dominates the spectra, whereas at high temperatures (low frequencies) in the melt, G'' dominates. Between these two dynamic extremes, relaxation behaviour is apparent and the complex shear modulus has contributions from both the elastic and viscous components. Hence, this is coined the viscoelastic regime.

3.1.1 Dynamic shear modulus measurements

Oscillatory shear modulus measurements were performed within the linear viscoelatic region (LVR) (the region where stress and strain are directly proportional, as explained in section 2.1.5) for angular frequencies in the range $\sim 0.01 - 50$Hz ($\sim 0.06 - 300$rad/s) for temperatures spanning the dynamic range from melt to glass (for PMMA $n = 2$, 162K$\leq T \leq$ 183K; and $n = 906$, 379K$\leq T \leq$ 473K) every $2 - 4$K. At least three decades in frequency per temperature is commonly

accepted to be a minimum required for constructing master curves using a TTS assumption[98]. If TTS is valid over the measured range of temperatures and frequencies, the horizontal shift factors are proportional to the relaxation timescale as per equation 3.2.

$$a_T = \frac{\tau_T}{\tau_{ref}} = \left(\frac{\omega_{ref}}{\omega_T}\right) \tag{3.2}$$

Here, a_T is the ratio of the characteristic timescales of the relaxation mechanism apparent in the dynamic window at T relative to that of a reference temperature T_{ref}. Initially, T_{ref} was chosen as the middle temperature in the range of those measured. Once all frequency data had been superimposed, this was subsequently altered to be $T_{ref} = T_g$ using an additional shift factor shown in equation 3.3.

$$S = \exp\left[DT_0\left(\frac{1}{T_{ref} - T_0} - \frac{1}{T_g - T_0}\right)\right] \tag{3.3}$$

Equation 3.3 is simply a ratio of two VFT expressions, where T_{ref} is the arbitrary reference temperature, and was used in order to normalise the frequency axis between different samples. Examples of TTS master curves are shown in figure 3.2.

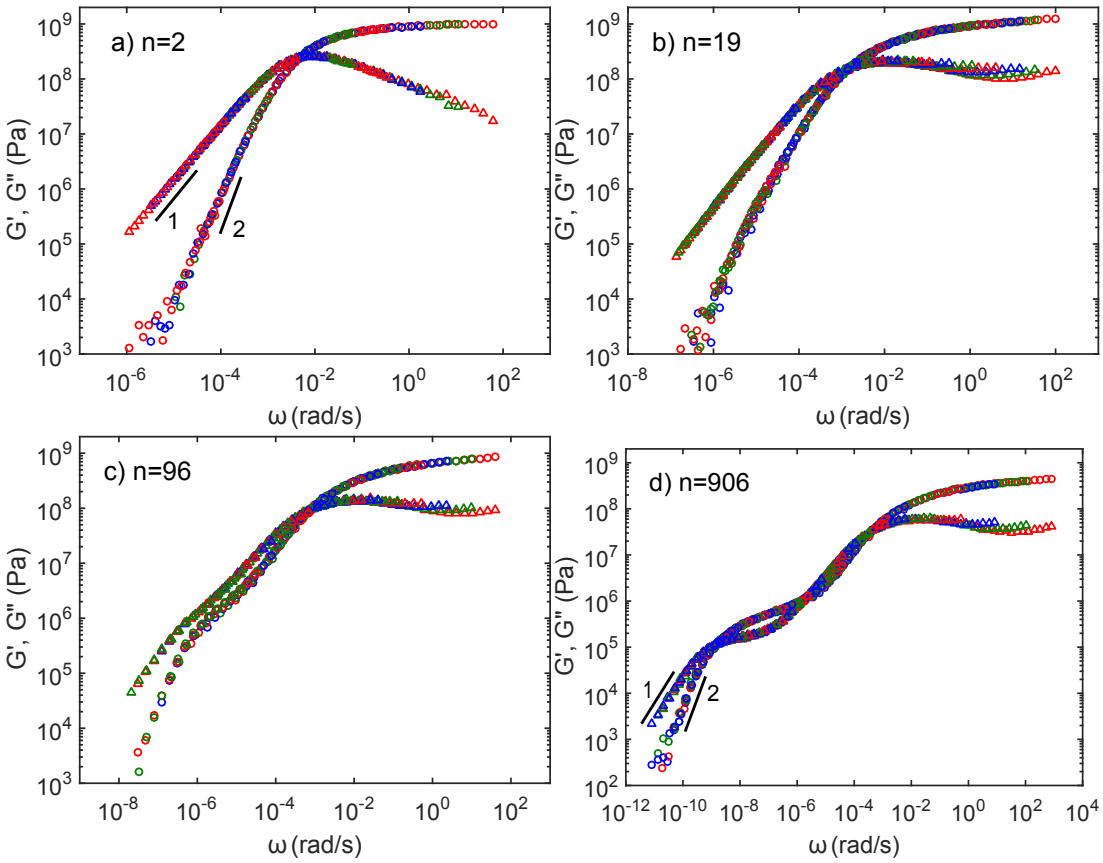

Figure 3.2: PMMA dynamic shear modulus TTS master curves for samples with different degrees of polymerisation (n). Alternating red, green, and blue sections indicate frequency sweeps taken as discrete temperatures, with circles and triangles represent G' and G'' respectively.

In figure 3.2, the alternating red, green, and blue data sets represent frequency data taken at discrete temperatures. Circles and triangles are used represent G' and G'' respectively. This notation will be used throughout this chapter when displaying TTS master curves.

The TTS master curves were produced by horizontally (frequency) shifting data only, with no vertical (modulus) shift applied. Commonly, TTS is carried out far above T_g, where chain modes dominate the spectra. In this regime, the rheological response is set by Rouse or reptation dynamics, and the effect of the temperature dependent density variations is taken into account using a simple

expression when the density is known. Although it has been suggested that even in the melt regime of polymers, more complex behaviour may apply[136].

However, acquiring the temperature dependence of density for this entire PMMA chain-length series is non-trivial. Casalini et. al.[88] measured PVT data for PMMA n=3, 4, 10, and 1500. Therefore, density as a function of temperature could be calculated for these samples, which allowed for temperature-density vertical shift factors to be determined for appropriate samples in our series (n=3, 4, and 1478). This had a marginal effect on the shape of the TTS master curves, as temperature-density effects are insignificant over the measured temperature range compared to errors due to small sample geometry. In addition to this, temperature-density behaviour would not be applicable in the intermediate and glassy parts of the spectra, and such a shift in this regime would have no physical basis. Therefore, no vertical shift was applied in the construction of these TTS master curves. This is also consistent with other studies in the literature, performing similar measurements from melt to glass[137].

Our TTS master curves shown in figure 3.2, show typical behaviour in the shear modulus as the chain-length of a polymeric glass-former increases from that of a small molecule to a fully entangled polymer. The smallest PMMA molecule in this chain-length series (figure 3.2 (a)) shows the α relaxation only, with low frequency power law behaviours of G' and G'' being 2 and 1 respectively. The intermediate samples (figure 3.2 (b) and (c)) are between $M_R < M < M_c$, where M_R is the Rouse molecular weight and M_c is the critical molecular weight ($M_c = 29500$g/mol[138]). In this range, there are additional contributions to the mechanical response from Rouse chain modes, which become apparent at lower frequencies. The more Rouse beads that exists within the molecule, the more Rouse modes are present in the spectra, this is noticeable in these two samples. The longest PMMA chain (figure 3.2 (d)) is above the critical moleclar weight, $M > M_c$, and therefore exhibits entanglement behaviour. For PMMA, the entanglement molecular weight is $M_e = 13600$g/mol[138], therefore this sample ($M_W = 90600$g/mol) has $90600/13600 \sim 6$ entanglements per chain. This entanglement behaviour is visible in the spectra as a rubber plateau at lower frequencies which is due to effective crosslinks hindering relaxation. At even lower frequencies, these chains are able to relax via reptation, whereby they move along their

own length. At high frequencies for all these PMMA samples, TTS breaks down due to a secondary (β) relaxation becoming apparent. Secondary relaxations such as this do not follow the same temperature dependence as the α relaxation, and therefore the spectra will not superimpose onto a common master curve. The β relaxation is particularly strong in PMMA, and is generally attributed to some cooperative motion involving both the ester side group and the polymer backbone[139, 140].

In order to directly evaluate the validity of TTS on these samples, so called Van-Gurp-Palmen (VGP) plots[141, 142] were produced, which remove any time dependence from the spectra, therefore assessing the validity of TTS without shifting data. Examples of VGP plots are shown in figure 3.3.

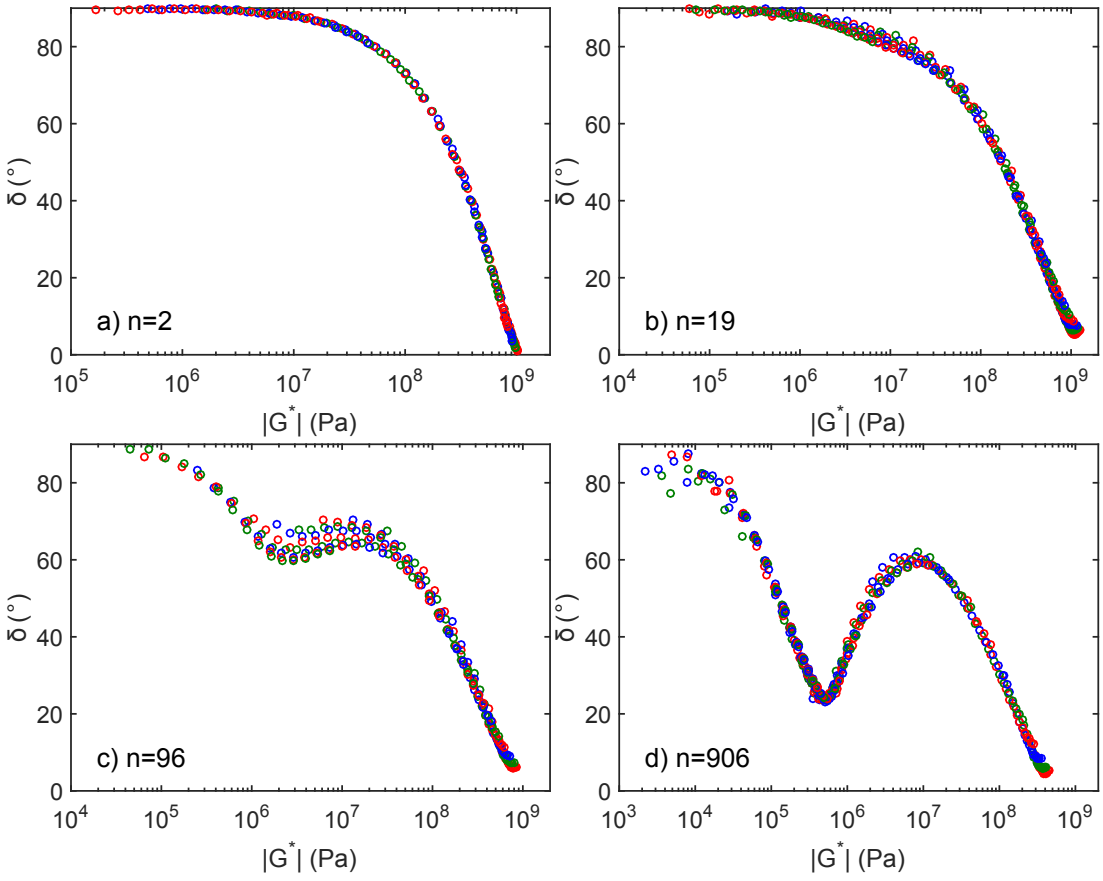

Figure 3.3: PMMA Van-Gurp-Palmen (VGP) plots for the samples shown in figure 3.2.

These VGP plots show the strain-stress phase angle, δ, versus dynamic shear modulus, $|G^*|$. For $n = 2$ (figure 3.3 (a)), TTS appears valid over this dynamic range, as indicated by a smooth continuous curve. As chain modes become apparent for $n = 19$, 96, and 906 (figure 3.3 (b), (c), and (d)), there is some decoupling between these two relaxation mechanisms in the modulus range $|G^*| \approx 10^6 - 10^7$Pa. This is observed as a discontinuity between frequency sweeps at different temperatures. At higher and lower moduli, the α relaxation and chain modes are the dominant relaxation modes respectively, and TTS appears valid. Ding and Sokolov[133] noticed a decoupling of α and chain dynamics for various polymeric systems for $\tau_\alpha \gtrsim 10^{-5} - 10^{-7}$s. This was apparent in measurements of more fragile polymers such as Polystyrene (PS), which exhibits similar relaxation behaviour to PMMA. Despite this, reasonable TTS master curves could be constructed over the region where there is a changeover between α and chain dynamics. This crossover between α and chain mode dominant regimes, and the validity of these TTS curves will be discussed further in section 3.5, whereby this data will be compared to other techniques which do not rely on TTS.

3.1.2 Dynamic shear modulus modelling

In the time domain, the α relaxation response is often described by a stretched exponential, or Kohlrausch-Williams-Watts (KWW) expression[94], as shown in equation 3.4.

$$G(t) = G_0 \exp\left[-(t/\tau)^\beta\right] \tag{3.4}$$

As discussed in section 2.1.2, this is a modified exponential decay, where the breadth of the response is set by a variation of the KWW stretching parameter, $0 < \beta < 1$. In the frequency domain, the stretched exponential decay manifests itself as a peak in $G''(\omega)$, characterised by low and high frequency power-laws of 1 and β respectively. Therefore, a variation of the stretching parameter β sets the high frequency power-law slope of $G''(\omega)$. In addition, it also affects the bluntness of the peak, as shown in figure 2.5.

The time-domain KWW decay does not have an analytical expression in the frequency domain. Thus, a numerical transform is required for each iteration of

a fitting procedure performed in the frequency domain. However, Bergman[95] produced a simple expression defined for the imaginary part of the relaxation response which matches a KWW response, shown in equation 3.5.

$$G''(\omega) = \frac{G''_p}{1-\beta+\frac{\beta}{1+\beta}[\beta(\omega_p/\omega)+(\omega/\omega_p)^{\beta}]} \tag{3.5}$$

Here, G''_p and ω_p describes the peak in the loss modulus, and β is the KWW stretching parameter. The real and imaginary components of the dynamic shear modulus obey a Kramer-Kronig relation[96], and therefore the storage modulus is attainable from this loss modulus. Rather than directly computing this, a relevant fitting routine was employed to describe the loss modulus modelled by equation 3.5, which is as follows:

1. An initial $G''(\omega)$ is generated from equation 3.5 using a set of initial parameters.
2. A sum of Maxwell modes (2 per frequency decade) is fitted to $G''(\omega)$, using a Nelder-Mead algorithm[143] to minimise χ^2, thus yielding both G' and G'' corresponding to the initial KWW response
3. χ^2 based on the TTS data and both G' and G'' is calculated
4. The fitting parameters of equation 3.5 are optimised iteratively until χ^2 is minimised.

An example of this fitting procedure is shown in figure 3.4.

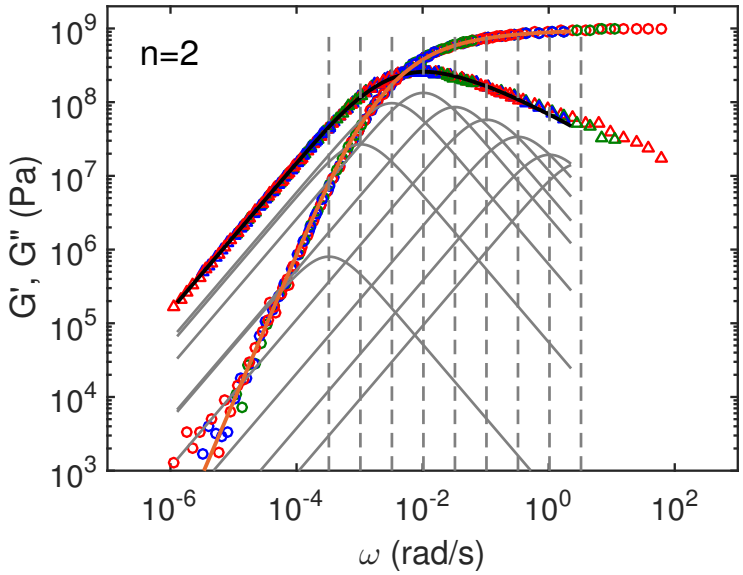

Figure 3.4: TTS master curve of PMMA n=2. Gray lines are a series of Maxwell modes (with peak positions shown by the gray dashed lines) fitted to the KWW approximation of G'', shown by the black line. The orange line indicates the real component sum of Maxwell modes.

This figure visualises the fitting procedure, with a sum of Maxwell modes appropriately distributed in order to describe the modelled loss modulus, as shown in equation 3.6.

$$G^*_{MW}(\omega) = \sum_{i=1}^{N} \Delta G_i \frac{i\omega\tau_i}{1 + i\omega\tau_i} \tag{3.6}$$

Here, the strengths ΔG_i are fitting parameters, and the time-scales of the modes τ_i are distributed logarithmically, two per frequency decade, around the peak in the G'' (ω_p in equation 3.5). This fitting procedure does not require a numerical transformation per iteration, and still adequately yields the KWW fit of the α relaxation of the TTS master curve.

For intermediate molecular weight samples, where $M_R < M < M_c$, the Rouse model[63] (described in detail in section 1.3.2) was additionally employed in order to fully describe the TTS master curves. The Rouse model describing the complex shear modulus is shown in equations 3.7 and 3.8[47, 64].

$$G^*_{Rouse}(\omega) = \frac{\rho RT}{M} \sum_{p=1}^{N} \frac{i\omega\tau_p}{1 + i\omega\tau_p} \tag{3.7}$$

$$\tau_p = \frac{\tau_1}{sin^2(p\pi/2(N+1))} \tag{3.8}$$

Here, ρ is the density, R is the gas constant, T is the temperature, M is the sample molar mass, N is the number of Rouse modes ($N = M/M_R$), τ_1 is the relaxation time of the slowest Rouse mode, and τ_p is the relaxation time of the pth Rouse mode. This relaxes the chain through a series of normal modes, each of which contributes $\rho RT/M$ to the modulus in this regime. The number of these modes depends upon the size of the Rouse bead and the molecular weight of the polymer.

In the $M_R < M < M_c$ range, a simple ansatz was applied, where the α and Rouse spectra were treated independently, and the mechanical response was described as a superposition of these two components, shown in equation 3.9.

$$G^*(\omega) = G^*_{\alpha}(\omega) + G^*_{Rouse}(\omega) \tag{3.9}$$

This ansatz has been applied to other polymeric systems, most notably polystyrene[137, 144, 145], 1-4-polyisoprene (PI)[146], 1,4-polybutadiene (PB)[147], and even for more complex poly(ethylene oxide) based sticky-Rouse systems[102]. This assumes that the measured stress is simply a sum of independent stress components. Alternatively, it has been suggested that strains, rather than stresses, might instead be additive[148]. The addition of strains is equivalent to summing compliance ($J^*(\omega) = 1/G^*(\omega)$) components, which is often carried out for polymeric systems from creep rheology measurements[149], amongst other techniques, such as; broadband dielectric spectroscopy (BDS)[150, 151] (complex permitivity) and fast-field cycling NMR (FFCNMR)[152] (complex permeability). Thus, both types of approaches can typically be applied successfully to describe data, and it is often not clear what is the most appropriate approach. Mott and Roland[153] have pointed out that in reality, the interplay of forces is generally too complicated for any simple addition ansatz to perfectly describe the behaviour. However, these simplifications can still typically describe data well and it is demonstrated

in this work, that a simple addition ansatz based on the moduli can descrice the data very well and this is thus used as a first approximation to monitor the chain-length dependent rheology.

Using this addition ansatz of modulus components, the loss modulus (G'') can be described as the sum of equation 3.5 and the imaginary component of equation 3.7, shown in equation 3.10.

$$G''(\omega) = \frac{G''_p}{1-\beta+\frac{\beta}{1+\beta}[\beta(\omega_p/\omega)+(\omega/\omega_p)^\beta]} + \frac{\rho RT}{M}\sum_{p=1}^{N}\frac{\omega\tau_p}{1+(\omega\tau_p)^2} \tag{3.10}$$

Here, G''_p, β, ω_p, and τ_1 are fitting parameters. $\tau_\alpha = 1/\omega_p$ denotes the characteristic relaxation time corresponding to the peak in the G'' of the α relaxation.

For higher molecular weight samples above M_c, the Rouse model does not describe all chain behaviour. As explained in section 1.3.2, at higher temperatures/lower frequencies than those relevant for Rouse dynamics, relaxation of polymer chains is impeded by adjacent chains. These constraints act as temporary cross-links, which give rise to rubbery behaviour, whereby a plateau region becomes apparent, with a modulus (G_e) determined by the density of the these entanglements[61]. To characterise this behaviour, the tube model is employed, which describes a single polymer chain as being contained in an imaginary tube, the shape of which is determined by the chemistry of the particular polymer system[64]. Eventually, the polymer chain is able to escape this tube in a mode of motion described by de Gennes[65] as "reptation", which finally relaxes the polymer chain at high temperatures/low frequencies.

In order to model Rouse and entanglement behaviours for samples where $M \geq M_c$, the Likhtman-McLeish (LM) model[5] was employed. As described in section 1.3.3, this model is based on a tube model, taking contour length fluctuations, constraint releases, and reptation along the tube into account. It also includes Rouse modes between entanglements, and therefore models all chain dynamics for entangled polymers.

Examples of the fitting procedures for these three M regimes are shown in figure 3.5.

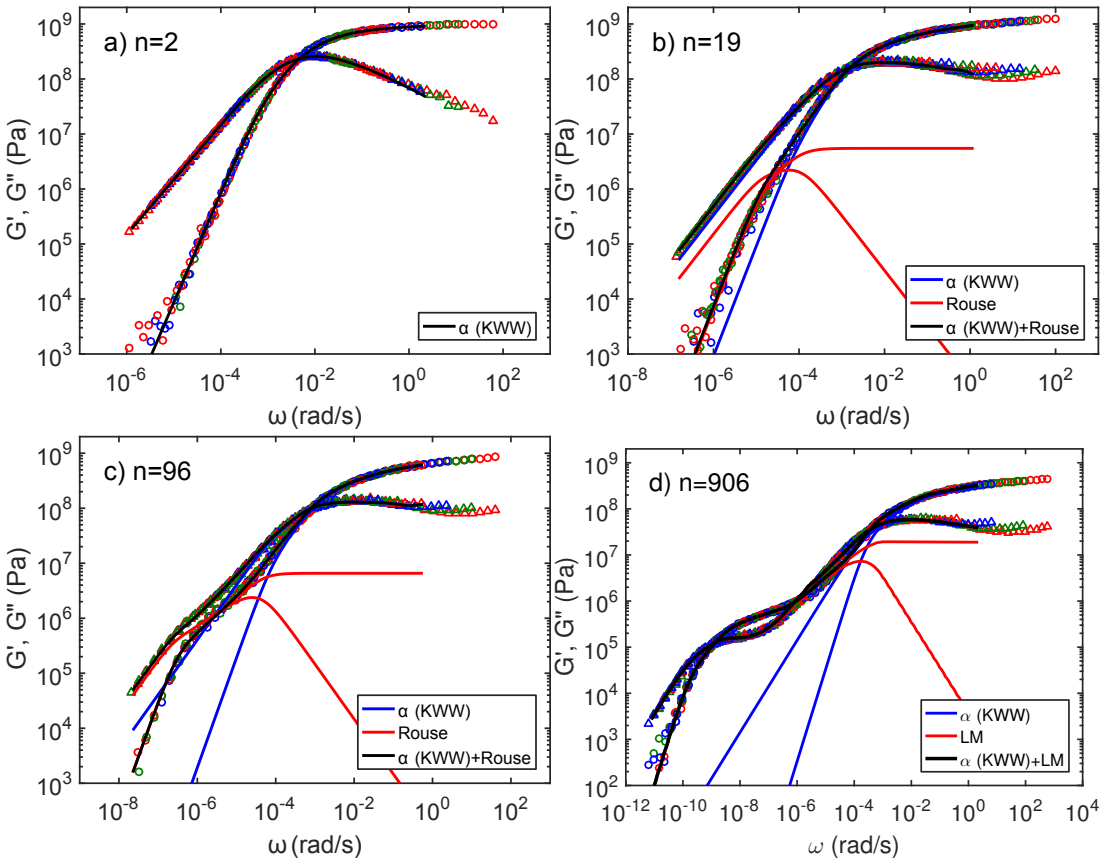

Figure 3.5: PMMA TTS master curves with appropriate models fitted for the samples shown in figure 3.2.

For low M PMMA samples ($M < M_R$, example in 3.5 (a)), a single KWW expression is adequate to describe the spectra from melt to $\sim T_g$, as shown by black lines describing G' and G''. The addition of a Rouse spectrum is necessary to describe intermediate M samples ($M_R < M < M_c$, examples in 3.5 (b) and (c)) spectra, which is shown by the red lines. The sum of this, and the blue lines representing a single KWW expression describing the α relaxation, yield the black lines describing the entire spectra (as described by equation 3.9 for both G' and G''). Entanglement dynamics become apparent for high M samples ($M > M_c$, example in 3.5 (d)), and the Likhtman-McLeish model is used to describe the chain behaviour, rather than a simple Rouse model. This ansatz works well in describing both the α relaxation and chain dynamics. From this fitting, infor-

mation on both the α relaxation and chain modes can thus be obtained for this PMMA M series.

3.2 The α relaxation

The horizontal TTS shift factors (a_T from equation 3.2) are proportional to the α relaxation timescale (τ_α) at shorter times, and chain modes (τ_n) at longer times. For thermorheologically simple matierals, it is assumed that these two relaxation mechanisms share the same temperature dependance[8]. Therefore TTS yields time-scales which are characteristic of both relaxation mechanisms. In order to associate the shift factors with an absolute α timescale, the peak in the loss modulus is taken as the τ_α at the reference temperature ($\tau_\alpha = 1/\omega_p$), which is obtained directly from the fitting procedure for the α relaxation in section 3.1.2. This yields τ_α for all temperatures involved in the construction of the TTS master curves.

The temperature dependence of the α relaxation is commonly empirically described using a Vogel-Fulcher-Tammann (VFT)[17–19] expression, shown in equation 3.11.

$$\tau_\alpha(T) = \tau_0 \exp\left(\frac{DT_0}{T - T_0}\right) \tag{3.11}$$

Here, the strength parameter, D, is a measure of the curvature, and therefore a measure of the deviation from Arrhenius behaviour, and Vogel temperature, T_0, is the temperature where τ_α diverges. The temperature dependence of τ_α for this chain-length series of PMMA are shown in figure 3.6.

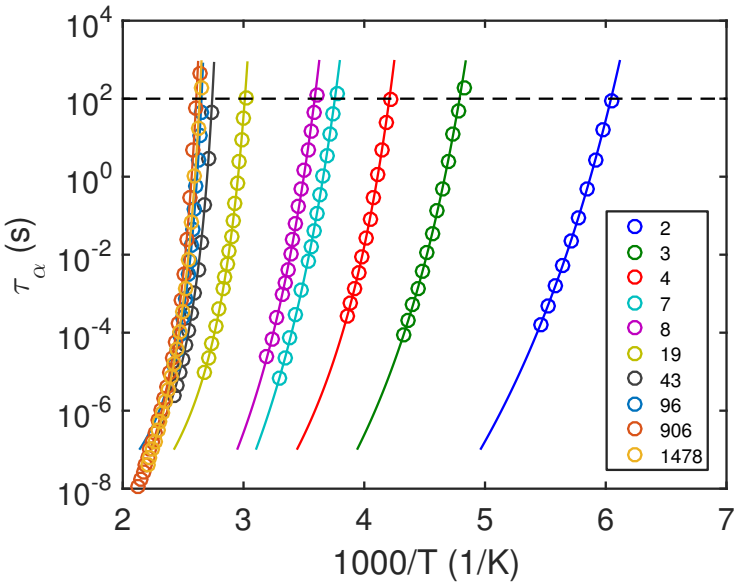

Figure 3.6: Arrhenius plot showing τ_α determined from the TTS master curves as a function of inverse T. The legend gives the degree of polymerisation, and solid lines are VFT fits to the data.

This shows the typical super-Arrhenius (VFT) behaviour of the α relaxation. The glass transition temperature is defined as the temperature where $\tau_\alpha = 100s$, as shown by the dashed line, and this is well known to increase with chain length[86]. In order to visualise the sensitivity to a T variation at T_g, a T_g-normalised Arrhenius, or Angell[23], plot was used. In addition to this, a derivative, or Stickel[24], analysis of the temperature dependence of τ_α was calculated. This is shown in equation 3.12.

$$Z = \left(\frac{\mathrm{d}\log\tau_\alpha}{\mathrm{d}(1000/T)}\right)^{-1/2} = \left(\frac{DT_0\log e^1}{1000(T_0/T-1)^2}\right)^{-1/2} \tag{3.12}$$

This derivative linearises VFT behaviour, whereby the slope of the Stickel parameter (Z) is related to the VFT parameters D and T_0, as shown in equation 3.13.

$$\frac{\mathrm{d}Z}{\mathrm{d}(1000/T)} = -\left(\frac{T_0}{1000D\log e^1}\right)^{1/2} \tag{3.13}$$

A change in the slope of Z therefore indicates a change in VFT behaviour, which is sometimes not apparent in a standard Arrhenius plot. In this type of analysis,

Arrhenius behaviour is displayed as simply a horizontal line (Z is invariant with temperature), and therefore the slope is in effect a measure of deviations from Arrhenius behaviour. It is also worth noting that both equations 3.12 and 3.13 are not dependant on the VFT pre-factor (τ_0). For this series, Angell and Stickel plots are shown in figure 3.7.

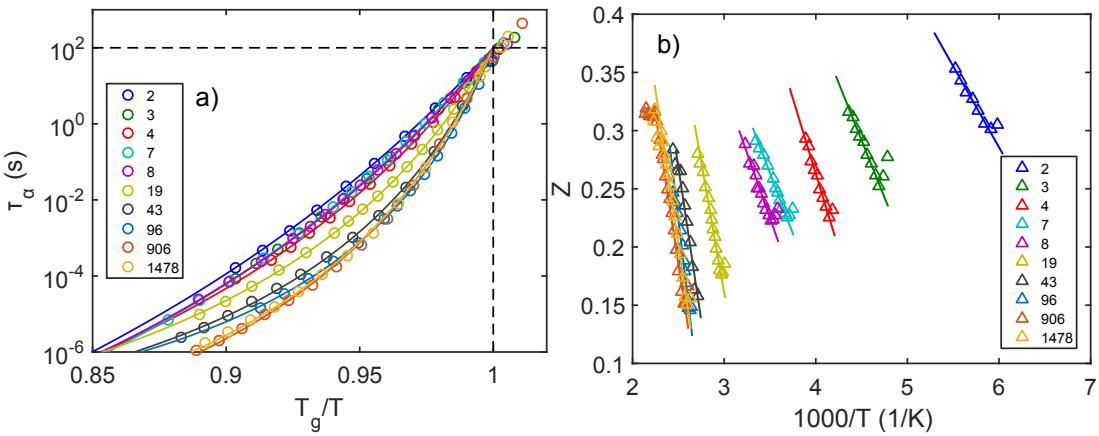

Figure 3.7: a) Angell plot, showing PMMA α relaxation timescales attained from TTS master curves as a function of T_g/T. b) Stickel plot linearising VFT behaviour. The legends give the degree of polymerisation, and solid lines are VFT fits to the data.

Figure 3.7 (a) and (b) show that as chain length increases, the temperature dependence of the α relaxation becomes less Arrhenius (more fragile). From the VFT expression, the fragility parameter can be determined, shown in equation 3.14.

$$m = \left.\frac{\mathrm{d}\log\tau_\alpha}{\mathrm{d}(T_g/T)}\right|_{T=T_g} = \frac{\ln(100/\tau_0)^2 + D\ln(100/\tau_0)}{D\ln(10)} \tag{3.14}$$

This is the slope of the VFT curve at the point where the grey dashed lines intersect in figure 3.7 (a), and hence is a measure of the change of α relaxation time with temperature at T_g. A higher fragility implies a large change of relaxation time with changing temperature at T_g.

3.2.1 Comparisons to BDS and DSC

Along with rheology, the $\tau_\alpha(T)$ behaviour was also determined using Broadband Dielectric Spectroscopy (BDS) and Differential Scanning Calorimetry (DSC).

BDS measurements were performed using a Novocontrol Alpha-A analyser, as discussed section 2.2. PMMA is an example of a so called type-C polymer, which has flexible dipoles associated with the side group, rather than along the polymer backbone[14]. Hence the relaxation of chain modes is not apparent in BDS measurements of PMMA. For the whole chain-length series, the α relaxation is observed together with faster, secondary, relaxation mechanisms. These are labelled β, γ, δ, etc in order of appearance with increasing frequency (or decreasing temperature)[14]. The β relaxation in PMMA has a strong mechanical response also, shown by a failure in TTS at high frequency in figure 3.2.

A common empirical expression used to model relaxations is a modified Debye relaxation, a Havriliak-Negami (HN) relaxation[109], as shown in equation 3.15.

$$\epsilon^*(\omega) = \epsilon_\infty + \frac{\Delta\epsilon}{(1 + (i\omega\tau_{HN})^\alpha)^\beta} \tag{3.15}$$

Here, $\epsilon^*(\omega)$ is the complex permittivity, ϵ_∞ is the permittivity at infinite frequency, and $\Delta\epsilon$ is the change in permittivity due to the relaxation. α and β are the empirical modifications to the shape of the Debye relaxation, which broaden the relaxation spectra, where α and $\alpha\beta$ are the low and high frequency power-law flaks in the imaginary permittivity (ϵ'') respectively. For the case of asymmetric relaxations, where $\beta \neq 1$, τ_{HN} does not correspond to either the average relaxation time, or the most probable relaxation time (the peak frequency in ϵ''), i.e. $1/\omega_p = \tau_\alpha \neq \tau_{HN}$. Therefore, to correct for this and attain τ_α, equation 3.16 is used[14].

$$\frac{1}{\tau_p} = \frac{1}{\tau_{HN}} \left[\sin \frac{\alpha\pi}{2 + 2\beta}\right]^{1/\alpha} \left[\sin \frac{\alpha\beta\pi}{2 + 2\beta}\right]^{-1/\alpha} \tag{3.16}$$

Over this wide frequency range, multiple relaxation processes may be visible. A superposition of relevant expressions may be used to describe the entire spectra, as shown in equation 3.17

$$\epsilon^*(\omega) = \frac{-i\sigma}{\omega} + \sum_{j=1}^{N} \frac{\Delta\epsilon_j}{(1 + (i\omega\tau_{HN,j})^{\alpha,j})^{\beta,j}} + \epsilon_\infty \tag{3.17}$$

This is a HN equation for N relaxations (α, β, γ, etc) visible in the frequency window at a particular temperature, along with a DC-conductivity contribution, which comes from the migration of charged species (ions) through the sample. The effects of both polymer system and chain length on the conductivity of ions will be explored in chapter 5. Examples of BDS fitting are shown in figure 3.8.

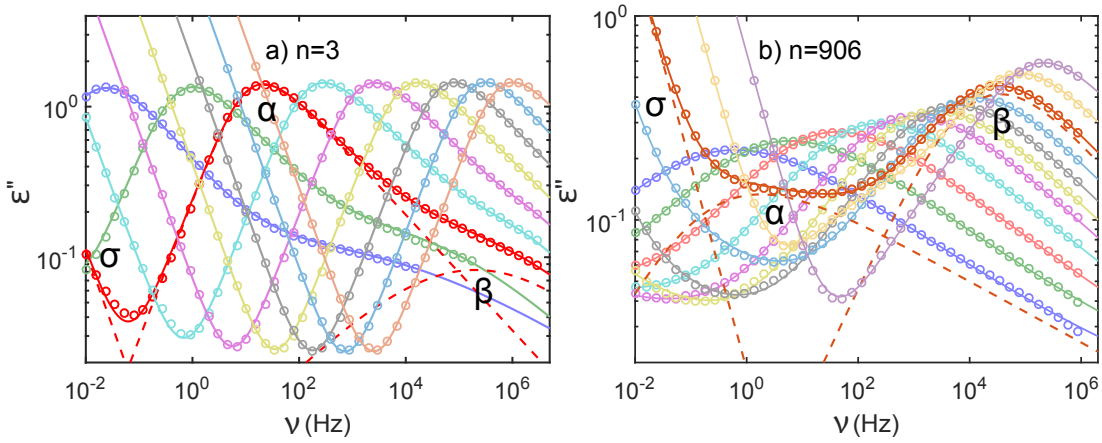

Figure 3.8: Dielectric loss at different temperatures for a) $n = 3$ and b) $n = 906$ PMMA samples. Solid line represent fitting of the entire spectra. Dashed line shows an example of individual contributions to the spectra.

For low M PMMA samples (example in 3.8 (a)), the α relaxation is visible and relatively easy to model (a large change in permittivity, $\Delta\epsilon$, visualised by a higher peak in ϵ''), with a weaker β relaxation at higher frequencies. However, as M increases, the β relaxation becomes more dominant, and obscures the α relaxation (example in 3.8 (b)). This makes differentiating the α relaxation from DC conductivity and the stronger β relaxation difficult for these samples. As discussed in section 2.2.5, for the highest M PMMA sample (n=906), ϵ' was converted to ϵ'' using an appxorimation of Kramer-Kronig relation[112] in order to better fit the α relaxation without a conductivity contribution.

DSC measurements were performed on the full PMMA chain-length series using a TA instruments Q2000 DSC, as discussed section 2.3. An example of a DSC trace is shown in figure 3.9.

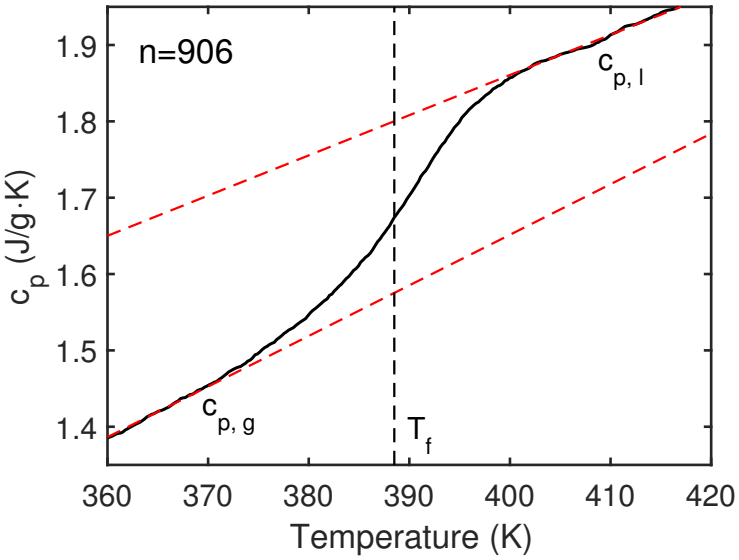

Figure 3.9: Specific heat capacity as a function of temperature for PMMA n=906. The red dashed lines indicate the behaviours in the glass ($c_{p,g}$) and liquid ($c_{p,l}$) states. The black dashed line shows the, so called, fictive temperature.

Figure 3.9 shows the typical step in heat capacity when the sample is cooled through the glass transition. The transition temperature is taken as the fictive temperature, calculated as per Moynihan et. al.[117] in equation 3.18.

$$\int_{T_f}^{T_2} (c_{P,l}(T) - c_{P,g}(T))dT = \int_{T_1}^{T_2} (c_P(T) - c_{P,g}(T))dT \tag{3.18}$$

Here T_1 and T_2 are arbitrary temperatures either side of the transition region, and $c_{P,l}$ and $c_{P,g}$ are the extrapolated heat capacities of both the liquid and glass respectively (red dashed lines in figure 3.9). This is sometimes referred to as the thermodynamic glass transition temperature, as it is the point where the temperature dependent enthalpy changes behaviour. It is used here as it is a more robust and comparable quantity than either the onset, midpoint, or offset definitions of the transition temperature.

In DSC, the cooling rate is inversely proportional to the α relaxation timescale. Hensel et. al.[119] compared transition temperatures obtained using temperature-modulated DSC (TMDSC), where the timescale is set by the modulation period, to transition temperatures at different cooling rates. It was shown that cooling rates of 10K/min correspond well to timescales of $\tau_\alpha \simeq 100$s for a variety of different non-polymeric and polymeric glass formers. In order to test this, the same TMDSC technique was performed on this PMMA chain-length series, and the relationship between cooling rate and α relaxation timescale was determined. Examples of this are shown in figure 3.10.

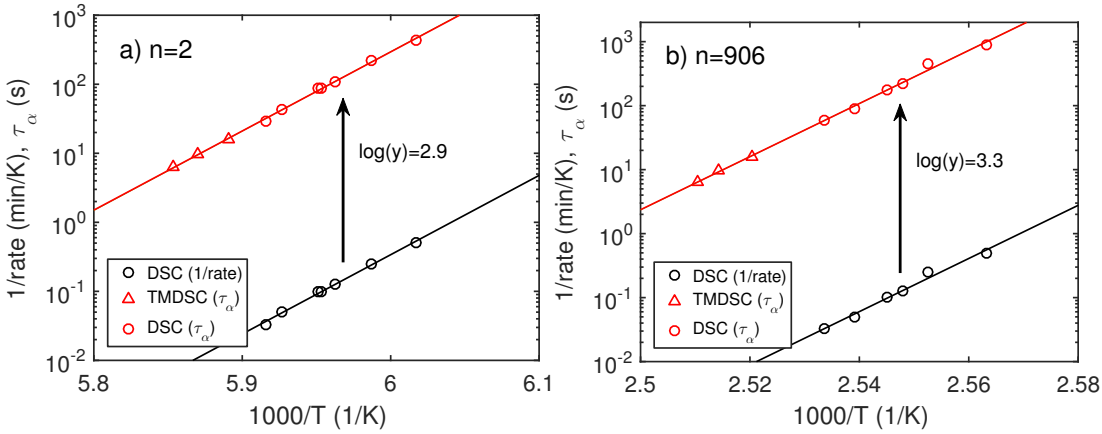

Figure 3.10: Transition temperatures from standard DSC measurements performed at different cooling rates (black circles), vertically shifted using shift factor, y, to transition temperatures from TMDSC (red triangles) for PMMA a) n=2 and b) n=906.

Figure 3.10 illustrates the relationship between inverse cooling rate and relaxation timescale ($\tau_\alpha = y/\text{rate}$) for both (a) low (n=2) and, (b) high (n=906) M PMMA samples. The transition (fictive) temperatures obtained at different cooling rates (black circles) were shifted using a vertical shift factor, y, in order to coincide with transition temperatures obtained using TMDSC (red triangles), where the α relaxation timescale is set by the modulation period (this will be discussed further is section 4.1). The data shown in red, along with the linear (Arrhenius) fit, describes the absolute timescale behaviour over this narrow dynamic window. The shift factor, y, therefore gives the system specific relationship

between cooling rate and α relaxation timescale. A value of $\log(y) = 3$ means that 10K/min corresponds to $\tau_\alpha = 100$s, indicating that PMMA, as shown in figure 3.10, is consistent with this conclusion. As well as the glass transition temperature, the change in heat capacity and transition width were also acquired from cooling rates of 10K/min, and will be discussed in section 3.3.

The α relaxation timescales determined from these techniques are shown in figure 3.11.

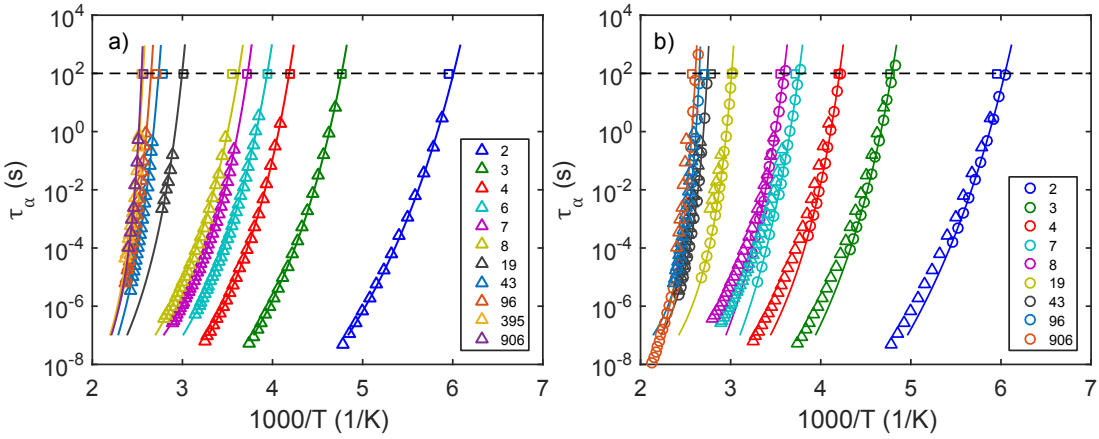

Figure 3.11: PMMA α relaxation Arrhenius plots. a) BDS (triangles) and DSC (squares) for all PMMA samples, with VFT fits through BDS data. b) Rheology (circles), BDS (triangles), and DSC (squares) for common samples, with VFT fits through rheology data. The legends show the degree of polymerisation (n).

The triangles in figure 3.11 (a) shows that $\tau_\alpha(T)$ determined directly from peak values in ϵ'', without relying on TTS, exhibits VFT behaviour. This also shows good agreement with T_g values determined from DSC, shown by the squares at $\tau_\alpha = 100$s. τ_α values from rheology, BDS, and DSC are shown in figure 3.11 (b), with the VFT fits to the rheology timescales. Once again there is good agreement between these techniques in determining τ_α within their particular timescale domains. However, there is a vertical (timescale) shift between rheology and BDS, which will be discussed in section 3.5.1.

3.2.2 The glass transition temperature

Rheology, BDS, and DSC all capture the timescale dependence of the α relaxation, and therefore the glass transition temperature (T_g) can be determined at the timescale where $\tau_\alpha = 100s$. T_g is well known to increase with M for linear polymers, and is generally attributed to the larger free-volume associated with end groups. It is suggested that an increase in free volume leads to a decrease in T_g. Therefore as the molecular weight increases, the density of end groups (and free volume) decreases, leading to an increase in T_g[31, 86]. A similar argument can be derived by considering configurational entropy, such as in the Gibbs-DiMarzio theory[154]. The effect was quantified by Fox and Flory, yielding the equation 3.19.

$$T_g(M_N) = T_g(\infty) - \frac{K}{M_n} \tag{3.19}$$

This is the Fox-Flory equation, where K is an empirical system specific constant, M_n is the number-average molecular weight (simply M for these relativly monodisperse PMMA sample), and $T_g(\infty)$ is the glass transition temperature at high M. Figure 3.12 shows T_g from rheology, BDS, and DSC for this PMMA molecular weight series, along with DTA[3] and DSC[4] literature data.

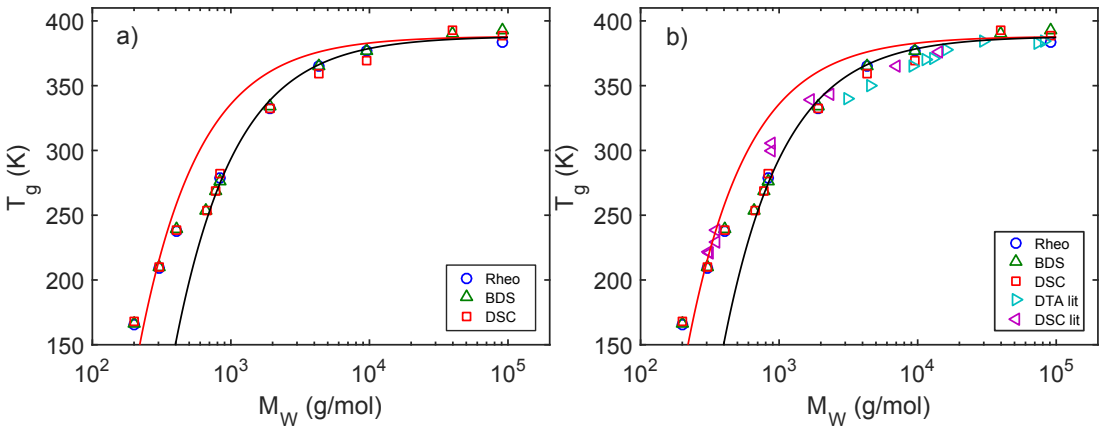

Figure 3.12: a) T_g vs M_W from Rheology TTS master curves, BDS, and DSC. b) Including literature data[3, 4]. Fox-Flory fits (equation 3.19) for the entire data set (red), and for data with $M_W > 10^3$g/mol (black).

As expected, figure 3.12 shows good agreement in T_g values from these three techniques (along with literature data). The slight variations in these techniques are due to differences in the determination of the α relaxation timescales: Rheology probing the complex shear modulus, using TTS and an extrapolation of a VFT expression for a T_g value; BDS probing the complex permittivity, also using an extrapolation of a VFT expression for a T_g value; and DSC measuring the heat capacity as a function of temperature, assuming a cooling rate of 10K/min corresponds to a relaxation time of 100s. A Fox-Flory equation can be used to describe T_g data above $M > 10^3$g/mol, as shown by the black curve fit. However, as shown by the red fit curve, a single Fox-Flory model is insufficient over this entire M range. Cowie[134, 155, 156] suggested that rather than continuous T_g behaviour, the variation of T_g is split into three distinct M regions. Cowie (for PαMS, PS, PB, and PI), and more recently Hintermeyer et. al.[135] (for PDMS, PS, and PB) attributed these regions to physical changes in polymeric behaviour. Regions I and II are two distinct regimes where T_g increases linearly with $\log M$, and region III a saturation in T_g behaviour, where an increase in M does not increase T_g. These three regions are show in figure 3.13 for this PMMA M series.

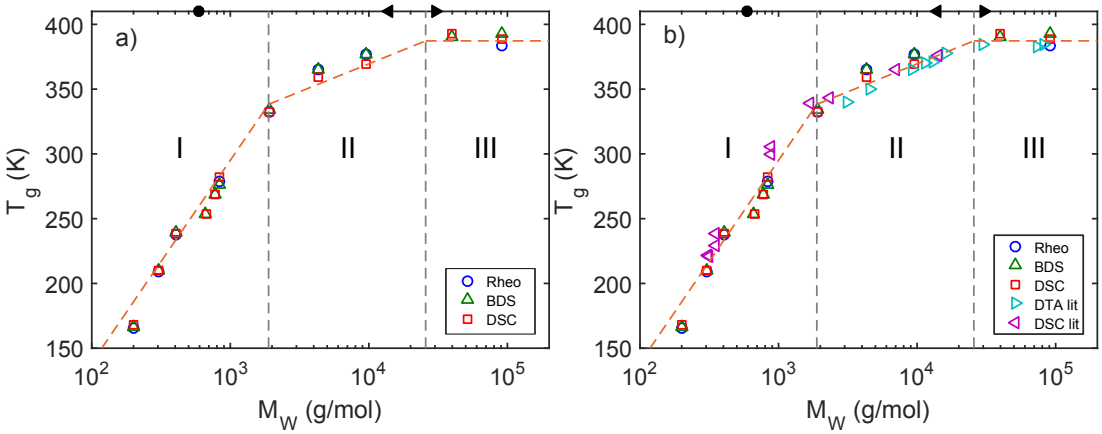

Figure 3.13: a) T_g vs M from rheology TTS master curves, BDS, and DSC. b) Inlcuding literature data[3, 4]. Region I, II, and III represent changes in polymer behaviour with M. Solid black symbols on the top axis indicate M_K (circle), M_e (left facing triangle), and M_c (right facing triangle).

Linear regional T_g fitting in figure 3.13 shows better agreement with low M

data than the single Fox-Flory fit shown in figure 3.12. It is noted that the region I to II boundary is above the Kuhn molecular weight (black circle on the top axis). This transition is observed not only in dynamic measurements such as T_g, but also structural measurements, such as a change in the ratio of the radius of gyration components, calculated using Flory's rotational isomeric state (RIS) theory. This has been carried out in collaboration with Prof. Peter Olmsted[157]. Therefore, this region I to II boundary is attributed to the folding of the polymer chains, leading to the onset of polymer behaviour and the formation of a dynamic bead. The region II to III boundary has been suggested to relate to the onset of entanglement dynamics, although Agapov et. al.[158] show that M_e (black left facing triangle on the top axis) does not describe this transition for PS or PDMS. However, T_g relates to dynamics, and therefore a more relevant comparison would be M_c (black right facing triangle on the top axis), rather than M_e. For PMMS and PS, M_c describes the transition very well[157]. This work agrees with Agapov et. al. for PDMS, whereby neither M_e or M_c describe the region II to III transition. However, for PDMS, due to the nature of the siloxane backbone, loop-like structures form, and therefore direct comparisons to PDMS regarding characteristic molecular weights are more difficult.

From this, it is clear that regional M behaviour of polymer dynamics occurs, and therefore PMMA T_g behaviour is better described using these regional boundaries, rather than a single continuous function.

3.2.3 Dynamic fragility

Figure 3.7 (a) shows an increase in fragility with increasing M, as described using rheology. BDS also probes the temperature dependence of τ_α, and therefore a dynamic fragility can also be determined, albeit requiring the extrapolation of a VFT fit to $\tau_\alpha = 100s$. The dynamic fragility, as calculated using equation 3.14 from VFT fits, is shown in figure 3.14.

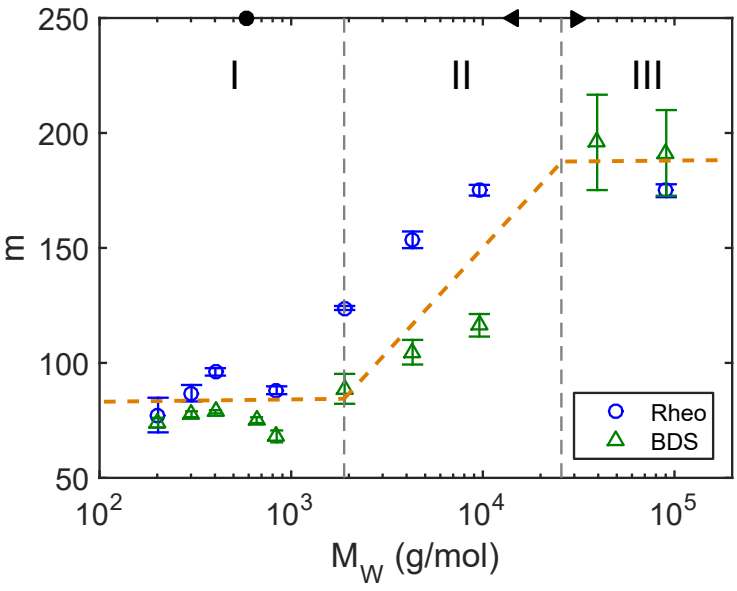

Figure 3.14: Dynamic fragility (m) vs M from rheology TTS master curves, and BDS. Orange dashed lines are guides to the eye, showing possible regional behaviour. Errors are calculated from errors in VFT fitting. Solid black symbols on the top axis indicate M_K (circle), M_e (left facing triangle), and M_c (right facing triangle).

Hintermeyer et. al.[135] also showed an increase in dynamic fragility in other linear polymer systems with increasing M, although regions I and II appeared to show continuous behaviour, until a saturation in region III. This may be he case with PMMA; the rheology data could be showing this behaviour, with the n=8 ($M = 840$g/mol) sample being an anomaly. However, within the accuracy of the data it appears that fragility may be M independent in region I. The relationship between the values of dynamic fragility from rheology and BDS is related to the vertical shift between $\tau_\alpha(T)$ values from these techniques, as mentioned in section 3.2.1. $\tau_\alpha(T)$ values from rheology are smaller than those attained from BDS at the same temperature (apparent in figure 3.11 (b)), and therefore values of m will be lower for rheology than BDS, which is apparent here. This vertical shift in $\tau_\alpha(T)$ between rheology and BDS will be discussed further in section 3.5.1.

The KWW stretching parameter (β_{KWW}) has been shown to correlate inversly to dynamic fragility for polymeric and non-polymeric systems[25]. This non-

exponential behaviour of the α relaxation is interpreted as either that; (i) the α relaxation has contributions from a heterogeneous series of environments, each of which are exponential, or (ii) a homogeneous series which themselves are non-exponential[10]. Also, in the coupling mode by Ngai[41], the stretching parameter has been linked to the degree of intermolecular coupling ($\beta_{KWW} = 1 - n$). For the PMMA chain-length series, β_{KWW} was measured directly through fitting of the TTS master curves, shown in figure 3.15.

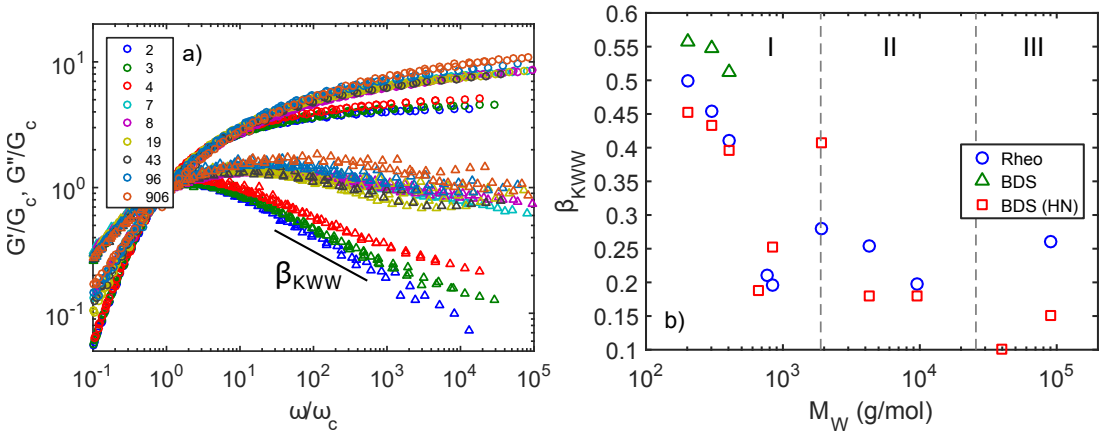

Figure 3.15: a) High frequency TTS master curves for PMMA M_W series, scaled on to the high frequency crossover point. Circles and triangles are G' and G'' respectively. b) KWW stretching parameter vs M_W from Rheology TTS master curves, and BDS at $\tau_\alpha \sim 1s$. BDS Havriliak-Negami high frequency exponents at $\tau_\alpha \sim 1s$ is also shown.

The values of β_{KWW} were attained directly from the fitting to the TTS master curves from rheology, and the low M samples from BDS (due to the relative strengths of the α and β relaxations in higher M PMMA). The red squares (BDS (HN)) in figure 3.15 (b) is the exponent describing the high frequency power-law flank in $\epsilon''(\omega)$ ($\alpha\beta$ parameters from a HN fit), which is consistently lower than a true value of β_{KWW}. The high frequency flank in $G''(\omega)$ (and $\epsilon''(\omega)$) relates to β_{KWW}, which, as shown in 3.15 (a), is clearly increasing with M. This high frequency flank also has contributions from the secondary (β) relaxation (which is apparent as a clear failure in TTS), causing exact fitting of a single KWW expression difficult in this frequency range.

It is uncertain whether the inverse correlation between β_{KWW} and m[25] holds for oligomeric systems. However, it seems unlikely to be the case considering the lack of obvious correlations between figures 3.15 (b) and 3.14. Interestingly, Santangelo et. al.[159] showed that for PS, the β_{KWW} does not increase with M using similar rheology measurements, although dynamic fragility did change comparably.

3.3 Differential scanning calorimetry

DSC measurements were carried out on the PMMA M series as discussed in section 3.2.1. The step increase in specific heat capacity (c_p) at the glass transition relates to an increase in the number of configurational degrees of freedom, and therefore an increase in entropy[20] between the glass and liquid states. The traces of c_p as a function of temperature increase systematically with M, as shown in figure 3.16.

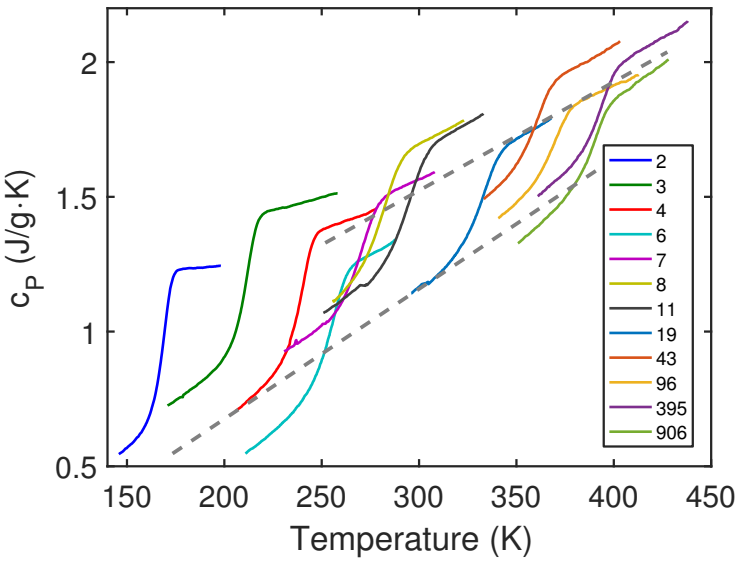

Figure 3.16: c_p as a function T from 10K/min DSC measurement on the PMMA M series. The dashed lines are a guide to the eye, showing systematically increasing glassy and liquid state specific heat capacities. The legend shows degree of polymerisation (n).

Figure 3.16 shows the increase in the glass transition temperature with increasing M (as discussed in section 3.2.2). This also shows, within some scatter, that the specific heat capacities of the liquid and glassy states ($c_{p,l}$ and $c_{p,g}$ respectively) seem to follow similar behaviour of $c_p(T)$ in this PMMA chain length series (indicated by the gray dashed lines). Huang et. al.[160] showed that polymeric ($n = 915$) poly($\alpha-$methylstyrene) (PαMS) understandably showed a reduction in T_g when blended with increasing mass fractions of PαMS pentamer ($n = 5$). Interestingly, for this series of plasticised PαMS, $c_{p,l}$ and $c_{p,g}$ followed common behaviour, regardless of mass fraction. This suggest that increasing the degree of polymerisation may be equivalent to mixing long and short chain polymers (hence altering the M_W of the mixed sample). They also noted that this common $c_{p,l}$ did not hold for units PαMS smaller than $n = 5$, which is also consistent with $n = 2 - 4$ for PMMA shown here as having a different slope than the rest of the series. Loufakis and Wunderlich[161] proposed that the heat capacity is a sum of three components, as shown in equation 3.20.

$$C_p = C_{vib} + C_{ext} + C_{conf} \tag{3.20}$$

Here, the heat capacity C_p is a sum of vibrational, external, and configurational contributions: C_{vib} accounts for the majority of the heat capacity, which is assumed to be the same for both the solid (glassy) and liquid, and hence does not change over the T_g step; C_{ext} (related to expansivity and compressibility of the material), which does vary between solid and liquid; and C_{conf}, which is related to the additional configurational degrees in the liquid state. Therefore, these quantities must depend, to first approximation, on temperature, but not increasing chain length in PMMA.

3.3.1 Width and height of the glass transition

Figure 3.16 shows the change in both the step height (Δc_p), and step width (ΔT) of the glass transition as a function of M, which are shown in figure 3.17.

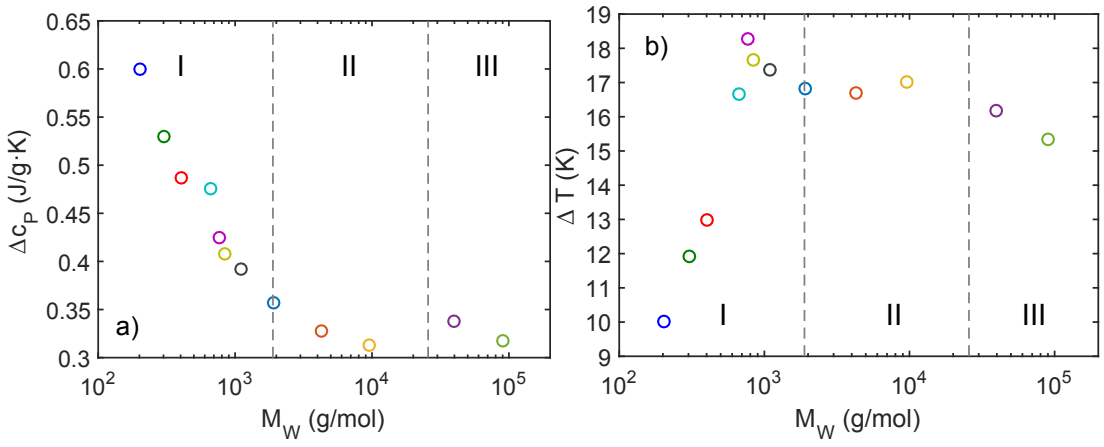

Figure 3.17: a) Change in c_p between $c_{p,liquid}$ and $c_{p,glass}$ at T_g as a function of M. b) Difference in temperature between onset and offset definitions of T_g (discussed in section 2.3) as a function of M. Dash lines indicate regional boundaries.

The values of Δc_p against M significantly decreases in region I, and become M independent withins regions II and III. This quantity, through Adam-Gibbs entropy model[28], is linked to dynamic fragility (m)[162], which also exhibits regional behaviour (shown in figure 3.14). ΔT as a function of M also exhibits similar regional behaviour, which relates to the KWW stretching parameter (β_{KWW}), as this is a time/frequency domain metric relating to the width of the α relaxation, and also dynamic fragility[163]. Isobaric heat capacity is defined in equation 3.21.

$$C_P = T\left(\frac{\partial S}{\partial T}\right)_p \tag{3.21}$$

Therefore, the difference in the rate of change of entropy at T_g between liquid and glassy states can be defined by equation 3.22.

$$\frac{\Delta C_p}{T_g} = \left[\left(\frac{\partial S_{liquid}}{\partial T}\right)_{T_g} - \left(\frac{\partial S_{glass}}{\partial T}\right)_{T_g}\right]_P \tag{3.22}$$

Normalising Δc_P by T_g therefore yields this difference in rate of change of entropy between liquid and glass[164], as shown for this M series in figure 3.18.

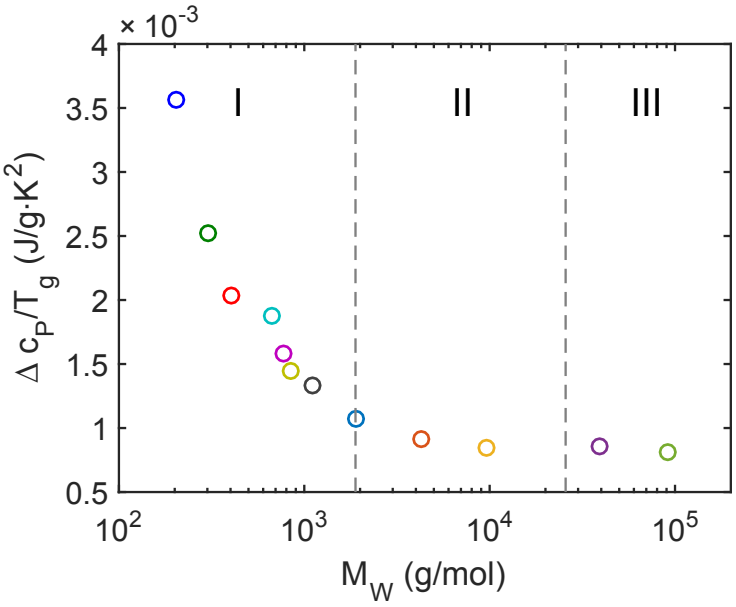

Figure 3.18: The heat capacity step (Δc_P) normalised by T_g as a function of M for this PMMA chain length series. Dash lines indicate regional boundaries.

Once again, this shows a distinct decrease in the difference in the rate of change of entropy between liquid and glass in region I, and a stabilisation in regions II and III. Δc_P decreases by ~ 2 and T_g increases by ~ 2, and therefore the quantity $\Delta c_P/T_g$ decreases by ~ 4 in region I.

Using these heat capacitiy responses (T_g, ΔT, and Δc_p), Donth[165] proposed a method to determine the size of the cooperatively rearranging region at T_g. Using temperature modulated DSC (TMDSC), a more robust measure of ΔT, and a timescale dependent T_α can be attained. These measurements, along with the M dependence of the size of the cooperatively rearranging region attained from TMDSC, along with other measures of the degree of molecular cooperativity will be discussed in chapter 4.

3.4 Chain modes

As discussed in section 1.3, polymer chains constantly reshape and move due to Brownian motion[64]. In rheology measurements, this movement of polymer chains is evident in the complex shear modulus. At the Rouse bead size (M_R),

polymer behaviour starts to become apparent in the form of Rouse modes, which relax the chain through a series of normal modes. Above the critical entanglement size (M_c), chains become entangled and entanglement and reptation dynamics become visible also. In PMMA, these chain dynamics are not obvious in BDS due to segmental dipoles not having a component along the polymer chain[14].

For PMMA, the critical entanglement size is quoted in literature as M_c = 29500g/mol[138]. In this work, two entangled ($M > M_c$) PMMA samples were measured using rheology: a monodisperse (PDI=1.04), n=906 (M_W = 90600g/mol) sample; and a polydisperse (PDI=2.46), n=1478 (M_W = 147800g/mol) sample. These were compared, along with two monodisperse literature samples (n=1080, and n=2000)[90] in figure 3.19.

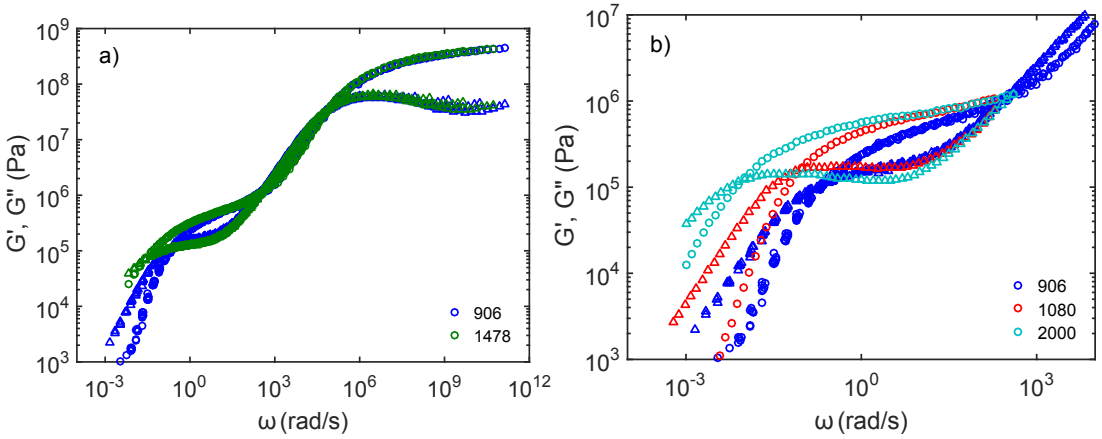

Figure 3.19: Comparison of entangled PMMA samples. a) Samples measured in this work (n=906, and n=1478) across the entire dynamic range from glass to melt. b) Monodisperse samples from this work and literature, focusing on low frequency entanglement and melt dynamics.

As shown in figure 3.19 (a), the complex shear modulus of both these samples agree at high frequencies within the glassy and Rouse regimes as expected, differing only at low frequencies once entanglement dynamics become apparent. In linear polymers, the plateau behaviour depends on polydispersity, whereby the rubber plateau region will be "slanted" in polydisperse samples due to shorter chains being able to reptate quicker than longer chains. In relatively monodisperse polymers, the frequency distance between entanglement and reptation depends

on M. Figure 3.19 (b) shows this increasing frequency distance, with the terminal relaxation time expected to scale as $\tau_d \propto M^{3.4}$[166].

3.4.1 The dynamic bead size

The dynamic bead (or Rouse bead, M_R) size can be estimated using a range of different techniques:

- Neutron spin echo (NSE) measurements on polymer systems can be used to determine the scatting vector (q), and therefore the length-scale ($\sim 2\pi/q$), where Rouse modelling breaks down. This lengthscale is often attributed to the size of the dynamic bead[167], although conversions between this length scale and M_R are non-trivial[168].
- Similar to this work, a chain-length series of oligomers/polymers can be studied using techniques such as fast-field cycling NMR (FFCNMR) for PPG, PI, and PDMS[152], and PB[169], or using BDS for so called type-A polymers[14] (which have dipole conponents along the polymer chain backbone) such as PPG[170] and PI[151], whereby M_R can be determined as the M when chain behaviour becomes visible in the spectra.
- Using a similar ansatz to that used in this work, whereby the mechanical modulus has contributions from both the α relaxation and Rouse modes (equation 3.9). M_R can be varied to best fit the spectra. This technique has been used to determine M_R for PS[144, 171].

For PMMA, no such studies exist in literature. Thus, in this work, the number of Rouse modes was determined simply by $n_R = M/M_R$, where M_R was taken as the Kuhn length (M_K), which for PMMA is $M_K = 598$g/mol[138]. As already mentioned, Inoue et. al.[137] carried out a similar fitting procedure on intermediate M PS, using a Rouse molecular weight of $M_R = 850 - 900$g/mol, which was determined from the high frequency modulus contribution of Rouse modes in extensional rheology[171]. Gray et. al.[144] determined that a Rouse bead size of $M_R = 500 - 510$g/mol was sufficient in describing intermediate M complex

shear modulus spectra of PS in the same manner. These values are in-line with the Kuhn size for PS, which is in the region of $M_K = 720$g/mol[60].

However, Ding and Sokolov[168] have pointed out that the longest Rouse mode contributes 92% of the total compliance in the Rouse regime, thus criticising the often used modulus determinations of the M_R. They suggested that the Kuhn length, as defined in section 1.3.1, is an oversimplification, and that the characteristic ratio, C_∞, which is the ratio of the mean-squared end-to-end distance and n number of Kuhn lengths in a random walk ($C_\infty =< R_0^2 > /nl_K^2$)[61], is not the only parameter which defines the dynamic bead size. The Kuhn length defined this way assumes that the polymer chain within the Kuhn unit is fully extended, i.e. in a fully trans configuration. However, in reality this is not the case, and chains begin to fold on themselves within these lengthscale. Using the determination of the Rouse length-scale from NSE measurements, they show that in poly(dimethyl siloxane) (PDMS), both M_K, and their calculated M_R are consistent. However, using the same calculation for PS, M_R could be as high as $M_R = 5000$g/mol, and they describe the complex shear modulus with a superposition of α and Rouse models on the same two samples as Inoue et. al. (n=101, and n=57) using this estimation.

To test this, complex shear modulus measurements were carried out in the same manner as the PMMA samples on a PS $M = 11300$g/mol (n=109) sample. This would contain either $n_R = 13$ or $n_R = 2$ Rouse modes, depending whether the size of the Rouse bead is $M_R = 850$g/mol, or $M_R = 5000$g/mol respectively. The same modelling procedure was carried out as with intermediate M PMMA samples (with M dependent density data from literature[172], described by a Fox-Flory model), which are shown in figure 3.20.

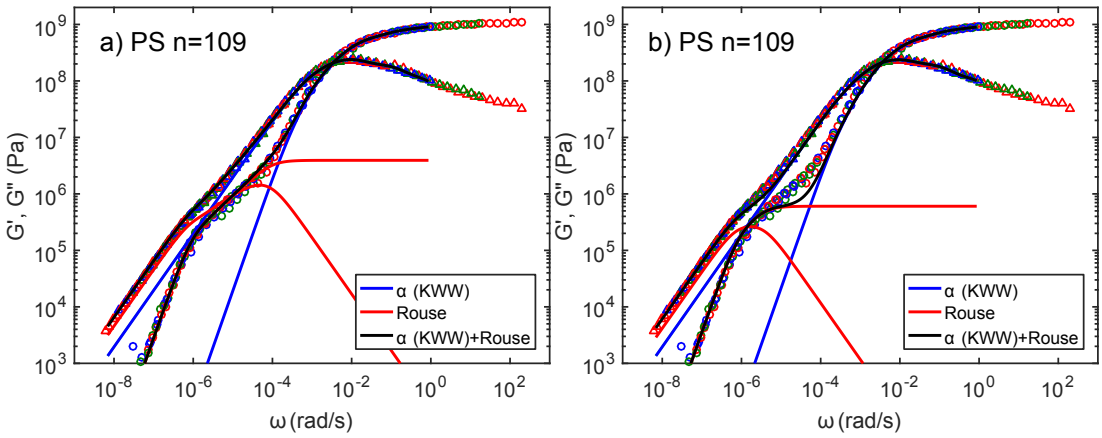

Figure 3.20: PS TTS master curves with a sum of glassy and Rouse models. a) $M_R = 850$g/mol. b) $M_R = 5000$g/mol.

Figure 3.20 (a) shows the fitting of the complex shear modulus using the Kuhn definition for the Rouse bead size, $M_R \approx M_K = 850$g/mol ($n_R = 13$), whereas 3.20 (b) was fitted using $M_R = 5000$g/mol ($n_R = 2$). This suggests that only 2 Rouse modes is insufficient in describing this TTS master curve, and that the Kuhn definition is in fact more representative of the dynamic bead than that defined by Ding and Sokolov. Additionally, the validity of fitting a Rouse model to the spectra of an oligomer with only 2 Rouse units would also need to be questioned. The failure of the fitting is more apparent in G' than G'', which is consistent with the statement that the longest Rouse mode contributes $\sim 92\%$ of the total compliance in the Rouse regime, as the total modulus is dominated by G'' in this regime. However, both components of the complex shear modulus are unable to be described with such a large dynamic bead size. Finally, it is worth pointing out that, as discussed by Jeong and Douglas[173], at least for some polymer systems such as polyethylene, Rouse theory does not hold for unentangled ($M < M_c$) polymers due to the lack of Gaussianity. However, the use of the Rouse model using the Kuhn molecular weight, M_K, as the dynamic bead size can describe chain dynamics well in both unentangled PMMA and PS, and therefore this approximation was used.

3.4.2 Sub-Rouse modes

In order to establish Rouse dynamics, a polymer chain must contain a number of basic Rouse units. Chain relaxation mechanisms smaller than those involving Rouse beads are coined sub-Rouse modes[174]. Sub-Rouse modes have been previously reported in polymeric PMMA using rheology[175], whereby the onset of such modes are attributed to the dynamic crossover in PMMA[176, 177], i.e. the temperature where there is a distinct change from one VFT behaviour to another.

For PMMA samples where the chain length is approximately that of the Rouse bead size (M_R), sub-Rouse modes may be visible due to the lack of Rouse modes. For this PMMA chain-length series, two samples fit this criteria, as shown in figure 3.21.

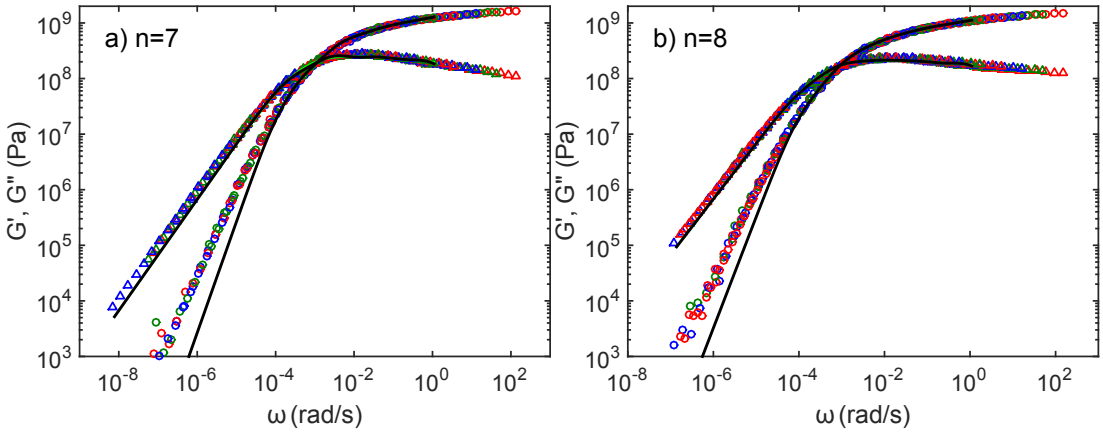

Figure 3.21: PMMA TTS master curves for a) n=7 and b) n=8. A single KWW fit of the α relaxation in insufficient to describe the entire spectra, shown by the black fit.

Figure 3.21 shows two similar spectra, of similar PMMA samples (M=771 and 840g/mol). The chain mode fitting performed in this work would only include a single Rouse mode for both of these samples, which would be equivalent to a single Maxwell mode at low frequencies, in addition to the KWW model describing the α relaxation shown in black. This is unable to describe the spectra at low frequencies, and therefore was not included. This suggests that Sub-Rouse

dynamics are evident, causing a broadening of the low frequency flank, which has previously also been reported from BDS[178], and photo-correlation spectroscopy (PCS)[179, 180]. While there does not seem to be a changeover in VFT behaviour, these samples also do not follow the trend of increasing fragility with the rest of the series. These two samples also show other anomalous behaviour, which will be discussed in section 3.5.1.

It is also worth noting that these samples are relatively polydisperse (PDI=1.18−1.44), and are in a molecular weight range (region I) where M has a large effect on glassy and polymer dynamics (T_g, m, and τ_1). It would be interesting to see if this behaviour was apparent in monodisperse samples, which will be a focus of future work.

3.5 Validity of TTS from glass to melt

The validity of TTS, particularly over a wide dynamic range, is often questioned[98, 181]. Ding and Sokolov[133, 182] compiled timescale data for both segmental and chain dynamics in a number of different polymer systems, and suggested that these two relaxation mechanisms decouple for time-scales $\tau_\alpha \sim 10^{-5} - 10^{-7}s$. The timescale where the temperature dependance starts to differ appears to be correlated to the fragility of the polymer. Less fragile polymers such as polypropylene glycol (PPG) and polyisoprene (PI) are coupled at higher values of τ_α than more fragile polymers such as polycarbonate (PC). For PS (which exhibits similar α and chain behaviour to PMMA, such as T_g, m, M_K), direct measures of $\tau_\alpha(T)$ using NMR spectrscopy[183], and chain-mode relaxation times, $\tau_n(T)$, using mechanical spectroscopy[184], compared over the same temperature range, agreed with this hypothesis. Hence we expect TTS to fail as we approach T_g from the melt (increasing values of τ_α). In order to assess whether decoupling in this timescale regime was an issue, the TTS master curves where chain modes could be observed ($M > M_R$) were split into three regions: an α relaxation dominant region, where $|G^*_{chain}| \leq 2|G^*_\alpha|$; a chain mode dominant region, where $|G^*_\alpha| \leq 2|G^*_{chain}|$; and an intermediate region between these two. Three scenarios are shown in figure 3.22.

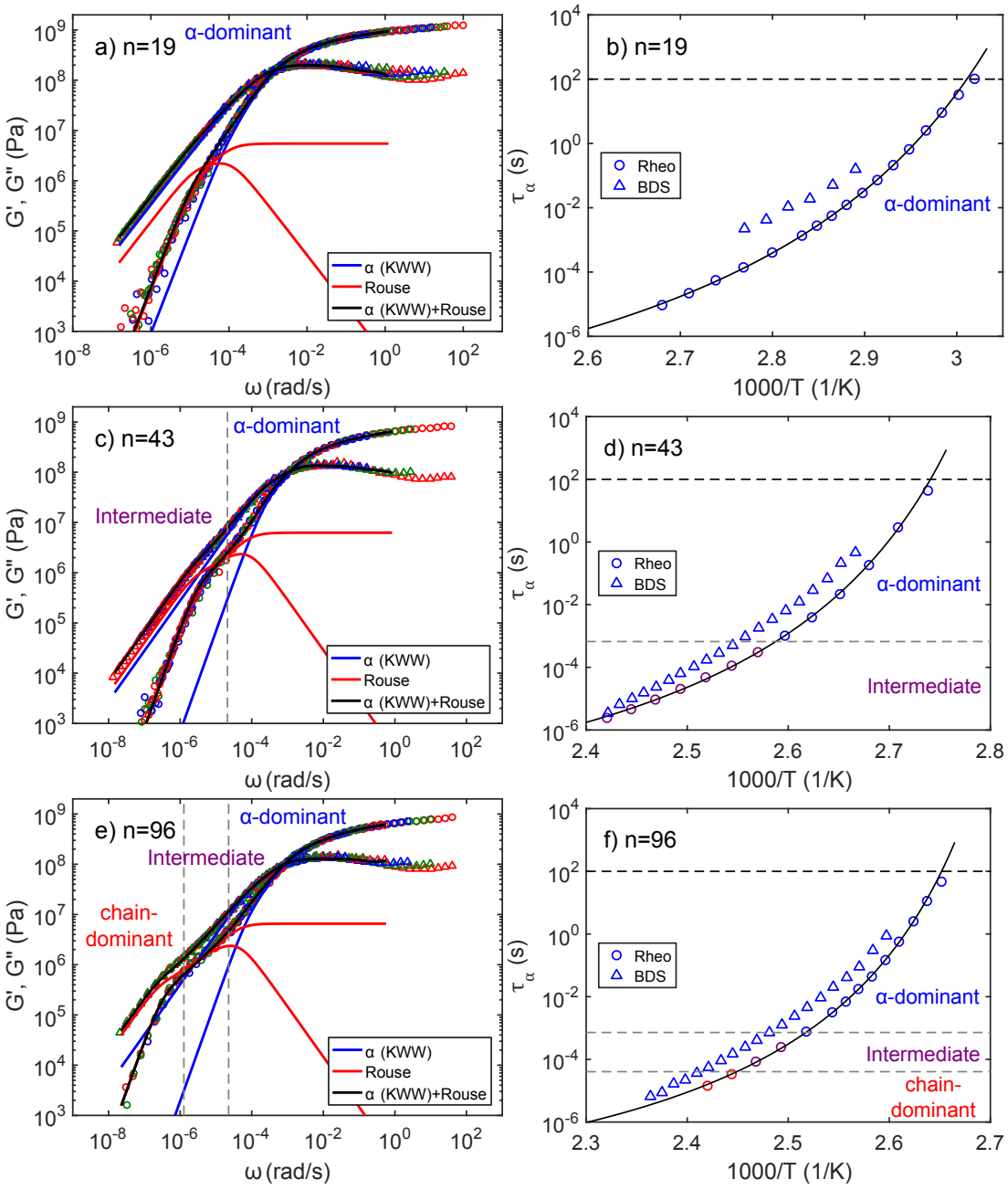

Figure 3.22: Left: TTS master curves for n=19, 43, and 96 PMMA showing fitting routine of segmental and chain dynamics. Dashed gray lines indicate changes from α dominant, to intermediate, to chain dominant regimes. Right: Approximate position of single frequency sweeps (using $f = 0.5$Hz as the representative frequency) indicating the α timescale where these regimes change. BDS timescale data is also shown (which is α dominant by definition.)

Figure 3.22 (a), (c), and (e) show TTS master curves with α and chain mode fitting. These were split into "α dominant", "intermediate", and "chain dominant" ranges as defined previously. Figure 3.22 (a) (and samples with lower M) are α dominant across this dynamic range due to either non-existent or few Rouse modes. In figure 3.22 (c) the intermediate regime becomes apparent. Finally, in figure 3.22 (e) (and samples with higher M), the chain dominant regime appears. By defining the middle value of the frequency sweep range ($f = 0.5$Hz) as the representative frequency at a particular temperature, the value of τ_α that correspond to these regime boundaries can be estimated. Figure 3.22 (b), (d), and (e) show this position on Arrhenius plots corresponding to these samples, along with BDS τ_α data (which is by definition α dominant).

Using this procedure for identifying the dominant relaxation mechanism, for low M samples (n=19 and below) the modulus is dominated by the segmental relaxation mechanism over the entire dynamic range. As chain modes become apparent as M increases, the chain mode contribution to the modulus become more and more prominent at lower frequencies. This eventually yields intermediate and chain mode dominant regimes for higher M samples. For the middle and high M samples (n=43 and above), the crossover from α dominant to an intermediate regime appears to happen at $\tau_\alpha \sim 10^{-3}$s. Above this timescale, we deem the shear modulus to be dominated by the segmental relaxation mode, and for any underlying chain modes which would cause TTS to fail to be effectively irrelevant due to their lack of contribution to the shear modulus. As previously mentioned, decoupling is expected to happen between $\tau_\alpha \sim 10^{-5} - 10^{-7}$s, which means this does span into the intermediate regime, where the shear modulus has both segmental and chain mode contributions. TTS in this range between the onset of this intermediate regime $\tau_\alpha \sim 10^{-3}$s, and the decoupling region $\tau_\alpha \sim 10^{-5} - 10^{-7}$s may show some failure.

3.5.1 Comparisons between rheology and BDS

BDS directly probes the α relaxation of PMMA over a broad frequency range without relying on TTS, and without an obvious influence of chain modes. The α relaxation timescales from BDS therefore can be compared to those from rheology,

which provides a means to identify any prominent chain mode effects on the dynamics. I.e. in order to assess whether the decoupling between the segmental relaxation and chain modes were an issue in the timescale region region below $\tau_\alpha \sim 10^{-3}$s for middle and high M (n=43 and above) samples.

As shown in figure 3.11 (b), there is a shift between α relaxation timescales from rheology and BDS. The complex permittivity is a compliance measurement, which is the inverse of a modulus measurement. Hence, it has been suggested that it would be more appropriate to compare the dielectric modulus ($M^* = 1/\epsilon^*$) to the mechanical modulus[47]. An example a conversion to a dielectric modulus is shown in figure 3.23.

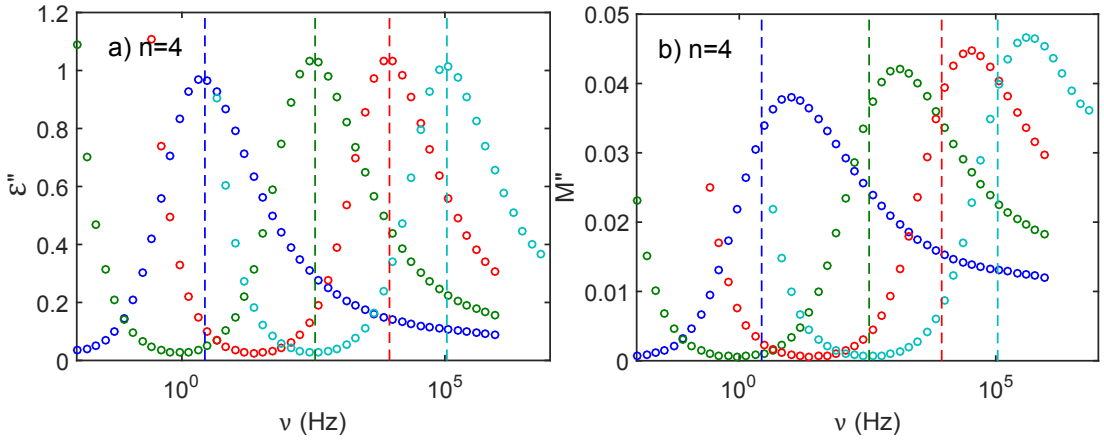

Figure 3.23: PMMA n=4. a) Imaginary permittivity for T=251, 263, 275, and 287K. b) Imaginary dielectric modulus of the same temperatures as in the left figure. Peak positions of the imaginary permittivity are shown by dashed lines.

The peak, which is taken as the relaxation timescale ($\tau_\alpha = 1/\omega_p$), clearly shifts to higher frequencies (shorter timescales) in the modulus representation. This is consistent with the shift between timescales attained from rheology and BDS, as shown in figure 3.24.

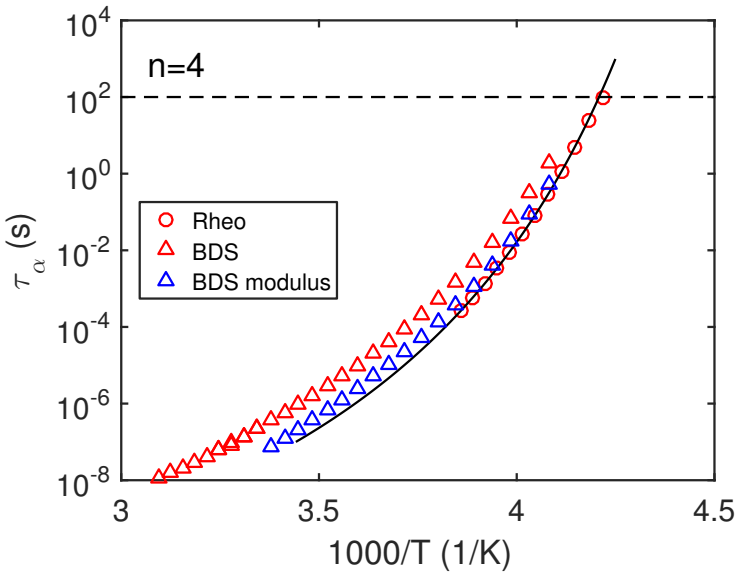

Figure 3.24: Arrhneius plot showing τ_α timescales attained from: Rheology TTS shift factors (modulus); BDS permittivity (compliance); and BDS modulus.

These α relaxation timescales from the dielectric modulus show better agreement with those determined using the mechanical modulus than those from the permittivity. However, this dielectric modulus representation is often regarded as unphysical, as not only features of rotational molecular dynamics, but translational diffusion (due to ion transport) and electronic polarisation is also present in dielectric spectra[185–187]. Despite this, a shift is apparent between either representation of the dielectric timescales and those determined from the mechanical modulus. Looking back at figure 3.22, across the entire M range for timescales attained from TTS shift factors (Rheo), the α relaxation is the dominant relaxation mechanism where $\tau_\alpha > 10^{-3}s$. Therefore, shifting between timescales from rheology and BDS should work above this timescale. To test this, rheology timescales were shifted to BDS timescales both above where $\tau_\alpha > 10^{-3}s$, and also across the entire timescale range. Examples of this is shown in figure 3.25.

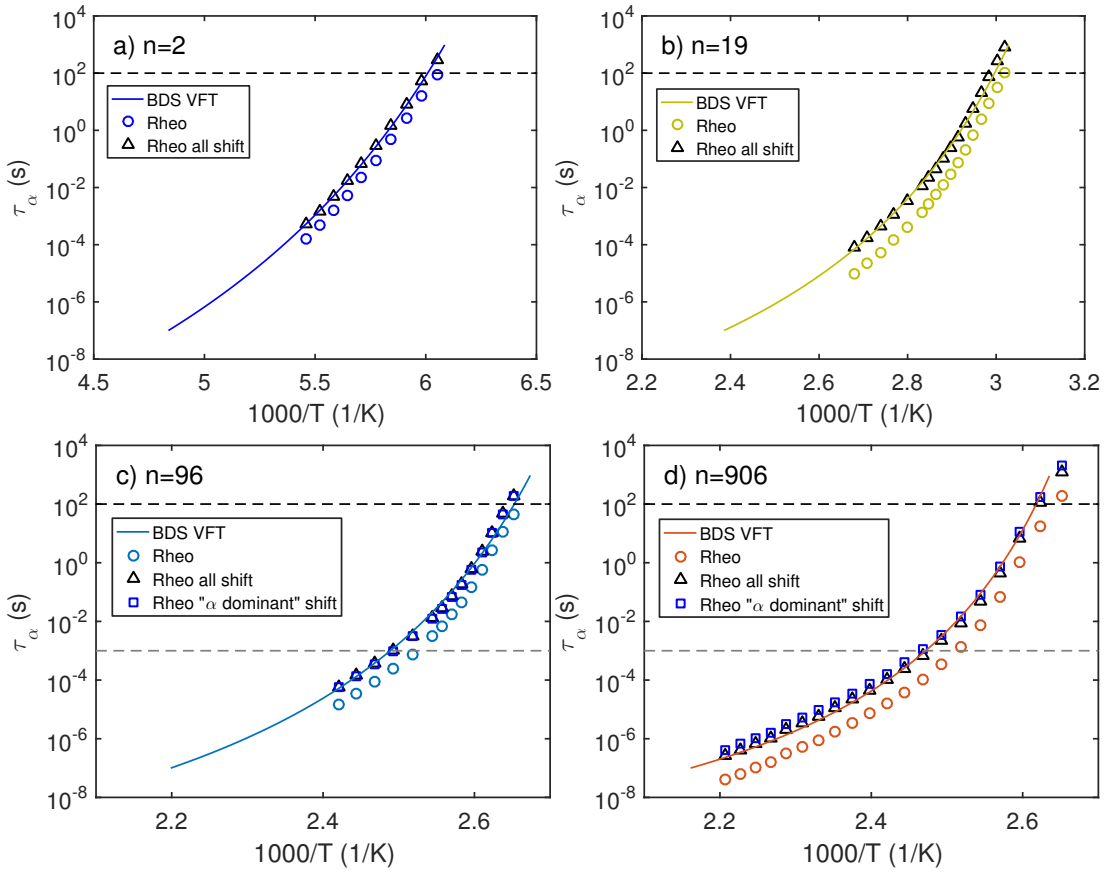

Figure 3.25: α relaxation Arrhenius plots for PMMA n=2, 19, 96, and 906. τ_α attained from rheology was shifted to BDS VFT fits across the entire τ_α range, and in the "α dominant" range, where $\tau_\alpha > 10^{-3}$s when applicable.

For n=2-19 (figure 3.25 (a) and(b)), τ_α values from the TTS master curve are always within the "α dominant" regime due to either the lack of, or insignificant contribution from chain modes, and hence should shift to BDS timescales across the entire τ_α range. For n=43-906 (figures 3.25 (c) and (d)), chain modes are more significant, and the "intermediate" and "chain dominant" regimes appear. However, this shifting from rheology to BDS indicates that across the M range (with the exception of n=7 and 8, to be discussed shortly), TTS captures the timescale dependence of the α relaxation not only in the α dominant regime, but across this entire timescale range. For other polymeric and non-polymeric systems, the shift is quoted as being between 0.5-1 decades[187] (with some ex-

ceptions, such as m-Toluidine which exhibits a very small shift[188, 189]), which is consistent with this data also, although this shows no obvious trend with M. The combination of α relaxation timescales shifted to BDS across the entire τ_α range for this PMMA M series is shown in figure 3.26.

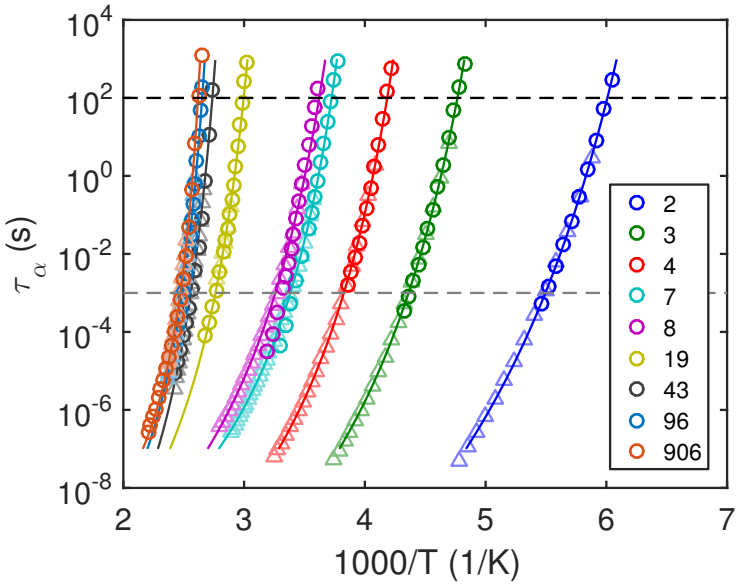

Figure 3.26: PMMA α relaxation Arrhenius plot. Timescales attained from TTS master curves (circles) are shifted across the entire τ_α range (with the expetion of n=7 and 8, which are shifted across the "α dominant" range ($10^{-3}s < \tau_\alpha$)) to timescales attained from BDS (triangles), with VFT fits. The legend indicates the degree of polymerisation (n).

Figure 3.26 shows excellent overlap of $\tau_\alpha(T)$ from rheology shifted to BDS with shift factors between $\sim 2-10$. However, a notable discrepancy can be seen clearly, whereby n=7 and 8 do not overlap below the α dominant range (hence, are only shifted within this timescale range). The reason for this is unknown. It is possible that polydispersity in this region plays an important role, whereby chains of different lengths have vastly different dynamics than others, causing complicated behaviour in the chain mode region (this was alluded to in section 3.4.2).

Despite this exception, by shifting τ_α from the TTS master curves to those directly from BDS, this shows that timescales attained in this manner follow the

timescale dependence of the α relaxation over the measured temperature range. Of course, log scales can obscure subtle differences, especially when capturing ~ 10 orders of magnitude in timescale data. However, considering that: (i) The decoupling between τ_α and τ_n in fragile systems such as PMMA occurs in a τ_α regime where chain modes are only beginning to start to dominate the dynamic shear modulus spectra[133] and; (ii) There is agreement between τ_α determined from this TTS procedure and to a direct measurement using BDS. TTS appears to be a valid technique in describing the dynamic shear modulus, the α relaxation, and chain dynamics in this PMMA M series from T_g to melt.

3.5.2 Other polymer systems

As TTS allowed us to describe $\tau_\alpha(T)$ for this PMMA chain-length series. The question arises as to the validity of TTS, and relationship between τ_α and τ_n in other polymeric systems. We picked two additional samples to investigate: (i) PS, with similar T_g and flexibility to PMMA; and (ii) PI, which has a lower T_g, and is more flexible than PMMA.

Considering the previous work done in both applying this ansatz whereby the dynamic shear modulus TTS spectra is described by a sum of an α and Rouse spectra[137, 144], and looking at the decoupling between τ_α and τ_n[133], shear modulus measurements were performed on an intermediate M (n=109) PS sample. TTS master curves were produced in the same manner as for the PMMA series, with the differences in the fitting of PS in the Rouse regime discussed in section 3.4.1. This is shown in figure 3.27.

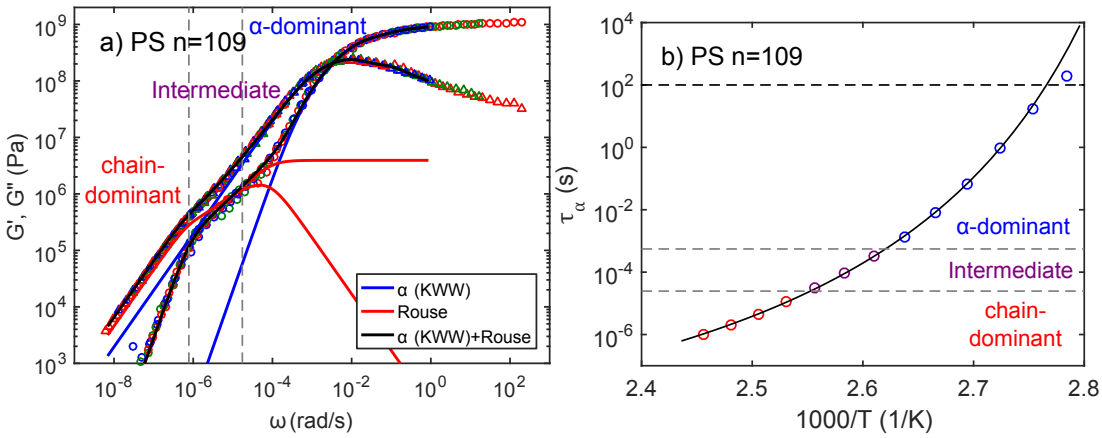

Figure 3.27: a) TTS master curve for n=109 PS showing fitting routine of segmental and chain dynamics. Dashed gray lines indicate changes from α dominant, to intermediate, to chain dominant regimes. b) Approximate position of single frequency sweeps (using $f = 0.5Hz$ as the representative frequency) indicating the α timescale where these regimes change.

Figure 3.27 shows PS n=109 analysed in the same manner as for PMMA in figure 3.22, whereby the complex shear modulus spectrum is split into "α dominant", "intermediate", and "chain dominant" regimes. PS n=109 is comparable to PMMA n=96 (figure 3.22 (e) and (f)). Both these samples are similar M, with similar properties (M_0, M_K, M_e, M_c, m, and T_g), and therefore exhibit a very similar shear modulus response. The boundaries between the three regimes are also situlated at approximately the same frequencies as for PMMA. However, comparing direct measures of τ_α using NMR[183], and τ_n using rheology and BDS[184], Ding and Sokolov[133] show decoupling in the region of $\tau_\alpha \sim 10^{-5}$s. As concluded for PMMA, this is in the intermediate regime, whereby approximately half of the dynamic shear modulus is being contributed to by the α relaxation ($|G^*_\alpha| \approx |G^*_{chain}|$), and because of this, any decoupling between τ_α and τ_n in this region may be negligible.

Due to the previously stated similarities between PMMA and PS, a less fragile polymeric system was also tested. Dynamic shear modulus measurements and BDS on a high M (n=1632) polyisoprene (PI) sample were performed. PI is an example of a type-A polymer, which has a dipole moment component along

the backbone of the polymer chain[14]. Because of this, chain modes are also directly observed in the BDS spectra along with the α relaxation. This makes it an ideal system to compare these two relaxation mechanisms directly using BDS. For rheology, the TTS master curves were split into the α relaxation and chain modes, which are shown in figure 3.28.

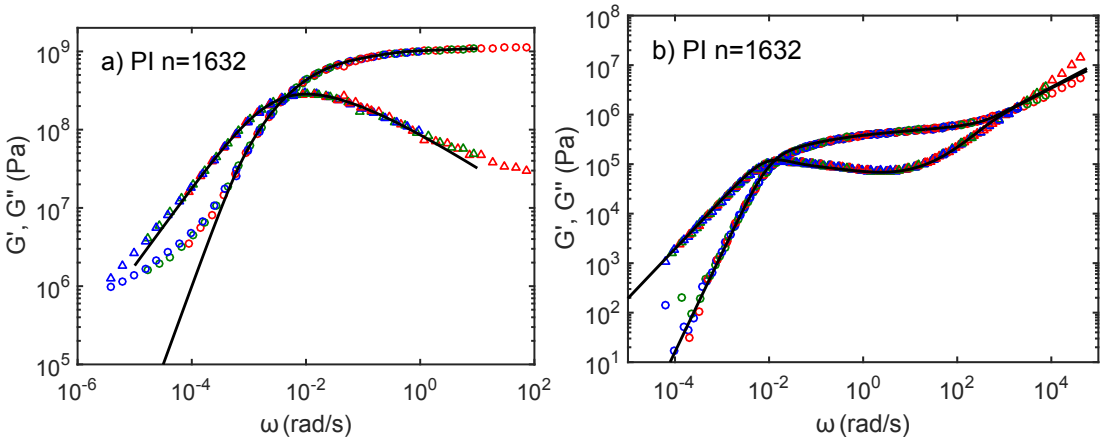

Figure 3.28: TTS master curves for PI n=1632. a) Low temperature data showing α relaxation, with a KWW fit. b) High temperature data showing chain modes, with a Likhtman-McLeish[5] fit.

Figure 3.28 shows PI n=1632 split into α relaxation (a) and chain mode (b) regimes so as to directly compare with BDS data. Elfadl et. al.[151] carried out a chain-length study study using both FFCNMR and BDS on PI, and showed that τ_α and τ_n decoupled at $T - T_g \sim 20K$ in and intermediate M range ($M_R < M < M_c$). Unfortunately, this decoupling of high M PI was not determined due to the large timescale differences between the α relaxation and chain modes. We thus chose to study, using rheology and BDS, a PI sample which was directly comparable one of these high M samples. This sample (n=1617), along with the sample studied in this project (n=1632) provides data from three techniques for both τ_α and τ_n over a large dynamic range. This timescale data is shown in figure 3.29

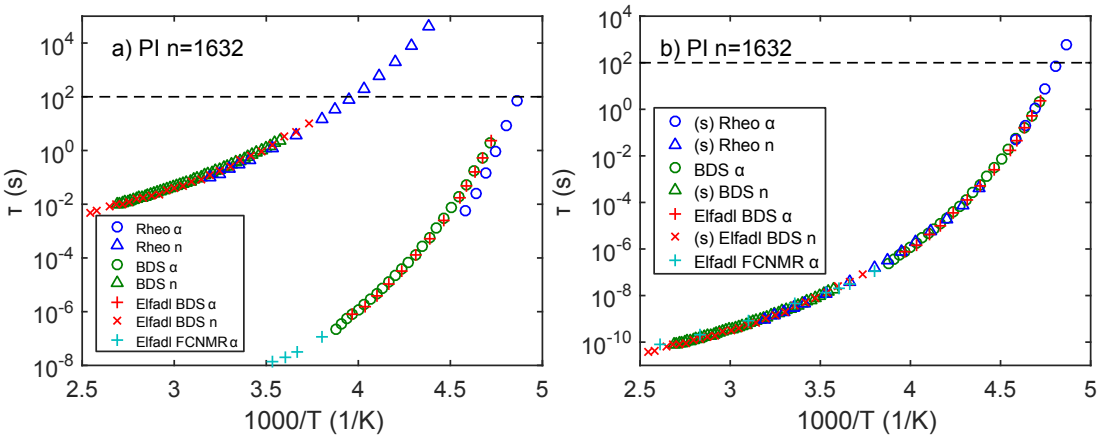

Figure 3.29: PI α relaxation and chain mode Arrhenius plots for PI n=1632. Left: Chain mode and α relaxation timescales for rheology, BDS, and FFCNMR. Right: Timescales from both the α relaxation and chain modes collapsed onto BDS and FFCNMR τ_α data, with "(s)" in the legend indicating which data sets have been shifted.

In figure 3.29 (a), the BDS timescale data from both samples overlap as expected, along with the FFCNMR τ_α data at short timescales. A comparable vertical shift as seen with PMMA exists between timescales from rheology and BDS/FFCNMR, which can be collapsed with a timescale shift in the same manner. Figure 3.29 (b) shows all data collapsed onto the BDS/FFCNMR τ_α data, which indicates very good coupling between τ_α and τ_n. Ding and Sokolov[133] suggested that less fragile polymers such as PI start to decouple in the region of $\tau_\alpha \sim 10^{-5}$s, which is below the timescale value of the collapsed chain mode rheology data. This suggests that despite intermediate M PI samples decoupling in this timescale regime, high M ($M_c < M$) PI may be more coupled. The degree of decoupling may also be so subtle, that a larger range of overlapping α and chain mode timescale data may be required in order to see the decoupling on this kind of plot.

Different polymer systems have different dynamic fragilities (m). Therefore, by definition, these will exhibit different $\tau_\alpha(T)$ behaviour on an Angell (τ_α vs T_g/T) plot. Interestingly, Ding and Sokolov[133] showed that τ_n data for a range of different polymer systems collapsed onto eachother with this kind of T_g/T

normalisation. Therefore, an important statement can be made: Considering that τ_n appears to show universal behaviour when normalised by T_g/T, and that $\tau_\alpha(T)$ and $\tau_n(T)$ are coupled at short τ_α timescales. It must follow that, $\tau_\alpha(T)$ for different polymer systems are universal when normalised by T_g/T at short timescales. To test this hypothesis, α relaxation and chain mode timescales for a variety of oligomeric/polymeric systems were measured. In an attempt to see how these timescales will collapse for systems of different fragilities, a T_g normalised Arrhenius plot was produced. This showed τ_α data, along with τ_n (for systems where it could be directly measured) and τ_α data vertically shifted onto a single master curve. This is shown in figure 3.30.

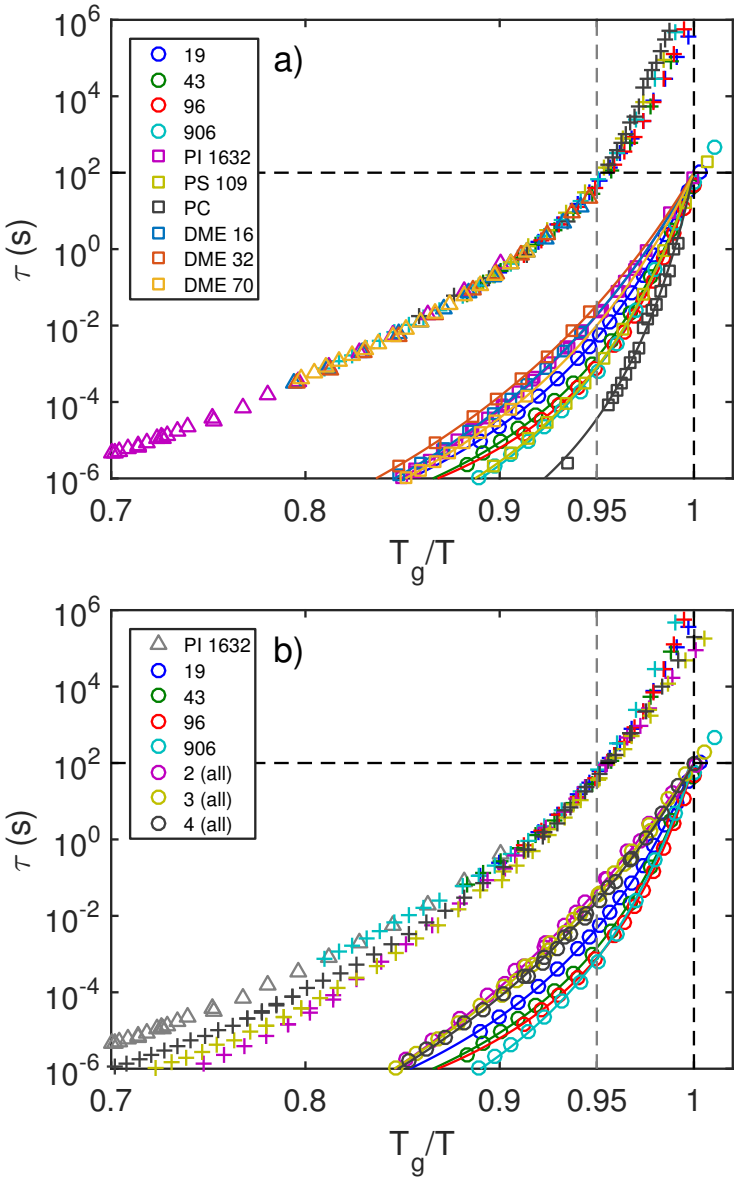

Figure 3.30: a) T_g scaled Arrhenius plot for a variety of oligomeric/polymeric systems: PMMA, PI, PS, polycarbonate (PC), and dimethyl-ethers (DME). Data shown is: τ_α (circles for PMMA, squares for other systems); Direct measurements of τ_n (triangles) which, along with all τ_α data ("+" symbols), are collapsed onto a master curve. b) PMMA and PI (τ_n) data from (a), along with all PMMA n=2, 3, and 4, τ_α data (from figure 3.26, including high frequency BDS data) from BDS and rheology shifted to $T_g/T \sim 0.95$.

Figure 3.30 (a) shows $\tau_\alpha(T)$ a variety of polymer systems with different chain-lengths and fragilities on a T_g normalised Arrhenius plot. Along with these, chain mode timescales, $\tau_n(T)$, for polyisoprene (PI) from BDS, rheology, and FFCNMR, along with dimethyl-ethers (DME) from BDS are rescaled in τ onto a common master curve (shown by the triangles). Considering that TTS is a good approximation at high enough temperatures, $\tau_\alpha(T)$ should also collapse in the same manner as $\tau_n(T)$. This is shown by the "+" symbols, whereby for $T_g/T \lesssim 0.95$ these $\tau_\alpha(T)$ and $\tau_n(T)$ fall onto a common master curve. Therefore, both chain modes dynamics, and the short timescale dynamics of the α relaxation are somehow set by T_g, where they have a common temperature dependant relaxation time. Understandably, the degree to which $\tau_\alpha(T)$ diverges from this common curve appears to relate to dynamic fragility, as this is a measure of α relaxation dynamics at T_g. This is consistent with the conclusions that Sokolov et. al.[133, 182] came to also, whereby the timescale τ_α and τ_n decouple relates to m.

However, figure 3.30 (a) does not include $\tau_\alpha(T)$ data for samples where chain modes are not established, i.e. region I, where $M < M_R$. Figure 3.30 (b) contains the PMMA samples from figure 3.30 (a), with the addition of $\tau_\alpha(T)$ for the three lowest M PMMA samples from BDS, superimposed onto $\tau_n(T)$ for PI. It is clear that these low M PMMA samples do not follow this $\tau_\alpha(T)$ behaviour at high temperatures, whereas other samples of varying fragility and T_g, where chain modes are established do.

This normalisation of $\tau_\alpha(T)$ and $\tau_n(T)$ at short timescales implies that when chain dynamics become applicable ($M > M_R$), the α dynamics become "universal" at high temperatures when normalised appropriately. This implies that dynamics which govern chain behaviour apply across polymer systems, differing only by some factor effecting T_g. It is also likely that this is related to the apparent "universality" of WLF parameters[99] (discussed in more detail in section 2.1.3), which suggests that for an appropriate reference temperature (close to T_g), parameters which set TTS shift factors are approximately universal in some polymer systems ($C_1 = 17.44$, and $C_2 = 51.6$K).

As will be shown in chapter 4, for PMMA, the number of correlated (cooperative) units in the α relaxation at T_g shows a large decrease in region I, slightly increasing in region II, followed by M invariant behaviour in region III. With

increasing temperature, the degree of molecular cooperativity in the α relaxation decreases. For PMMA samples in region II and III, at $T_g/T \sim 0.95$ the number of cooperative units in the α relaxation reaches approximately that of the dynamic bead size ($\sim$ 10 monomers). This suggests that once this dynamic bead has been established, dynamics become more universal. However, the link between this and other polymer systems is unclear.

3.6 Conclusions

In this chapter, dynamic shear mechanical spectroscopy measurements were performed on a PMMA chain length series series, spanning from small molecular glass former, to oligomer, to fully entangled polymer. A summary of these measurements and conclusions, along with those carried out using broadband dielectric spectroscopy (BDS), and standard differential scanning calorimetry (DSC) are shown below:

- Using time-temperature superposition (TTS), complex shear modulus measurements probing both α and chain dynamics were able to be superimposed using a single set of shift factors from melt to $\sim T_g$ for this PMMA M series.
- These TTS spectra could be modelled by a simple ansatz, whereby a superposition of a KWW stretched exponential, and either a Rouse or Likhtman-McLeish model could describe both G' and G'' across the appropriate dynamic ranges.
- Glassy properties, such as the glass transition temperature (T_g), and dynamic fragility (m) exhibit regional behaviours. Whereas traditional models, such as describing T_g behaviour with a Fox-Flory model across the entire M range, fail.
- Heat capacity measurements show regional behaviours, suggesting that there may be regional differences in molecular cooperativity as chain connectivity increases in linear polymers. This is to be explored in chapter 4.

- The use of the Kuhn M (M_K) as an approximation of the Rouse M (M_R) appears to be sufficient in describing Rouse dynamics in intermediate M ($M_R < M < M_c$) samples for both PMMA and PS.

- Due to the swap over between "α dominant", and "chain dominant" regions in the mechanical spectra, significant decoupling between τ_α and τ_n is not captured using this particular experimental technique in fragile systems such as PMMA.

- A timescale shift exists between τ_α data attained from rheology and BDS. This allows for a direct comparison, and further justification, that TTS works in describing τ_α from these dynamic shear modulus measurements.

- τ_α and τ_n values for a variety of linear oligomeric/polymeric systems seem to show "universal" behaviour at short timescales if appropriately normalised. We speculate that this is related to molecular cooperativity occurring on the lengthscale of the dynamic bead, which will be explored in chapter 4

Chapter 4

Molecular cooperativity in glass-forming oligomers and polymers

Previously in chapter 3, we looked at the mechanical, dielectric, and calorimetric responses for a PMMA chain-length series, noting regional M behaviour in glassy properties (T_g, m, β_{KWW}, etc), which has been observed in other polymeric systems[134, 135]. From DSC measurements on the PMMA series, it was alluded to that molecular cooperativity at the glass transition temperature, T_g, may also exhibit some change in behaviour as the chain length increases and chain dynamics become apparent. This phenomenon is explored in this chapter.

As temperature decreases, molecular motions slow down. With this decreasing temperature, the number of units moving in a correlated manner, or cooperatively, must increase in order for the molecules of a material to relax, i.e. the number of units relating to the structural (α) relaxation which are dynamically correlated increases[28]. These cooperative regions also become more dynamically heterogeneous, whereby "hot-spots" of mobility form, and the roughness of the potential energy landscape becomes more and more influential at lower temperatures[7].

Measurements of the cooperative lengthscale have been determined using various techniques, notably: DSC[165], 4D NMR[190], and molecular dynamics simulations (MD)[191, 192]. At T_g, the lengthscale of this cooperative region has

been found to be typically $\sim 1.0 - 3.5$nm[79]. This lengthscale is system dependent and, along with the number of cooperative "units" (molecules or monomers), has been shown to correlate to properties such as dynamic fragility[193] and activation volume (defined through the pressure dependence of the α relaxation timescale)[80, 194] for both small molecular and polymeric glass formers.

While measurements of this cooperative lengthscale at T_g have been performed on a variety of both small molecular and polymeric glass formers[79, 195–197], only two previous studies have determined the effects of chain-length[198, 199]. Moreover, neither of these two studies included a sufficient molecular weight (M) range, or had a sufficient resolution to fully explore how size of correlated regions changes as a polymeric system grows from small molecular glass former to long-chain polymer.

The aim of this chapter is to determine the role of M on the number of dynamically correlated units characteristic of the α relaxation, both as a function of timescale (or temperature), and at T_g. Three relatively monodisperse, linear, polymeric M series, ranging from dimer to fully entangled polymer were chosen: poly(methyl methacrylate) (PMMA); polystyrene (PS); and poly(dimethyl siloxane) (PDMS). The sample specifications are shown in figure 4.1 and table 4.1.

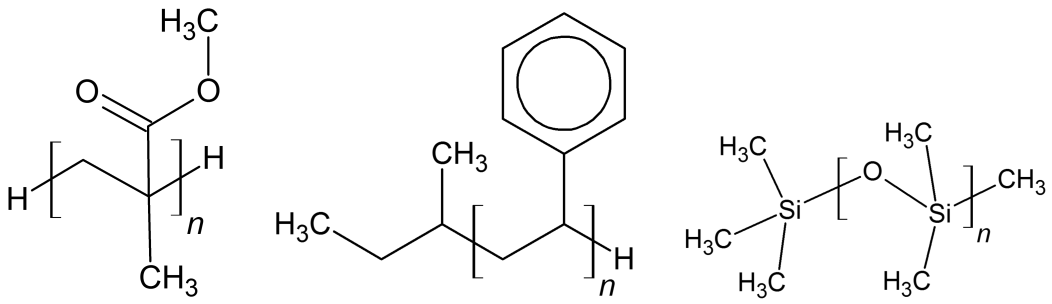

Figure 4.1: From left to right: PMMA, PS, and PDMS molecules. The end groups reported by the manufacturer are also shown.

PMMA			PS			PDMS		
n	M_W (g/mol)	PDI	n	M_W (g/mol)	PDI	n	M_W (g/mol)	PDI
2	202	1.00	2	266	1.00	2	237	1.00
3	302	1.00	3	370	1.00	3	311	1.00
4	402	1.00	5	545	1.16	14	1150	1.27
6	660	1.21	6	725	1.09	20	1600	1.37
7	771	1.18	9	970	1.12	66	4980	1.29
8	840	1.44	18	1920	1.08	623	46200	1.12
11	1100	1.17	28	2960	1.04			
19	1900	1.10	108	11300	1.02			
43	4300	1.05	456	47500	1.03			
96	9590	1.05	30k	3.15M	1.05			
395	39500	1.04						
906	90600	1.04						

Table 4.1: Specifications of PMMA, PS, and PDMS samples used in this work.

Figure 4.1 shows, from left to right, the monomers of PMMA, PS, and PDMS. These have monomer molecular weights of M_0=100g/mol, 104g/mol, and 74g/mol respectively. The manufacturer reported PMMA to be proton terminated, PS to be sec-butyl terminated, and PDMS to be silioxane-trimethyl siloxy terminated. Table 4.1 shows the degree of polymerisation (n), the weight average molecular weight, M_W, and the polydispersity index (PDI) of the samples used in this work, as characterised by the supplier. These samples were purchased from Polymer Standards Service (PSS), and were used as received, with the exception of PMMA $n = 6-11$, which were heated far above T_g in a vacuum oven for at least 24 hours to remove any solvent remaining from the manufacturing process (this was not necessary for the other samples).

PMMA and PS have relatively similar properties such as: monomer molecular weight (M_0), T_g, dynamic fragility (m), and chain flexibility[200]. Literature data also exists for the number of cooperative units at T_g for a PS M series[198], which allowed for a direct comparison, although $n = 5$ was the smallest sample in this

study. PDMS has a lower T_g and m, and is more flexible compared to both PMMA and PS.

In order to determine the number of cooperative units involved in the α relaxation, two techniques were employed. The first technique, proposed by Donth[9, 165], yields the size of the cooperative region from thermal fluctuations at T_g. These fluctuations are shown to relate to the size of independently rearranging regions, thus yielding information of the number of cooperative units involved in the α relaxation. This was performed using temperature-modulated differential scanning calorimetry (TMDSC). The second technique proposed by Berthier et. al.[201] estimates the four-point dynamic susceptibility, χ_4, from temperature dependent measurements of the dynamic permittivity. This yields the size of dynamically correlated regions involved in the α relaxation. χ_4 in this work was estimated using broadband dielectric spectroscopy (BDS).

In this work, the timescale dependence of the number of correlated units in the α relaxation was investigated. We found that for the more fragile, less flexible polymers, PMMA and PS, correlated behaviour could be split into distinct M regions. Below a molecular weight corresponding to where a change in T_g is observed, which corresponds approximately to the size of a dynamic bead ($M < M_R$), there was a large decrease in the number of correlated monomer units with increasing M. Above this molecular weight ($M > M_R$), the number of correlated units at a particular τ_α was relatively invariant (or slightly increasing) with M. We suggest that the cooperativity of the α relaxation at T_g may experience a crossover from intermolecular to largely intramolecular behaviour at M_R. We also related this behaviour to the dynamics of the β relaxation in PMMA, which are shown to also experience a significant change in dynamics at M_R.

4.1 Heat capacity determination of N_a

The first of the two techniques employed here to determine the number of cooperative units in the α relaxation was proposed by Donth[165, 202, 203], which estimates the size of the cooperative region through temperature fluctuations using heat capacity measurements. This reasoning will closely follow literature by Sillescu[26], Donth[9, 165, 203], and Landau and Lifshitz[204].

A sample can be described as a set of subsystems of equal volume, each described by different values of their dynamics and thermodynamic characteristics, with mean square fluctuations $\langle(\Delta\rho)^2\rangle$, $\langle(\Delta T)^2\rangle$, $\langle(\Delta S)^2\rangle$, and $\langle(\Delta E)^2\rangle$[26]. Therefore, each subvolume will have its own characteristic relaxation timescale, τ, and glass transition temperature, T_g, as visualised in figure 4.2.

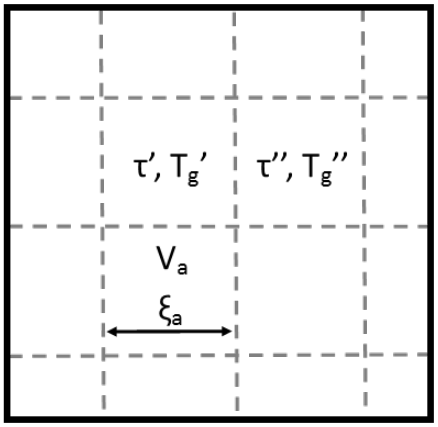

Figure 4.2: Visualisation of a system comprised of dynamically independent subvolumes, V_a, with lengthscale $\xi_a = V_a^{1/3}$.

Figure 4.2 visualises a system comprised of dynamically and thermodynamically independent subvolumes with volume V_a, and lengthscale defined as $\xi_a = V_a^{1/3}$, which are assumed to be large enough that thermodynamic variables can be defined. The probability of a molecular fluctuation in a subsystem of a volume, V, is given by Einstein's fluctuation formula, shown in equation 4.1,

$$w_{fluc} \propto \exp(-W_{min}(V)/k_B T). \tag{4.1}$$

Here, W_{min} is the minimum work required for a fluctuation to occur. This quantity takes the form of the Gibb's free energy of the system at constant pressure, given by equation 4.2,

$$W_{min} = \Delta E + P\Delta V - T\Delta S, \tag{4.2}$$

Where P and T are the equilibrium (mean) pressure and temperature and temperature of the system. The change in these quantities, Δ, is not necessarily infinitesimally small, which allows for subsystem fluctuations. Landau and Lifshitz[204]

point out that the variable pairs $P\Delta V$ and $T\Delta S$ must be treated in the same manner so as not to exclude temperature fluctuations[9]. From a second order series expansion in ΔE, the probability of a fluctuation becomes equation 4.3:

$$w_{fluc} \propto \exp\left(\frac{\Delta P\Delta V - \Delta T\Delta S}{2k_BT}\right). \tag{4.3}$$

From this, fluctuations in thermodynamic quantities can be found. If V and T are treated as independent variables, then ΔP and ΔS can be expressed as equations 4.4 and 4.5 respectively:

$$\Delta P = \left(\frac{\partial P}{\partial T}\right)_V \Delta T + \left(\frac{\partial P}{\partial V}\right)_T \Delta V. \tag{4.4}$$

$$\Delta S = \left(\frac{\partial S}{\partial T}\right)_V \Delta T + \left(\frac{\partial S}{\partial V}\right)_T \Delta V = \frac{C_V}{T}\Delta T + \left(\frac{\partial P}{\partial T}\right)_V \Delta V, \tag{4.5}$$

Where C_V is the heat capacity at constant volume. Inserting equations 4.5 and 4.4 into equation 4.3 yields equation 4.6.

$$w_{fluc} \propto \exp\left(\frac{1}{2k_BT}\left(\frac{\partial P}{\partial V}\right)_T (\Delta V)^2 - \frac{C_V}{2k_BT^2}(\Delta T)^2\right). \tag{4.6}$$

Fluctuations of volume and temperature are statistically independent, i.e. $\langle \Delta V \Delta T \rangle = 0$. Therefore, equation 4.6 is able to be seperated into two components, one depending only on ΔV, and the other only on ΔT. If these fluctuations can be described using a Gaussian function[204], the mean square fluctuations of volume and temperature become equations 4.7 and 4.8 respectively:

$$\langle (\Delta V)^2 \rangle = \delta V^2 = -k_BT\left(\frac{\partial V}{\partial P}\right)_T \tag{4.7}$$

$$\langle (\Delta T)^2 \rangle = \delta T^2 = \frac{k_BT^2}{C_V} \tag{4.8}$$

Where δV and δT are the half width at half maximum of a Gaussian function describing the fluctuation. It is worth noting that P and S can also be taken as independent variables in equation 4.3. Therefore, the mean square fluctuations, δP^2 and δS^2 can be quantified in a similar manner. However, the quantity of interest is the mean temperature fluctuation, δT. Once again, this is defined in equation 4.9,

$$\delta T^2 = k_B T^2 C_V^{-1}. \tag{4.9}$$

C_V is proportional to the volume of the subsystem, V_a, related via $C_V = c_V/\rho V_a$, where c_V and ρ are the isochoric specific heat capacity, and density respectively. In addition to this, only contributions to the heat capacity from the α relaxation should be considered, i.e. assuming independence of α cooperativity from other molecular motions. Therefore $T \to T_\alpha$, and $c_V^{-1} \to \Delta c_V^{-1}$, where $\Delta c_V^{-1} = c_{V,glass}^{-1} - c_{V,liquid}^{-1}$. Taking these into account, the volume of the subsystem is given by equation 4.10,

$$V_a = k_B T_\alpha^2 \Delta c_V^{-1}/\rho \delta T^2. \tag{4.10}$$

Here, the volume of the cooperative region is dependent on the transition temperature (T_α), density (ρ), mean temperature fluctuation (δT), and the change in inverse constant volume specific heat capacity[202]). However, rather than c_V, measurements of the specific heat capacity at constant pressure, c_p, were performed and used instead. This will overestimate the size of the cooperative region. A correction factor based on the ratio of $\Delta c_V^{-1}/\Delta c_P^{-1} = 0.74 \pm 0.22$ has been determined, which is based on a wide range of glass forming systems[79]. This correction could be applied, but is not commonly done so, and was considered to not add the the overall conclusions.

Donth demonstrated that the mean temperature fluctuation, δT, can be obtained from the width of the calorimetric response[9, 165, 202, 203]. More specifically, that of the half width at half maximum of the imaginary heat capacity, $c_P''(T)$, as described by a Gaussian, shown in equation 4.11:

$$c_P''(T) = \frac{A}{2\delta T\sqrt{\pi/2}} \exp\Big[-\frac{1}{2}\Big(\frac{T - T_\alpha}{\delta T}\Big)^2\Big]. \tag{4.11}$$

Here, parameters A, δT, and T_α are the amplitude, breadth (half width at half maximum), and peak temperature respectively.

In addition to V_a, as estimate of the the cooperative length can be calculated as simply the cube-root of the cooperative volume, shown in equation 4.12.

$$\xi_a \approx V_a^{1/3} \tag{4.12}$$

Exactly how the volume of this region will translate to a lengthscale will depend on the shape and topology of the cooperative volume. However, for a simple approximation of ξ_a, this is often used[79, 205]. Both V_a and ξ_a depend on sample density. This would be the density at T_α for each of these samples. Instead, the cooperative region can be expressed as the number of cooperative monomer units, rather than as a cooperative volume or lengthscale. This is calculated using equation 4.13.

$$N_a = \rho V_a A / M_0 \tag{4.13}$$

In equation 4.13, A is Avogadro's number, and M_0 is the monomer molecular weight. By inserting equation 4.10 into 4.13, this removes the density dependence, and is replaced with monomer molecular weight dependence (PMMA: 100g/mol, PS: 104g/mol, and PDMS: 74g/mol).

Therefore, in order to determine the size of the cooperative region, measurements of the complex heat capacity needs to be performed across the glass transition.

4.1.1 The complex heat capacity

In order to attain the number of cooperative units involved in the α relaxation in this way, δT, T_α, and Δc_p^{-1} need to be determined. These quantities can be obtained from the complex heat capacity, c_p^*, response[79], which is measured using temperature modulated DSC (TMDSC). c_p^* is calculated from the reversing capacity, $|c_p^*|$, and the heat flow phase angle, δ, as outlined in section 2.3.2. This is defined in equation 4.14.

$$c_P^* = |c_P^*| \mathrm{e}^{-i\delta} = c_P' - i c_P'' \tag{4.14}$$

Here, c_P^* is separated into in-phase (c_P'), and out-of-phase components (c_P'')[113]. Figure 4.3 illustrates the typical behaviour of these components across the glass transition.

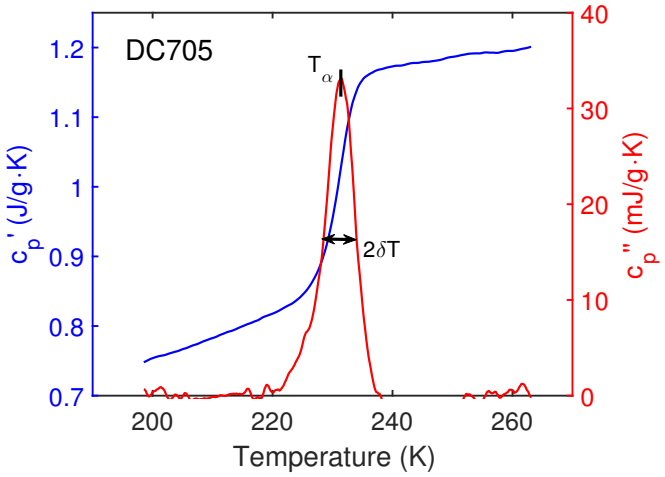

Figure 4.3: Example of the real, c_p', and imaginary, c_p'', components of the complex heat capacity for a non-polymeric glass former (DC705). T_α and δT define the peak temperature, and the half width at half maximum of c_p'' respectively.

The real and imaginary components of c_p^* across the glass transition are shown in figure 4.3 for a non-polymeric glass forming material (DC705). c_p' shows the typical step observed in a heat capacity measurement across the glass transition, whereas c_p'' shows a peak. T_a and δT can be determined from the peak temperature, and the half width at half maximum of a Gaussian fit to c_P''. Δc_p^{-1} can be determined from the change in step in $|c_p^*|(T)$, as the difference in reciprocal heat capacities of the glassy and liquid states at T_α ($\Delta c_p^{-1} = c_{p,g}^{-1} - c_{p,l}^{-1}$)[79, 119].

In this project TMDSC measurements were performed using a TA Q2000 heat-flux DSC with a liquid nitrogen cooling system, as described in section 2.3. As detailed in section 2.3.2, the temperature profile of a simple sinusoidal TMDSC experiment is shown in equation 4.15.

$$T(t) = T(0) + Bt + A\sin\left(\frac{2\pi t}{P}\right) \tag{4.15}$$

Where B is the underlying heating rate, A is the modulation amplitude, and P is the oscillation, or modulation, period. Taking the derivative of equation 4.15 yields the heating rate, as is shown in equation 4.16.

$$\frac{\mathrm{d}T}{\mathrm{d}t} = B + \frac{2\pi A}{P}\cos\left(\frac{2\pi t}{P}\right) \tag{4.16}$$

From this heating rate, and the resulting heat flow into the sample, the heat capacity is obtained, as shown in equation 4.17.

$$C_P = \frac{\mathrm{d}Q}{\mathrm{d}t} \Big/ \frac{\mathrm{d}T}{\mathrm{d}t} \tag{4.17}$$

Equation 4.17 shows that the heat flow ($\mathrm{d}Q/\mathrm{d}t$) depends on the sample heat capacity (C_P), and the heating rate ($\mathrm{d}T/\mathrm{d}t$).

Experiments were performed across the glass transition region (-40K$< T_g <$40K) for each sample using three modulation periods (P=40, 60, and 100s). The experiments were performed on cooling (negative B) for PMMA and PS, i.e. starting in the liquid state, and cooling into a glassy state. However, due to sample crystallisation, PDMS had to be quenched in order to form a glass. Therefore, for PDMS, experiments had to be performed on heating (positive B), i.e. starting in a glassy state, and heating into the liquid state.

It is apparent from equation 4.16 that in order to obtain comparable responses for different modulation periods, the parameters A/P and $B \cdot P$ should be kept constant. These were chosen appropriately to see the effect of modulation period on each sample, rather due to different heat flow (set by A/P), or resolution due to the number of oscillations within the transition region (set by $B \cdot P$). The values chosen are shown in table 4.2.

P (s)	A (K)	$\lvert B \rvert$ (K/min)
40	0.8	1.25
60	1.2	0.83
100	2.0	0.50

Table 4.2: TMDSC temperature profile parameters. Note $A/P \simeq 0.02$ and $|B| \cdot P \simeq 50$ for each period.

The parameters in table 4.2 were used on all samples (B values were positive for PMMA and PS, and negative for PDMS). An example of this experiment across the glass transition is shown in figure 4.4.

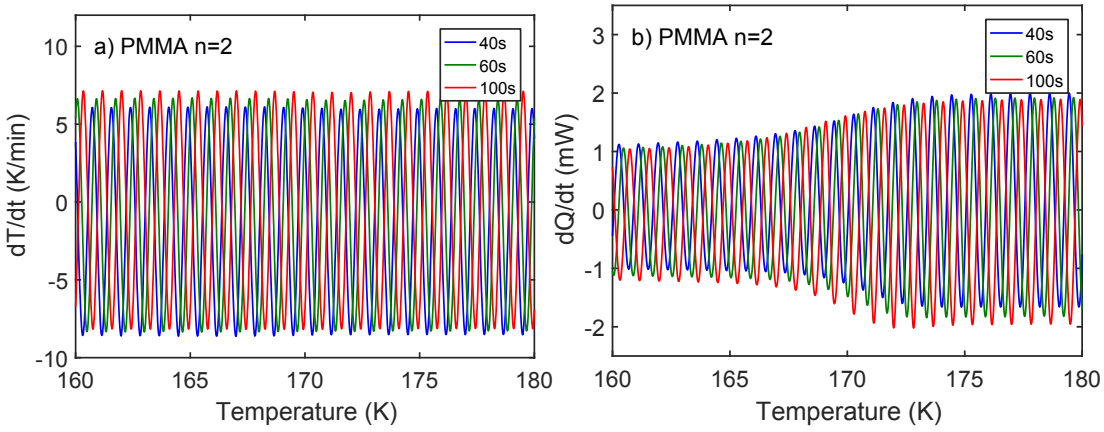

Figure 4.4: a) Heating rate ($\mathrm{d}T/\mathrm{d}t$), and b) Heat flow ($\mathrm{d}Q/\mathrm{d}T$) for PMMA n=2. For each modulation period (shown in different colours), $\mathrm{d}T/\mathrm{d}t$ and $\mathrm{d}Q/\mathrm{d}t$ are approximately the same amplitude, and contain the same number of oscillations across the temperature range.

Figure 4.4 shows that both the temperature profile of the DSC, $\mathrm{d}T/\mathrm{d}t$ (a), and the response of the sample (PMMA n=2), $\mathrm{d}Q/\mathrm{d}T$ (b), are similar for the three different modulation periods. This was expected using the tailoring of $\mathrm{d}T/\mathrm{d}t$ as mentioned above. As explained in section 2.3.2, the underlying heating rate, B, is subtracted from $\mathrm{d}T/\mathrm{d}t$, and then equation 4.17 yields the reversing heat capacity of the sample[120], shown in equation 4.18.

$$|C_P^*| = \frac{A_{\mathrm{d}T/\mathrm{d}t}}{A_{\mathrm{d}Q/\mathrm{d}t}} \tag{4.18}$$

Where $A_{\mathrm{d}T/\mathrm{d}t}$ and $A_{\mathrm{d}Q/\mathrm{d}t}$ are the instantaneous values (amplitudes) of the heat flow ($\mathrm{d}T/\mathrm{d}t$) and heat response ($\mathrm{d}Q/\mathrm{d}T$) respectively. As outlined in section 2.3.3, this reversing heat capacity is calibrated for each period by running the same experiment on a sapphire sample across the same temperature range. Sapphire samples have a very well defined heat capacity, and the average ratio between the specific heat capacity measured, and literature values gave a calibration value for each measurement. Standard temperature and sample cell calibrations were also carried out over the temperature range.

Equation 4.14 shows that the complex heat capacity can be calculated from both the reversing heat capacity, $|C_p^*|$, and the phase angle, δ, between $\mathrm{d}T/\mathrm{d}t$

and $\mathrm{d}Q/\mathrm{d}T$. However, an offset appeared in δ, which was not due to the sample response. This was corrected for using a method proposed by Weyer et. al.[206], whereby the offset in δ is attributed to the finite time it takes for heat to transfer between the DSC and the sample. It is assumed that this additional component to δ would simply be proportional to the reversing heat capacity, as shown in equation 4.19.

$$\delta_{ht} = a + b|C_p^*| \tag{4.19}$$

Equation 4.19 shows the offset of the heat flow phase angle due to heat transfer, scaling linearly with $|C_p^*|$, with fitting parameters a and b. This function is fitted outside the transition region of δ, where δ should be zero. δ_{ht} is then subtracted from δ to obtain the corrected phase angle, as shown in equation 4.20.

$$\delta_{corr} = \delta - \delta_{ht} \tag{4.20}$$

Using this correction, δ_{corr} should be the phase angle due to the sample response only, with no offset due to heat transfer. An example of this procedure is shown in figure 4.5.

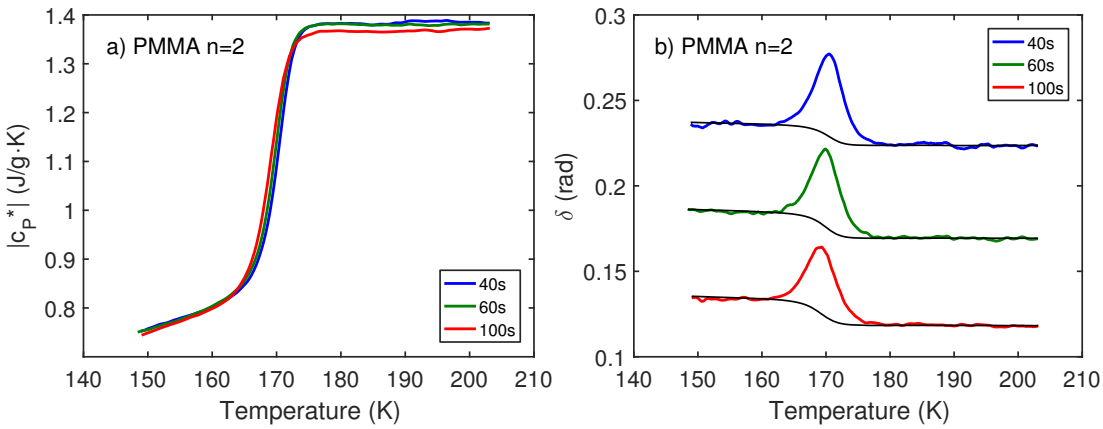

Figure 4.5: a) Reversing heat capacity. b) Phase angle signal, with reversing heat capacity fitting shown in black (right) for PMMA $n = 2$ sample for each period.

Figure 4.5 (b) clearly shows the offset in δ, which should be zero outside of the transition (peak) region. $|c_p^*|$ (4.5 (a)) is fitted to δ outside of the transition region, as described by equation 4.19 (with fitting parameters a and b).

It is apparent in figure 4.5 (b) that δ takes a negative step with increasing temperature over the transition region ("b" parameter in equation 4.19 is negative). However, this was not always the case, and for many samples this took a positive step with increasing temperature as expected. This method of phase angle correction assumes that the offset of the phase angle is entirely due to heat transfer effects, whereas in reality the situation may be more complex. Thus, it is somewhat arbitrary which step function is used to correct the phase angle due to the unknown origin of the offset in the phase angle. Therefore this method was used regardless, as the effect on the final result was negligible, and is also commonly observed in the literature[78, 119].

Using δ_{corr} and $|c_p^*|$, the phase-corrected corrected complex specific heat capacity was calculated, as shown in equation 4.21.

$$c_p^* = |c_p^*|\mathrm{e}^{-i\delta_{corr}} = c_p' - ic_p'' \tag{4.21}$$

Using equation 4.21, the in-phase (c_p') and out-of-phase (c_p'') components of the complex heat capacity can be written as equations 4.22 and 4.23.

$$c_p' = |c_p^*| \cos \delta_{corr} \tag{4.22}$$

$$c_p'' = |c_p^*| \sin \delta_{corr} \tag{4.23}$$

These phase-corrected components of the complex heat capacity are often referred to as the phase-corrected reversing heat capacity (c_P'), and the phase-corrected kinetic heat capacity (c_P'')[120].

4.1.2 Heat capacity response

As discussed earlier in section 4.1.1, in order to obtain information from the imaginary (kinetic) component of the complex heat capacity, a Gaussian function is fitted to $c_p''(T)$ (shown previously in equation 4.11). The fitting parameters A, δT, and T_α are the amplitude, breadth (half width at half maximum), and peak temperature respectively. This function was only fitted above and around the peak in $c_p''(T)$, negating lower temperatures ($T > T_\alpha - 5\mathrm{K}$) where δ, and therefore

c_P'' data measured in the non-equilibrium state are less reliable. This is due to there being a small phase angle contribution from the heat capacity from the average heating rate, which has a different temperature dependence (lower T_g) than that from the modulation[119]. This can be clearly seen in figure 4.9 (a), whereby at temperature lower than T_α, $c_p''(T)$ behaves unexpectedly. For PMMA, PS, and PDMS, figure 4.6 shows this fitting procedure for both high and low M examples.

Figure 4.6 show c_p'' with Gaussian fits for the dimer and fully entangled polymer for PMMA ((a) n=2 and (b) n=395), PS ((c) n=2 and (d) n=30k), and PDMS ((e) n=2 and (f) n=643) for three different modulation periods. There are obvious similarities between PMMA and PS, whereby the breadth in $c_p''(T)$ for the dimers (n=2, (a) and (c)) are relatively narrow ($\delta T \approx 2.2$K for PMMA, and ≈ 2.4K for PS), whereas the polymers ((b) and (d)) are relatively broad ($\delta T \approx 4.1$K for PMMA, and ≈ 3.2K for PS). The breadth in c_P'' for PDMS ((e) and (f)) appears relatively invariant with M, only varying between $\delta T \approx 1$ for the dimer and $\delta T \approx\sim 1.3K$ for the polymer. The breadth variation in PDMS for different modulation periods is unexpected, as this implies an increase in molecular cooperativity with decreasing relaxation time; this is unrealistic, and will be discussed in section 4.1.

As expected, T_α increases with decreasing period because unlike conventional DSC, where the transition temperature is inversely proportional to the heating/cooling rate, in TMDSC experiments the timescale is set by the modulation period ($\tau_\alpha = P/2\pi$). For a single modulation period ($P = 60$s), figure 4.7 shows the effect of M on c_p'' for all three polymer systems.

To directly compare $c_p''(T)$ behaviour for different M, $c_p''(T)$ is plotted in 4.7 for PMMA (a), PS (b) and PDMS (c) for a single modulation period ($P = 60$s). The three systems clearly show the expected increase in T_α with increasing M[86]. Interestingly, PMMA and PS display a large T_α range between dimer to fully entangled polymer, where PMMA ranges ~ 230K, and PS ranges ~ 180K. However, for PDMS, T_α ranges only ~ 25K between dimer and fully entangled polymer. This suggests that the α relaxation is less affected by chain length for more flexible systems such as PDMS, than for more rigid systems such as PMMA and PS.

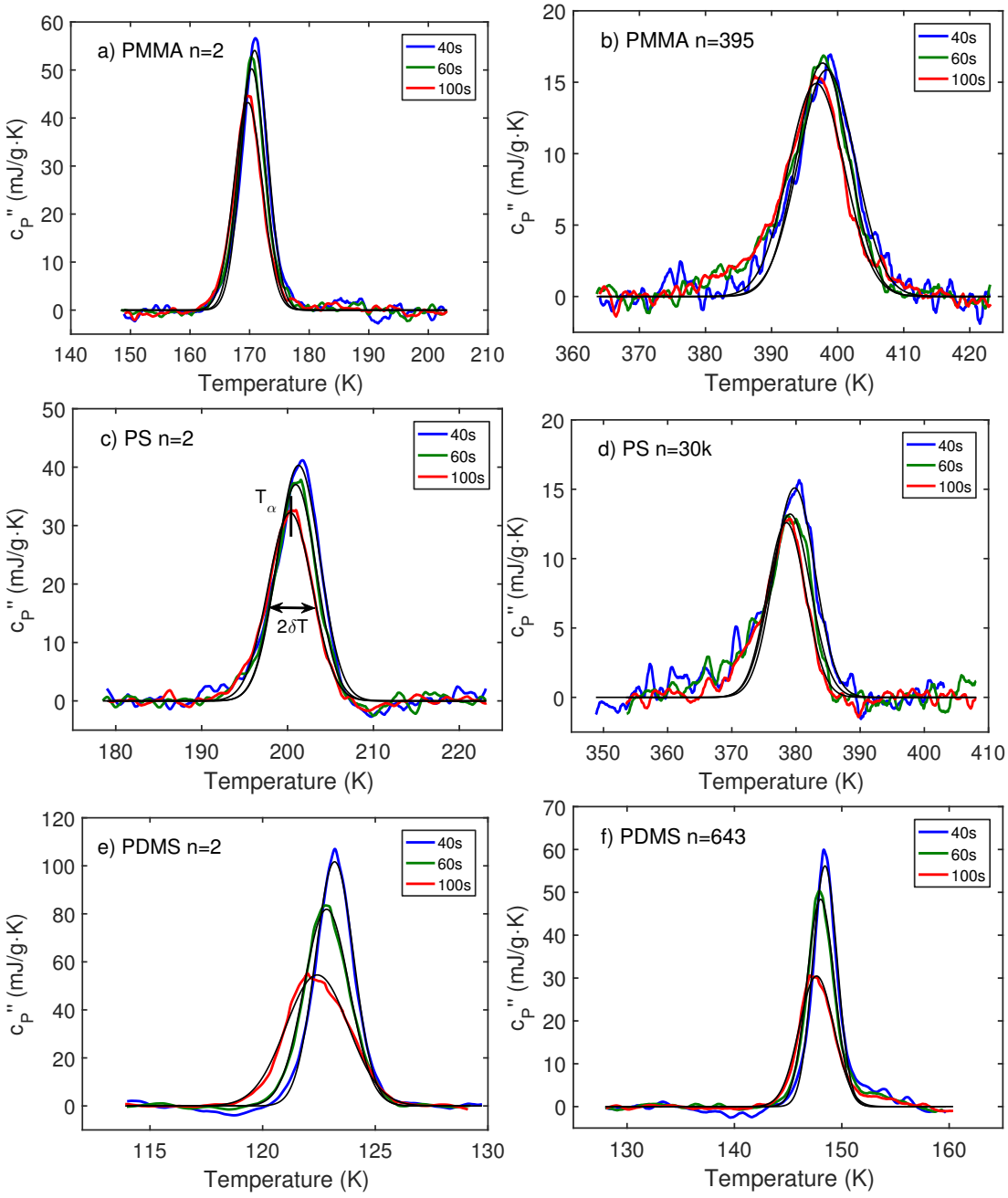

Figure 4.6: c_P'' vs T for low (left) and high (right) M PMMA, PS, and PDMS samples. The three different oscillation periods are shown for each, with Gaussian fits shown by the black lines.

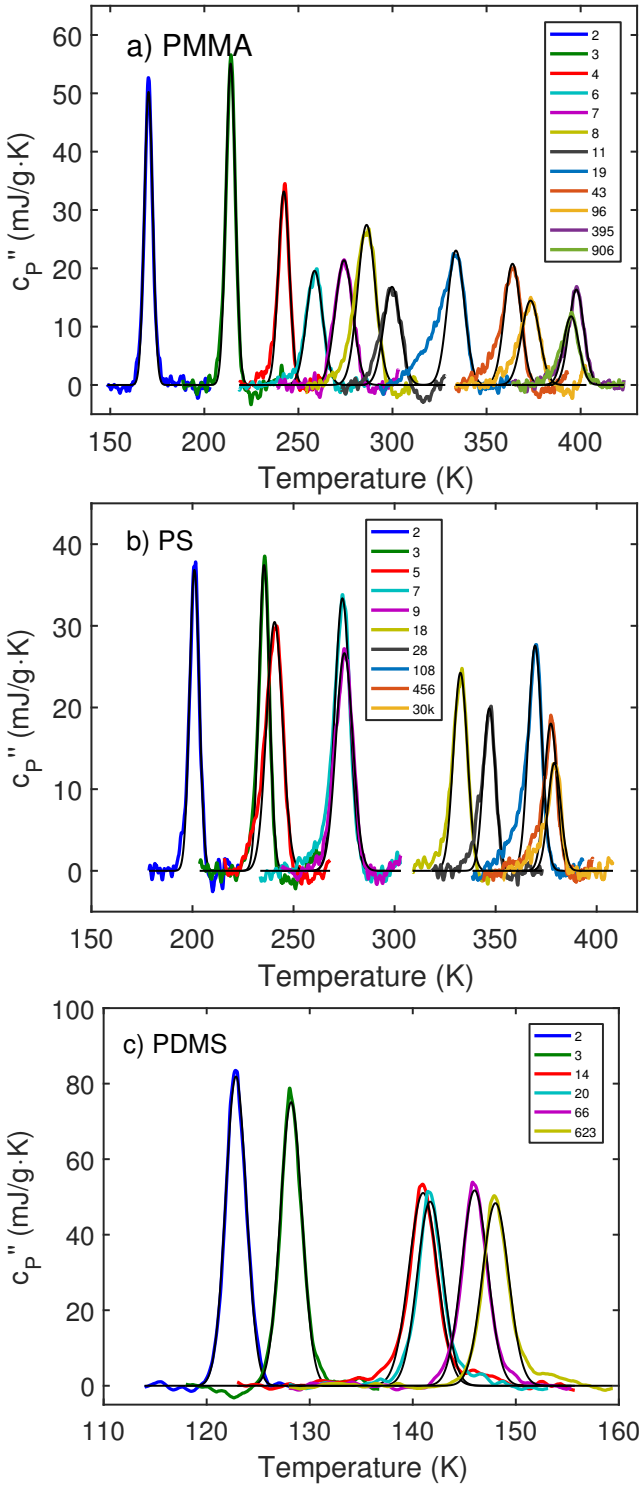

Figure 4.7: c_P'' (P = 60s) vs T for all (a) PMMA, (b) PS, and (c) PDMS, samples with Gaussian fits shown in black. The legends indicate the degree of polymerisation (n).

In section 3.2.2, values of T_g, defined as when $\tau_\alpha = 100$s, were compiled from rheology, BDS, and DSC for the PMMA M series. T_α, defined here as when $\tau_\alpha \approx 10$s, is expected to behave with M in the same manner (albeit slightly shifted to higher temperatures due to the timescale difference). For PMMA, PS, and PDMS, this is shown in figure 4.8.

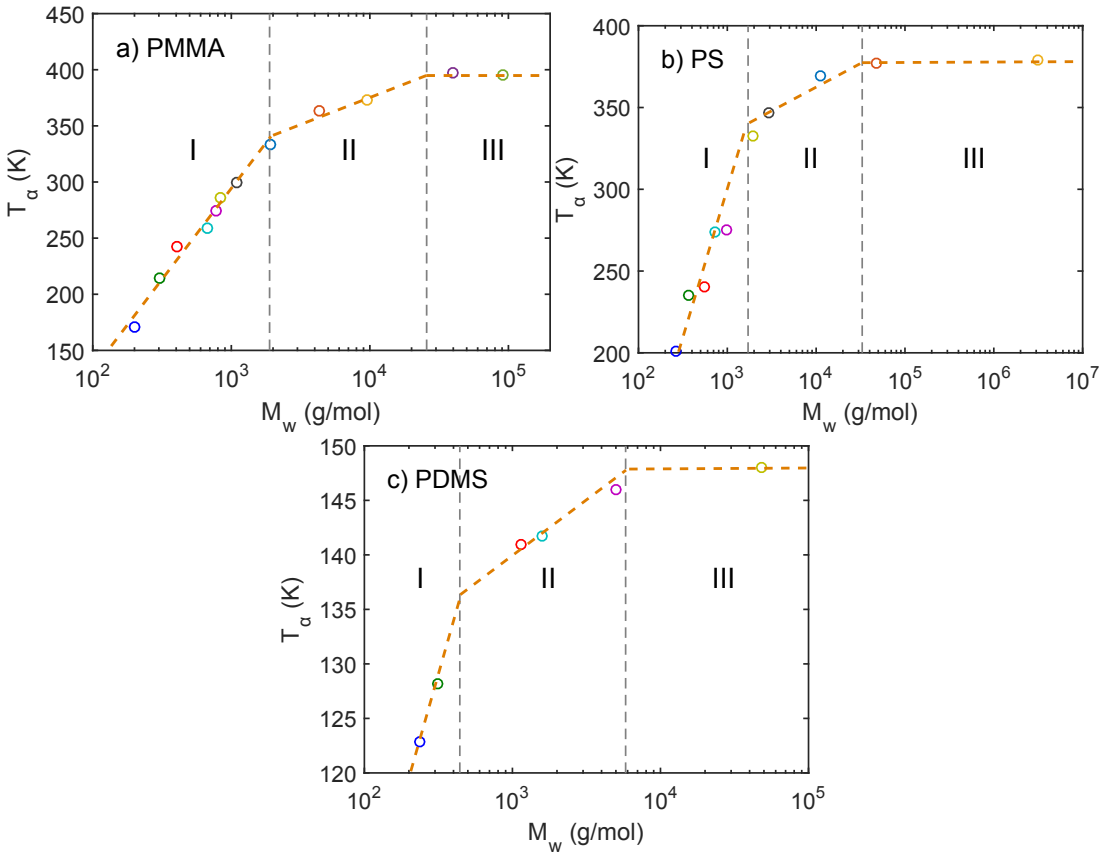

Figure 4.8: τ_α vs M for PMMA, PS, and PDMS from TMDSC measurements, with regional boundaries indicated.

In figure 4.8, PMMA (a), PS (b), and PDMS (c) appear to exhibit the same regional behaviour which was found by Cowie[134, 156] for PMMA and PDMS, and later by Hintermeyer[135] for PS and PDMS. As stated in section 3.2.2, Cowie and Hintermeyer attributed the region I to II boundary to the size of the Rouse bead. For PS, Meier et. al.[207] report the onset of Rouse modes at $M_R \sim 1500$g/mol using fast-field cycling NMR (FFCNMR) measurements on a

PS M series, which is consistent with the value of this region I to II boundary from Hintermeyer and this work. Inoue and Osaki[208] determined a value of M_R = 850g/mol from Rouse mode contributions in rheology, although this method in determining M_R is not ideal[168]. For PDMS, Hofmann et. al.[152] observer onset of Rouse modes at M_R = 600g/mol using FFCNMR measurements on a PDMS M series. This is consistent with the value of the region I to II boundary from this work also. Unfortunately, a value for M_R has not been found in literature for PMMA in order to compare.

Similar to section 3.3, whereby the heat capacity response of the PMMA M series was measured using standard DSC, a variation in the transition width is also apparent in figure 4.7 for TMDSC, whereby δT increases with M. This is shown in figure 4.9 for PMMA, PS, and PDMS.

Figure 4.9 shows the clear increase in δT for all three polymer systems in region I, followed by a stabilisation in regions II and III. For PMMA, this is consistent with ΔT shown in figure 3.17 (a) measured using standard 10K/minDSC. Although, due to the differences in definitions of the transition width, the absolute values are different.

The heat capacity measured using standard 10K/min DSC, shown for PMMA for samples with different M in figure 3.16, is equivalent to measurements of $|c_p*|$ from TMDSC. These are shown in figure 4.10 for the PMMA, PS, and PDMS M series.

Figures 4.10 (a) and (b) show that $|c_p^*|(T)$ for PMMA and PS exhibit the same behaviour as discussed for standard DSC in section 3.3, whereby the liquid ($|c_p^*|_{liquid}$) and glass ($|c_p^*|_{glass}$) heat capacities (indicated by the dashed lines) share a similar temperature dependence across the M range, although interestingly for the more flexible PDMS this is not the case. A similar behaviour was also seen by Huang et. al.[160] on a PαMS series of samples blended with different mass ratios of PαMS pentamer (n = 5). It was concluded that that increasing the degree of polymerisation is equivalent to mixing long and short chain polymers (hence altering the M of the mixed sample). This was consistent with the conclusions of Loufakis and Wunderlich[161]. This common $|c_p^*|_{liquid}$ did not hold for PαMS smaller than $n = 5$, which is also consistent with $n = 2$ and 3 for PMMA and PS

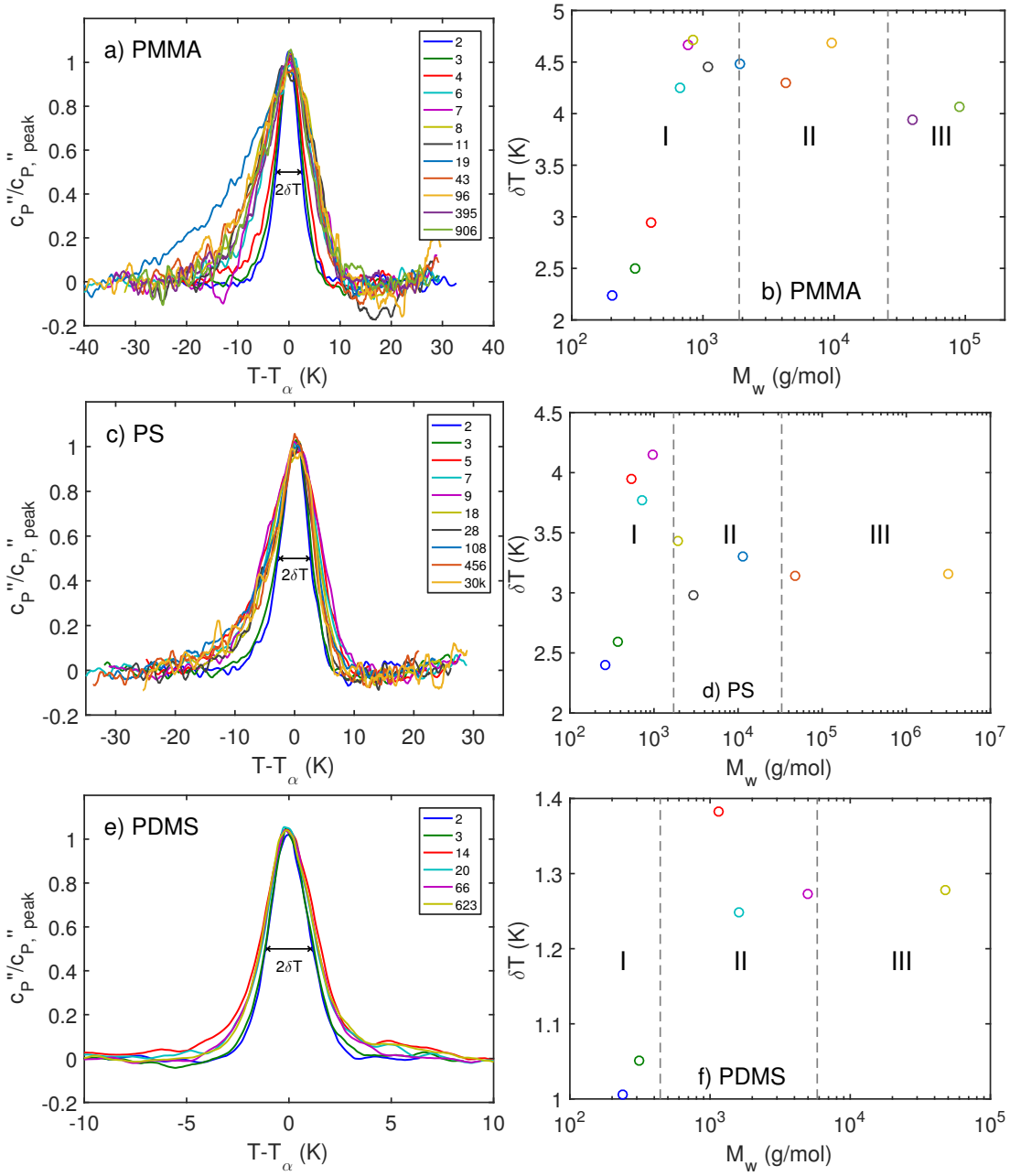

Figure 4.9: Left: c_p'' as a function of temperature normalised onto the peak position from Gaussian fitting for PMMA (a), PS (c), and PDMS (e). The legends indicate the degree of polymerisation (n). Right: The half width at half maximum from Gaussian fits to c_p'', interpreted as the mean fluctuation temperature.

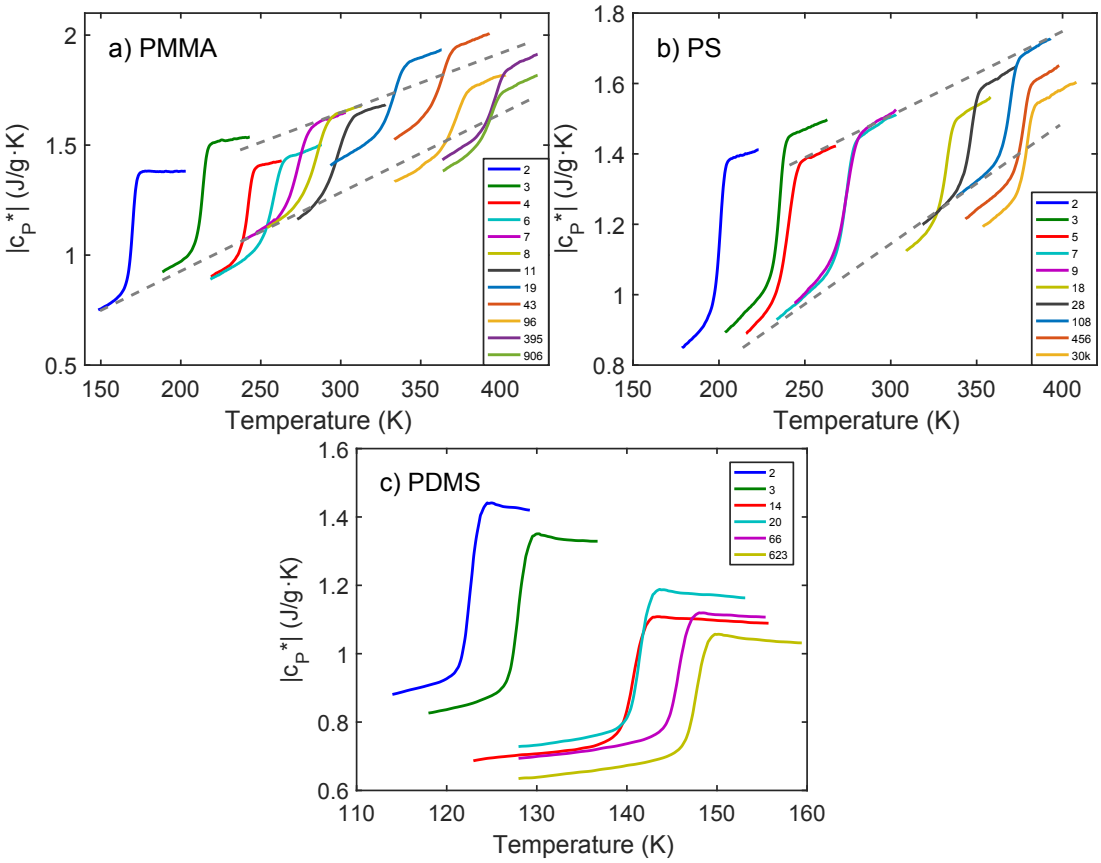

Figure 4.10: Reversing heat capacity measurements from TMDSC for M series' of a) PMMA, b) PS, and c) PDMS. The legends indicate the degree of polymerisation (n).

shown here (this is clearer in PMMA, whereby there is a distinctly lower slope for these two samples).

As for the step height of the glass transition, this was determined in the same manner as in section 3.3.1 for PMMA, which is directly calculating $\Delta|c_P^*|$ as the difference between $|c_P^*|_{liquid}$ and $|c_P^*|_{glass}$ at T_α. Likewise, the measure of the rate of change of entropy was calculated[164], using equation 4.24.

$$\frac{\Delta C_p}{T_g} = \left[\left(\frac{\partial S_{liquid}}{\partial T}\right)_{T_g} - \left(\frac{\partial S_{glass}}{\partial T}\right)_{T_g}\right]_P \tag{4.24}$$

For PMMA, PS, and PDMS these are shown in figure 4.11.

For PMMA, figure 4.11 shows the same behaviour as figures 3.17 (a) and 3.18. The slight differences in absolute values ($\sim$ 10%) may be due to these two techniques probing timescales approximately an order of magnitude apart and/or slight experimental errors. All three of these systems exhibit the regional behaviour: a decrease in both $\Delta|c_P^*|$ and the rate of change of entropy in region I, and a stabilisation in regions II and III. Interestingly for both of these quantities PDMS is higher than PMMA and PS. This suggests that the configurational degrees of freedom contribute more to the heat capacity of PDMS across the M range than in PMMA or PS, this may be due to the relative flexibilities of these polymer systems.

From these complex heat capacity measurement, and the Gaussian fits of c_P'', information on the size of the cooperatively rearranging region was determined, which will be shown in section 4.1.3.

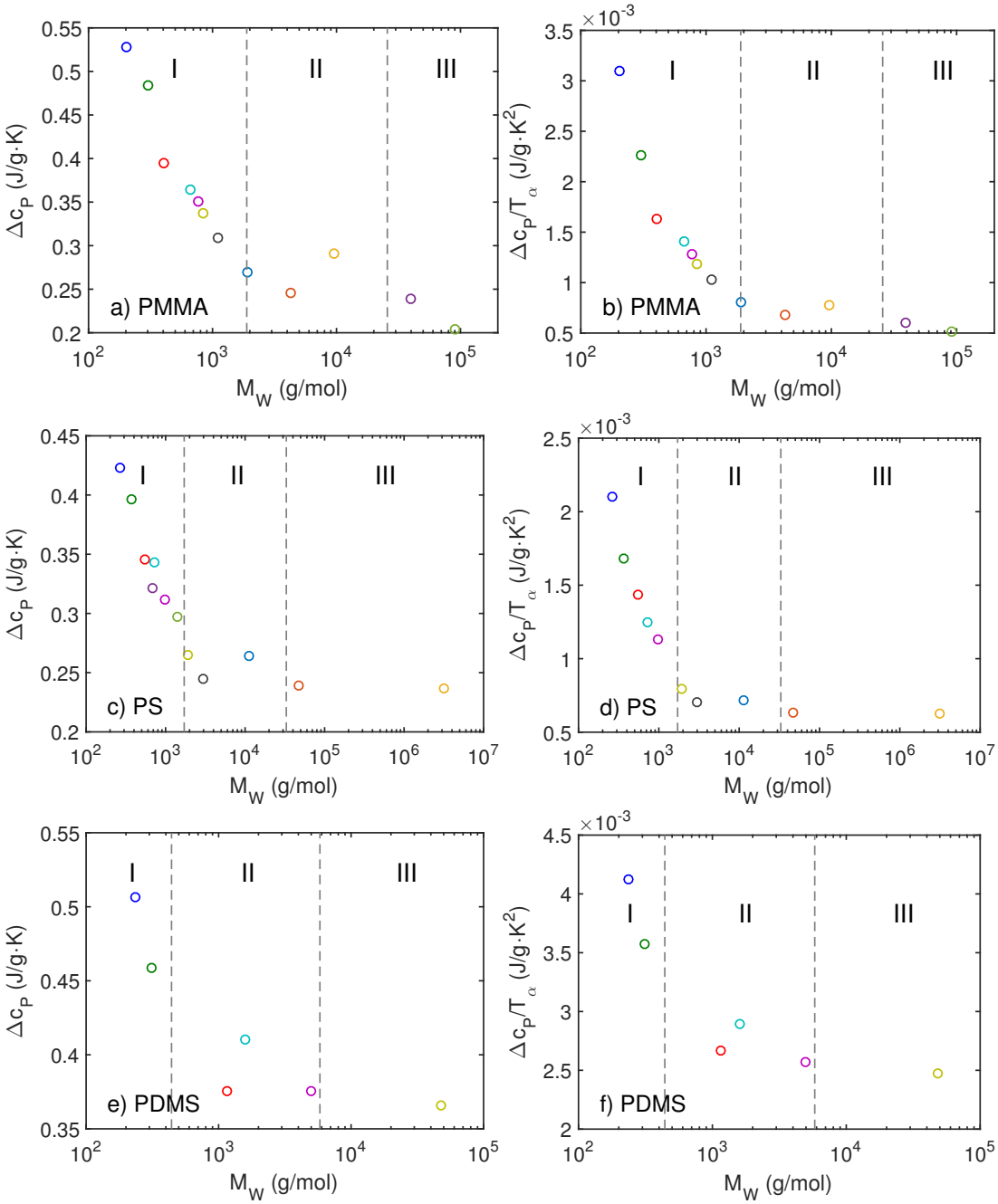

Figure 4.11: Left: Change in reversing heat capacity between liquid and glass as a function of M for PMMA, PS, and PDMS. Right: The rate of change of entropy between liquid and glass as a function of M.

4.1.3 The size of the cooperative region

As outlined in section 4.1, values of δT, T_α, and Δc_p^{-1} yield information about the size of the cooperative region of the α relaxation. These values can be determined using TMDSC, as discussed in section 4.1.1. TMDSC measurements were performed across the glass transition for the PMMA, PS, and PDMS M series. Using these measurements, along with M dependent density values from literature (PMMA and PS[172], and PDMS[209]), allow for the calculation of the volume, V_a, and lengthscale, ξ_a, of this region using equations 4.10 and 4.12 respectively. These are shown in figure 4.12.

As discussed in section 4.1.2, the regional M boundaries shown in figure 4.12 were determined from changes in T_g behaviour with M[134, 135]. Figures 4.12 (a), (b), (c), and (d) show a sharp decrease in the volume/lengthscale of the cooperative region in region I, followed by a stabilisation, or slight increase, in regions II and III. The lenghscale of the cooperative region falls from $\xi_a \approx 3.2$nm for PMMA and PS to $\xi_a \approx 1.8$nm for PMMA, and $\xi_a \approx 2.2$nm for PS between dimer (n=2) and the region I to II boundary. The subsequent increase in region II is less pronounced in PMMA than PS, whereby it increases to $\xi_a \approx 2.1$nm in PMMA, and $\xi_a \approx 2.7$nm for PS. The M dependence of ξ_a for PS, and high M PMMA were compared to literature, which will be discussed in section 4.1.4.

Due to the timescale (τ_α) dependence, it is expected that the size of the cooperative region increases with increasing modulation period. This behaviour is not clear due to scatter in the data, i.e. any timescale dependence in the size of the cooperative region appears to be within the error of the measurements. Quantifying errors here is difficult due to how c_p'' is calculated and subsequently fitted. From the fitting, standard errors of δT, T_α, and Δc_p^{-1} were low ($< 1\%$). This is because of both the sheer number of data points taken by the DSC, and the assumptions made when limiting the fitting range ($T > T_\alpha - 5$K). For instance, for PMMA n=4 P=60s, the errors from fitting lead to an error in V_a of $\sim 5\%$. However, from figure 4.12 (a), this is clearly too small. Further errors are also introduced from phase angle correction, and the subsequent calculation of c_p''. Despite this, regional behaviour in M is clear for PMMA and PS. An error of $\sim 10\%$ in V_a is likely to be more reasonable.

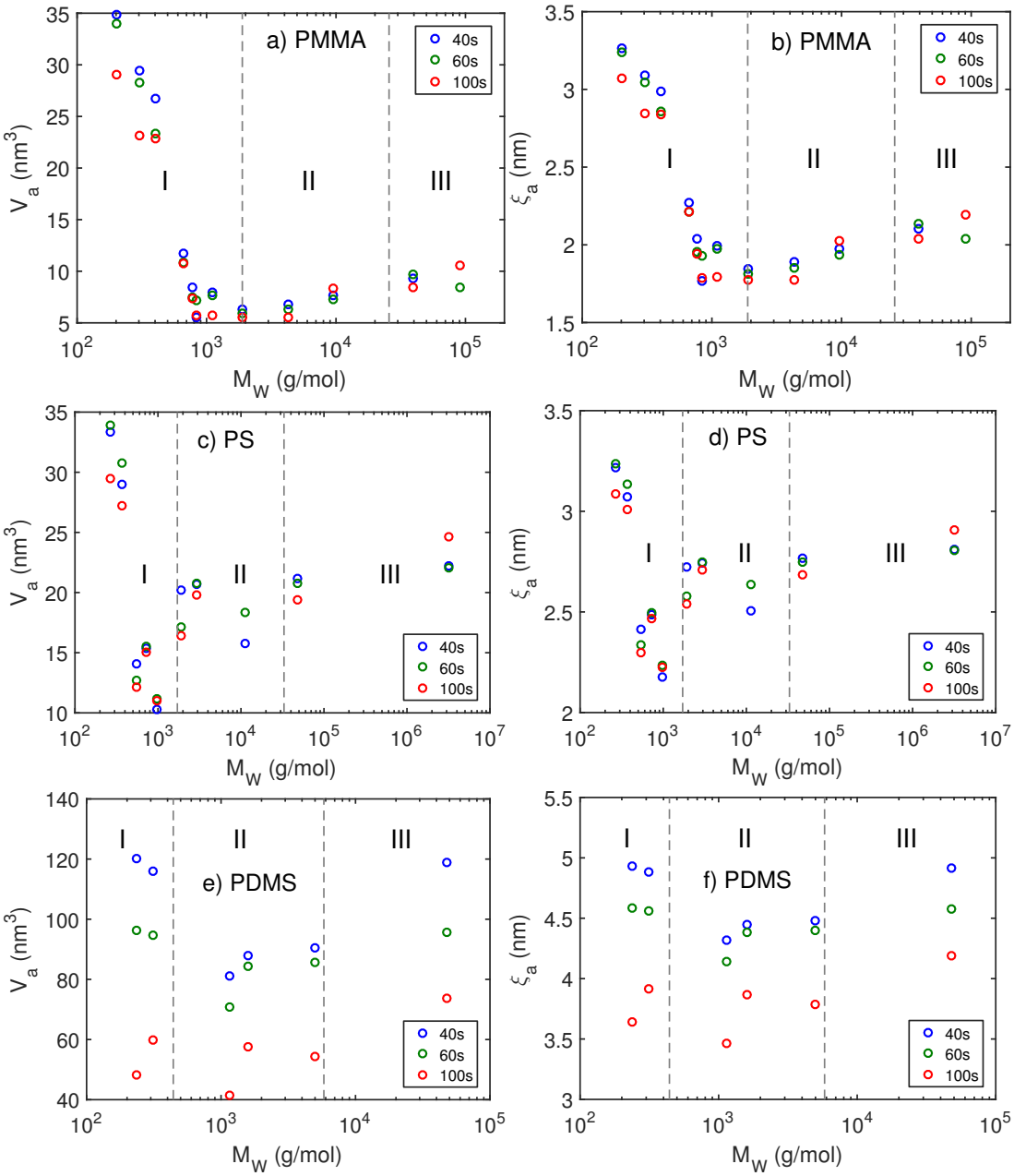

Figure 4.12: Size of the cooperative region for PMMA, PS, and PDMS for three modulation periods (P=40, 60, and 100s). (a), (c), and (e): Volume, calculated using equation 4.10. (b), (d), and (f): Lengthscale, calculated using equation 4.12.

Figures 4.12 (e) and (f) show that for PDMS, this regional behaviour is much less pronounced. It appears that there is a decrease in the size of the cooperative region in region I, followed by an increase in regions II and III. However, this is not clear. Interestingly, the size of the cooperative region appears much larger in PDMS than both PS and PMMA across the entire M range, with a lengthscale of $\xi_a \approx 4.5$nm (P=60s). The large shifts in the size of the cooperative region between modulation periods in PDMS is an anomaly. However the reason for these values is clear in figures 4.6 (e) and (f), whereby there was a large change in δT between periods ($V_a \propto 1/\delta T^2$, from equation 4.10). One possible explanation is that because PDMS samples had to be quenched, and the measurements performed on heating, there may be some crystallisation around $\sim T_\alpha$. Further work will be performed to investigate this.

Due to the fact that: (i) for PMMA and PS, the difference in the size of the cooperative region for different modulation periods (of those measured) is within experimental/fitting error; and (ii) for PDMS, there is an unexplained broadening of δT with increasing oscillation period, only data for P=60s will be analysed further when describing the size of the cooperative region.

As stated in section 4.1, both V_a and ξ_a depend on sample density. Expressing the size of the cooperative region as a number of monomer units, N_a, rather than as a volume or lengthscale removes this density dependence. This is calculated using equation 4.13, which replaces the density dependence with that of the monomer molecular weight. Figure 4.13 shows these calculated values for all three systems as a function of molecular weight, along with guides to the eye pointing out regional behaviour.

Figures 4.13 (a) and (b) demonstrate that the number of cooperative monomer units for n=2 is $N_a \approx 220$ for PMMA, and $N_a \approx 180$ for PS. This falls to $N_a \approx 50$ for PMMA, and $N_a \approx 70$ for PS as M increases to the region I to II boundary. The increase of N_a with M in region II for PS is more pronounced (rising to $N_a \approx 130$) than in PMMA (which appears more stable at $N_a \approx 50$). This is consistent with an M series study in literature for PS[198], which also shows an increase in this M range; this comparison will be shown in section 4.1.4.

As shown in figure 4.13 (c), it is difficult to say if PDMS shows this regional behaviour. The relative change in N_a with M is much less pronounced than

in either PMMA or PS, and the number of cooperative monomer units appears relatively stable at $N_a \approx 650$. This is also much higher in PDMS than for PMMA and PS across the entire M range (as noted for V_a and ξ_a previously).

These observations of the number of cooperative monomer units at $\tau_\alpha \approx 10$s will be explored further in section 4.4.3.

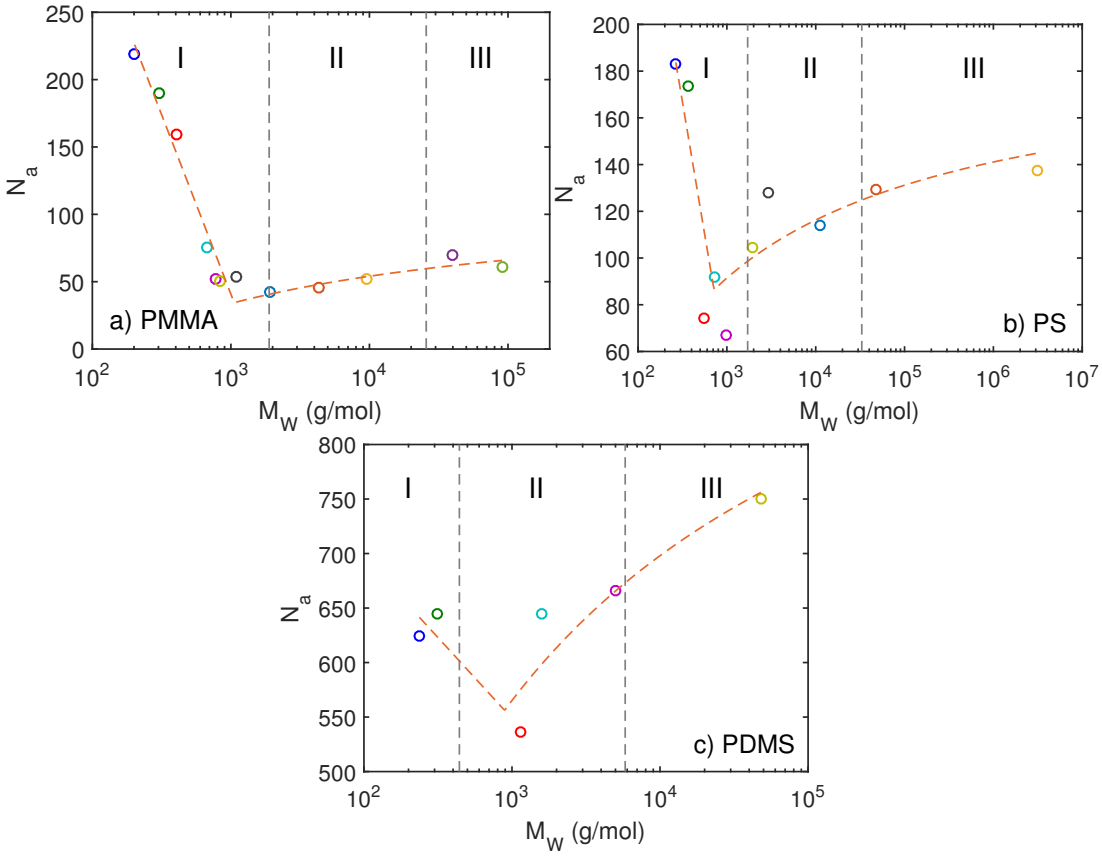

Figure 4.13: Number of monomer units in the cooperative region calculated from TMDSC ($P = 60s$) using equation 4.13 for (a) PMMA, (b) PS, and (c) PDMS M_W series. Orange dashed lines are guides to the eye, with regional boundaries indicated.

4.1.4 Comparisons to literature

Hempel et. al.[79] determined the lengthscale of the cooperative region for polymeric PMMA and PS using TMDSC to be $\xi_{a,PMMA} \sim 1.1$nm and $\xi_{a,PS} \sim 2.5$nm.

From our study, the values polymer value observed (ξ_a values for high M in figure 4.12) are $\xi_{a,PMMA} \sim 2.2$nm and $\xi_{a,PS} \sim 2.8$nm. These comparisons of ξ_a for PS is within experimental uncertainty, whereas PMMA is different by a factor of ~ 2. However, Hempel et. al. reported that the PMMA sample in their study was plasticised ($T_g \sim 10 - 15$K lower than expected for bulk PMMA), which may have been the cause of this discrepancy in their value of ξ_a.

Although extensive work has been done in calculating the size of the co-operative region using this technique for a wide range of both polymeric and non-polymeric systems in literature[79, 195–197], only two systematic studies of chain-length series were found. The first of these studies in literature was conducted on PS[198], which allowed for a direct comparison to this work. This study did not include the lowest M samples in our study, which exhibit a large decrease in N_a in region I (as shown figure 4.13 (b)). The values of N_a as a function of M for PS, along with their data, is shown in figure 4.14.

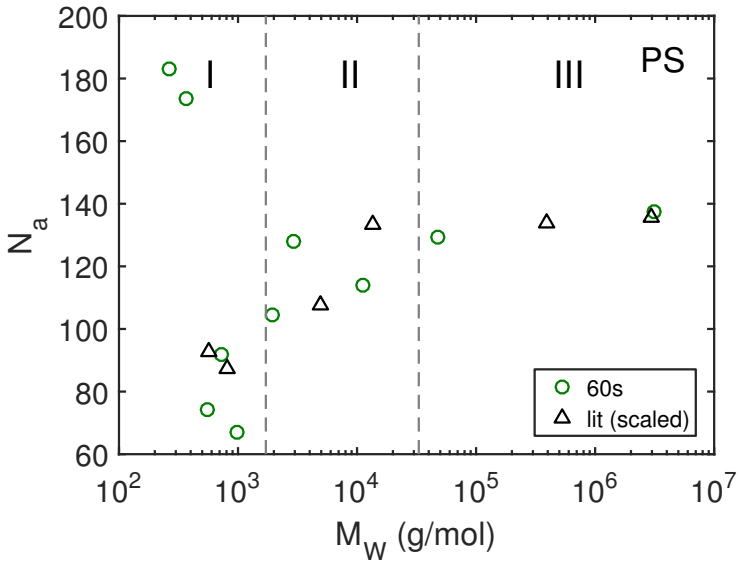

Figure 4.14: Number of monomer units in the cooperative region for PS including: Data from this work is from TMDSC (P=60s); and literature data measured using standard (10K/min) DSC, which have been collapsed onto our data using a single shift factor. Regional boundaries are indicated.

Both our data and the scaled literature data shown in figure 4.14 exhibit the

same trend with M, although the literature data lacked the lowest M range. A vertical shift factor (~ 0.6) was also required to bring the literature data into line with data from our work. The likely reason for this was the use of standard (10K/min) DSC in determining these values, rather than TMDSC. This would effect the results in two ways: (i) As described in section 2.3, a heat/cooling rate of 10K/min corresponds to $\tau_\alpha \approx 100$s for polymeric PS[119] (although this may also have an M dependence), whereas a modulation period of $P = 60$s corresponds to $\tau_\alpha \approx 10$s; and more importantly (ii) both of these techniques will have different definitions of the transition width (δT), and it has been shown that standard DSC underestimates this[79]. Both of these factors are consistent with the direction of the shift in N_a between their data and ours. Therefore, applying a vertical shift factor is justified in order to compare with our data. Figure 4.14 shows the same trend for both data sets across the series, showing an increase in N_a with M around the region I to II boundary, and a stabilisation in region III.

The second existing literature study of a chain-length series was of poly(n-butylmethacrylate) (PnBMA)[199], which is structurally similar to that of PMMA (containing a butyl, rather than a methyl group in the ester side group). Unlike the previous PS study, this series spanned from monomer (n=1) to fully entangled polymer, using TMDSC with the same modulation period as our study ($P = 60s$). Their values of N_a as a function of M for a PnBMA are shown in figure 4.15.

Figure 4.15 shows a clear decrease in N_a as the polymer chain grows from monomeric to oligomeric (region I) as seen with PMMA and PS (shown in figure 4.13 (a) and (b)). After this decrease, N_a appears relatively stable, which is consistent with PMMA. However, N_a for PMMA stabilises at $N_a \sim 50$, whereas PnBMA appears lower at $N_a \sim 10$. This increase in N_a with increasing side-group chain length was also observed by Hempel et. al.[79] for side-group chain lengths between $n = 1 - 5$ for a poly(n-alkylmethacrylate) series, suggesting that the increase in the length of the side chain reduces the number of cooperative monomers in the α relaxation.

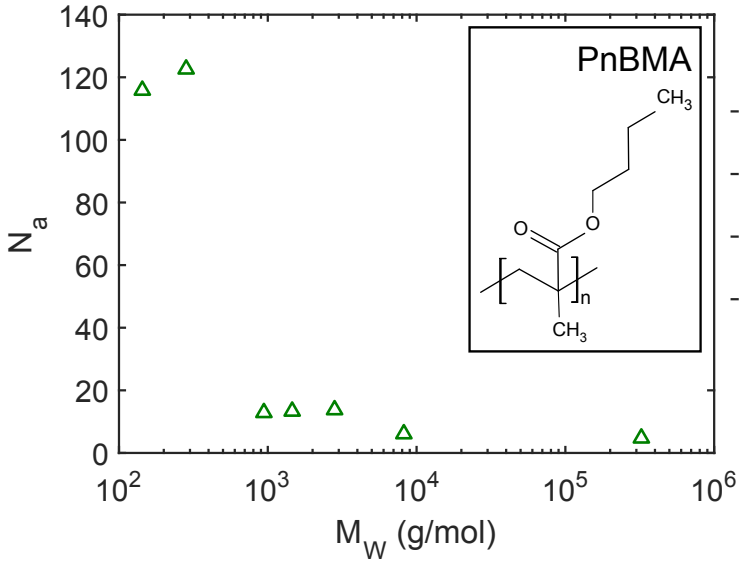

Figure 4.15: Number of monomer units in the cooperative region for PnBMA calculated from TMDSC ($P = 60s$). Inset shows PnBMA molecule.

4.2 Susceptibility determination of $N_{corr,4}$

The second of the two technique employed to determine the number of correlated (cooperative) units in the α relaxation involved estimating a dynamic four-point correlation function, often referred to as the dynamic susceptibility, χ_4. This is a technique that was proposed by Berthier et. al.[201]. It involves measurements of the complex susceptibility, related to a two-point correlation function, and performing these measurement at different temperatures provides a three-point dynamic susceptibility, which allows for an estimation of χ_4. In turn, this yields information on the number of correlated units in the α relaxation. This reasoning will closely follow literature by Berthier et. al.[201, 210–213].

A spontaneous fluctuation of some variable, $O(t)$ (such as polarisation), can be written as equation 4.25.

$$\delta O(t) = O(t) - \langle O \rangle \tag{4.25}$$

Where $O(t)$ is the value of the variable at time t, and $\langle O \rangle$ is the mean value. From this, a two-point correlation function can be defined, shown in equation

4.26.

$$C(0,t) = \delta O(0)\delta O(t) \tag{4.26}$$

This correlates fluctuations in O between times 0 and t. The average value of this quantity characterises the overall dynamics of the system, defined in equation 4.27.

$$F(t) = \langle C(0,t)\rangle \tag{4.27}$$

The fluctuation of $C(0,t)$ around its mean is show in equation 4.28.

$$\delta C(0,t) = C(0,t) - \langle C(0,t)\rangle = C(0,t) - F(t) \tag{4.28}$$

From this fluctuation, information about the amplitude is given by the varience, $\langle \delta C(0,t)^2\rangle$. Dynamic correlations, or heterogeneities, are manifested in the fluctuations of $C(0,t)$, as measured by the dynamic susceptibility, $\chi_4(t)$, shown in equation 4.29.

$$\chi_4(t) = N\langle \delta C(0,t)^2\rangle \tag{4.29}$$

Where N is the number of particles in the system. $C(0,t)$ can also be defined as a sum of local dynamics[214], shown in equation 4.30.

$$C(0,t) = \frac{1}{V}\int \mathrm{d}^3\boldsymbol{r}c(\boldsymbol{r};0,t) \tag{4.30}$$

Here, V is the volume of the system ($V = N/\rho$), and $c(\boldsymbol{r};0,t)$ is a "local" probe of dynamics at point $\boldsymbol{r}$. From equations 4.29 and 4.30, $\chi_4(t)$ can be defined by equation 4.31.

$$\chi_4(t) = \frac{N}{V}\int \mathrm{d}^3\boldsymbol{r}\langle \delta c(\mathbf{0};0,t)\delta c(\boldsymbol{r};0,t)\rangle \tag{4.31}$$

Where $N/V = \rho$ is the mean desnity of the system. This shows that $\chi_4(t)$ measures the degree of spatial correlation of dynamic events in a system occuring between time 0 and t, i.e. a measure of dynamic heterogeneities over time t[212]. This quantity is difficult to measure directly, as it requires dynamic measurements to be performed at multiple points in both space and time[215].

Berthier et al.[201, 212] showed that a more experimentally feasible route in estimating $\chi_4(t)$ involved looking at how dynamic measurements are effected by a small change in temperature. For a fluid obeying Newton's equations at constant number of particles, pressure, and temperature (NPT ensemble), the fluctuation-dissipation theorem shown in equation 4.32 holds.

$$\chi_T^{NPT}(t) = \frac{\rho}{k_B T^2} \int \mathrm{d}^3\boldsymbol{r} \langle \delta h(\mathbf{0};0)\delta c(\boldsymbol{r};0,t)\rangle_{NPT} \tag{4.32}$$

Here, $\delta h(\boldsymbol{r};0)$ is the enthalpy density per molecule. $\chi_T^{NPT}(t)$ is the three-point dynamic susceptibility, which measures the degree of spatial correlation between a fluctuation of enthalpy at time 0 at point $\boldsymbol{r} = \mathbf{0}$, and the dynamics between time 0 and t at point $\boldsymbol{r}$. More simply, this is the derivative of $F(t)$ with respect to T at constant number of particles and pressure[212]. Integrating this expression leads to equation 4.33.

$$\chi_T^{NPT}(t) = \frac{\partial F(t)}{\partial T}\Big|_{NP} = \frac{\rho}{k_B T^2}\langle \delta H(0)\delta C(0,t)\rangle_{NPT} \tag{4.33}$$

Where $\delta H(0) = H(0) - \langle H\rangle$ is the fluctuation of enthalpy per molecule at $t = 0$, and $\delta C(0,t)$ is the resulting fluctuation in dynamics between 0 and t.

Both $\chi_4(t)$ and $\chi_T(t)$ contain information on spatial correlations that are associated with dynamics. Assuming that the spatial correlations die out over large distances, the integration over space means that both $\chi_4(t)$ and $\chi_T(t)$ contain information about a correlation volume, at a given time. Both $\chi_T(t)$ and $\chi_4(t)$ reach a maximum at $t \sim \tau_\alpha$[212]. Therefore, the maxima of χ_4 relates to the number of correlated units at τ_α, shown in equation 4.34.

$$N_{corr,4} = max\{\chi_4(t)\} \tag{4.34}$$

$N_{corr,4}$ is defined as the number of units whose dynamics are correlated among themselves. An equivalent to this from the three-point dynamic susceptibility is given by equation 4.35.

$$N_{corr,T} \sim \rho \Big| \int d^3\boldsymbol{r} \langle \delta\bar{h}(\mathbf{0};0)\delta c(\boldsymbol{r};0,t\sim\tau_\alpha)\rangle \Big| = \sqrt{\frac{k_B T^2}{\Delta c_p}} max|\chi_T(t)| \tag{4.35}$$

$N_{corr,T}$ is defined as the number of units whose dynamics are correlated with a local fluctuation of enthalpy. $\delta\bar{h}$ is a dimensionless fluctuation of energy density, which leads to the prefactor term, which contains the heat capacity over the α relaxation, Δc_p[212]. It has been shown that the relation between equations 4.34 and 4.35 can be approximated by equation 4.36[212].

$$N_{corr,4} \sim N_{corr,T}^2 \tag{4.36}$$

Thus, $N_{corr,T}$ can be determined experimentally, and using this relation $N_{corr,4}$ can be estimated. These relations are also applicable in the frequency domain. Therefore, the number of correlated units defined by a four-point correlation function can be estimated by equation 4.37.

$$N_{corr,4} \approx \frac{R}{m_0 \Delta c_P} T^2 max\{|\mathrm{d}\chi(\omega,T)/\mathrm{d}T|\}^2 \tag{4.37}$$

Here, $m_0\Delta c_P$ is the difference in isobaric monomer molar heat capacity between liquid and glass, and $\chi(\omega,T)$ is the normalised dynamic susceptibility[212], which, based on BDS data, is defined in equation 4.38.

$$\chi(\omega,T) = \frac{\epsilon'(\omega) - \epsilon_\infty}{\Delta\epsilon} \tag{4.38}$$

Where $\epsilon'(\omega)$ is the real part of the complex permittivity. In this work, $\chi(\omega,T)$ was determined using appropriate function fits of the α relaxation from measurements of the complex permittivity at discrete temperatures.

4.2.1 The complex permittivity

In order to determine the dynamic susceptibility, the frequency dependent complex permittivity, $\epsilon^*(\omega)$, is required. This is obtained from the frequency dependent dielectric response, measured using broadband dielectric spectroscopy (BDS). $\epsilon^*(\omega)$ is defined in equation 4.39.

$$\epsilon^*(\omega) = |\epsilon^*|(\omega)\mathrm{e}^{-i\delta(\omega)} = \epsilon'(\omega) - i\epsilon''(\omega) \tag{4.39}$$

Equation 4.39 shows $\epsilon^*(\omega)$ separated into an in-phase, $\epsilon'(\omega)$, and an out-of-phase, $\epsilon''(\omega)$, component. As outline in section 2.2, measurements of the complex permitivity were performed using broadband dielectric spectroscopy (BDS), using a Novocontrol Alpha-A analyser. As already shown in section 3.2.1, BDS measurements are performed at discrete temperatures over a broad frequency range ($\nu \sim 10^{-2} - 10^{6}$Hz). Within this frequency range at a particular temperature, several relaxation mechanisms may be apparent, and the spectra are fitted with a sum of Havriliak-Negami (HN) expressions[109]. This HN expression is shown in equation 4.40.

$$\epsilon^*(\omega) = \epsilon_\infty + \frac{\Delta\epsilon}{(1 + (i\omega\tau_{HN})^\alpha)^\beta} \tag{4.40}$$

Where ϵ_∞ is the high frequency permittivity, $\Delta\epsilon$ is the change in permittivity due to the relaxation, and α and β are parameters which describe the broadness of the relaxation (relating to high and low frequency power-law flanks in $\epsilon''(\omega)$). An example of this fitting is shown in figure 4.16.

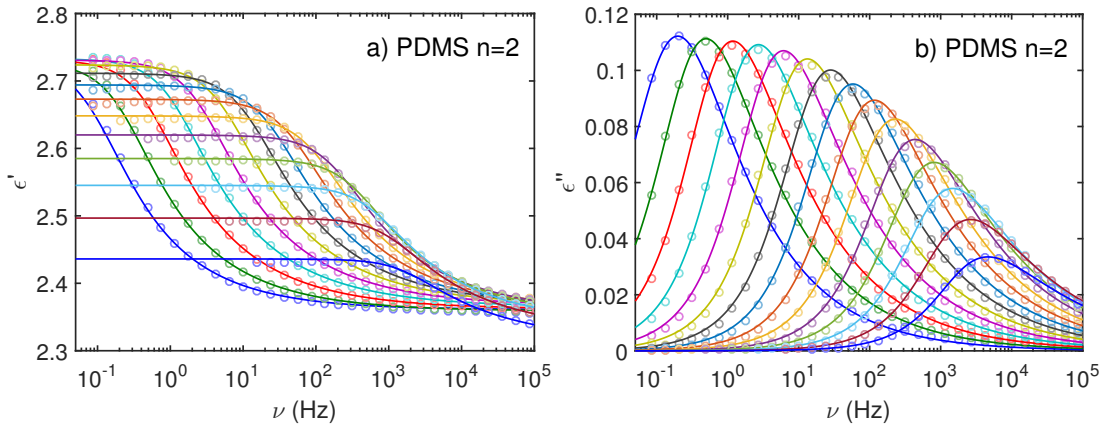

Figure 4.16: ϵ' (a) and ϵ'' (b) with HN fitting for PDMS n=2. Different colours represent different temperatures between $T = 121.5 - 128.5$K.

Figure 4.16 shows ϵ' (a) and ϵ'' (b) for PDMS n=2, with a single HN expression describing the α relaxation. From the HN fits, τ_{HN} relates to the characteristic relaxation time (the inverse of the ϵ'' peak frequency, $\tau_p = 1/\omega_p$) by equation 4.41[14].

$$\frac{1}{\tau_p} = \frac{1}{\tau_{HN}} \left[\sin \frac{\alpha\pi}{2+2\beta} \right]^{1/\alpha} \left[\sin \frac{\alpha\beta\pi}{2+2\beta} \right]^{-1/\alpha} \tag{4.41}$$

Using this fitting procedure, the response shape in $\epsilon^*(\omega)$ of individual relaxation mechanisms (along with DC conductivity) can be isolated from each other (an example of this fitting procedure with multiple components is shown previously in figure 3.8). This was necessary in order to determine the temperature derivative of the permittivity response due to the α relaxation alone.

4.2.2 χ_4 determination of the number of correlated units

As discussed in section 4.2.1, the normalised susceptibility, $\chi(\omega, T)$, can be calculated using an appropriate fitting function to the complex permittivity. This fitting procedure is used to isolate the α relaxation response from other contributions to the complex permittivity. $\chi(\omega, T)$ is then calculated using equation 4.38 from values of $\epsilon'(\omega)$, ϵ_∞, and $\Delta\epsilon$ determined from these fits at discrete temperatures. For the example shown in figure 4.16, $\chi(\omega, T)$ is shown in figure 4.17.

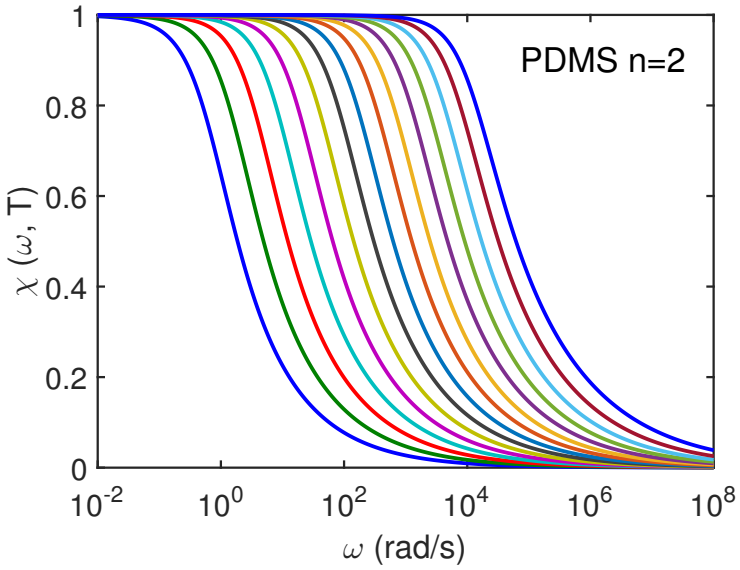

Figure 4.17: Normalised susceptibility (calculated using equation 4.38 from Havriliak-Negami parameters) for PDMS n=2 as a function of frequency. The different colours correspond to the same temperatures as in figure 4.16.

Figure 4.17 shows the values of $\chi(\omega, T)$ for the α relaxation as a function of frequency at different temperatures. From this, small temperature derivatives were necessary in order to calculate the number of correlated units in the α relaxation, $N_{corr,4}$ (as shown in equation 4.37). The importance of small temperature derivatives is shown in figure 4.18.

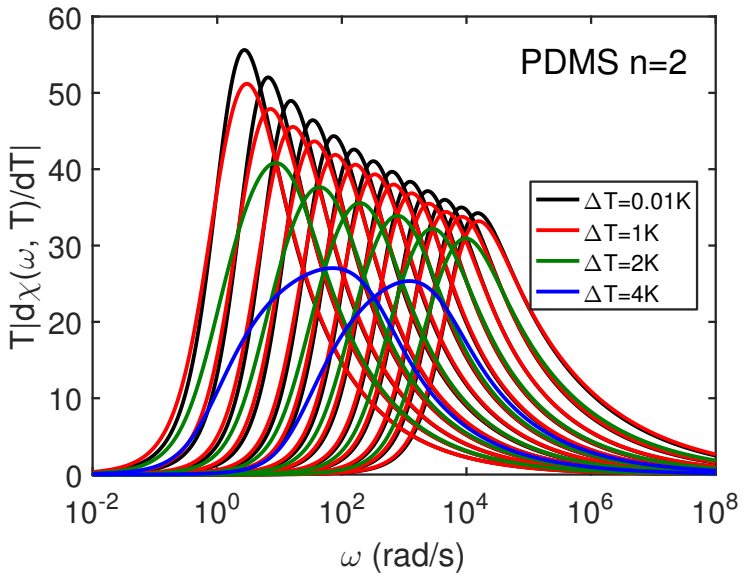

Figure 4.18: Temperature derivative of this normalised real permittivity for PDMS n=2. The different colours represent different temperature differences used in order to compute the derivatives.

$T|\mathrm{d}\chi(\omega, T)/\mathrm{d}T|$ is the temperature derivative of $\chi(\omega, T)$ (multiplied by T), shown for PDMS n=2 in figure 4.18. The maximum of the peaks is required to calculate $N_{corr,4}$ (using equation 4.37) at a particular temperature. Figure 4.18 illustrates the effect of temperature differences used in order to compute the derivatives. In this particular experiment, $\epsilon^*(\omega)$ was measured at every 0.5K, therefore derivatives taken between $T = \pm 0.5$K would yield the red curves ($\Delta T =$ 1K). The effect of larger temperature differences would yield the green and blue curves, for $\Delta T = 2$K and 4K respectively. What is clear from this is that small temperature steps are required in order to determine accurate values of the peak maximum.

Therefore, from the HN fits, some form of modelling of the fitting parameters was needed in order to calculate $\epsilon^*(\omega)$ at $T \pm \delta T$, where δT was adequately small[212]. Three modelling techniques were explored in order to achieve this.

a) Full Havriliak-Negami modelling

The first technique involved the modelling of all HN parameters using some analytical functions. Examples of this is shown in figure 4.19.

Figure 4.19 (a), (b), (c), and (d) show HN parameters as a function of T fitted with polynomials, and figure 4.19 (e) shows standard VFT fitting to τ_α (calculated from τ_{HN} using equation 4.41). Using these expressions describing HN parameters as a function of T, small temperature derivatives of $\chi(\omega, T)$ could be calculated. An example of this is shown by the black curve in figure 4.18, whereby $\chi(\omega, T)$ were generated at $T \pm 0.005$K, yielding more accurate values of $T|\mathrm{d}\chi(\omega, T)/\mathrm{d}T|$.

However, it is apparent in figure 4.19 (c) and (d) that the HN shape parameters (α and β) change unrealistically at high and low temperatures. This is due to the over-parametrisation of the HN expression as the α relaxation moves out of the measured frequency window (shown by the data at the high and low frequency extremes in figure 4.16). It may therefore be unrealistic to calculate $\chi(\omega, T)$ using these generated HN expressions. It is worth noting that ϵ_∞ and $\Delta\epsilon$ have little effect on $\chi(\omega, T)$ compared to τ_α, or the shape parameters, α and β.

b) τ_α only modelling

The second technique assumed that the shape of the α relaxation does not change with small temperature differences, thus, taking into account the difference in timescale only. This removed the need for describing HN parameters using arbitrary functional shapes, and only VFT fitting of $\tau_\alpha(T)$ was needed. For the PMMA, PS, and PDMS, this is shown in an Arrhenius plot in figure 4.20.

Figure 4.20 shows PMMA (a), PS (b), and PDMS (c) exhibit VFT behaviour across the chain-length series. In the same manner as for the full Havriliak-Negami modelling, $\chi(\omega, T)$ was calculated at $T \pm 0.005$K. This technique assuming that the other HN parameters did not vary over such a small temperature difference. It is a sensible assumption that the shape of $\chi(\omega, T)$ does not vary much

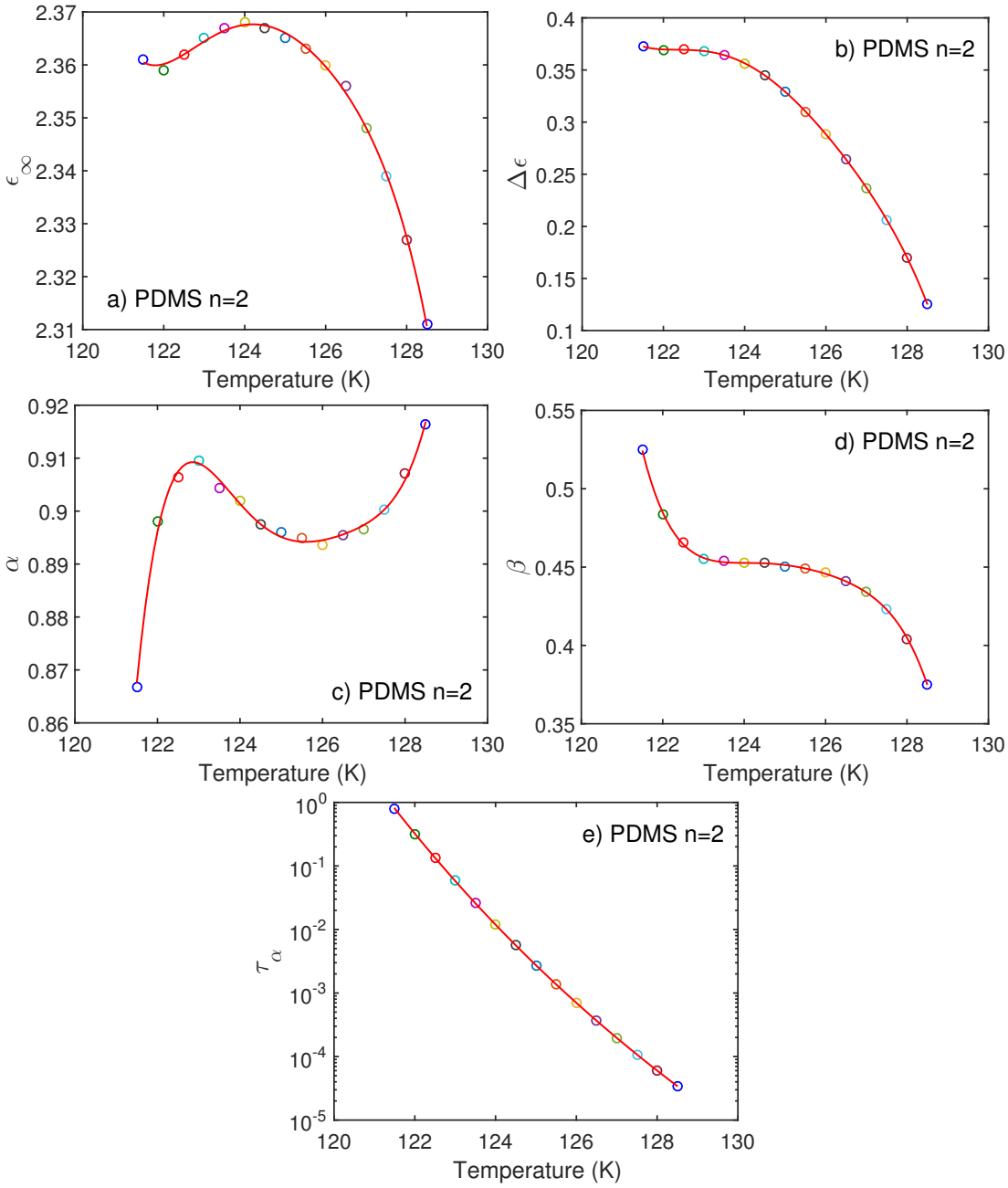

Figure 4.19: Havriliak-Negami fitting parameters: (a) ϵ_∞, (b) $\Delta\epsilon$, (c) α, (d) β, and (e) τ_α for PDMS n=2 as a function of temperature. Polynomials are fitted to all except (e), which is fitted with a VFT expression. The different colours correspond to the same temperatures as in figure 4.16.

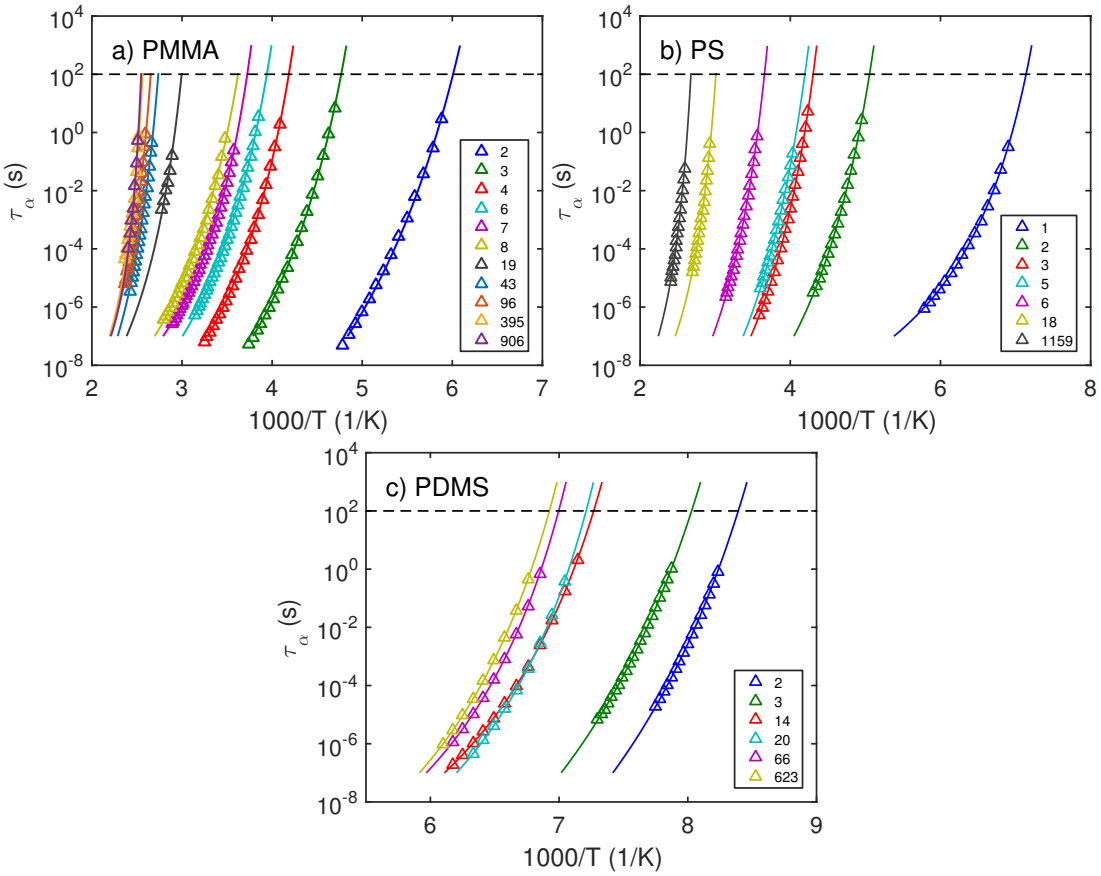

Figure 4.20: Arrhenius plots for a) PMMA, b) PS, and c) PDMS. The fitted lines are VFT expressions. The temperature where $\tau_\alpha = 100s$ (dashed line) is commonly taken as the glass transition temperature. The legend shows the degree of polymerisation (n).

with such a small temperature difference, and therefore that $T|\mathrm{d}\chi(\omega,T)/\mathrm{d}T|$ is mainly due to the temperature dependence of τ_α.

c) Time-temperature superposition modelling

The third technique assumed that the α relaxation obeys time temperature superposition over the measured temperature range, i.e. the shape of the response in $\epsilon^*(\omega)$ does not change with temperature. It was also assumed that the shape of the response could be adequately described by a stretched exponential, or Kohlrausch-Williams-Watts (KWW) expression[94] (as described in section 2.1.2). From these two assumptions, it has been shown that $Tmax\{|\mathrm{d}\chi(\omega,T)/\mathrm{d}T|\}$ can be expressed simply in terms of the temperature dependence of τ_α, and the KWW stretching parameters, β_{KWW}[216], shown in equation 4.42.

$$Tmax\{|\mathrm{d}\chi(\omega,T)/\mathrm{d}T|\} \approx \left(\frac{\beta_{KWW}}{e}\right)\left(\frac{\partial \ln \tau_\alpha}{\partial \ln T}\right) \tag{4.42}$$

From this, $N_{corr,4}$ (from equation 4.37) approximates to equation 4.43.

$$N_{corr,4} \approx \frac{R}{m_0 \Delta c_P}\left(\frac{\beta_{KWW}}{e}\right)^2\left(\frac{\partial \ln \tau_\alpha}{\partial \ln T}\right)^2 \tag{4.43}$$

By calculating the number of correlated units this way, this function is very similar to the number of cooperative units in the cooperative region, as calculated from TMDSC in section 4.1 using similar approximations. This will be discussed in section 4.3

Comparison of the three modelling techniques

Each of the three modelling technique described above yield values for: $T|\mathrm{d}\chi(\omega,T)/\mathrm{d}T|$ in the case of (a) full Havriliak-Negami modelling, and (b) τ_α only modelling; or $Tmax\{|\mathrm{d}\chi(\omega,T)/\mathrm{d}T|\}$ in the case of (c) time-temperature superposition modelling. An example of these three modelling techniques for PDMS n=2 is shown in figure 4.21.

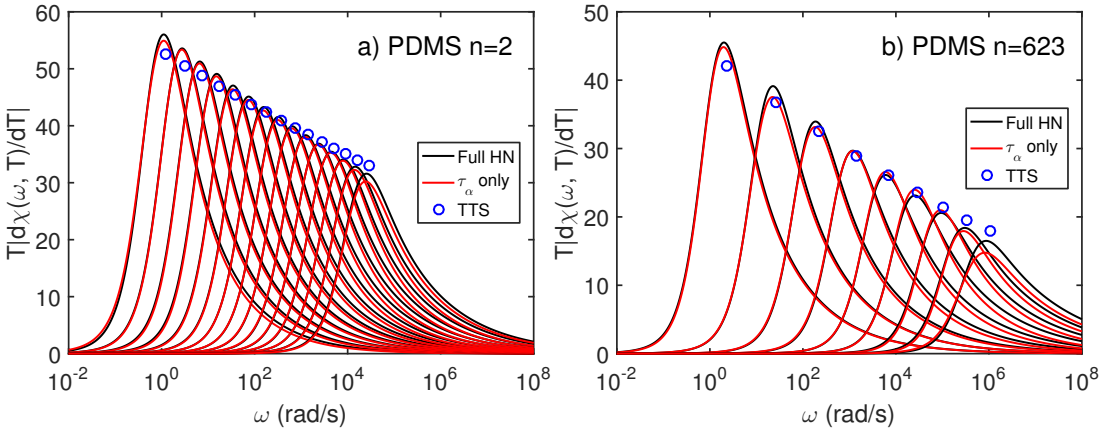

Figure 4.21: Low (a) and high (b) M PDMS samples showing $T|\mathrm{d}\chi(\omega,T)$, with different curves representing temperatures where measurements were taken. The two methods of HN parametrisation are shown, with single data points represent TTS approximations for the peak value.

The "full Havriliak-Negami" (black curves in figure 4.21) and "τ_α only" (red curves) modelling techniques gave only slightly different peak values at each temperature for PDMS (within a few %). However, for higher M PMMA and PS ($M \gtrsim 1000$g/mol), secondary (β) relaxation modes become prominent in $\epsilon^*(\omega)$ (either as a second, high frequency, peak for PMMA; or a high frequency flank for PS). This causes uncertainty in the shape HN parameters, complicating these methods. The single blue data points in figure 4.21 were calculated (from equation 4.43) by assuming that the spectra obeys TTS, and can be described by a KWW expression. For appropriate values of β_{KWW}, this TTS method is valid in describing this general behaviour in PDMS.

Using these three modelling techniques in determining $N_{corr,4}$, figure 4.22 shows this as a function of τ_α for the chain-length series of PMMA, PS, and PDMS.

Figure 4.22 shows $N_{corr,4}$ as a function of τ_α for the M series of PMMA (a), PS (b), and PDMS (c) calculated using the three modelling techniques outlined in this section: full HN modelling (circles); τ_α only modelling (triangles); and TTS approximation (squares). For PDMS (and also PMMA and PS for a few monomer units ($n \sim 1-5$), there is good agreement between these three techniques for

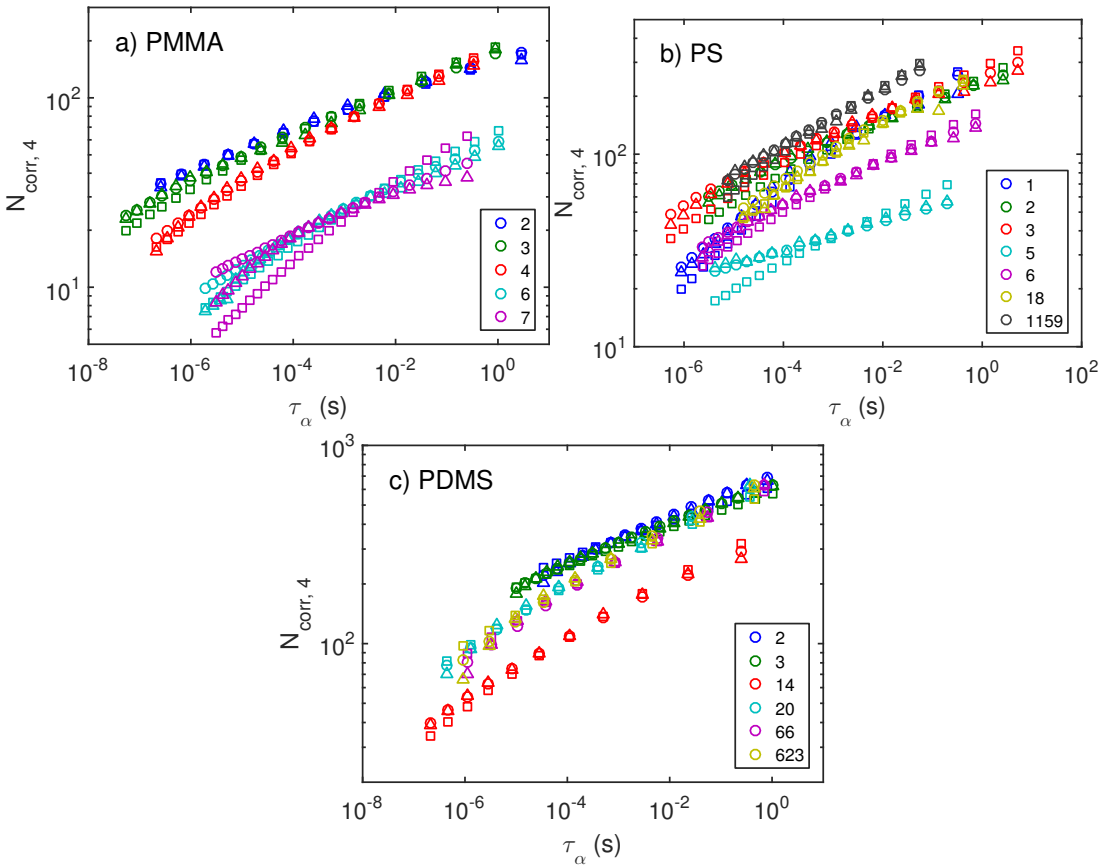

Figure 4.22: $N_{corr,4}$ for a) PMMA, b) PS, and c) PDMS as a function of τ_α calculated using three techniques: full HN modelling (circles), τ_α only modelling (triangles), and TTS approximation (squares). The legends indicate the degree of polymerisation (n).

determining $N_{corr,4}$ due to a clear and isolated α peak in the BDS spectra, and these being adequately described by a KWW expression for the TTS approximation. For longer M PMMA and PS samples, the presence of secondary relaxation modes made isolating the relaxation difficult, and obscured the response shape. Due to this, $N_{corr,4}$ for only small oligomers was calculated for PMMA. In addition to this, these responses were not adequately described by a KWW expression, as they often had a broadening of both the low and high frequency power-law flanks in $\epsilon''(\omega)$, causing the TTS technique to be less appropriate.

The values of $N_{corr,4}$ from τ_α only modelling (triangles in figure 4.22) were chosen as the most reliable modelling technique. Trying to model the shape parameters (α and β from the HN expression) with some arbitrary expression was unreliable, as these could scatter from temperature to temperature for the more difficult to fit samples. The TTS description relies on both TTS being applicable across this wide dynamic range, and also that the response spectra could be modelled by a KWW expression, which was not the case.

All samples in this work show an increase in $N_{corr,4}$ with τ_α as expected[212, 216]. For PMMA, shown in figure 4.22 (a), and PS (b), as M increases from small molecular glass former to oligomer, $N_{corr,4}$ decreases by a factor of ~ 5. With further increasing M, PS shows an increase in $N_{corr,4}$ (which is not shown here for PMMA due to the lack of data). For PDMS (c), the M variation of $N_{corr,4}$ is less obvious than PMMA and PS, with exception of $n = 14$, which is lower by a factor of ~ 2. The absolute values in $N_{corr,4}$ for PDMS are also higher across the entire τ_α and M range than for PMMA and PS. This is consistent with the number of cooperative units calculated from TMDSC, as discussed in section 4.1.3.

4.3 Comparison between N_a and $N_{corr,4}$

The estimate of the number of cooperative/correlated monomer units determined from TMDSC, N_a, and BDS, $N_{corr,4}$, were compared. As discussed in section 4.1, the number of units in the cooperative region obtained from TMDSC is described using equation 4.44.

$$N_a = \frac{RT_\alpha^2 \Delta c_P^{-1}}{m_0 \delta T^2} \tag{4.44}$$

This describes the number of correlated units from the heat capacity responses measured using TMDSC: T_α and δT are the peak and the width of the imaginary specific heat capacity respectively, and Δc_P^{-1} is the change in inverse specific heat capacity between glass and liquid. It has been shown that if the calorimetric response of the α relaxation can be described by a KWW expression, the transition width, δT, can be approximated as equation 4.45[9, 217].

$$\delta T \approx \frac{\delta ln\tau_\alpha}{\partial ln\tau_\alpha / \partial T} = \frac{1.07T}{\beta_{KWW}} \left(\frac{\mathrm{d} \ln \tau_\alpha}{\mathrm{d} \ln T} \right)^{-1} \tag{4.45}$$

Inserting this approximation into equation 4.44 yields equation 4.46.

$$N_a \approx \frac{R\Delta c_P^{-1}}{m_0} \left(\frac{\beta_{KWW}}{1.07} \right)^2 \left(\frac{\mathrm{d} \ln \tau_\alpha}{\mathrm{d} \ln T} \right)^2 \tag{4.46}$$

Equation 4.46 is similar to the KWW approximation of $N_{corr,4}$ shown in equation 4.43. These two expressions of the number of cooperative units involved in the α relaxation differ by some factor proportional to the difference between $(\Delta c_P)^{-1}$ and Δc_P^{-1}.

These two techniques have often been compared in literature[78, 217–219]. Casalini et. al. quantified the difference between $(\Delta c_P)^{-1}$ and Δc_P^{-1} for both poly(methyl acrylate)[78], and three polychlorostyrenes[218], and determined a factor of $N_a = 6.45 N_{corr,4}$ for these samples. This naturally lead to agreement between N_a and $N_{corr,4}$ values when calculated using this KWW assumption. However, no single shift factor can truly account for uncertainties and assumptions when calculating either N_a and $N_{corr,4}$. Hence, these two measures of the number of correlated units of the α relaxation were directly compared. For PMMA, PS, and PDMS, this is shown in figure 4.23.

Figure 4.23 shows that PMMA (a), PS (b), and PDMS (c) show the expected increase in number of cooperative units with relaxation time[7]. The apparent changeover in behaviour at $\tau_\alpha \sim 10^{-4}$s (shown by the arrow in figure 4.23 (a)) is well documented[220], and is consistent with the dynamic crossover as discussed in section 1.2.3.

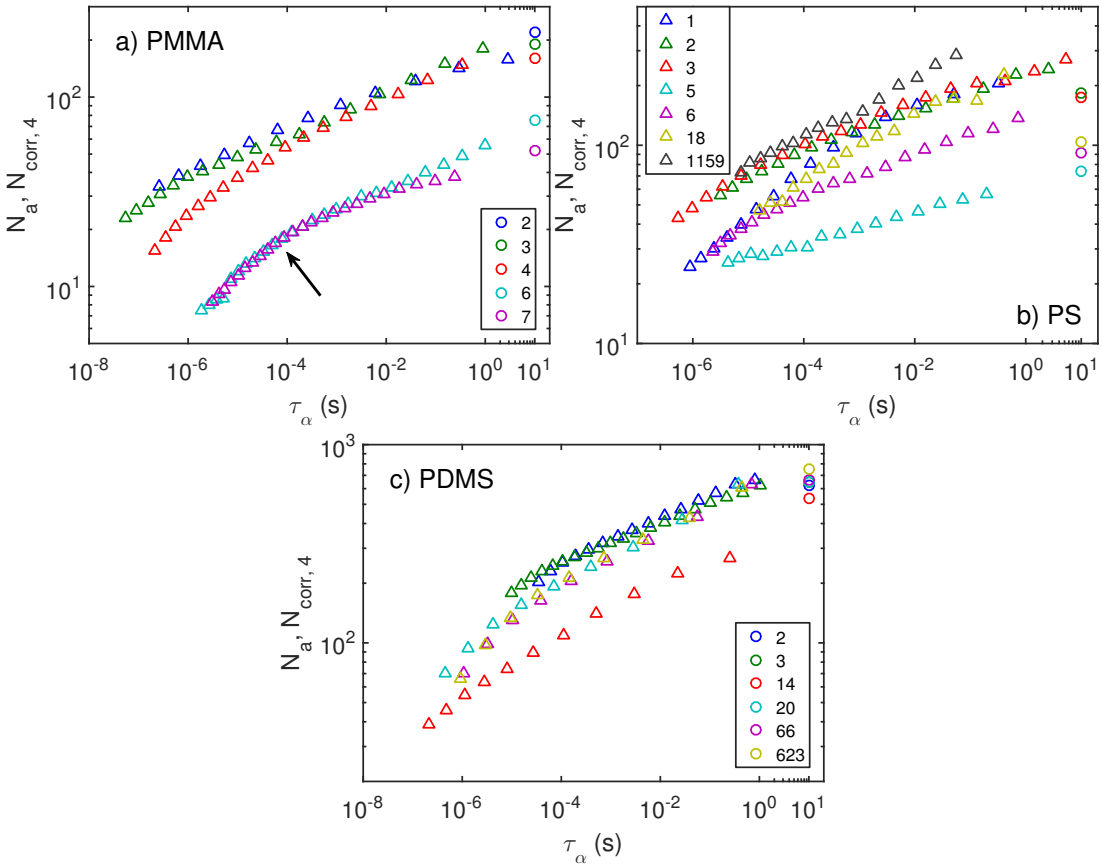

Figure 4.23: N_a (circles) and $N_{corr,4}$ (triangles) for PMMA (a), PS (b), and PDMS (c) as a function of τ_α. The legend indicates degree of polymerisation (n).

For PMMA (figure 4.23 (a)), there is good agreement between N_a and $N_{corr,4}$ measures of the number of cooperative monomer units in the α relaxation. As stated in section 4.2.2, $N_{corr,4}$ was only calculated for oligomeric ($n = 2 - 7$) samples due to difficulties accurately determining the shape of the α relaxation response due to a strong β relaxation response relative to the α relaxation in BDS. This was likely an issue for higher M PS samples also, whereby the presence of a high frequency wing alters the α response shape. For PDMS, no β relaxation response was apparent in BDS across the entire M range. Therefore, accurately determine the shape of the α response was not an issue. As such, there was good agreement between the values of N_a and $N_{corr,4}$ (figure 4.23 (c)).

PMMA and PS (figures 4.23 (a)and (b)) also show a distinct decrease in the number of cooperative monomer units in the α relaxation in region I. For PDMS, this appears less M dependent, although still clear. PS and PDMS also show the subsequent increase in regions II and III.

4.3.1 N_a from broadband dielectric spectroscopy

Saiter et. al.[221] suggested a technique to determine the size of the cooperative region using both TMDSC and BDS. They demonstrate that the response shape of isofrequency measurements of $c_P''(T)$ and $\epsilon''(T)$ are scalable. An example of this is shown in figure 4.24.

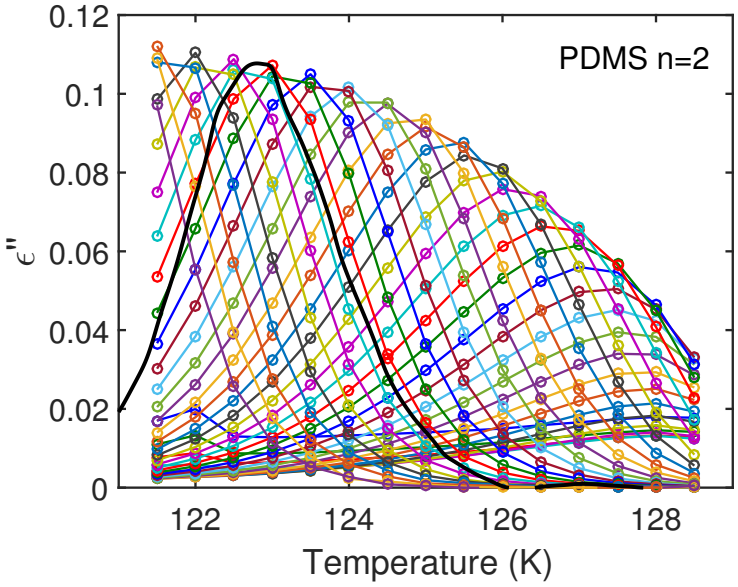

Figure 4.24: BDS measurements of the ϵ'' as a function of temperature for PDMS n=2. Alternating colours are isofrequency measurements. The solid black curve is c_p'' rescaled from TMDSC ($P = 60s$) measurement.

Figure 4.24 shows $\epsilon''(T)$ as a function of temperature, with TMDSC (P=60s) scaled to this data. This illustrates that both $c_P''(T)$ and $\epsilon''(T)$ exhibit similar response shapes. Therefore, this approach suggests that the same Gaussian fitting routine can be carried out in order to determine T_α and δT, and obtain the size of the cooperative region, as outlined in section 4.1, using BDS. Due to the broad frequency range of BDS, this yields the size of the cooperative region over a much wider timescale range than what would normally be accessible using TMDSC.

Unfortunately, this technique relies on a narrow temperature resolution in BDS measurements. Typically, BDS measurements were performed every 2K (with the exception to PDMS n=2 and 3, that were performed every 0.5K), which was generally insufficient in providing a reliable shape of the response in the temperature domain. However, the ability to describe both BDS and TMDSC with the same functional response shapes suggest that the TTS/KWW assumptions of both N_a (equation 4.46) and $N_{corr,4}$ (equation 4.43) should be directly comparable.

4.4 Molecular cooperativity of the α relaxation from oligomer to polymer

Using both TMDSC and BDS, the number of cooperative units were determined as a function of τ_α (shown in figure 4.23) for a chain-length series of PMMA, PS, and PDMS. This section will focus on TMDSC measurements of the size of the cooperative region, as this is measure of the number of cooperative units at the same α relaxation timescale ($\tau_\alpha \approx 10$s, with a modulation period of $P = 60$s). For the more fragile polymers (PMMA and PS), there was a distinct decrease of N_a with increasing M in region I, followed by a levelling out in regions II and III (shown in figure 4.13 (a) and (b)). For the less fragile and more flexible PDMS, the number of cooperative units was more level across all three three M regions (shown in figure 4.13 (c)). The number of units involved in the α relaxation in PDMS was also higher than for PMMA and PS across the entire M range.

As well as the number of monomer units within the cooperative region, it was interesting to look at the number of oligomers/polymers involved, which was determined using equation 4.47.

$$N_p = N_a \frac{M_0}{M} \tag{4.47}$$

Equation 4.47 is simply the number of monomer units in the cooperative region (N_a) divided by the degree of polymerisation ($n = M/M_0$), where M is the molecular weight of the oligomer/polymer, and M_0 is the monomer molecular weight. For the three investigated polymer systems, this is shown in figure 4.25.

Figures 4.25 (a) and (b) show that for PMMA and PS there is a change in the power law dependence of N_p with increasing M at around the region I and II boundary. This behaviour can be described as $N_P \propto M^{-a}$, and in region I, this is described with approximate values of $a \sim 2.1$ and $a \sim 1.8$ for PMMA and PS respectively. In regions II and III, this power law behaviour changes to $a \sim 0.9$ and $a \sim -1.0$ for PMMA and PS respectively. Figure 4.25 (c) shows that for PDMS across the entire M range, this power law behaviour follows $a \sim -1.0$, which indicates that N_a is relatively invariant with M in these regions (apparent in figure 4.13 (c)). It is worth noting that N_p in this definition is not necessarily a

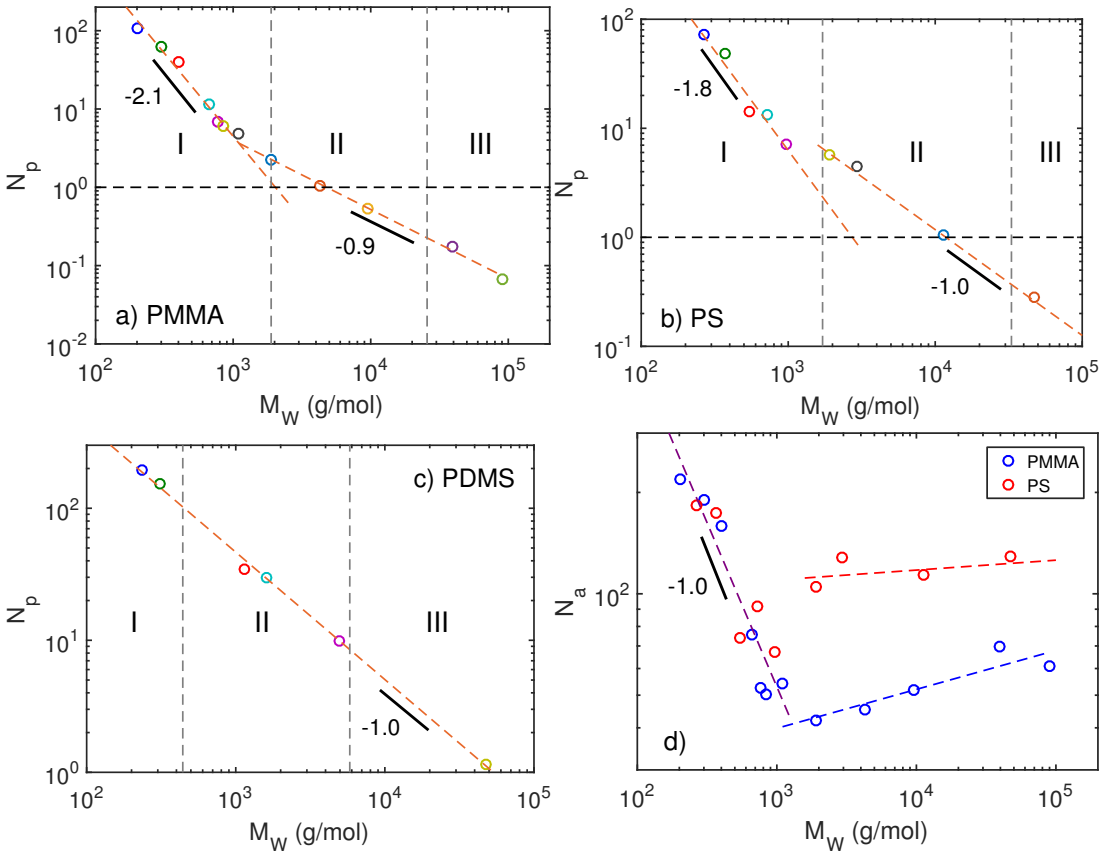

Figure 4.25: Number of oligomers/polymers in the cooperative region calculated from TMDSC ($P = 60s$) for (a) PMMA, (b) PS, and (c) PDMS M series. Orange dashed lines indicate a change in behaviour, regional boundaries indicated by vertical dashed lines, and horizontal dashed line is when $N_p = 1$. The number of monomers in the cooperative region is also shown for (d) PMMA and PS.

measure of the number of entire oligomers/polymers in the cooperative region at T_α, as that would assume that the α relaxation is entirely intramolecular, whereas this is unlikely to be the case.

Figure 4.25 (d) shows that N_a behaves approximately the same for PMMA and PS in region I, whereby $N_a \propto M^{-1}$, as indicated by the dashed purple line fitting both sets of data. However, there is a distinct difference in regions II and III between these samples, whereby PS has more cooperative monomers in the α relaxation (by a factor of ~ 2).

As outlined in section 1.2.3, Johari and Goldstein[48] noted that non-polymeric glass-forming materials exhibit a secondary relaxation. Due to the cooperative nature of this relaxation, it is often seen as a precursor to the α relaxation[222, 223]. This particular secondary relaxation is typically called the Johari-Goldstein β relaxation. The heterogeneous nature of this relaxation is the topic of much discussion[52, 53]. At low temperatures close to T_g, it has been suggested that there exists "islands of mobility", whereby some regions relax, while others are relatively immobile[54]. Fragiadakis and Roland[224] showed using MD simulations that, in the glassy state, the β relaxation in diatomic glass formers occur is these "islands of mobility", whereby some molecules relax completely, whereas others are immobile over a period ~ 500 times that of the β relaxation timescale. In contrast to diatomic glass formers, they showed that a polymeric glass former appeared to be dynamically homogeneous.

We suggest that a similar changeover in behaviour may extend to the α relaxation at T_g. Figure 4.25 shows that in region I, multiple molecules are involved in the α relaxation ($N_p > 1$), i.e. the α relaxation is largely an intermolecular process. However, in regions II and III for PMMA and PS (figure 4.25 (a) and (b)), fewer monomers are involved than in a single polymer ($N_p < 1$), although these may be within different polymers. An extrapolation of the region I fit in figure 4.25 (a) and (b) for PMMA and PS intercepts $N_p = 1$ at approximately the molecular weight of the dynamic bead (M at the region I to II crossover). Therefore, the α relaxation may become more intramolecular, and for more fragile, less flexible polymers, once the dynamic bead has been established, the number of cooperative monomer units in the α relaxation does not increase significantly with increasing M.

In the case of PDMS, the number of cooperative monomer units in the α relaxation is larger than the molecule ($N_p > 1$) until region III, with the behaviour with increasing M described by a power law of $N_p \propto M^{-1.0}$. This suggests that the inter/intramolecular nature of the α relaxation in PDMS does not vary significantly with chain-length. However, as will be discussed in section 4.4.3, PDMS displays anomalous conformational behaviour, and therefore this cooperative behaviour may not be universal for all less fragile, more flexible polymers.

This measure of the size of the cooperative region of the α relaxation at T_g was compared to other dynamic properties, which will be outlined in the following sections, and compared in section 4.4.3.

4.4.1 Secondary relaxations

As discussed in section 1.2.3, secondary relaxation mechanisms faster than the α relaxation also occur in glass forming materials. These are labelled β, γ, δ, etc in order of appearance with increasing frequency (or decreasing temperature)[14].

As previously stated, PMMA is a type-C polymer, meaning that it contains a dipole moment in the side group, which is able to reorientate relatively independently of the polymer backbone[14]. The ester side group in PMMA contains a large dipole moment, and therefore these secondary relaxations in PMMA exhibits a strong dielectric response, and timescale data can be determined using BDS. In PMMA, β and γ relaxation modes are visible in both rheology and BDS. This β relaxation is generally attributed to some cooperative motion involving both the ester side group and the polymer backbone[139, 140]. Whereas the γ relaxation has been attributed to some more local reorientation[58].

Is PS, β and γ relaxation modes are weaker in both rheology and BDS than PMMA (the β relaxation is apparent as an additional high frequency flank of the α relaxation, rather than a separate, distinguishable, peak in $\epsilon''(\omega)$). NMR studies have suggested that the β relaxation in PS involves large phenol ring motions, whereas the γ relaxation is attributed to smaller, faster, motions of the phenol rings[225, 226], and by necessity, these side group motions are coupled to the backbone motions. However, a more recent study by Arrese-Igor et. al.[227]

determined, using Quasielastic Neutron Scattering (QENS), that large scale motions of the phenol rings do not occur at $T < T_g$.

As is typical of secondary relaxation modes, relaxation timescales (τ_β and τ_γ) exhibit Arrhenius behaviour[14], meaning that they can be described by an Arrhenius expression, shown in equation 4.48.

$$\tau = \tau_0 \exp\left(\frac{\Delta H}{RT}\right) \tag{4.48}$$

Here, ΔH is the activation enthalpy, R is the gas constant, and τ_0 is the relaxation rate at high temperatures. This is visualised by a straight line in an Arrhenius plot, with the slope being proportional to ΔH. For this PMMA chain-length series, this is shown in figure 4.26

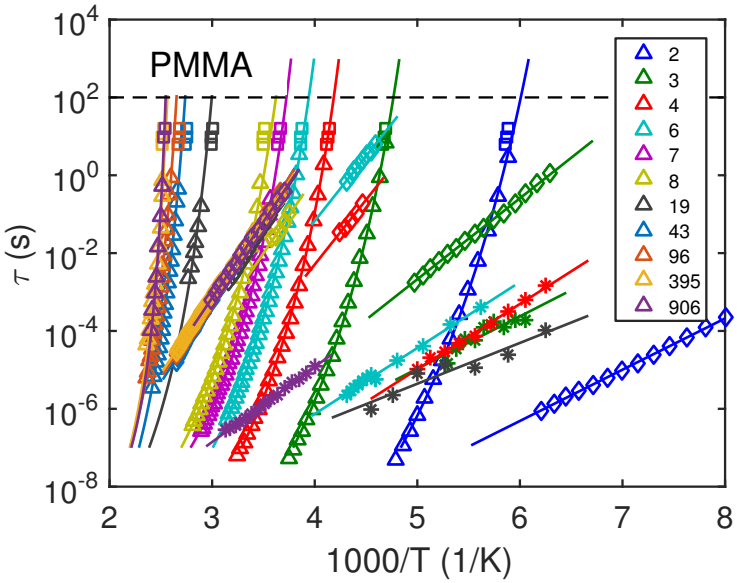

Figure 4.26: Arrhenius plot for PMMA showing α (triangles), β (diamonds), and γ (stars) relaxations from BDS, with VFT (α) or Arrhenius (β and γ) fits. TMDSC α relaxation data is also shown (squares). The legend indicates the degree of polymerisation (n).

Figure 4.26 shows α relaxation timescales with VFT fits, and the β and γ relaxations with Arrhenius fits for the PMMA chain-length series measured using BDS. From the Arrhenius fits to the $\tau_\beta(T)$ and $\tau_\gamma(T)$ data within the glassy state,

it is apparent that ΔH_β (which is proportional to the slope) increases with M for the n=2-8 samples; above this, ΔH_β is relatively constant. ΔH_γ is relatively invariant with M across the entire M range. This is shown clearly in figure 4.27.

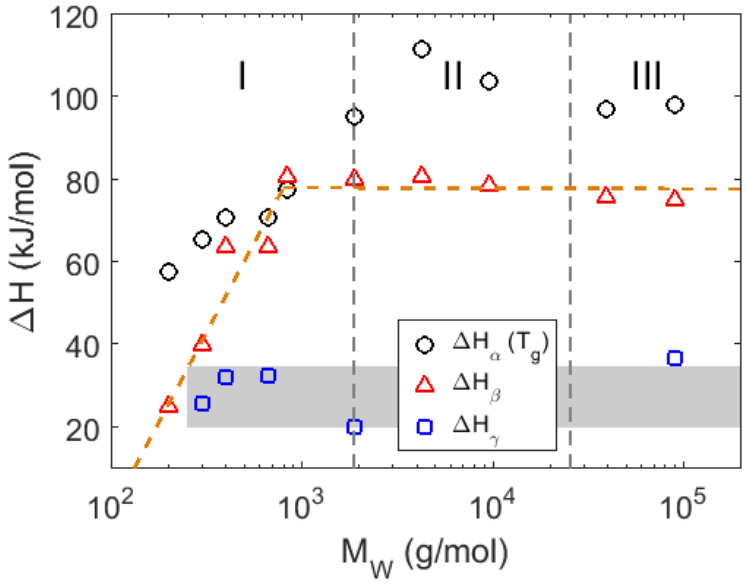

Figure 4.27: Activation enthalpies for α (calculated at T_g, to be discussed in section 4.4.2), β, and γ relaxations as a function of M for PMMA. Regional boundaries are indicated by dashed lines.

Figure 4.27 shows that ΔH_γ has no obvious trend with M. ΔH_β does exhibit regional behaviour, where it an increases in region I, and stabilises in regions II and III. Interestingly, ΔH_γ is approximately equal to ΔH_β for the lowest M sample, which suggests that this may be a similar relaxation mechanisms, and that the β relaxation grows out from a more fundamental γ relaxation as chain length increases.

Various connections between features of the α and β have been observed, which will be looked at in this work:

- A simple relation between ΔH_β and T_g has been observed for a variety of small molecular and polymeric systems[228].
- An extrapolation of $\tau_\beta(T)$ to higher T intersects $\tau_\alpha(T)$ at a certain timescale,

$\tau_{\alpha,\beta}$. This relates to the dynamic crossover point, has been shown to correlate to dynamic fragility, m.

- A correlation between the β relaxation timescale at T_g, $\tau_\beta(T_g)$, and the KWW stretching parameter, β_{KWW} has been observed for small molecular and polymeric systems[41].

Kudlik et. al.[228] determined that for a selection of glass forming materials, there is an empirical relation between ΔH_β (a feature of the β relaxation) and T_g (a feature of the α relaxation), shown in equation 4.49.

$$\Delta H_\beta = (24 \pm 3) R T_g \tag{4.49}$$

Where R is the gas constant. Ngai and Capaccioli[229] determined that this also holds for a variety of small molecular and long-chain polymer systems. However, nothing has been stated for intermediate M oligomers/polymers. For PMMA, this relation was tested across the M series in order to determine any discrepancy in the M range between simple glass former and polymer using equation 4.50.

$$K = \frac{R T_g}{\Delta H_\beta} \tag{4.50}$$

As previously stated, this value of 24 ± 3 was shown to hold for a variety of small molecular and polymeric materials. However, it may not necessarily hold for oligomers. Therefore, this value was replaced with the parameter K and was calculated for the PMMA M series, as shown in figure 4.28.

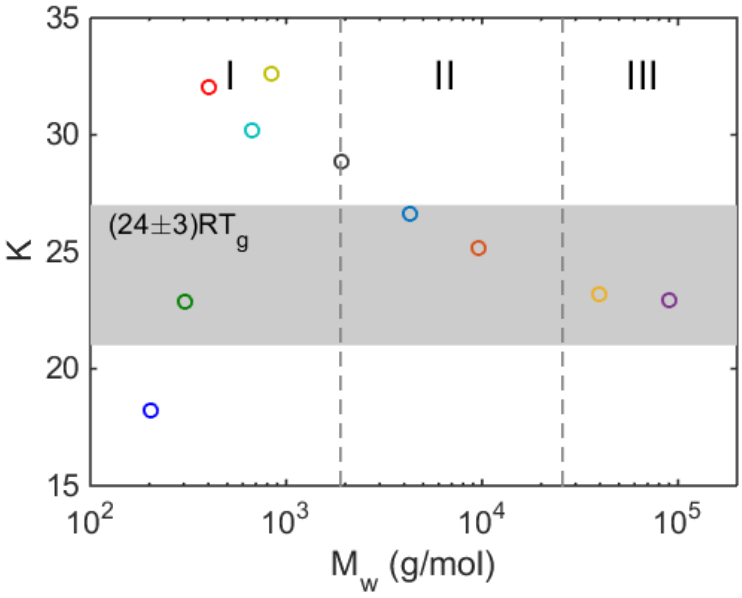

Figure 4.28: K parameter determined using equation 4.50 from BDS measurements of T_g and ΔH_β for PMMA M series. Shaded area indicates the prediction from equation 4.49. Regional boundaries are also indicated.

Figure 4.28 shows the K parameter increases in region I to a maximum value greater than 24 ± 3. In regions II it falls back into this boundary, whereup in region III is stabilises. Therefore, the approximation in equation 4.49 is only valid for small M PMMA (n$\sim$3) and PMMA in regions II and III. However, it does not seem to hold for oligomers at around the dynamic bead size (region I to II boundary).

$\tau_\beta(T)$ is this work was determined in the glassy state. In figure 4.26, an extrapolation $\tau_\beta(T)$ to higher T indicates a point where this merges with $\tau_\alpha(T)$, $\tau_{\alpha,\beta}$. It has been observed that there there are several changes in dynamic behaviour at this $\tau_{\alpha,\beta}$ transition, such as: i) a decoupling between translational and rotational diffusion below this temperature[55]; ii) a change in dielectric strength ($\Delta\epsilon$) behaviour of the α relaxation occurs above this temperature[56]; iii) and there is distinct change in VFT behaviour, which has been observed in various small molecular and polymeric systems[57]. The trend of $\tau_{\alpha,\beta}$ as M increases for PMMA is better visualised on a T_g normalised Arrhenius, or Angell[23], plot, as shown in figure 4.29.

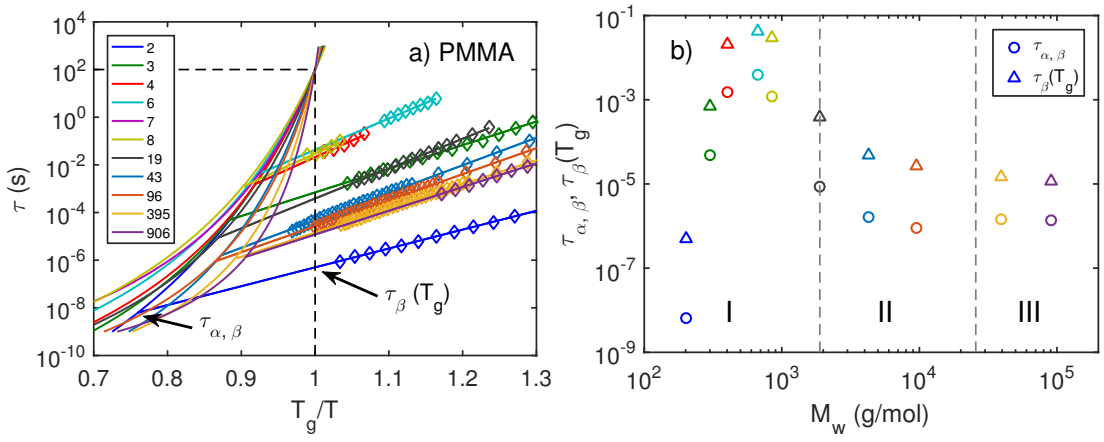

Figure 4.29: a) Angell plot displaying VFT fits of τ_α data, and τ_β data with Arrhenius fits extrapolated to where the two relaxation timescales are equal ($\tau_{\alpha,\beta}$). b) $\tau_{\alpha,\beta}$ (circles) and $\tau_\beta(T_g)$ (triangles) as a function of M, with regional boundaries indicated.

Figure 4.29 (a) and (b) show the similar regional behaviour of $\tau_{\alpha,\beta}$ (shown by the circles) and $\tau_\beta(T_g)$ (shown by the triangles), increasing in region I, and decreasing and stabilising in regions II and III. These two quantities have been shown to correlate to dynamic fragility, m, and the KWW stretching parameter, β_{KWW}[41] for small molecular and polymeric glass formers. However, these correlations fail across the entire PMMA chain-length series.

4.4.2 Activation enthalpy of the α relaxation

The relations between ΔH_β and T_g shown in figure 4.28, and $\tau_{\alpha,\beta}$ and $\tau_\beta(T_g)$ shown in figure 4.29 show similar regional M behaviour in PMMA. These quantities are links between the α and β relaxations.

In general terms, $\tau_\alpha(T)$ can be expressed as a thermally activated process, with a temperature dependent activation free energy, as expressed as equation 4.51.

$$\tau_\alpha(T) = \tau_0 \exp\left(\frac{\Delta G_\alpha(T)}{k_B T}\right) = \tau_0 \exp\left(\frac{\Delta H_\alpha(T)}{k_B T}\right) \exp\left(\frac{-\Delta S_\alpha(T)}{k_B}\right) \qquad (4.51)$$

Here, $\Delta G_\alpha(T)$ is the activation free energy (Gibbs free energy) of the α relaxation. This contains both an enthalpic ($\Delta H_\alpha(T)$) and entropic ($\Delta S_\alpha(T)$) contribution. Both for small molecular and polymeric glass formers the activation entropy can be non-zero[230]. However, if as a first estimate one assumes that this quantity is negligible, then an Arrhenius equation with a temperature dependent activation enthalpy is obtained, shown in equation 4.52.

$$\tau_\alpha(T) = \tau_0 \exp\left(\frac{\Delta H_\alpha(T)}{RT}\right) \tag{4.52}$$

At T_g ($\tau_\alpha = 100$s), equation 4.52 shows the simple relation shown in equation 4.53.

$$\Delta H_\alpha(T_g) \propto T_g \tag{4.53}$$

This is a simple proportionality between the activation enthalpy at T_g, and $\Delta H_\alpha(T_g)$, and T_g. Equation 4.50 indicates relationship between ΔH_β and T_g. Therefore the proportionality between $\Delta H_\alpha(T_g)$ and ΔH_β is of interest, defined in equation 4.54.

$$n_c = \frac{\Delta H_\alpha(T_g)}{\Delta H_\beta} \tag{4.54}$$

Where n_c is defined as the ratio of the activation enthalpies of the α and β relaxations. To investigate this, the value $\Delta H_\alpha(T_g)$ is needed to be obtained. Figure 4.26 shows that the α relaxation above T_g exhibits VFT behaviour, which can be described as Arrhenius behaviour with a temperature dependent activation enthalpy, $\Delta H_\alpha(T)$, as shown in equation 4.55.

$$\tau_\alpha(T) = \tau_0' \exp\left(\frac{DT_0}{T - T_0}\right) = \tau_0' \exp\left(\frac{\Delta H_\alpha(T)}{RT}\right) \tag{4.55}$$

Here, τ_0' contains both the prefactor τ_0, and the entropy contrition from the free energy. Once out of equilibrium (below $\sim T_g$), the temperature dependence of τ_α becomes Arrhenius, rather than VFT, due to the glass not being able to relax on experimental timescales. Casalini and Roland[231] demonstrated using BDS, that a decay in the dielectric strength ($\Delta\epsilon$) of the β relaxation over time corresponded to out of equilibrium α relaxation timescales. Using this method,

they determined the out of equilibrium α relaxation activation enthalpy (ΔH_α) for a PMMA $n = 19$ sample[76]. They showed that this agreed with a technique Hodge[232] proposed, whereby he derived an expression for describing the temperature dependence of the α relaxation in the glassy state, shown in equation 4.56.

$$\tau_\alpha(T) = \tau_0 \exp\left(\frac{DT_0}{T(1 - T_0/T_g)}\right) \tag{4.56}$$

This is an Arrhenius equation where τ_0, D, and T_0 are all parameters of the VFT expression describing $\tau_\alpha(T)$ in equilibrium, and is equivalent to equating the VFT and Arrhenius expressions exponents, as shown in equation 4.57.

$$\frac{DT_0}{T_g - T_0} = \frac{\Delta H_\alpha(T_g)}{RT_g} \tag{4.57}$$

It is apparent from equations 4.56 and 4.57 that ΔH_α is modulated by the high temperature prefactor of the VFT expression (τ_0), and T_g. Both of these values are extrapolations of the VFT expression, outside the range of a typical BDS measurement. Therefore, determining accurate values for τ_0 can be difficult, especially for higher T_g polymers (PS, PMMA, PC, etc), causing significant uncertainties when calculating values of ΔH_α using this assumption. Regardless of this uncertainty, this technique was used to calculate $\Delta H_\alpha(T_g)$ values for the α relaxation. These values are shown alongside ΔH_β and ΔH_γ for PMMA in figure 4.27. $\Delta H_\alpha(T_g)$ (shown by the circles) also appears to show regional behaviour, with an increase in region I, slightly increasing in region II (although this is difficult to say due to scatter), and stabilising in region III. Interestingly, at the region I to II boundary, ΔH_α and ΔH_β are approximately equal. This behaviour will be discussed further in section 4.4.3.

The coupling model (CM), as described in section 1.2.2, suggests a link between the out of equilibrium α relaxation and Johari-Goldstein (β) process[37, 42, 48], given by equation 4.58.

$$\tau_0 = t_c^n \tau^{1-n} \tag{4.58}$$

In equation 4.58, τ is the cooperative relaxation time (τ_α), t_c is a fundamental timescale of molecular motion ($\sim 2ps$), n is the coupling parameter, relating to

the KWW stretching parameter[94] ($\beta_{KWW} = 1 - n$), and τ_0 is the primitive relaxation time, taken as the timescale of the Johari-Goldstein β process (τ_β). Although the β relaxation in PMMA is a Johari-Goldstein process (it involves all atoms in the monomer unit[139]), this relation has been shown not to hold for either oligomeric or polymeric PMMA[233].

This work also showed that this relation does not hold for this PMMA M series, which would have connected directly measured values of τ_β, and β_{KWW} (shows in figure 3.15 (b)) to τ_α in the glassy state, and hence allowing the calculation of ΔH_α. Interestingly, while CM can sometimes, relatively well, describe the relationship of τ_β and τ_α in colloidal and simple molecular glass formers, it also applies to more flexible polymers such as polyisoprene[234, 235].

4.4.3 Correlations of cooperativity to dynamic behaviours

While regional M behaviour was visible in many quantities shown in this work (T_α, δT, Δc_P, N_a, $N_{corr,4}$, etc), three quantities in particular follow similar M behaviour in PMMA. These were:

- The cooperative lengthscale, ξ_a, defined as the cube-root of the volume of a cooperative region, V_a. As discussed in section 4.1, this was calculated using a technique proposed by Donth[165], from temperature fluctuations measured using TMDSC.
- The ratio of the activation enthalpies of the α and β relaxation, n_c, as discussed in section 4.4.2
- The K parameter, which is related to the proportionality between the activation enthalpy of the β relaxation, ΔH_β, and T_g. Similar behaviour was also seen in $\tau_{\alpha,\beta}$ and $\tau_\beta(T_g)$, which also connect the α and β relaxations.

As previously stated, these three behaviours outlined above show distinct regional behaviour, exhibiting a large change in region I, followed by a stabilisation (or slight change) in regions II and III. These were scaled to each other, and plotted in figure 4.30.

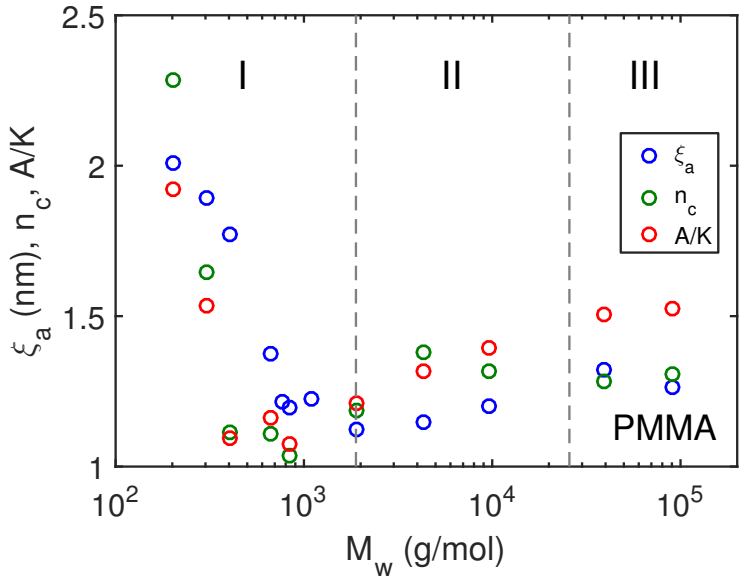

Figure 4.30: Length of the CRR (ξ_a), ratio of α and β activation energies (n_c), and scaled ratio of ΔH_β to T_g (A/K) as a function of M for PMMA.

Figure 4.30 shows the correlation between the lenthscale of the cooperative region at T_g with n_c and $1/K$. All three of these quantities exhibit comparable regional behaviour: decreasing with increasing M in region I, increasing relatively little in region II, and stabilising in region III.

Looking back at figure 4.27, ΔH_β increases in region I, implying an increased growth of cooperativity up the the dynamic bead size. In regions II and III, ΔH_β flattens out. Therefore, for $M > M_R$, the β relaxation is characterised by this lengthscale. At T_g, the number of correlated units are significant, and it is reasonable that the "cooperative" nature is captured in $\Delta H_\alpha(T_g)$. Thus, n_c gives a scale of this in bead units. Therefore, it is understandable that both K and n_c relate to some metric which gives information on the correlated nature of the α relaxation.

Due to the similarities between PMMA and PS, this behaviour may be applicable to more fragile, less flexible polymeric systems. However, PDMS was not an ideal system to study, as it is not a typical less fragile, more flexible polymeric system. As outlined in section 3.2.2, it has been shown using RIS simulations that PDMS forms look-like structures at the region I to II boundary[157], and

therefore these definitions may not be applicable to such a system. Therefore, this chain-length dependence of the number of correlated units in the α relaxation will also be investigated for propylene glycol dimethyl-ether (PPG-DME), which is considered to be a more standard less fragile, more flexible system

4.5 Conclusions

In this chapter, the number of cooperative units involved in the α relaxation was calculated for a chain-length series of PMMA, PS, and PDMS, ranging from dimer to fully entangled polymer, using two independent techniques: Using the complex permitivity measured with TMDSC to determine the size of the of the cooperative region[28, 195]; and using the complex permittivity measured with BDS to calculate the number of specially correlated units involved in the α relaxation[201, 212]. This work shows that:

- These two independent measures of the number of cooperative/correlated units in the α relaxation show good agreement when both could be applied.
- T_g for PMMA, PS, and PDMS showed regional behaviour with M. For PMMA and PS, this could not be described by a Fox-Flory[86] expression below M_R, although it could be PDMS. This suggests that the M dependence of T_g may be dependant of the number of chain-end in more less fragile/more flexible oligomers only.
- The heat capacity responses (T_α, δT, and $\Delta|c_P^*|$) of PMMA, PS, and PDMS all show similar regional behaviours, albeit more subtly in PDMS than PMMA or PS.
- The number of cooperative units in the cooperative region at T_g (defined as the temperature where $\tau_\alpha \approx 10s$) for PMMA, PS, and PDMS shows regional M behaviour, decreasing in region I, and stabilising (or possibly slightly increasing) in regions II and III. This is less obvious for PDMS, where this regional behaviour is much more subtle, if at all existent. This general behaviour has been seen in literature also for a PS[198], and a PnBMA[199] chain-length series.

- Both the number of cooperative units in the cooperative region at T_g, and dynamically correlated units across the τ_α range are higher in PDMS than PMMA and PS across the entire M range.

- For the more fragile/less flexible PMMA and PS, the number of cooperative units in the cooperative region at T_g decreases in region I ($M < M_R$). This is interpreted as a decrease in the intermolecular nature of the α relaxation as chain-length increases. Once the dynamic bead size has been established (M_R), the size of the cooperative region changes more weakly with increasing M. This suggests that the α relaxation may be more intramolecular at this point.

- For the less fragile/more flexible PDMS, the number of cooperative units in the cooperative region at T_g is more stable across all three regions. The number of correlated units is greater than the number of monomer involved in the α relaxation until approximately region III. Therefore the α relaxation is likely always intermolecular.

- In PMMA, secondary relaxation mechanisms (β and γ) were detectable using BDS. The β relaxation shows regional M behaviour, increasing in region I, and stabilising in region II and III. For the smallest sample ($n = 2$), this had the same activation enthalpy (ΔH_β) as the γ relaxation (ΔH_γ) across the M range. We suggest this may be the same processes, and the β relaxation forms from this more fundamental γ relaxation in region I.

- Around the region I to II boundary (M_R), ΔH_β no longer scales with T_g[228], but rather shows regional behaviour also: increasing in region I, and decreasing and stabilising in regions II and III for PMMA.

- The out of equilibrium activation energy of the α relaxation ($\Delta H_\alpha(T_g)$) was approximated[232] for PMMA, which also exhibited regional behaviour: Increasing sharply in region I, less so in region II, and stabilising in region III. Interestingly, $\Delta H_\alpha(T_g)$ was equal to ΔH_β at approximately M_R.

- Both the intersection of τ_α and τ_β ($\tau_{\alpha,\beta}$), and τ_β at T_g ($\tau_\beta(T_g)$) for PMMA show regional behaviour: increasing in region I, and decreasing and stabilising in regions II and III. These does not correlate across the entire M range with either dynamic fragility, m, or the KWW stretching parameter, β_{KWW}, which has been shown for small molecular liquids and long-chain polymers[41].

- The lengthscale of the cooperative region at T_g, ξ_a, correlated with the ratio of $\Delta H_\alpha(T_g)$ and ΔH_β, and also the ratio of ΔH_β and T_g. This suggests that the β relaxation plays a role is setting the scale of the dynamic bead.

4.5.1 Future work

Future work will include measuring the size of the cooperative region on a chain-length series of propylene glycol dimethyl-ether (PPG-DME). This is a more standard flexible polymeric system than PDMS, as it does not exhibit loop-like formation caused by the siloxane backbone.

Chapter 5

Decoupling of ion conductivity and the α relaxation in polymer systems

In chapters 3 and 4, results from broadband dielectric spectroscopy (BDS) measurements on different polymer systems spanning from small molecular glass former to polymer were analysed. This primarily focused on the temperature dependence of relaxation dynamics. However, along with the relaxation mechanisms, ionic conductivity was also apparent in the spectra, as shown in figure 3.8. This allowed us to look at how conductivity couples to α dynamics, in particular, how molecular weight, M, effects this coupling in polymer systems with different properties, such as T_g, m, etc. The link between diffusion and α dynamics in glass forming materials is not well understood[236]. It has become of increased interest recently due to the demand for safer, solid electrolytes for use in batteries. A better understanding of how ions diffuse through glass forming materials could provide the means to produce an amorphous electrolyte which is both mechanically strong, while also allowing for adequate ionic conductivity. Therefore, the effect of chain-length and flexibility reflected through T_g and m on ionic conductivity is explored in this chapter.

A Li-ion battery consists of two electrodes, a positive anode and negative cathode, which are are in contact with current collectors. Between the two electrodes is an electrolyte material, and a mechanical separator. When the battery

discharges, oxidation takes place at the anode, and lithium ions migrate through the electrolyte towards the cathode, whereupon reduction takes place. This movement of charge allows for electrons to flow in the opposite direction through a circuit. When charging, this process is reversed[237]. While liquid electrolytes with mechanical spacers may be adequate for technologies such as mobile phones, the increasing demand from applications such as electric cars is pushing the need for safer electrolyte materials. Solid electrolytes which can be used in modern Li-ion batteries are the holy grail of battery technology, because not only would a solid electrolyte be safer, but also becuase they would remove the need for costly mechanical spacers. However, with increased mechanical rigidity, tends to come reduced ion mobility. In order for an electrode material to be suitible for use in batteries, amongst other things, they need to have[238, 239]:

- Good ionic conductivity over wide operating temperatures ($\sigma_{Li} > 10^{-3}$S/cm between $-40 < T < 90°$C).
- Low electron conductivity ($\sigma_e < 10^{-10}$S/cm).
- High cation mobility, if possible with a transference number $\sigma_{Li}/\sigma \approx 1$, i.e. low anion mobility.
- Appropriate mechanical properties, e.g. high mechanical modulus, deforms elastically, and is not brittle.
- The ability to form good interfacial contact with electrodes.
- Chemical stability with respect to the electrode materials over wide temperature ranges (electrochemically stable).
- Relevantly easy and cheap to process.
- Low toxicity and safe.

Various kinds of solid electrolyte materials have been tried, examples of these include: (i) Gel electrolytes, which have large ion mobility, are free standing and relatively flexible. However, they are comprised of a large amount of solvent, and therefore they tend not to be mechanically strong. The solvent itself tends to

have a low vapour pressure, and therefore the conductivity decreases as solvent is lost[240]; (ii) Ceramic electrolytes, which have large mechanical modulus and thermal stability, however they tend to lack in other respects, for instance, requiring high temperatures to operate[241], or are brittle[242]; (iii) Solid polymer electrolytes, which tend to be mechanically suited for batteries. However, these usually have low ionic conductivity[243, 244].

As previously stated, one of the biggest issues in solid polymer electrolytes (SPE) is the lack of sufficient ionic conductivity. One of the most commonly studied polymer electrolyte material is that of poly(ethylene oxide) (PEO)[238]. This is due to he fact that: it readily dissociates lithium salts, it is electrochemically stable, and it is cheap and safe. However, due to high crystallinity, it often lacks the required ion conductivity, especially at low temperatures. Modifications of PEO, such as the addition of plasticisers, or blending it with another polymers yield improved conductivity, but often effect other properties[245].

Polymers have relatively slow α dynamics due to chain connectivity, and therefore the coupling between this and conductivity leads to poor ionic conductivity. Therefore, decoupling between α dynamics and conductivity is important for polymer electrolytes. In polymer systems such as PEO, conductivity is strongly coupled to the α relaxation[246], i.e. a change in the characteristic α relaxation timescale, τ_α, leads to a proportional change in ionic conductivity, σ. However, Agapov and Sokolov[247] have shown that some long-chain polymer systems exhibit a decoupling between these two mechanisms. This decoupling was more apparent in more higher T_g, fragile polymers such as poly(methyl methacrylate) (PMMA) and polycarbonate (PC), than for lower T_g, less fragile polymers such as PEO and poly(vinylidene chloride) (PVDC). In non-polymeric liquids, it is well known that ion diffusion couples to viscosity (and therefore α dynamics)[248, 249], and that, as previously mentioned, for long-chain PMMA there is significant decoupling.

Therefore, an interesting question arises; at what point does decoupling occur as the chain-length in PMMA increases? It is worth noting that pure PMMA is not a good electrolyte material, but is still as ideal system to study considering the strong decoupling at the long-chain limit, and that it has been shown to readily

dissolve lithium salts[250–252]. Along with PMMA, two low T_g, less fragile chain-length polymer systems were also studied. These were two poly(propylene glycol) systems, one with methoxy end-groups (PPG-DME), and one with hydroxyl end-groups (PPG). PPG is structurally similar to PEO, which also readily dissolves lithium salts, whereby the lithium ions coordinate to the ether oxygen in polymer backbone[253]. An advantage of studying PPG in this work is that, unlike PEO, it is easy to avoid crystallisation, so both conductivity and α dynamics can be determined without any influence from semicrystallinity. The sample specifications of these systems are shown in figure 5.1 and table 5.1.

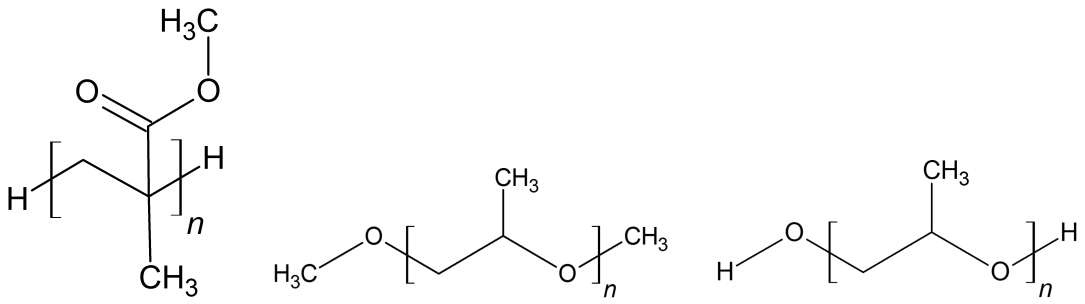

Figure 5.1: From left to right: PMMA, PPG-DME, and PPG molecules. The end groups reported by the manufacturer are also shown..

PMMA			PPG-DME			PPG		
n	M_W (g/mol)	PDI	n	M_W (g/mol)	PDI	n	M_W (g/mol)	PDI
2	202	1.00	2	150	1.00	2	124	1.00
3	302	1.00	3	196	1.00	3	170	1.00
4	402	1.00	7	380	1.02	4	216	1.00
6	660	1.21	16	794	-	7	354	1.02
7	771	1.18	32	1530	-	70	3252	1.05
8	840	1.44						
19	1900	1.10						
43	4300	1.05						
96	9590	1.05						
395	39500	1.04						
906	90600	1.04						

Table 5.1: Specifications of PMMA, PPG-DME, and PPG samples used in this work. The PDI was unknown for PPG-DME $n = 16$ and 32.

Figure 5.1 shows, from left to right, the monomers of PMMA, PPG-DME, and PPG. These have monomer molecular weights of; M_0=100g/mol for PMMA, and 58g/mol for both PPG-DME and PPG. The manufacturer reported PMMA to be proton terminated, PPG-DME is methoxyl terminated, and PPG is hydroxyl terminated. Table 5.1 shows the degree of polymerisation, n, the weight average molecular weight, M_W, and the polydispersity index (PDI) of the sample used in this work, as characterised by the supplier. PMMA samples were purchased from Polymer Standards Service (PSS), and were used as received, with the exception of PMMA $n = 6 - 11$, which were heated far above T_g in a vacuum oven for at least 24 hours to remove any solvent remaining from the manufacturing process (the other samples in this series were tested to be fine). PPG-DME and PPG samples were originally sourced from Aldrich, Fluka, and Polysciences[38, 254]. In these results, PPG n=70 will also be included in the analysis of PPG-DME, as it is considered that this molecule is long enough that hydrogen bonding of the hydroxyl end-groups yields negligible effects, and that true PPG-DME n=70 would have comparable dynamics.

As previously stated, the coupling between σ and τ_α, as a function of both polymer system and chain-length was the focus of this work. Both σ and τ_α were measured simultaneously as a function of temperature using broadband dielectric spectroscopy (BDS). It was found that the decoupling of these two properties exhibits regional molecular weight, M, behaviour in PMMA. This regional behaviour has been seen previously in a variety of different polymer systems[134, 135, 155], whereby T_g exhibits distinct M behaviour between three regions. Samples in region I (the lowest M samples) were coupled, and become more decoupled with increasing M in region II (the intermediate M samples), up until a maximum at in region III, where the decoupling becomes invariant with M. However, neither PPG-DME or PPG exhibited such M behaviour, and σ and τ_α were coupled across the M range measured. This is consistent with Agapov and Sokolov[247], where they showed that these properties are coupled for low T_g, less fragile, long-chain polymers. In BDS, chain dynamics are also accessible for PPG-DME and PPG due to these being type-A polymers, whereby dipoles are oriented along the polymer backbone[14]. σ and the chain mode relaxation time, τ_n, were also shown to correlate, which is consistent with the correlation between τ_α and τ_n, as discussed in section 3.5.2. Along with these polymer systems, a few examples of small molecular glass formers were also looked at, which also displayed strong coupling between σ and τ_α.

5.1 Dielectric determination of τ_α and σ

DC ionic conductivity is defined by the sum of mobilities of the free ions in a system[6], as shown in equation 5.1.

$$\sigma = \sum_i n_i \mu_{q,i} q_i \tag{5.1}$$

Where σ is the DC ionic conductivity, and n_i, $\mu_{q,i}$, and q_i are the number density, mobility, and charge of a specific charged species, i. For simplicity, this can also be expressed as an average mobility of all ions, i.e. $\sigma = n\mu_q q$, where n, μ_q, and q are the average number density, mobility, and charge of all charged species. Mobility

of an ion with charge q is related to the diffusion coefficient, D, according to the Einstein relation, shown in equation 5.2.

$$\mu_q = \frac{Dq}{k_B T} \tag{5.2}$$

Here, D is the self diffusion coefficient, and $k_B T$ is thermal energy. In turn, according the the Stokes-Einstein relation, D relates to viscosity, η, as shown in equation 5.3.

$$D = \frac{k_B T}{6\pi\eta r} \tag{5.3}$$

Where r is the hydrodynamic radius of the diffusing ions. Equations 5.1, 5.2, and 5.3 yield a relation between conductivity and viscosity, known as the Walden rule[249, 255], as shown in equation 5.4.

$$\Lambda\eta = \text{constant} \tag{5.4}$$

Here, Λ is the molar conductivity ($\Lambda = \sigma/n$). According to this rule, a log-log plot of Λ against $1/\eta$, or $1/\tau_\alpha$, which is related to viscosity through $\eta = G_\infty \tau_\alpha$[15], should yield a straight line with a slope of 1. This is known as a Walden plot, and an example of this is shown in figure 5.2.

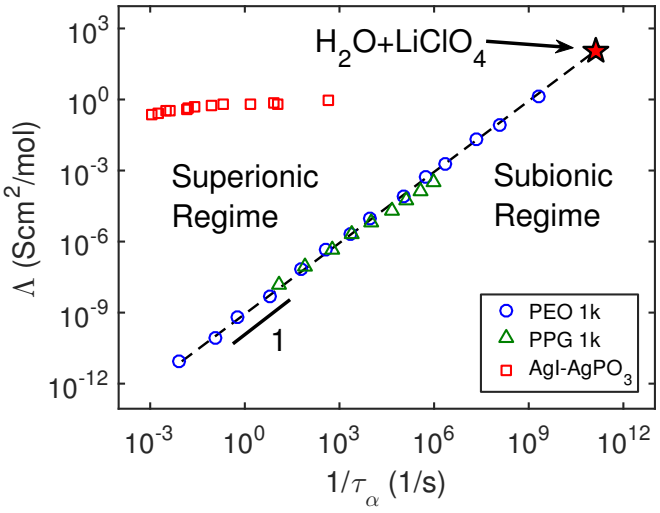

Figure 5.2: Example of a Walden plot, with molar ionic conductivity, Λ, against inverse α relaxation timescale, $1/\tau_\alpha$. Superionic and subionic regimes are indicated. PEO 1k, PPG 1k, AgI-$AgPO_3$, and the H_2O+$LiClO_4$ reference point are from literature[6].

In a Walden plot, a system which falls onto a straight line with a slope of 1 indicates coupling between conductivity and α dynamics (such as PEO 1k and PPG 1k in figure 5.2), i.e. obeying the Walden rule, shown in equation 5.4. The gray dashed line in figure 5.2 passes through a reference point. This is a dilute salt (in this case lithium perchlorate ($LiClO_4$)[246]) aqueous solution, which assumes complete ion dissociation, i.e. all Li cations and ClO_4 anions are contributing towards conductivity. This defines superionic and subionic regimes above and below this ideal line (which are not that greatly affected by the choice of reference[6]). Materials that exhibit a different coupling between conductivity and α dynamics, or fail to dissociate ions, may fall into the subionic regime. However, materials where conductivity is decoupled from α dynamics may fall into the superionic regime (such as AgI-$AgPO_3$ in figure 5.2). This superionic scenario is key in finding an amorphous SPE which is both mechanically strong, but also allows for the ionic transport, which may be coupled to some other relaxation mechanism.

This decoupling between σ and τ_α is generally observed as a slope of less than 1 on the Walden plot (figure 5.2). This behaviour is described by the "fractional"

Walden rule[256], shown in equation 5.5.

$$\Lambda\eta^\gamma = \text{constant} \tag{5.5}$$

This is the Walden rule (equation 5.4), with an additional decoupling parameter, γ, which describes the slope on the Walden plot. For decoupled systems, this values is between $0 < \gamma < 1$, where values closer to 1 indicate more coupling between σ and τ_α.

In order to determine this decoupling parameter, the complex permittivity needed to be measured at different temperatures where both the α relaxation and ionic conductivity could be distinguished.

5.1.1 Complex permittivity measurements

In order to determine both $\sigma(T)$ and $\tau_\alpha(T)$, the frequency dependent complex permittivity was measured at discrete temperatures. The complex permittivity is defined in equation 5.6.

$$\epsilon^*(\omega) = |\epsilon^*|(\omega)\mathrm{e}^{-i\delta(\omega)} = \epsilon'(\omega) - i\epsilon''(\omega) \tag{5.6}$$

The complex permittivity, $\epsilon^*(\omega)$, is separated into a real ($\epsilon'(\omega)$), and imaginary ($\epsilon''(\omega)$) component. As discussed in section 2.2, measurements of $\epsilon^*(\omega)$ were performed using broadband dielectric spectroscopy (BDS), using a Novocontrol Alpha-A analyser. At any temperature, both conductivity and relaxation mechanisms (α, β, γ, etc) may be visible in $\epsilon^*(\omega)$. As discussed in section 3.2.1, each temperature is fitted with a superposition of different functions, as shown in equation 5.7.

$$\epsilon^*(\omega) = \frac{-i\sigma}{\omega} + \sum_{j=1}^{N} \frac{\Delta\epsilon_j}{(1 + (i\omega\tau_{HN,j})^{\alpha,j})^{\beta,j}} + \epsilon_\infty \tag{5.7}$$

Here, $\epsilon^*(\omega)$ at a particular temperature can be described as a sum of Havriliak-Negami (HN) expressions[109], each describing a relaxation mechanism, and a conductivity contribution. From the HN fits, τ_{HN} relates to the characteristic relaxation time (the inverse of the ϵ'' peak frequency, $\tau_p = 1/\omega_p$) by equation 5.8[14].

$$\frac{1}{\tau_p} = \frac{1}{\tau_{HN}} \left[\sin \frac{\alpha\pi}{2+2\beta} \right]^{1/\alpha} \left[\sin \frac{\alpha\beta\pi}{2+2\beta} \right]^{-1/\alpha} \tag{5.8}$$

Using this fitting procedure, the $\epsilon^*(\omega)$ responses of conductivity and the α relaxation (and other relaxation mechanisms) can be isolated from each other. Therefore, σ and τ_α (τ_p relating to the α relaxation) can be obtained when both are apparent in the spectra. It is clear from equation 5.7 that conductivity only manifests in the imaginary of the permittivity, $\epsilon''(\omega)$, shown once again in equation 5.9.

$$\epsilon''(\omega) = \frac{\sigma}{\omega} \tag{5.9}$$

This is visible as a low frequency power behaviour (a slope of -1 on a log-log plot) in $\epsilon''(\omega)$. Therefore, fitting equation 5.8 to $\epsilon''(\omega)$ only yields both σ and τ_α. An example of this fitting procedure with multiple components is shown previously in figure 3.8.

5.2 The α relaxation and DC conductivity

As stated in section 1.2.1, $\tau_\alpha(T)$ is commonly described by Vogel-Fulcher-Tammann (VFT)[17–19] behaviour, as shown in equation 5.10.

$$\tau_\alpha(T) = \tau_0 \exp\left(\frac{DT_0}{T - T_0}\right) \tag{5.10}$$

Where τ_0 is the relaxation time at high temperatures, D is the strangth parameter, and T_0 is the so-called Vogel temperature, where $\tau_\alpha(T)$ diverges in equilibrium. Conductivity also obeys VFT behaviour[257], as shown in equation 5.11.

$$\sigma(T) = \sigma_0 \exp\left(\frac{-D_\sigma T_{0,\sigma}}{T - T_{0,\sigma}}\right) \tag{5.11}$$

By definition, if τ_α and σ are coupled, the VFT parameters D and T_0 in both equations 5.10 and 5.11 will be the same, i.e. $D = D_\sigma$ and $T_0 = T_{0,\sigma}$. For the PMMA M series, $\tau_\alpha(T)$ and $\sigma(T)$ from BDS are shown in figure 5.3.

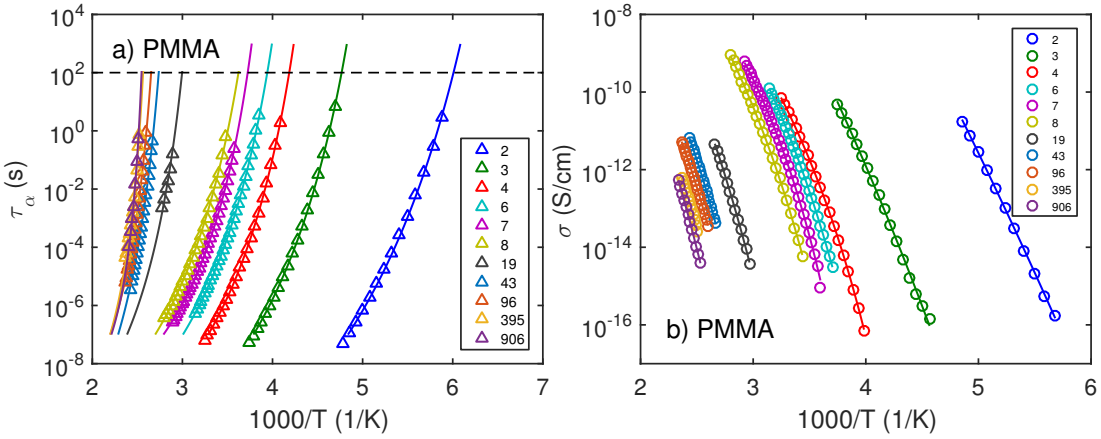

Figure 5.3: PMMA Arrhenius plots: a) $\tau_\alpha(T)$, with VFT fits (from equation 5.10). The temperature where $\tau_\alpha = 100$s (dashed line) is commonly taken as the T_g. b) $\sigma(T)$, with VFT fits (from equation 5.11). The legends indicate the degree of polymerisation, n.

As previously discussed in section 3.2.1, figure 5.3 (a) shows that $\tau_\alpha(T)$ determined from the peak frequency in ϵ'' exhibits VFT behaviour (equation 5.10) across the entire M range. T_g (defined as the temperature where $\tau_\alpha = 100$s) increases with M[86], as shown previously in figure 3.13. Dynamic fragility, m, also shows M variation in PMMA. This is defined in equation 5.12.

$$m = \left.\frac{\mathrm{d}\log\tau_\alpha}{\mathrm{d}(T_g/T)}\right|_{T=T_g} = \frac{\ln(100/\tau_0)^2 + D\ln(100/\tau_0)}{D\ln(10)} \tag{5.12}$$

This shows that m is defined as the slope of $\tau_\alpha(T)$ at T_g in a T_g normalised Arrehnius (Angell) plot[23]. This m variation with M is shown previously in figure 3.14.

Figure 5.3 (b) shows that $\sigma(T)$ also exhibits VFT behaviour (equation 5.11). This shows that for a particular sample, σ increases with increasing temperature, which is consistent with the fact that as temperature increases, ion mobility also increases. The conductivity, although not normalised by number density of free ions, also decreases with increasing M. The coupling of τ_α to σ across this M range for PMMA will be explored in section 5.2.1.

The data for the M series of PPG-DME and PPG used in this work has been published previously[254, 258], but was re-analysed in order to obtain conductivity. For these samples $\tau_\alpha(T)$ data is shown in figure 5.4.

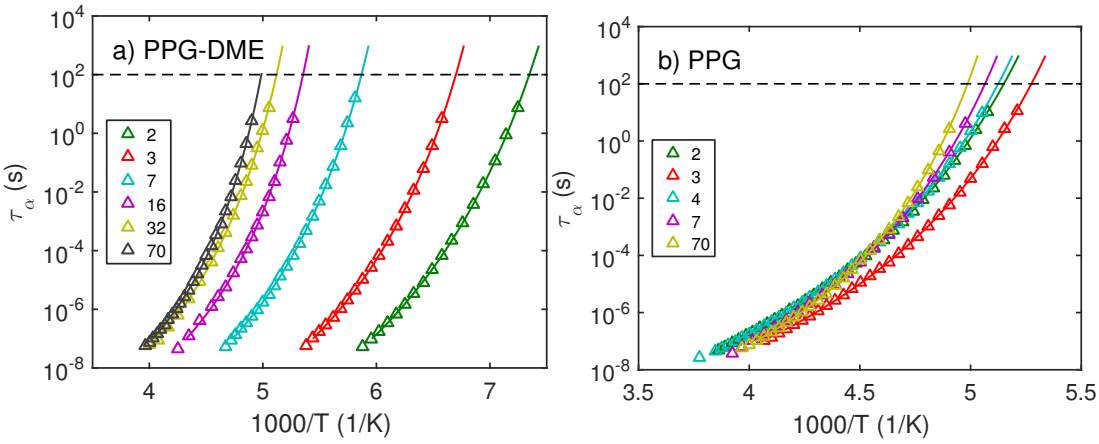

Figure 5.4: Arrhenius plots showing $\tau_\alpha(T)$ for PPG-DME (a) and PPG (b) M series (with VFT fits, from equation 5.10). The temperature where $\tau_\alpha = 100$s (dashed line) is commonly taken as the T_g. The legends indicate the degree of polymerisation, n.

Figure 5.4 shows that $\tau_\alpha(T)$ for both PPG-DME (a) and PPG (b) M series are described by a VFT expression, as described by equation 5.10. The PPG-DME M series in figure 5.4 (a) shows an increase in T_g with increasing M. However, the PPG M series in figure figure 5.4 (b) shows that $\tau_\alpha(T)$, and therefore T_g, are relatively invariant with M. This difference in chain-length dependence of the α dynamics between methoxyl (PPG-DME) and hydroxyl (PPG) terminated PPGs is well documented[150, 254, 259]. This is attributed to the fact that the hydroxyl groups in PPG allow for hydrogen bonding at the chain ends, which effectively leads to longer chains. PPG is an example of a type-A polymer, whereby dipoles are oriented along the polymer backbone[14], as such chain dynamics are also visible with BDS. $\tau_\alpha(T)$, along with the relaxation time of chain modes, $\tau_n(T)$, are shown in Angell plots in figure 5.5 for PPG-DME and PPG.

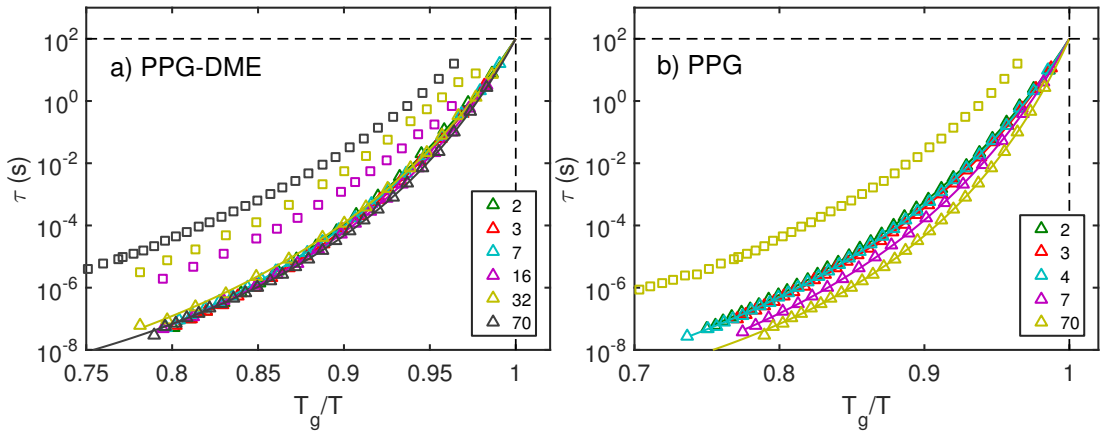

Figure 5.5: T_g normalised Arrhenius (Angell) plots for PPG-DME (a) and PPG (b) M series. Triangles represent τ_α data (with VFT fits from equation 5.10), and squares represent τ_n data. The legends indicate the degree of polymerisation, n.

Figure 5.5 (a) shows that m, defined as the slope of τ_α (triangles) at $T_g/T = 1$ from equation 5.12, has no significant M dependence for PPG-DME. Whereas figure 5.5 (b) shows a decrease in m with increasing M for PPG[258]. For higher M samples, chain modes become visible as an additional, low frequency relaxation mode in $\epsilon^*(\omega)$, and therefore $\tau_n(T)$ (squares) can be determined from fitting in the same manner as for $\tau_\alpha(T)$. All of the samples in this series are unentangled, and therefore $\tau_n(T)$ represents the longest Rouse time, as outlined in section 1.3.2, whereby this is expected to increase as $\tau_n \propto M^2$[60].

The conductivity measured for the PMMA, PPG-DME, and PPG M series was due to charged species (ionic impurities) already present in the sample, rather than specific ions introduced. For this reason, conductivity values were relatively low ($10^{-16} < \sigma < 10^{-10}$S/cm). This will be discussed further in section 5.2.2.

5.2.1 The coupling of τ_α and σ

From the measurements of $\tau_\alpha(T)$, $\tau_n(T)$, and $\sigma(T)$, the decoupling between these could be determined for the PMMA, PPG-DME, and PPG chain-length series. As shown in equation 5.5, a decoupling between σ ($\propto \Lambda$, although we do not know the ion concentration) and τ_α ($\propto \eta$) results in a power law slope of less

than $0 < \gamma < 1$ in a Walden plot[256], shown in figure 5.2. For the PMMA chain-length series, σ was plotted against $1/\tau_\alpha$ in order to determine any M dependence on γ (γ_α). This is shown in figure 5.6.

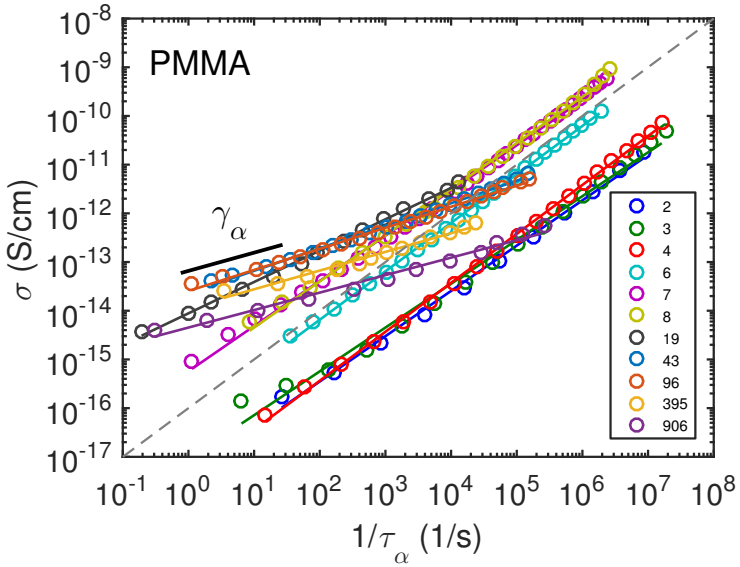

Figure 5.6: Un-normalised Walden plot of σ against $1/\tau_\alpha$ determined from BDS for PMMA M series. The gray dashed line represents a slope of 1, and γ_α is the decoupling exponent of each data set. The legend indicates the degree of polymerisation, n.

Figure 5.6 shows an un-normalsied Walden plot of σ against $1/\tau_\alpha$ for the PMMA M series. The decoupling parameter, γ_α, is the slope in this plot, and is specifically defined by equation 5.13.

$$\sigma \propto \tau_\alpha^{-\gamma_\alpha} \tag{5.13}$$

As outlined in section 5.1, $\gamma_\alpha = 1$ indicates a direct relationship between conductivity and α dynamics via the Stokes-Einstein relation. As mentioned previously, this has been shown to hold for small molecular liquids[248, 249] and less fragile, low T_g polymers, such as PEG[247]. For $0 < \gamma_\alpha < 1$, this suggests decoupling between the mechanisms which dictate ion diffusion and the α relaxation. In figure 5.6, $\gamma_\alpha \sim 1$ for PMMA oligomers where $n < 8$. Therefore, these mechanisms are coupled, which is consistent with other small molecular systems. However,

for $n > 8$, these mechanisms begin to decouple, as visualised by a decrease in γ_α with increasing M. Eventually this decoupling saturates at high M. γ_α as a function of M for PMMA is shown in figure 5.7.

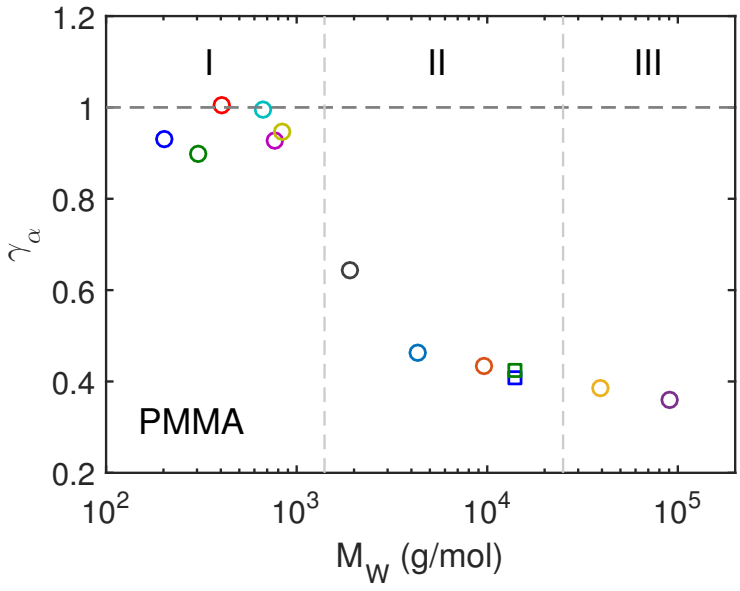

Figure 5.7: The decoupling parameter, γ_α, as a function of M for PMMA. Circles: γ_α values corresponding to figure 5.6. Squares: γ_α values corresponding to PMMA $n = 140$ with $LiBF_4$ salt (discussed in section 5.2.2).

As discussed in section 3.2.2, T_g as a function of M can be split into different regions, which has been seen for a variety of polymer systems[134, 135, 155]. The region I to II boundary is attributed to the onset of polymer behaviour, and is approximately that of the dynamic bead size, M_R, and the region II to III boundary is approximately at the critical entanglement, M_c, in PMMA. These regional boundaries defining this T_g behaviour are also shown by the gray dashed lines in figure 5.7. As with other properties shown in this thesis (T_g, m, N_a, etc), γ_α also exhibits this regional behaviour. In region I, $\gamma_\alpha \sim 1$, which is consistent with the behaviour of other small molecular liquids[248, 249]. However, in region II γ_α decreases from $0.4 \lesssim \gamma_\alpha \lesssim 1$, therefore displaying greater decoupling between α relaxation dynamics and ion diffusion with increasing M. In region III, the M dependence of γ_α is stabilised at $\gamma_\alpha \sim 0.4$. Agapov and Sokolov[247] correlated

the degree of decoupling with m and T_g for a variety of long-chain polymers. To investigate this behaviour for the PMMA M series, γ_α was plotted against m and T_g, shown in figure 5.8.

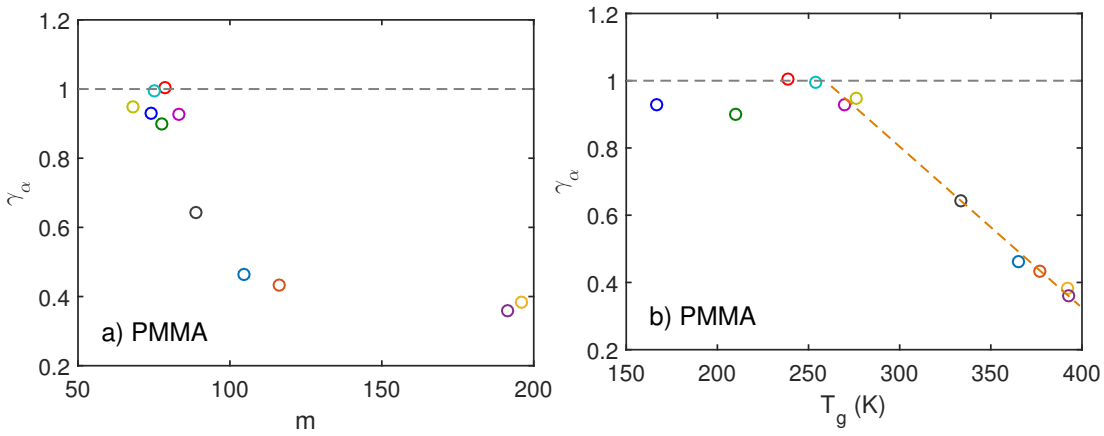

Figure 5.8: The decoupling parameter between σ and τ_α, γ_α, for the PMMA M series, as a function of: (a) dynamic fragility, m; and b the glass transition temperature, T_g.

In figure 5.8 (a), there is no clear correlation between γ_α and m (except for region I, where both are approximately invariant with M). Figure 5.8 (b) shows a potential correlation between γ_α and T_g in regions II and III (shows by the orange dashed line).

The exact mechanisms which cause a decoupling between α dynamics and diffusion are unclear[182, 260]. It has been shown to be related to an increase in dynamic heterogeneity[247], although both experimental and computer simulations question this link[236, 261]. Others link the breakdown to how α dynamics and diffusion couple differently to varying intermolecular cooperativity, or the link between diffusion and the β relaxation that emerges below the dynamic crossover temperature, $T_{\alpha,\beta}$[262, 263], as discussed in section 1.2.3. Recently, Zulli et. al.[91] measured the rotational diffusion timescales of a probe molecule using electron spin resonance (ESR), along with viscosity using standard rheology, of a PMMA chain-length series. These mechanisms were always decoupled below $T_{\alpha,\beta}$, although they attribute this to some decoupling between the probe and rotational diffusion. Interestingly, above $T_{\alpha,\beta}$ this decoupling was reduced. They

found a change in decoupling behaviour at $M \gtrsim 1200$g/mol, which is consistent with the decoupling of ion diffusion and the α relaxation in this work.

For the PPG-DME and PPG M series, σ was plotted against $1/\tau_\alpha$ in the same manner as for PMMA to determine the M dependence of γ_α. These are shown in figure 5.9.

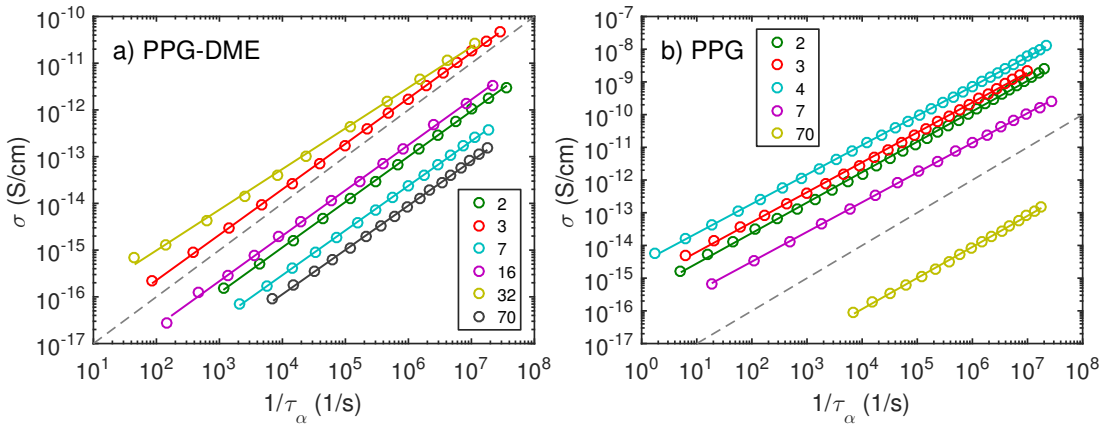

Figure 5.9: Un-normalised Walden plot of σ against $1/\tau_\alpha$ determined from BDS for (a) PPG-DME and (b) PPG M series. The gray dashed line represents a slope of 1. The legend indicates the degree of polymerisation, n.

Figure 5.9 shows that (a) PPG-DME and (b) PPG show no clear decoupling between σ and τ_α (which would be visualsied by a slope, $\gamma_\alpha \neq 1$) across the M range. As discussed in section 5.2, chain modes were also apparent in BDS, and values of τ_n could be obtained for higher M samples. For PPG-DME, σ was plotted against $1/\tau_n$ is shown in figure 5.10.

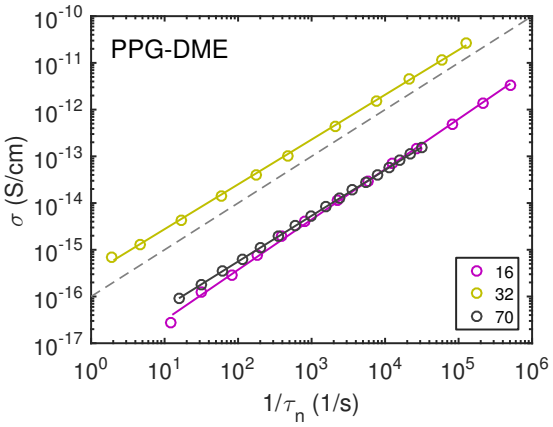

Figure 5.10: Un-normalised Walden plot of σ against $1/\tau_n$ determined from BDS for PPG-DME M series. The gray dashed line represents a slope of 1. The legend indicates the degree of polymerisation, n.

Once again, figure 5.10 shows no clear decoupling between σ and τ_n (which would be visualised by a slope, $\gamma_n \neq 1$) across the M range. These γ_α and γ_n values as a function of M for PPG-DME and PPG are shown in figure 5.11.

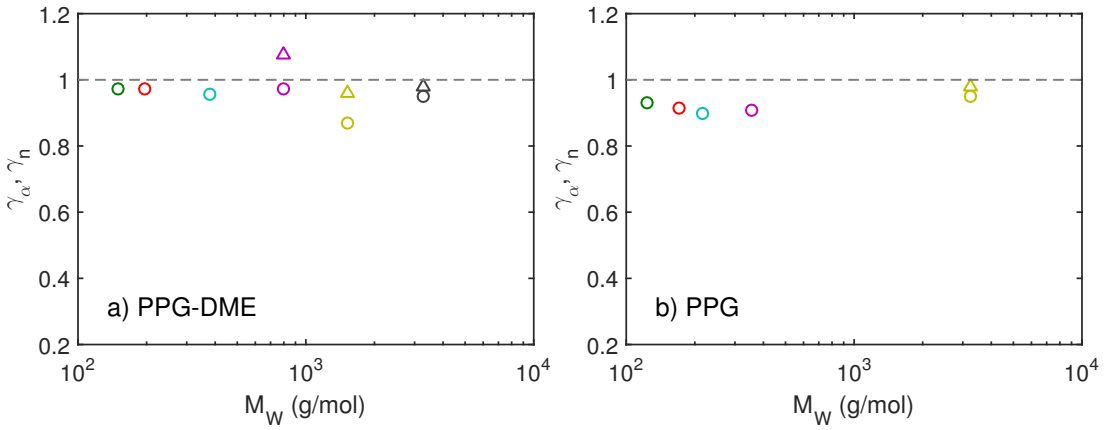

Figure 5.11: The decoupling parameter, γ, as a function of M for (a) PPG-DME and (b) PPG. Circles: γ_α values corresponding to figure 5.9. Triangles: γ_n values corresponding to figure 5.10.

Figure 5.11 shows no clear M variation in either γ_α or γ_n for PPG-DME (a), or PPG (b). This is consistent with PEG, and other low fragility, low T_g, long-chain polymers[247]. Interestingly, this implies that α and chain dynamics are also

correlated in this dynamic range, which has been shown previously for PPG[133]. This was also discussed in section 3.5.2, where $\tau_\alpha(T)$ and $\tau_n(T)$ were able to be collapsed onto a single master curve (along with other oligomer/polymer systems, shown in figure 3.30 (a)).

5.2.2 Effects of ion concentration on DC conductivity

As mentioned in section 5.2, the conductivity measured in these systems was due to charged species (ionic impurities) already present in the samples. A standard electrolyte lithium salt was added to a PMMA sample where decoupling was expected in order to see if the decoupling parameter, γ_α, was affected. The salt added was lithium tetrafluoroborate ($LiBF_4$)[264, 265], as shown in figure 5.12.

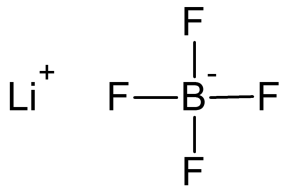

Figure 5.12: Lithium tetrafluoroborate ($LiBF_4$) salt. This dissociates into a Li cation, and BF_4 anion.

Glycols such as PEG have excellent solubility for lithium salts[245], which means a relatively large quantity of $LiBF_4$ can be added to PEG, which dissociate, and increase the ion conductivity. PMMA based systems have also been shown to dissolve lithium salts[250–252]. Therefore, $LiBF_4$ was added to a PMMA n=140 sample, which would be expected to have a decoupling parameter of $\gamma_\alpha \sim 0.4$. This was done by dissolving an appropriate amount of PMMA and $LiBF_4$ salt in acetone, and drying in a vacuum oven far above T_g. T_g was compared to that of the unsalted sample using DSC in order to ensure no acetone remained. BDS was then performed, and σ and τ_α were obtained in the same manner as outlined in section 5.1.1. In order to find an appropriate amount of salt to add, three different salt concentrations were tested, these were: 1000:1, 500:1, and 250:1, which indicate the ratios of PMMA monomers to Li ions. The BDS results at a single temperature for these salt concentrations is shown in figure 5.13.

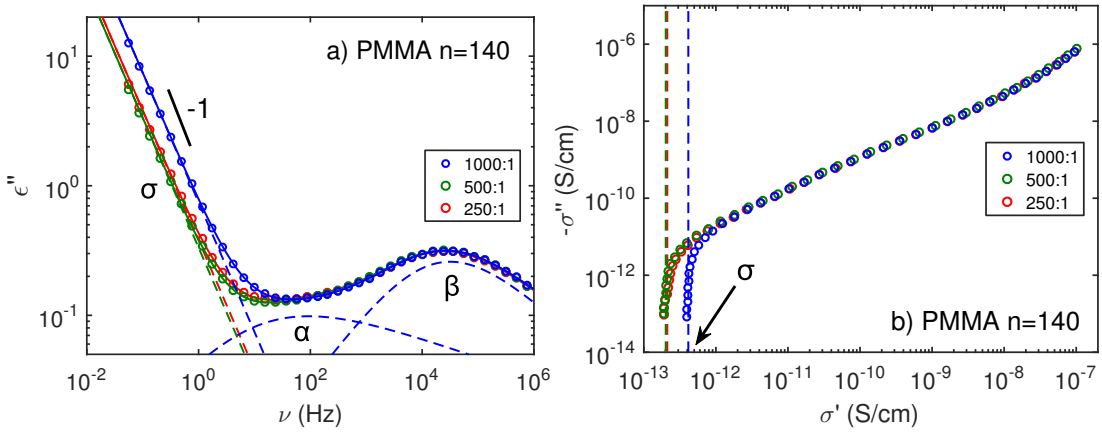

Figure 5.13: T=393K.

Naively, one would expect that increasing salt concentration would linearly increase ionic conductivity (assuming that the salt fully dissociates). However an increase in ion concentration can also reduce overall conductivity due to an increase in ion-ion interactions, resulting in aggregate formation[266, 267]. Figure 5.13 (a) shows $\epsilon''(\omega)$ for PMMA n=140 at T=393K, whereby conductivity, σ, falls with increasing salt concentration (1000:1 having half the amount of $LiBF_4$ than 500:1). However, both α and β dynamics remain unchanged. BDS results can also be expressed as a complex conductivity, $\sigma^*(\omega)$, as shown in equation 5.14.

$$\sigma^*(\omega) = i\omega\epsilon^*(\omega) \tag{5.14}$$

Figure 5.13 (b) is a so-called Cole-Cole plot[14], with the imaginary conductivity, $-\sigma''(\omega)$, plotted against the real conductivity, $\sigma'(\omega)$. In this plot, DC conductivity can be read off as the the value of σ' when $-\sigma'' \to 0$, as indicated by the dashed lines.

From these values of τ_α and σ at different temperatures, the decoupling parameter, γ_α, was obtained in the same manner as described in section 5.2.1. These values are shown by the squares in figure 5.7, which shows a clear decoupling of $\gamma_\alpha \sim 0.4$, fully in agreement with γ_α as obtained from the decoupling between τ_α and the unknown charged species (impurities) already present in the other samples. However, in order to be completely certain, $LiBF_4$ will be added to samples

either side of the region I to II boundary to confirm this M dependent decoupling behaviour holds.

In addition to this, future work will include adding a series of perchlorate salts with different alkali metal cation size to these polymer systems, i.e. lithium perchlorate ($LiClO_4$), sodium perchlorate ($NaClO_4$), potassium perchlorate ($KClO_4$), and rubidium perchlorate ($RbClO_4$). This will explore the effect of the size of the anion on the decoupling between σ and τ_α in these different polymer systems. The size of ions has been shown previously to influence coupling differently for different glass forming systems[249]. However, a systematic study of this kind on a chain-length polymeric series has not been performed.

5.2.3 Small molecular glass formers

The difference between the M dependence of γ_α for the relatively fragile, less flexible ($C_\infty = 9.0$[60]) PMMA and the less fragile, flexible ($C_\infty = 5.1$[150]) PPG-DME/PPG is clear. As stated before, Agapov and Sokolov observed an increase decoupling between σ and τ_α with increasing T_g and m for long-chain polymers[247]. However, the trends of T_g and m with increasing M in PMMA, PPG-DME, and PPG do not correlate to γ_α.

Therefore, in addition to the PMMA, PPG-DME, and PPG M series, α dynamics and conductivity for small molecular systems with different M, T_g, and m were looked at. The small molecular liquids were Propylene carbonate (PC), Phenyl salicylate (Salol), ortho-Terphenyl (OTP), and o-Cresolphthalein dimethylether (KDE). The molecular structure these samples is shown in figure 5.14.

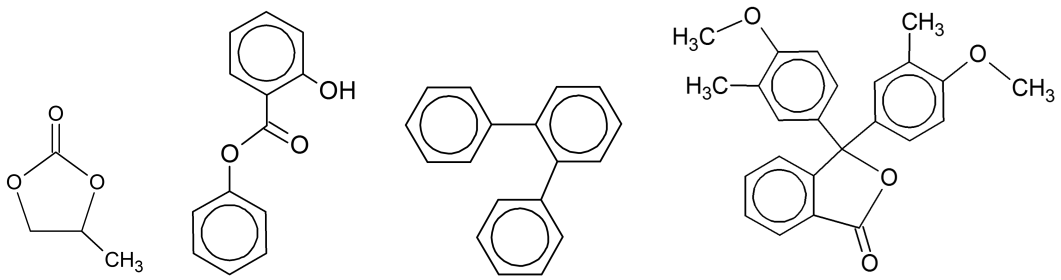

Figure 5.14: Molecular structures of small molecular glass formers. From left to right: Propylene carbonate (PC), Phenyl salicylate (Salol), ortho-Terphenyl (OTP), and o-Cresolphthalein dimethylether (KDE).

BDS measurements on these systems were performed by Franz-Josef Stickel[268], who measured both $\tau_\alpha(T)$ and $\sigma(T)$ across a wide dynamic range. $\tau_\alpha(T)$ data was fitted with a VFT expression, shown in equation 5.10, and was used to calculate T_g (T where $\tau_\alpha = 100$s), and m, using equation 5.12. These values are shown in table 5.2.

Molecule	M (g/mol)	T_g (K)	m
PC	102	157	113
Salol	214	219	87
OTP	230	230	80
KDE	374	374	72

Table 5.2: Properties of small molecular glass formers shown in figure 5.14.

Small molecular glass formers, such as those shown in figure 5.14 and table 5.2, do not to have the same systematic increase in intramolecular conformational freedom that oligomers/polymers have with increasing M. Therefore, the T_g and m dependence of these systems behaves differently to that of oligomers. For small molecular systems such as these, T_g has been shown to increase with M[157, 269]. However, correlations between M, T_g, and m is complicated, and depends a lot on the structure of the moleculue, i.e. organic, aromatic, etc[270].

In the same manner as for the PMMA, PPG-DME, and PPG M series, σ was plotted against $1/\tau_\alpha$. From this, the decoupling parameter, γ_α was determined

from the slope. These are shown in figure 5.15.

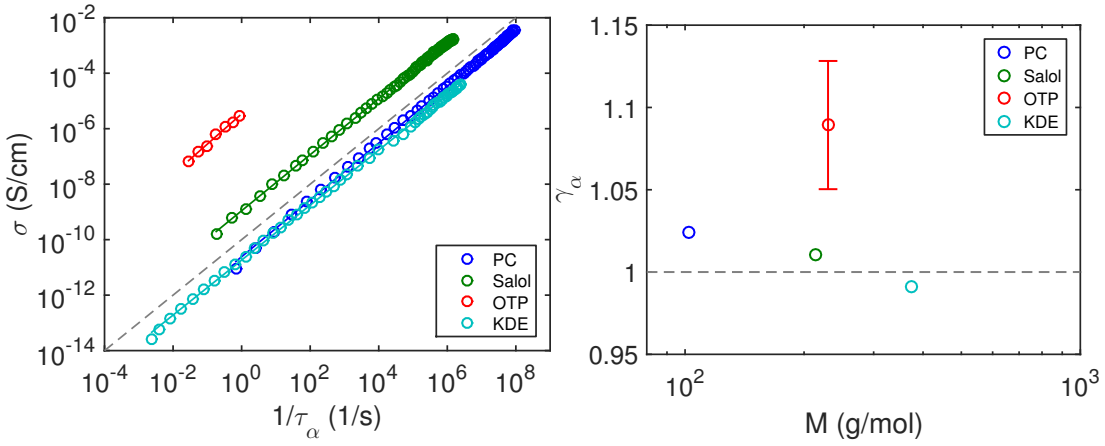

Figure 5.15: a) Un-normalised Walden plot of σ against $1/\tau_\alpha$ determined from BDS small molecular glass formers. The gray dashed line represents a slope of 1. b) The decoupling parameter γ_α, defined as the slope in (a), as a function of molecular weight, M.

Figure 5.15 shows that σ and τ_α are coupled in these small molecular systems, whereby the slope in (a) is $\gamma_\alpha \approx 1$ (shown in (b)) for these systems. This shows that, unlike polymer systems such as PMMA, where decoupling becomes apparent with increasing T_g and m, for small molecular systems there is no correlation between between α dynamics and decoupling. Therefore the decoupling in PMMA is a feature of the onset of polymer behaviour, i.e. above the region I to II boundary.

5.3 Conclusions

In this chapter, results of α relaxation timescales, $\tau_\alpha(T)$, and conductivity, $\sigma(T)$, from BDS measurements on chain-length series of PMMA, PPG-DME, and PPG ranging from dimer to polymer, along with a few examples of small molecular glass formers, were discussed. This focused on how the decoupling between σ and τ_α varies with both M and properties, such as T_g and m. The decoupling of σ (relating to diffusion), and τ_α (relating to structural dynamics) is not well

understood[236], and is of particular importance to the production of solid, amorphous, electrolytes which can be used in batteries. This works shows that:

- The decoupling between σ and τ_α in PMMA as a function of M shows regional behaviour, as defined by regions with different T_g behaviour. In region I (small M range), σ and τ_α were coupled, which is consistent with other small molecular liquids[248, 249]. In region II (intermediate M range), σ and τ_α were decoupled, whereby the degree of decoupling increased until region III (high M range), where the decoupling become M independent. This decoupling at high M is consistent with other fragile, high T_g, long-chain polymers[247]. A similar trend was also observed by Zulli et. al.[91], whereby the decoupling between the rotation diffusion of a probe molecule and viscosity showed the same regional behaviour in PMMA.

- PPG-DME (methoxy end-groups) and PPG (hydroxyl end-groups) M series showed no decoupling between σ and τ_α across the M range studied. This is consistent with other less fragile, low T_g, long-chain polymer systems[247].

- A selection of small molecular glass formers with different properties also exhibit a coupling between σ and τ_α. However, unlike long-chain polymers, these do not demonstrate decoupling with varying M, T_g or m.

5.3.1 Future work

In addition to the work outlined, these additional steps will be taken to complete this story:

- Lithium based salts will be added to PMMA samples with different decoupling behaviour, i.e. samples either side of the M region I to II boundary to ensure this decoupling behaviour persists.

- Another fragile, high T_g polymer systems such as polystyrene (PS) will be tested in the same manner. Due to the poor dipole strength in PS, this will require the addition of an appropriate salt.

- A series of perchlorate salts; $LiClO_4$, $NaClO_4$ $KClO_4$, and $RbClO_4$ will be added to these polymer systems to explore the effect of the size of the anion on the decoupling between σ and τ_α.
- A detailed investigation of lithium ion diffusion mechanism will be performed in these systems using NMR, with the additional possibility of dynamic neutron scattering in order to probe the detailed diffusion mechanisms.

5. DECOUPLING OF ION CONDUCTIVITY AND THE α RELAXATION IN POLYMER SYSTEMS

Chapter 6

Conclusions

The main aim of this thesis was to better understand the role chain-length plays on glassy properties such as T_g, fragility, etc. A large range of experimental techniques were used through this work, which included; dynamic shear rheology, broadband dielectric spectroscopy (BDS), differential scanning calorimetry (DSC), and temperature modulated DSC (TMDSC). These techniques were performed on a variety of polymeric systems; from the relatively fragile and stiff poly(methyl methacrylate) (PMMA) and polystyrene (PS), to the relatively strong and flexible poly(dimethyl siloxane) (PDMS) and poly(propylene glycol) (PPG).

In chapter 3 the rheological response of a chain-length series of PMMA ranging from small molecular glass formers to fully entangled polymer was studied. This data spanned from glass to melt, and was analysed using time-temperature superposition (TTS). The TTS master curves were well modelled using a sum of a KWW expression describing the α relaxation, and either the Rouse model or the Likhtman-McLeish model for chain dynamics when applicable. We note regional molecular weight, M, behaviour in properties relating to α dynamics, whereby T_g, fragility, and heat capacity responses (measured using DSC) exhibit distinctly different behaviour in different M regions, which appear to correspond to the onset of chain dynamics at a molecular weight, M_R, corresponding to the chain folding and the formation of an effective "dynamic bead", and the critical entanglement molecular weight, M_c. For PMMA samples where $M > M_R$ chain

dynamics become apparent, which have been shown to decouple from the α relaxation close to T_g. Therefore, the application of TTS was investigated. This was done by comparing the α relaxation timescales, τ_α, obtained from rheology to those from BDS, which yields τ_α without the need to rely on TTS. We observed that TTS is approximately valid in describing the α relaxation, whereby τ_α values obtained from TTS and BDS can be superimposed over a wide dynamic range. We compared these τ_α data to other polymer systems, and we note a "universal" scaling of chain dynamics, and τ_α at longer times when normalised by T_g/T. From this, we suggest a link between this behaviour and the size of the correlated region of the α relaxation.

In chapter 4, the number of correlated units in the α relaxation was determined for PMMA, PS, and PDMS chain-length series as a function of τ_α. This was obtained by measuring thermal fluctuations using TMDSC, and from an approximation of the four-point dynamic susceptibility, χ_4, determined using BDS. PMMA and PS exhibit clear regional M behaviour in the number of monomers involved in the α relaxation, whereby for $M < M_R$, there is a large decrease with increasing M. At M_R, the number of monomers involved in the α relaxation is approximately that of the dynamic bead size. We surmise that rigid/fragile polymer systems such as PMMA and PS exhibit a changeover between a mostly intermolecular to a more intramolecular cooperativity as chain behaviour becomes apparent. This is further supported by measurements of the activation enthalpies of the α and β relaxations measured using BDS, whereby both increase with increasing M. However, at M_R, the activation enthalpies of the α and β relaxations are approximately equal, which suggests similarities between these two processes. The activation enthalpy of the β relaxation also becomes relatively M invariant above M_R, suggesting that this is a lenghscale which characterises the β relaxation in PMMA.

In chapter 5, the ionic conductivity was measured for the chain-length series of PMMA, and for two PPG chain-series. We show that the α relaxation and ionic diffusion begin to decouple in PMMA at M_R, whereas the two PPG systems shows coupling across the entire M range. It has been suggested that this decoupling relates to T_g and fragility, which may be the case for long-chain polymers. However, we show that this does not hold for non-polymeric liquids, where the

α relaxation and ionic conductivity are coupled despite having different T_g and fragilities.

This work outlines the important role chain-length has on the dynamics and properties of glass forming polymers. In particular the clear differences between relatively fragile, rigid polymer systems such as PMMA and PS, and relatively strong, flexible polymer systems such as PDMS and PPG.

The importance of M_R as a crossover between small molecular and polymeric glassy behaviour in PMMA is clear. It is the molecular weight where: i) "universal" scaling of τ_α can be applied; ii) there is a crossover between a mostly intermolecular to to a more intramolecular cooperativity; and iii) the α relaxation and ionic diffusion begin to decouple.

References

[1] R. L. Kroes, "Photoluminescence and optical transmission of diffusion-pump oils," *Applied optics*, vol. 12, no. 9, pp. 2075–2078, 1973. x, 41, 42

[2] L. C. Thomas, "Mdsc paper# 2 modulated dsc basics; calculation and calibration of mdsc signals," 2005. xii, 71

[3] E. V. Thompson, "Dependence of the glass transition temperature of poly (methyl methacrylate) on tacticity and molecular weight," *Journal of Polymer Science Part B: Polymer Physics*, vol. 4, no. 2, pp. 199–208, 1966. xiv, 26, 96, 97

[4] K. O'Driscoll and R. A. Sanayei, "Chain-length dependence of the glass transition temperature," *Macromolecules*, vol. 24, no. 15, pp. 4479–4480, 1991. xiv, 26, 96, 97

[5] A. E. Likhtman and T. C. McLeish, "Quantitative theory for linear dynamics of linear entangled polymers," *Macromolecules*, vol. 35, no. 16, pp. 6332–6343, 2002. xvi, 13, 22, 86, 119

[6] Y. Wang, F. Fan, A. L. Agapov, T. Saito, J. Yang, X. Yu, K. Hong, J. Mays, and A. P. Sokolov, "Examination of the fundamental relation between ionic transport and segmental relaxation in polymer electrolytes," *Polymer*, vol. 55, no. 16, pp. 4067–4076, 2014. xx, 194, 196

[7] P. G. Debenedetti and F. H. Stillinger, "Supercooled liquids and the glass transition," *Nature*, vol. 410, no. 6825, p. 259, 2001. 1, 6, 10, 11, 127, 169

[8] J. D. Ferry, *Viscoelastic properties of polymers*. John Wiley & Sons, 1980. 1, 29, 33, 37, 88

[9] E. Donth, *The glass transition: relaxation dynamics in liquids and disordered materials*, vol. 48. Springer Science & Business Media, 2013. 1, 6, 7, 59, 130, 132, 133, 169

[10] M. D. Ediger, C. A. Angell, and S. R. Nagel, "Supercooled liquids and glasses," *The journal of physical chemistry*, vol. 100, no. 31, pp. 13200–13212, 1996. 2, 7, 100

[11] J. C. Dyre, "Colloquium: The glass transition and elastic models of glass-forming liquids," *Reviews of modern physics*, vol. 78, no. 3, p. 953, 2006. 2, 6, 7, 9

[12] W. Kauzmann, "The nature of the glassy state and the behavior of liquids at low temperatures.," *Chemical reviews*, vol. 43, no. 2, pp. 219–256, 1948. 2

[13] R. J. Speedy, "Kauzmann's paradox and the glass transition," *Biophysical chemistry*, vol. 105, no. 2-3, pp. 411–420, 2003. 2

[14] F. Kremer and A. Schönhals, *Broadband Dielectric Spectroscopy*. Springer Berlin Heidelberg, 2012. 3, 11, 49, 50, 51, 52, 56, 57, 91, 105, 106, 119, 159, 176, 177, 194, 197, 200, 208

[15] J. C. Maxwell *et al.*, "Iv. on the dynamical theory of gases," *Philosophical transactions of the Royal Society of London*, vol. 157, pp. 49–88, 1867. 3, 195

[16] L. Berthier and G. Biroli, "Theoretical perspective on the glass transition and amorphous materials," *Reviews of Modern Physics*, vol. 83, no. 2, p. 587, 2011. 3

[17] H. Vogel, "The law of the relation between the viscosity of liquids and the temperature," *Phys. Z*, vol. 22, pp. 645–646, 1921. 3, 88, 198

[18] G. S. Fulcher, "Analysis of recent measurements of the viscosity of glasses," *Journal of the American Ceramic Society*, vol. 8, no. 6, pp. 339–355, 1925.

[19] G. Tammann and W. Hesse, "Die abhängigkeit der viscosität von der temperatur bie unterkühlten flüssigkeiten," *Zeitschrift für anorganische und allgemeine Chemie*, vol. 156, no. 1, pp. 245–257, 1926. 3, 88, 198

[20] C. A. Angell and W. Sichina, "Thermodynamics of the glass transition: empirical aspects," *Annals of the New York Academy of Sciences*, vol. 279, no. 1, pp. 53–67, 1976. 4, 101

[21] F. H. Stillinger, P. G. Debenedetti, and T. M. Truskett, "The kauzmann paradox revisited," *The Journal of Physical Chemistry B*, vol. 105, no. 47, pp. 11809–11816, 2001. 4

[22] C. A. Angell, "Formation of glasses from liquids and biopolymers," *Science*, vol. 267, no. 5206, pp. 1924–1935, 1995. 4

[23] C. A. Angell, "Structural instability and relaxation in liquid and glassy phases near the fragile liquid limit," *Journal of non-crystalline solids*, vol. 102, no. 1-3, pp. 205–221, 1988. 5, 89, 180, 199

[24] F. Stickel, E. W. Fischer, and R. Richert, "Dynamics of glass-forming liquids. i. temperature-derivative analysis of dielectric relaxation data," *The Journal of chemical physics*, vol. 102, no. 15, pp. 6251–6257, 1995. 5, 89

[25] R. Böhmer, K. Ngai, C. A. Angell, and D. Plazek, "Nonexponential relaxations in strong and fragile glass formers," *The Journal of chemical physics*, vol. 99, no. 5, pp. 4201–4209, 1993. 6, 99, 101

[26] H. Sillescu, "Heterogeneity at the glass transition: a review," *Journal of Non-Crystalline Solids*, vol. 243, no. 2-3, pp. 81–108, 1999. 130, 131

[27] C. A. Angell, K. L. Ngai, G. B. McKenna, P. F. McMillan, and S. W. Martin, "Relaxation in glassforming liquids and amorphous solids," *Journal of Applied Physics*, vol. 88, no. 6, pp. 3113–3157, 2000. 6, 11

[28] G. Adam and J. H. Gibbs, "On the temperature dependence of cooperative relaxation properties in glass-forming liquids," *The journal of chemical physics*, vol. 43, no. 1, pp. 139–146, 1965. 7, 103, 127, 186

[29] J. H. Gibbs and E. A. DiMarzio, "Nature of the glass transition and the glassy state," *The Journal of Chemical Physics*, vol. 28, no. 3, pp. 373–383, 1958. 7

[30] H. Tanaka, "Relation between thermodynamics and kinetics of glass-forming liquids," *Physical review letters*, vol. 90, no. 5, p. 055701, 2003. 7

[31] M. H. Cohen and D. Turnbull, "Molecular transport in liquids and glasses," *The Journal of Chemical Physics*, vol. 31, no. 5, pp. 1164–1169, 1959. 8, 96

[32] G. S. Grest and M. H. Cohen, "Liquids, glasses, and the glass transition: A free-volume approach," *Advances in chemical physics*, pp. 455–525, 1981. 8

[33] R. P. White and J. E. Lipson, "Polymer free volume and its connection to the glass transition," *Macromolecules*, vol. 49, no. 11, pp. 3987–4007, 2016. 9

[34] C. Roland and R. Casalini, "Effect of chemical structure on the isobaric and isochoric fragility in polychlorinated biphenyls," *The Journal of chemical physics*, vol. 122, no. 13, p. 134505, 2005. 9

[35] C. Zhang and R. D. Priestley, "Fragility and glass transition temperature of polymer confined under isobaric and isochoric conditions," *Soft Matter*, vol. 9, no. 29, pp. 7076–7085, 2013. 9

[36] K. Ngai, "Kl ngai, comments solid state phys. 9, 127 (1979)," *Comments Solid State Phys.*, vol. 9, p. 127, 1979. 9

[37] K. Ngai, "An extended coupling model description of the evolution of dynamics with time in supercooled liquids and ionic conductors," *Journal of Physics: Condensed Matter*, vol. 15, no. 11, p. S1107, 2003. 9, 183

[38] J. Mattsson, *Glass transition dynamics in soft condensed matter*. PhD thesis, 2002. 9, 53, 193

[39] K. Ngai, "Dynamic and thermodynamic properties of glass-forming substances," *Journal of Non-Crystalline Solids*, vol. 275, no. 1-2, pp. 7–51, 2000. 9

[40] K. Ngai, "Coupling model explanation of salient dynamic properties of glass-forming substances," *IEEE Transactions on Dielectrics and Electrical Insulation*, vol. 8, no. 3, pp. 329–344, 2001. 9, 10

[41] K. Ngai, "Relation between some secondary relaxations and the α relaxations in glass-forming materials according to the coupling model," *The Journal of chemical physics*, vol. 109, no. 16, pp. 6982–6994, 1998. 10, 100, 179, 181, 188

[42] S. Capaccioli, M. Paluch, D. Prevosto, L.-M. Wang, and K. Ngai, "Many-body nature of relaxation processes in glass-forming systems," *The journal of physical chemistry letters*, vol. 3, no. 6, pp. 735–743, 2012. 10, 183

[43] M. Goldstein, "Viscous liquids and the glass transition: a potential energy barrier picture," *The Journal of Chemical Physics*, vol. 51, no. 9, pp. 3728–3739, 1969. 10

[44] C. A. Angell, "Perspective on the glass transition," *Journal of Physics and Chemistry of Solids*, vol. 49, no. 8, pp. 863–871, 1988. 11

[45] F. H. Stillinger, "A topographic view of supercooled liquids and glass formation," *Science*, vol. 267, no. 5206, pp. 1935–1939, 1995. 11

[46] D. Baker, *Relaxation dynamics in molecular glass-formers with systematic structure modifications*. PhD thesis, 2014. 11

[47] N. G. McCrum, B. E. Read, and G. Williams, *Anelastic and dielectric effects in polymeric solids*. Wiley, 1967. 11, 19, 25, 37, 84, 113

[48] G. P. Johari and M. Goldstein, "Viscous liquids and the glass transition. ii. secondary relaxations in glasses of rigid molecules," *The Journal of Chemical Physics*, vol. 53, no. 6, pp. 2372–2388, 1970. 11, 175, 183

[49] G. P. Johari, "Intrinsic mobility of molecular glasses," *The Journal of chemical physics*, vol. 58, no. 4, pp. 1766–1770, 1973. 11

[50] J. Heijboer, "Molecular origin of relaxations in polymers," *Annals of the New York Academy of Sciences*, vol. 279, no. 1, pp. 104–116, 1976. 11

[51] R. F. Boyer, "Mechanical motions in amorphous and semi-crystalline polymers," *Polymer*, vol. 17, no. 11, pp. 996–1008, 1976. 11

[52] R. Böhmer, G. Hinze, G. Diezemann, B. Geil, and H. Sillescu, "Dynamic heterogeneity in supercooled ortho-terphenyl studied by multidimensional deuteron nmr," *EPL (Europhysics Letters)*, vol. 36, no. 1, p. 55, 1996. 12, 175

[53] H. Sillescu, R. Böhmer, G. Diezemann, and G. Hinze, "Heterogeneity at the glass transition: what do we know?," *Journal of Non-Crystalline Solids*, vol. 307, pp. 16–23, 2002. 12, 175

[54] G. Johari, "Localized molecular motions of β-relaxation and its energy landscape," *Journal of non-crystalline solids*, vol. 307, pp. 317–325, 2002. 12, 175

[55] E. Rössler, "Indications for a change of diffusion mechanism in supercooled liquids," *Physical review letters*, vol. 65, no. 13, p. 1595, 1990. 12, 180

[56] A. Schönhals, "Evidence for a universal crossover behaviour of the dynamic glass transition," *EPL (Europhysics Letters)*, vol. 56, no. 6, p. 815, 2001. 12, 180

[57] V. Novikov and A. Sokolov, "Universality of the dynamic crossover in glass-forming liquids: A magic relaxation time," *Physical Review E*, vol. 67, no. 3, p. 031507, 2003. 12, 180

[58] M. A. Desando, M. A. Kashem, M. A. Siddiqui, and S. Walker, "Dielectric studies of the β 1 and β 2 processes of poly (alkyl methacrylate) polymers," *Journal of the Chemical Society, Faraday Transactions 2: Molecular and Chemical Physics*, vol. 80, no. 7, pp. 747–762, 1984. 12, 176

[59] U. W. Gedde, *Polymer physics*. Springer Science & Business Media, 2013. 12

[60] M. Rubinstein and R. H. Colby, *Polymer physics*, vol. 23. Oxford university press New York, 2003. 13, 14, 15, 16, 17, 18, 19, 20, 21, 74, 107, 201, 209

[61] J. M. Dealy, D. J. Read, and R. G. Larson, *Structure and rheology of molten polymers: from structure to flow behavior and back again*. Carl Hanser Verlag GmbH Co KG, 2018. 13, 15, 19, 22, 23, 24, 37, 86, 107

[62] G. Cui, *Synthesis, Relaxation Dynamics and Rheology of Supramolecular Polymers*. PhD thesis, 2017. 15, 18

[63] P. E. Rouse Jr, "A theory of the linear viscoelastic properties of dilute solutions of coiling polymers," *The Journal of Chemical Physics*, vol. 21, no. 7, pp. 1272–1280, 1953. 16, 18, 84

[64] M. Doi and S. F. Edwards, *The theory of polymer dynamics*, vol. 73. oxford university press, 1988. 19, 20, 22, 84, 86, 104

[65] P.-G. de Gennes, "Reptation of a polymer chain in the presence of fixed obstacles," *The journal of chemical physics*, vol. 55, no. 2, pp. 572–579, 1971. 20, 21, 22, 86

[66] S. Milner and T. McLeish, "Parameter-free theory for stress relaxation in star polymer melts," *Macromolecules*, vol. 30, no. 7, pp. 2159–2166, 1997. 22

[67] A. E. Likhtman and R. S. Graham, "Simple constitutive equation for linear polymer melts derived from molecular theory: Rolie–poly equation," *Journal of Non-Newtonian Fluid Mechanics*, vol. 114, no. 1, pp. 1–12, 2003.

[68] C. Das, N. J. Inkson, D. J. Read, M. A. Kelmanson, and T. C. McLeish, "Computational linear rheology of general branch-on-branch polymers," *Journal of Rheology*, vol. 50, no. 2, pp. 207–234, 2006. 22

[69] I. Ward, "Mechanical properties of polymers," *Wiley, Chichester, 1983) p*, vol. 418, 1983. 22

[70] S. Murahashi, S. Nozakura, M. Sumi, H. Yuki, and K. Hatada, "Nmr study of the tacticity of poly (vinyl acetate)," *Journal of Polymer Science Part B: Polymer Letters*, vol. 4, no. 1, pp. 65–69, 1966. 24

[71] T. Kawamura, N. Toshima, and K. Matsuzaki, "Comparison of 13c nmr spectra of polystyrenes having various tacticities and assignment of the spectra," *Macromolecular rapid communications*, vol. 15, no. 6, pp. 479–486, 1994. 24

[72] A. Alexandrov and J. Lazurkin *Acta Physicochim*, vol. 12, p. 647, 1940. 25

[73] X. Wu, X. Zhou, C. Liu, and Z. Zhu, "Slow dynamics of the α and α relaxation processes in poly (methyl methacrylate) through the glass transition studied by mechanical spectroscopy," *Journal of Applied Physics*, vol. 106, no. 1, p. 013527, 2009. 25

[74] E. Muzeau, J. Perez, and G. Johari, "Mechanical spectrometry of the. beta.-relaxation in poly (methyl methacrylate)," *Macromolecules*, vol. 24, no. 16, pp. 4713–4723, 1991. 25

[75] R. Bergman, F. Alvarez, A. Alegrıa, and J. Colmenero, "The merging of the dielectric α-and β-relaxations in poly-(methyl methacrylate)," *The Journal of chemical physics*, vol. 109, no. 17, pp. 7546–7555, 1998. 26

[76] R. Casalini and C. Roland, "Aging of a low molecular weight poly (methyl methacrylate)," *Journal of Non-Crystalline Solids*, vol. 357, no. 2, pp. 282–285, 2011. 26, 183

[77] I. M. Hodge, "Effects of annealing and prior history on enthalpy relaxation in glassy polymers. 4. comparison of five polymers," *Macromolecules*, vol. 16, no. 6, pp. 898–902, 1983. 26

[78] R. Casalini, D. Fragiadakis, and C. Roland, "Relaxation dynamics of poly (methyl acrylate) at elevated pressure," *Macromolecules*, vol. 44, no. 17, pp. 6928–6934, 2011. 26, 139, 169

[79] E. Hempel, G. Hempel, A. Hensel, C. Schick, and E. Donth, "Characteristic length of dynamic glass transition near t g for a wide assortment of glass-forming substances," *The Journal of Physical Chemistry B*, vol. 104, no. 11, pp. 2460–2466, 2000. 26, 128, 133, 134, 135, 152, 153, 154

[80] L. Hong, V. Novikov, and A. P. Sokolov, "Is there a connection between fragility of glass forming systems and dynamic heterogeneity/cooperativity?," *Journal of Non-Crystalline Solids*, vol. 357, no. 2, pp. 351–356, 2011. 26, 128

[81] L. Weisenberger and J. L. Koenig, "An nmr imaging study of methanol desorption from partially swollen pmma rods," *Macromolecules*, vol. 23, no. 9, pp. 2454–2459, 1990. 26

[82] A. White and F. E. Filisko, "Tacticity determination of poly (methyl methacrylate)(pmma) by high-resolution nmr," *Journal of Polymer Science: Polymer Letters Edition*, vol. 20, no. 10, pp. 525–529, 1982. 26

[83] A. Soldera, "Comparison between the glass transition temperatures of the two pmma tacticities: A molecular dynamics simulation point of view," in *Macromolecular Symposia*, vol. 133, pp. 21–32, Wiley Online Library, 1998. 26

[84] A. Soldera and Y. Grohens, "Local dynamics of stereoregular pmmas using molecular simulation," *Macromolecules*, vol. 35, no. 3, pp. 722–726, 2002.

[85] M. Mohammadi, J. Davoodi, *et al.*, "The glass transition temperature of pmma: A molecular dynamics study and comparison of various determination methods," *European Polymer Journal*, vol. 91, pp. 121–133, 2017. 26

[86] T. G. Fox Jr and P. J. Flory, "Second-order transition temperatures and related properties of polystyrene. i. influence of molecular weight," *Journal of Applied Physics*, vol. 21, no. 6, pp. 581–591, 1950. 26, 89, 96, 140, 186, 199

[87] L. Andreozzi, M. Faetti, M. Giordano, and F. Zulli, "Molecular-weight dependence of enthalpy relaxation of pmma," *Macromolecules*, vol. 38, no. 14, pp. 6056–6067, 2005. 27

[88] R. Casalini, C. Roland, and S. Capaccioli, "Effect of chain length on fragility and thermodynamic scaling of the local segmental dynamics in poly (methylmethacrylate)," *The Journal of chemical physics*, vol. 126, no. 18, p. 184903, 2007. 27, 80

[89] T. Masuda, K. Kitagawa, and S. Onogi, "Viscoelastic properties of poly (methyl methacrylates) prepared by anionic polymerization," *Polymer Journal*, vol. 1, no. 4, pp. 418–424, 1970. 27

[90] K. Fuchs, C. Friedrich, and J. Weese, "Viscoelastic properties of narrow-distribution poly (methyl methacrylates)," *Macromolecules*, vol. 29, no. 18, pp. 5893–5901, 1996. 27, 105

[91] F. Zulli, M. Giordano, and L. Andreozzi, "Chain-length dependence of relaxation and dynamics in poly (methyl methacrylate) from oligomers to polymers," *Macromolecules*, vol. 51, no. 5, pp. 1798–1810, 2018. 27, 204, 212

[92] L. Carus, C. Bailey, *et al.*, "Lucretius on the nature of things," 1910. 29

[93] I. M. Ward and J. Sweeney, *Mechanical properties of solid polymers*. John Wiley & Sons, 2012. 33

[94] G. Williams and D. C. Watts, "Non-symmetrical dielectric relaxation behaviour arising from a simple empirical decay function," *Transactions of the Faraday society*, vol. 66, pp. 80–85, 1970. 34, 82, 165, 184

[95] R. Bergman, "General susceptibility functions for relaxations in disordered systems," *Journal of Applied Physics*, vol. 88, no. 3, pp. 1356–1365, 2000. 35, 83

[96] H. Booij and G. Thoone, "Generalization of kramers-kronig transforms and some approximations of relations between viscoelastic quantities," *Rheologica Acta*, vol. 21, no. 1, pp. 15–24, 1982. 36, 83

[97] T. G. Mezger, *Applied Rheology: With Joe Flow on Rheology Road*. Anton Paar, 2015. 37

[98] D. J. Plazek, "1995 bingham medal address: Oh, thermorheological simplicity, wherefore art thou?," *Journal of Rheology*, vol. 40, no. 6, pp. 987–1014, 1996. 37, 38, 78, 110

[99] M. L. Williams, R. F. Landel, and J. D. Ferry, "The temperature dependence of relaxation mechanisms in amorphous polymers and other glass-forming liquids," *Journal of the American Chemical society*, vol. 77, no. 14, pp. 3701–3707, 1955. 38, 123

[100] C. Maggi, B. Jakobsen, T. Christensen, N. B. Olsen, and J. C. Dyre, "Supercooled liquid dynamics studied via shear-mechanical spectroscopy," *The Journal of Physical Chemistry B*, vol. 112, no. 51, pp. 16320–16325, 2008. 43, 46

[101] K. Schröter, S. Hutcheson, X. Shi, A. Mandanici, and G. McKenna, "Dynamic shear modulus of glycerol: Corrections due to instrument compliance," *The Journal of chemical physics*, vol. 125, no. 21, p. 214507, 2006. 45

[102] Q. Chen, G. J. Tudryn, and R. H. Colby, "Ionomer dynamics and the sticky rouse model," *Journal of Rheology*, vol. 57, no. 5, pp. 1441–1462, 2013. 45, 85

[103] L. Onsager, "Electric moments of molecules in liquids," *Journal of the American Chemical Society*, vol. 58, no. 8, pp. 1486–1493, 1936. 49

[104] J. G. Kirkwood, "The dielectric polarization of polar liquids," *The Journal of Chemical Physics*, vol. 7, no. 10, pp. 911–919, 1939.

[105] C. P. Gainaru, *Dielectric Properties of Molecular Glass Formers; from the Liquid State to the Tunneling Regime*. PhD thesis, 2008. 49

[106] T. Dakin, "Conduction and polarization mechanisms and trends in dielectric," *IEEE Electrical Insulation Magazine*, vol. 22, no. 5, pp. 11–28, 2006. 51

[107] C. Böttcher, O. Van Belle, P. Bordewijk, A. Rip, and D. D. Yue, "Theory of electric polarization," *Journal of The Electrochemical Society*, vol. 121, no. 6, pp. 211C–211C, 1974. 51

[108] G. Katana, F. Kremer, E. W. Fischer, and R. Plaetschke, "Broadband dielectric study on binary blends of bisphenol-a and tetramethylbisphenol-a polycarbonate," *Macromolecules*, vol. 26, no. 12, pp. 3075–3080, 1993. 53

[109] S. Havriliak and S. Negami, "A complex plane representation of dielectric and mechanical relaxation processes in some polymers," *Polymer*, vol. 8, pp. 161–210, 1967. 55, 91, 159, 197

[110] K. S. Cole and R. H. Cole, "Dispersion and absorption in dielectrics i. alternating current characteristics," *The Journal of chemical physics*, vol. 9, no. 4, pp. 341–351, 1941. 55

[111] D. W. Davidson and R. H. Cole, "Dielectric relaxation in glycerol, propylene glycol, and n-propanol," *The Journal of Chemical Physics*, vol. 19, no. 12, pp. 1484–1490, 1951. 56

[112] M. Wübbenhorst and J. Van Turnhout, "Analysis of complex dielectric spectra. i. one-dimensional derivative techniques and three-dimensional modelling," *Journal of Non-Crystalline Solids*, vol. 305, no. 1-3, pp. 40–49, 2002. 58, 92

[113] G. Höhne, W. F. Hemminger, and H.-J. Flammersheim, *Differential scanning calorimetry*. Springer Science & Business Media, 2013. 59, 60, 62, 64, 68, 69, 70, 134

[114] I. M. Hodge, "Enthalpy relaxation and recovery in amorphous materials," *Journal of Non-Crystalline Solids*, vol. 169, no. 3, pp. 211–266, 1994. 60

[115] G. B. McKenna, "Mechanical rejuvenation in polymer glasses: fact or fallacy?," *Journal of Physics: Condensed Matter*, vol. 15, no. 11, p. S737, 2003. 61

[116] G. B. McKenna and S. L. Simon, "50th anniversary perspective: Challenges in the dynamics and kinetics of glass-forming polymers," *Macromolecules*, vol. 50, no. 17, pp. 6333–6361, 2017. 61

[117] C. T. Moynihan, A. J. Easteal, M. A. BOLT, and J. Tucker, "Dependence of the fictive temperature of glass on cooling rate," *Journal of the American Ceramic Society*, vol. 59, no. 1-2, pp. 12–16, 1976. 62, 93

[118] C. Moynihan, P. Macedo, C. Montrose, C. Montrose, P. Gupta, M. DeBolt, J. Dill, B. Dom, P. Drake, A. Easteal, *et al.*, "Structural relaxation in vitreous materials," *Annals of the New York Academy of Sciences*, vol. 279, no. 1, pp. 15–35, 1976. 62

[119] A. Hensel and C. Schick, "Relation between freezing-in due to linear cooling and the dynamic glass transition temperature by temperature-modulated dsc," *Journal of non-crystalline solids*, vol. 235, pp. 510–516, 1998. 63, 94, 135, 139, 140, 154

[120] M. Reading and D. J. Hourston, *Modulated temperature differential scanning calorimetry: theoretical and practical applications in polymer characterisation*. Springer, 2006. 64, 66, 68, 137, 139

[121] H. Gobrecht, K. Hamann, and G. Willers, "Complex plane analysis of heat capacity of polymers in the glass transition region," *Journal of Physics E: Scientific Instruments*, vol. 4, no. 1, p. 21, 1971. 64

[122] S. L. Simon, "Temperature-modulated differential scanning calorimetry: theory and application," *Thermochimica acta*, vol. 374, no. 1, pp. 55–71, 2001. 65

[123] TA Instruments, "Choosing conditions in modulated dsc," unknown. 67

[124] TA Instruments, "Purge gas recommendations for use in modulated dsc," unknown. 69

[125] T. Narasimhan, "Fourier's heat conduction equation: History, influence, and connections," *Reviews of Geophysics*, vol. 37, no. 1, pp. 151–172, 1999. 69

[126] R. L. Danley, "New heat flux dsc measurement technique," *Thermochimica acta*, vol. 395, no. 1-2, pp. 201–208, 2002. 70

[127] D. G. Archer and S. Rudtsch, "Enthalpy of fusion of indium: A certified reference material for differential scanning calorimetry," *Journal of Chemical & Engineering Data*, vol. 48, no. 5, pp. 1157–1163, 2003. 71

[128] R. L. Blaine, "Adamantane–a new certified and traceable reference material for subambient dsc temperature and enthalpy calibration on heating and cooling," 71

[129] D. Plazek, X. Zheng, and K. Ngai, "Viscoelastic properties of amorphous polymers. i. different temperature dependences of segmental relaxation and terminal dispersion," *Macromolecules*, vol. 25, no. 19, pp. 4920–4924, 1992. 74

[130] A. Schönhals and E. Schlosser, "Relationship between segmental and chain dynamics in polymer melts as studied by dielectric spectroscopy," *Physica Scripta*, vol. 1993, no. T49A, p. 233, 1993.

[131] P. Santangelo and C. Roland, "Temperature dependence of mechanical and dielectric relaxation in cis-1, 4-polyisoprene," *Macromolecules*, vol. 31, no. 11, pp. 3715–3719, 1998.

[132] K. Adachi and H. Hirano, "Slow dielectric relaxation of cis-polyisoprene near the glass transition temperature," *Macromolecules*, vol. 31, no. 12, pp. 3958–3962, 1998. 74

[133] Y. Ding and A. P. Sokolov, "Breakdown of time- temperature superposition principle and universality of chain dynamics in polymers," *Macromolecules*, vol. 39, no. 9, pp. 3322–3326, 2006. 75, 82, 110, 117, 118, 120, 123, 207

[134] J. Cowie, "Some general features of tg-m relations for oligomers and amorphous polymers," *European Polymer Journal*, vol. 11, no. 4, pp. 297–300, 1975. 77, 97, 127, 143, 149, 194, 203

[135] J. Hintermeyer, A. Herrmann, R. Kahlau, C. Goiceanu, and E. Rossler, "Molecular weight dependence of glassy dynamics in linear polymers revisited," *Macromolecules*, vol. 41, no. 23, pp. 9335–9344, 2008. 77, 97, 99, 127, 143, 149, 194, 203

[136] R. H. Colby, L. J. Fetters, and W. W. Graessley, "The melt viscosity-molecular weight relationship for linear polymers," *Macromolecules*, vol. 20, no. 9, pp. 2226–2237, 1987. 80

[137] T. Inoue, T. Onogi, M.-L. Yao, and K. Osaki, "Viscoelasticity of low molecular weight polystyrene. separation of rubbery and glassy components," *Journal of Polymer Science Part B: Polymer Physics*, vol. 37, no. 4, pp. 389–397, 1999. 80, 85, 106, 117

[138] L. Fetters, D. Lohse, and R. Colby, "Chain dimensions and entanglement spacings," in *Physical properties of polymers handbook*, pp. 447–454, Springer, 2007. 80, 105, 106

[139] K. Schmidt-Rohr, A. Kulik, H. Beckham, A. Ohlemacher, U. Pawelzik, C. Boeffel, and H. W. Spiess, "Molecular nature of the. beta. relaxation in poly (methyl methacrylate) investigated by multidimensional nmr," *Macromolecules*, vol. 27, no. 17, pp. 4733–4745, 1994. 81, 176, 184

[140] C. Chen, J. K. Maranas, and V. García-Sakai, "Local dynamics of syndiotactic poly (methyl methacrylate) using molecular dynamics simulation," *Macromolecules*, vol. 39, no. 26, pp. 9630–9640, 2006. 81, 176

[141] M. Van Gurp and J. Palmen, "Time-temperature superposition for polymeric blends," *Rheol Bull*, vol. 67, no. 1, pp. 5–8, 1998. 81

[142] S. Trinkle and C. Friedrich, "Van gurp-palmen-plot: a way to characterize polydispersity of linear polymers," *Rheologica Acta*, vol. 40, no. 4, pp. 322–328, 2001. 81

[143] J. C. Lagarias, J. A. Reeds, M. H. Wright, and P. E. Wright, "Convergence properties of the nelder–mead simplex method in low dimensions," *SIAM Journal on optimization*, vol. 9, no. 1, pp. 112–147, 1998. 83

[144] R. Gray, G. Harrison, and J. Lamb, "Dynamic viscoelastic behaviour of low-molecular-mass polystyrene melts," *Proc. R. Soc. Lond. A*, vol. 356, no. 1684, pp. 77–102, 1977. 85, 106, 117

[145] J.-C. Majeste, J.-P. Montfort, A. Allal, and G. Marin, "Viscoelasticity of low molecular weight polymers and the transition to the entangled regime," *Rheologica acta*, vol. 37, no. 5, pp. 486–499, 1998. 85

[146] M. Abdel-Goad, W. Pyckhout-Hintzen, S. Kahle, J. Allgaier, D. Richter, and L. J. Fetters, "Rheological properties of 1, 4-polyisoprene over a large molecular weight range," *Macromolecules*, vol. 37, no. 21, pp. 8135–8144, 2004. 85

[147] S. J. Park, P. S. Desai, X. Chen, and R. G. Larson, "Universal relaxation behavior of entangled 1, 4-polybutadiene melts in the transition frequency region," *Macromolecules*, vol. 48, no. 12, pp. 4122–4131, 2015. 85

[148] D. J. Plazek, "Whats wrong with the moduli charley brown? or get the h out and go to l," *Journal of Rheology*, vol. 36, no. 8, pp. 1671–1690, 1992. 85

[149] C. Roland, L. Archer, P. Mott, and J. Sanchez-Reyes, "Determining rouse relaxation times from the dynamic modulus of entangled polymers," *Journal of Rheology*, vol. 48, no. 2, pp. 395–403, 2004. 85

[150] C. Gainaru, W. Hiller, and R. Bohmer, "A dielectric study of oligo-and poly (propylene glycol)," *Macromolecules*, vol. 43, no. 4, pp. 1907–1914, 2010. 85, 200, 209

[151] A. Abou Elfadl, R. Kahlau, A. Herrmann, V. Novikov, and E. Rossler, "From rouse to fully established entanglement dynamics: a study of polyisoprene by dielectric spectroscopy," *Macromolecules*, vol. 43, no. 7, pp. 3340–3351, 2010. 85, 106, 119

[152] M. Hofmann, A. Herrmann, A. Abou Elfadl, D. Kruk, M. Wohlfahrt, and E. Rossler, "Glassy, rouse, and entanglement dynamics as revealed by field cycling 1h nmr relaxometry," *Macromolecules*, vol. 45, no. 5, pp. 2390–2401, 2012. 85, 106, 144

[153] P. Mott and C. Roland, "Birefringence of polymers in the softening zone," *Macromolecules*, vol. 31, no. 20, pp. 7095–7098, 1998. 85

[154] E. A. Di Marzio and A. J. Yang, "Configurational entropy approach to the kinetics of glasses," *Journal of research of the National Institute of Standards and Technology*, vol. 102, no. 2, p. 135, 1997. 96

[155] J. Cowie and I. McEwen, "Molecular motions in poly (dimethyl siloxane) oligomers and polymers," *Polymer*, vol. 14, no. 9, pp. 423–426, 1973. 97, 194, 203

[156] J. M. G. Cowie and V. Arrighi, *Polymers: chemistry and physics of modern materials*. CRC press, 2007. 97, 143

[157] D. Baker, R. Masurel, M. Reynolds, P. Olmsted, and J. Mattsson, "Chain-length, flexibility and the glass-transition of polymers." to be published. 98, 185, 210

[158] A. Agapov and A. Sokolov, "Does the molecular weight dependence of t g correlate to m e?," *Macromolecules*, vol. 42, no. 7, pp. 2877–2878, 2009. 98

[159] P. Santangelo and C. Roland, "Molecular weight dependence of fragility in polystyrene," *Macromolecules*, vol. 31, no. 14, pp. 4581–4585, 1998. 101

[160] D. Huang, S. L. Simon, and G. B. McKenna, "Equilibrium heat capacity of the glass-forming poly (α-methyl styrene) far below the kauzmann temperature: the case of the missing glass transition," *The Journal of chemical physics*, vol. 119, no. 7, pp. 3590–3593, 2003. 102, 144

[161] K. Loufakis and B. Wunderlich, "Computation of heat capacity of liquid macromolecules based on a statistical mechanical approximation," *The Journal of Physical Chemistry*, vol. 92, no. 14, pp. 4205–4209, 1988. 102, 144

[162] D. Cangialosi, A. Alegria, and J. Colmenero, "A thermodynamic approach to the fragility of glass-forming polymers," *The Journal of chemical physics*, vol. 124, no. 2, p. 024906, 2006. 103

[163] M. J. Pikal, L. L. Chang, and X. C. Tang, "Evaluation of glassy-state dynamics from the width of the glass transition: Results from theoretical simulation of differential scanning calorimetry and comparisons with experiment," *Journal of pharmaceutical sciences*, vol. 93, no. 4, pp. 981–994, 2004. 103

[164] J. Sjöström, J. Mattsson, R. Bergman, and J. Swenson, "Hydrogen bond induced nonmonotonic composition behavior of the glass transition in aqueous binary mixtures," *The Journal of Physical Chemistry B*, vol. 115, no. 33, pp. 10013–10017, 2011. 103, 147

[165] E. Donth, "The size of cooperatively rearranging regions at the glass transition," *Journal of Non-Crystalline Solids*, vol. 53, no. 3, pp. 325–330, 1982. 104, 127, 130, 133, 184

[166] S. Milner and T. McLeish, "Reptation and contour-length fluctuations in melts of linear polymers," *Physical Review Letters*, vol. 81, no. 3, p. 725, 1998. 106

[167] A. Arbe, M. Monkenbusch, J. Stellbrink, D. Richter, B. Farago, K. Almdal, and R. Faust, "Origin of internal viscosity effects in flexible polymers: A comparative neutron spin-echo and light scattering study on poly (dimethylsiloxane) and polyisobutylene," *Macromolecules*, vol. 34, no. 5, pp. 1281–1290, 2001. 106

[168] Y. Ding and A. Sokolov, "Comment on the dynamic bead size and kuhn segment length in polymers: Example of polystyrene," *Journal of Polymer Science Part B: Polymer Physics*, vol. 42, no. 18, pp. 3505–3511, 2004. 106, 107, 144

[169] B. Kresse, M. Hofmann, A. Privalov, N. Fatkullin, F. Fujara, and E. Rossler, "All polymer diffusion regimes covered by combining field-cycling and field-gradient 1h nmr," *Macromolecules*, vol. 48, no. 13, pp. 4491–4502, 2015. 106

[170] C. Gainaru and R. Bohmer, "Oligomer-to-polymer transition of poly (propylene glycol) revealed by dielectric normal modes," *Macromolecules*, vol. 42, no. 20, pp. 7616–7618, 2009. 106

[171] T. Inoue, H. Okamoto, and K. Osaki, "Birefringence of amorphous polymers. 1. dynamic measurement on polystyrene," *Macromolecules*, vol. 24, no. 20, pp. 5670–5675, 1991. 106

[172] T. Callaghan and D. Paul, "Interaction energies for blends of poly (methyl methacrylate), polystyrene, and poly (. alpha.-methylstyrene) by the critical molecular weight method," *Macromolecules*, vol. 26, no. 10, pp. 2439–2450, 1993. 107, 149

[173] C. Jeong and J. F. Douglas, "Mass dependence of the activation enthalpy and entropy of unentangled linear alkane chains," *The Journal of chemical physics*, vol. 143, no. 14, p. 144905, 2015. 108

[174] P. Santangelo, K. Ngai, and C. Roland, "Distinctive manifestations of segmental motion in amorphous poly (tetrahydrofuran) and polyisobutylene," *Macromolecules*, vol. 26, no. 11, pp. 2682–2687, 1993. 109

[175] X. Wu, C. Liu, Z. Zhu, K. Ngai, and L.-M. Wang, "Nature of the sub-rouse modes in the glass- rubber transition zone of amorphous polymers," *Macromolecules*, vol. 44, no. 9, pp. 3605–3610, 2011. 109

[176] X. Wang, Y. Nie, G. Huang, J. Wu, and K. Xiang, "Dynamic crossover of the sub-rouse modes in the glass–rubber transition region in poly (n-alkyl methacrylates) with different side chain lengths," *Chemical Physics Letters*, vol. 538, pp. 82–85, 2012. 109

[177] X. Wu, C. Liu, and K. Ngai, "Origin of the crossover in dynamics of the sub-rouse modes at the same temperature as the structural α-relaxation in polymers," *Soft Matter*, vol. 10, no. 46, pp. 9324–9333, 2014. 109

[178] M. Paluch, S. Pawlus, A. P. Sokolov, and K. Ngai, "Sub-rouse modes in polymers observed by dielectric spectroscopy," *Macromolecules*, vol. 43, no. 6, pp. 3103–3106, 2010. 110

[179] D. Plazek, I.-C. Chay, K. Ngai, and C. Roland, "Viscoelastic properties of polymers. 4. thermorheological complexity of the softening dispersion in polyisobutylene," *Macromolecules*, vol. 28, no. 19, pp. 6432–6436, 1995. 110

[180] A. K. Rizos, K. L. Ngai, and D. J. Plazek, "Local segmental and sub-rouse modes in polyisobutylene by photon correlation spectroscopy," *Polymer*, vol. 38, no. 25, pp. 6103–6107, 1997. 110

[181] D. Plazek, E. Schlosser, A. Schönhals, and K. Ngai, "Breakdown of the rouse model for polymers near the glass transition temperature," *The Journal of chemical physics*, vol. 98, no. 8, pp. 6488–6491, 1993. 110

[182] A. P. Sokolov and K. S. Schweizer, "Resolving the mystery of the chain friction mechanism in polymer liquids," *Physical review letters*, vol. 102, no. 24, p. 248301, 2009. 110, 123, 204

[183] Y. He, T. Lutz, M. Ediger, C. Ayyagari, D. Bedrov, and G. D. Smith, "Nmr experiments and molecular dynamics simulations of the segmental dynamics of polystyrene," *Macromolecules*, vol. 37, no. 13, pp. 5032–5039, 2004. 110, 118

[184] D. Ferri and L. Castellani, "Fine structure and thermorheological complexity of the softening dispersion in styrene-based copolymers," *Macromolecules*, vol. 34, no. 12, pp. 3973–3981, 2001. 110, 118

[185] D. L. Sidebottom, B. Roling, and K. Funke, "Ionic conduction in solids: Comparing conductivity and modulus representations with regard to scaling properties," *Physical Review B*, vol. 63, no. 2, p. 024301, 2000. 114

[186] K. Niss, B. Jakobsen, and N. B. Olsen, "Dielectric and shear mechanical relaxations in glass-forming liquids: A test of the gemant-dimarzio-bishop model," *The Journal of chemical physics*, vol. 123, no. 23, p. 234510, 2005.

[187] B. Jakobsen, K. Niss, C. Maggi, N. B. Olsen, T. Christensen, and J. C. Dyre, "Beta relaxation in the shear mechanics of viscous liquids: Phenomenology and network modeling of the alpha-beta merging region," *Journal of Non-Crystalline Solids*, vol. 357, no. 2, pp. 267–273, 2011. 114, 115

[188] A. Mandanici, R. Richert, M. Cutroni, X. Shi, S. A. Hutcheson, and G. B. McKenna, "Relaxational features of supercooled and glassy m-toluidine," *Journal of non-crystalline solids*, vol. 352, no. 42-49, pp. 4729–4734, 2006. 116

[189] S. Hutcheson and G. McKenna, "The measurement of mechanical properties of glycerol, m-toluidine, and sucrose benzoate under consideration of corrected rheometer compliance: an in-depth study and review," *The Journal of chemical physics*, vol. 129, no. 7, p. 074502, 2008. 116

[190] U. Tracht, M. Wilhelm, A. Heuer, H. Feng, K. Schmidt-Rohr, and H. W. Spiess, "Length scale of dynamic heterogeneities at the glass transition determined by multidimensional nuclear magnetic resonance," *Physical Review Letters*, vol. 81, no. 13, p. 2727, 1998. 127

[191] A. I. Mel'Cuk, R. A. Ramos, H. Gould, W. Klein, and R. D. Mountain, "Long-lived structures in fragile glass-forming liquids," *Physical review letters*, vol. 75, no. 13, p. 2522, 1995. 127

[192] J. Horbach, W. Kob, K. Binder, and C. A. Angell, "Finite size effects in simulations of glass dynamics," *Physical Review E*, vol. 54, no. 6, p. R5897, 1996. 127

[193] E. Bouthegourd, A. Esposito, D. Lourdin, A. Saiter, and J. Saiter, "Size of the cooperative rearranging regions vs. fragility in complex glassy systems: Influence of the structure and the molecular interactions," *Physica B: Condensed Matter*, vol. 425, pp. 83–89, 2013. 128

[194] L. Hong, P. Gujrati, V. Novikov, and A. Sokolov, "Molecular cooperativity in the dynamics of glass-forming systems: A new insight," *The Journal of chemical physics*, vol. 131, no. 19, p. 194511, 2009. 128

[195] E. Donth, "The size of cooperatively rearranging regions in polystyrene and styrene-dimethylsiloxane diblock copolymers at the glass transition temperature," *Acta polymerica*, vol. 35, no. 2, pp. 120–123, 1984. 128, 153, 186

[196] S. Kahle, J. Korus, E. Hempel, R. Unger, S. Höring, K. Schröter, and E. Donth, "Glass-transition cooperativity onset in a series of random copolymers poly (n-butyl methacrylate-stat-styrene)," *Macromolecules*, vol. 30, no. 23, pp. 7214–7223, 1997.

[197] S. Cerveny, J. Mattsson, J. Swenson, and R. Bergman, "Relaxations of hydrogen-bonded liquids confined in two-dimensional vermiculite clay," *The Journal of Physical Chemistry B*, vol. 108, no. 31, pp. 11596–11603, 2004. 128, 153

[198] C. J. Ellison, M. K. Mundra, and J. M. Torkelson, "Impacts of polystyrene molecular weight and modification to the repeat unit structure on the glass transition- nanoconfinement effect and the cooperativity length scale," *Macromolecules*, vol. 38, no. 5, pp. 1767–1778, 2005. 128, 129, 151, 153, 186

[199] K. Schröter, S. Reissig, E. Hempel, and M. Beiner, "From small molecules to polymers: relaxation behavior of n-butyl methacrylate based systems," *Journal of Non-Crystalline Solids*, vol. 353, no. 41, pp. 3976–3983, 2007. 128, 154, 186

[200] L. Fetters, D. Lohse, D. Richter, T. Witten, and A. Zirkel, "Connection between polymer molecular weight, density, chain dimensions, and melt viscoelastic properties," *Macromolecules*, vol. 27, no. 17, pp. 4639–4647, 1994. 129

[201] L. Berthier, G. Biroli, J.-P. Bouchaud, L. Cipelletti, D. El Masri, D. L'Hôte, F. Ladieu, and M. Pierno, "Direct experimental evidence of a growing length scale accompanying the glass transition," *Science*, vol. 310, no. 5755, pp. 1797–1800, 2005. 130, 155, 157, 186

[202] E. Donth, "Characteristic length of the glass transition," *Journal of Polymer Science Part B: Polymer Physics*, vol. 34, no. 17, pp. 2881–2892, 1996. 130, 133

[203] E. Donth, S. Kahle, J. Korus, and M. Beiner, "Small characteristic length at the glass transition cooperativity onset," *Journal de Physique I*, vol. 7, no. 4, pp. 581–598, 1997. 130, 133

[204] L. D. Landau, E. M. Lifshitz, and L. Pitaevskii, "Statistical physics, part i," 1980. 130, 131, 132

[205] B. Rijal, L. Delbreilh, and A. Saiter, "Dynamic heterogeneity and cooperative length scale at dynamic glass transition in glass forming liquids," *Macromolecules*, vol. 48, no. 22, pp. 8219–8231, 2015. 134

[206] S. Weyer, A. Hensel, and C. Schick, "Phase angle correction for tmdsc in the glass-transition region," *Thermochimica acta*, vol. 304, pp. 267–275, 1997. 138

[207] R. Meier, A. Herrmann, M. Hofmann, B. Schmidtke, B. Kresse, A. Privalov, D. Kruk, F. Fujara, and E. Rossler, "Iso-frictional mass dependence of diffusion of polymer melts revealed by 1h nmr relaxometry," *Macromolecules*, vol. 46, no. 14, pp. 5538–5548, 2013. 143

[208] T. Inoue and K. Osaki, "Role of polymer chain flexibility on the viscoelasticity of amorphous polymers around the glass transition zone," *Macromolecules*, vol. 29, no. 5, pp. 1595–1599, 1996. 144

[209] G. Dee, T. Ougizawa, and D. Walsh, "The pressure-volume-temperature properties of polyethylene, poly (dimethyl siloxane), poly (ethylene glycol) and poly (propylene glycol) as a function of molecular weight," *Polymer*, vol. 33, no. 16, pp. 3462–3469, 1992. 149

[210] L. Berthier, G. Biroli, J.-P. Bouchaud, W. Kob, K. Miyazaki, and D. Reichman, "Spontaneous and induced dynamic fluctuations in glass formers. i. general results and dependence on ensemble and dynamics," *The Journal of chemical physics*, vol. 126, no. 18, p. 184503, 2007. 155

[211] L. Berthier, G. Biroli, J.-P. Bouchaud, W. Kob, K. Miyazaki, and D. R. Reichman, "Spontaneous and induced dynamic correlations in glass formers. ii. model calculations and comparison to numerical simulations," *The Journal of chemical physics*, vol. 126, no. 18, p. 184504, 2007.

[212] C. Dalle-Ferrier, C. Thibierge, C. Alba-Simionesco, L. Berthier, G. Biroli, J.-P. Bouchaud, F. Ladieu, D. LHôte, and G. Tarjus, "Spatial correlations in the dynamics of glassforming liquids: Experimental determination of their temperature dependence," *Physical Review E*, vol. 76, no. 4, p. 041510, 2007. 156, 157, 158, 162, 168, 186

[213] L. Berthier, "Dynamic heterogeneity in amorphous materials," *arXiv preprint arXiv:1106.1739*, 2011. 155

[214] J.-P. Hansen and I. R. McDonald, *Theory of simple liquids: with applications to soft matter*. Academic Press, 2013. 156

[215] P. Mayer, H. Bissig, L. Berthier, L. Cipelletti, J. P. Garrahan, P. Sollich, and V. Trappe, "Heterogeneous dynamics of coarsening systems," *Physical review letters*, vol. 93, no. 11, p. 115701, 2004. 156

[216] S. Capaccioli, G. Ruocco, and F. Zamponi, "Dynamically correlated regions and configurational entropy in supercooled liquids," *The Journal of Physical Chemistry B*, vol. 112, no. 34, pp. 10652–10658, 2008. 165, 168

[217] D. Fragiadakis, R. Casalini, R. Bogoslovov, C. Robertson, and C. Roland, "Dynamic heterogeneity and density scaling in 1, 4-polyisoprene," *Macromolecules*, vol. 44, no. 5, pp. 1149–1155, 2011. 169

[218] R. Casalini and C. Roland, "Effect of regioisomerism on the local dynamics of polychlorostyrene," *Macromolecules*, vol. 47, no. 12, pp. 4087–4093, 2014. 169

[219] J. Qiao, R. Casalini, J.-M. Pelletier, and H. Kato, "Characteristics of the structural and johari–goldstein relaxations in pd-based metallic glass-forming liquids," *The Journal of Physical Chemistry B*, vol. 118, no. 13, pp. 3720–3730, 2014. 169

[220] C. Toninelli, M. Wyart, L. Berthier, G. Biroli, and J.-P. Bouchaud, "Dynamical susceptibility of glass formers: Contrasting the predictions of theoretical scenarios," *Physical Review E*, vol. 71, no. 4, p. 041505, 2005. 169

[221] A. Saiter, L. Delbreilh, H. Couderc, K. Arabeche, A. Schönhals, and J.-M. Saiter, "Temperature dependence of the characteristic length scale for glassy dynamics: Combination of dielectric and specific heat spectroscopy," *Physical Review E*, vol. 81, no. 4, p. 041805, 2010. 171

[222] J. Cavaille, J. Perez, and G. Johari, "Molecular theory for the rheology of glasses and polymers," *Physical review B*, vol. 39, no. 4, p. 2411, 1989. 175

[223] K. Ngai, "Correlation between the secondary β-relaxation time at t g with the kohlrausch exponent of the primary α relaxation or the fragility of glass-forming materials," *Physical Review E*, vol. 57, no. 6, p. 7346, 1998. 175

[224] D. Fragiadakis and C. Roland, "Participation in the johari–goldstein process: Molecular liquids versus polymers," *Macromolecules*, vol. 50, no. 10, pp. 4039–4042, 2017. 175

[225] A. Kulik and K. Prins, "2h nmr study of high pressure effects on the molecular dynamics in polystyrene: 2. phenyl group motion," *Polymer*, vol. 34, no. 22, pp. 4635–4641, 1993. 176

[226] J. Zhao, Y. H. Chin, Y. Liu, A. A. Jones, P. T. Inglefield, R. P. Kambour, and D. M. White, "Deuterium nmr study of phenyl group motion in glassy polystyrene and a blend of polystyrene with polyphenylene oxide," *Macromolecules*, vol. 28, no. 11, pp. 3881–3889, 1995. 176

[227] S. Arrese-Igor, A. Arbe, B. Frick, and J. Colmenero, "Glassy dynamics of polystyrene by quasielastic neutron scattering," *Macromolecules*, vol. 44, no. 8, pp. 3161–3168, 2011. 176

[228] A. Kudlik, S. Benkhof, T. Blochowicz, C. Tschirwitz, and E. Rössler, "The dielectric response of simple organic glass formers," *Journal of molecular structure*, vol. 479, no. 2-3, pp. 201–218, 1999. 178, 179, 187

[229] K. Ngai and S. Capaccioli, "Relation between the activation energy of the johari-goldstein β relaxation and t g of glass formers," *Physical Review E*, vol. 69, no. 3, p. 031501, 2004. 179

[230] H. W. Starkweather Jr, "Aspects of simple, non-cooperative relaxations," *Polymer*, vol. 32, no. 13, pp. 2443–2448, 1991. 182

[231] R. Casalini and C. Roland, "Aging of the secondary relaxation to probe structural relaxation in the glassy state," *Physical review letters*, vol. 102, no. 3, p. 035701, 2009. 182

[232] I. Hodge, "Effects of annealing and prior history on enthalpy relaxation in glassy polymers. 6. adam-gibbs formulation of nonlinearity," *Macromolecules*, vol. 20, no. 11, pp. 2897–2908, 1987. 183, 187

[233] R. Casalini and C. Roland, "Density scaling of the structural and johari–goldstein secondary relaxations in poly (methyl methacrylate)," *Macromolecules*, vol. 46, no. 15, pp. 6364–6368, 2013. 184

[234] S. Kołodziej, S. Pawlus, K. Ngai, and M. Paluch, "Verifying the approximate coinvariance of the α and johari–goldstein β relaxation times to variations of pressure and temperature in polyisoprene," *Macromolecules*, 2018. 184

[235] T. Ransom, D. Fragiadakis, and C. Roland, "The α and johari–goldstein relaxations in 1, 4-polybutadiene: Breakdown of isochronal superpositioning," *Macromolecules*, 2018. 184

[236] H. C. Price, J. Mattsson, and B. J. Murray, "Sucrose diffusion in aqueous solution," *Physical Chemistry Chemical Physics*, vol. 18, no. 28, pp. 19207–19216, 2016. 189, 204, 212

[237] B. Sun, *Functional Polymer Electrolytes for Multidimensional All-Solid-State Lithium Batteries*. PhD thesis, Acta Universitatis Upsaliensis, 2015. 190

[238] B. Scrosati and C. A. Vincent, "Polymer electrolytes: the key to lithium polymer batteries," *Mrs Bulletin*, vol. 25, no. 3, pp. 28–30, 2000. 190, 191

[239] J. B. Goodenough and Y. Kim, "Challenges for rechargeable li batteries," *Chemistry of materials*, vol. 22, no. 3, pp. 587–603, 2009. 190

[240] J. Song, Y. Wang, and C. C. Wan, "Review of gel-type polymer electrolytes for lithium-ion batteries," *Journal of Power Sources*, vol. 77, no. 2, pp. 183–197, 1999. 191

[241] X. Lu, G. Xia, J. P. Lemmon, and Z. Yang, "Advanced materials for sodium-beta alumina batteries: Status, challenges and perspectives," *Journal of Power Sources*, vol. 195, no. 9, pp. 2431–2442, 2010. 191

[242] R. Koksbang, I. I. Olsen, and D. Shackle, "Review of hybrid polymer electrolytes and rechargeable lithium batteries," *Solid State Ionics*, vol. 69, no. 3-4, pp. 320–335, 1994. 191

[243] W. H. Meyer, "Polymer electrolytes for lithium-ion batteries," *Advanced materials*, vol. 10, no. 6, pp. 439–448, 1998. 191

[244] K. Murata, S. Izuchi, and Y. Yoshihisa, "An overview of the research and development of solid polymer electrolyte batteries," *Electrochimica acta*, vol. 45, no. 8-9, pp. 1501–1508, 2000. 191

[245] Z. Xue, D. He, and X. Xie, "Poly (ethylene oxide)-based electrolytes for lithium-ion batteries," *Journal of Materials Chemistry A*, vol. 3, no. 38, pp. 19218–19253, 2015. 191, 207

[246] Y. Wang and A. P. Sokolov, "Design of superionic polymer electrolytes," *Current Opinion in Chemical Engineering*, vol. 7, pp. 113–119, 2015. 191, 196

[247] A. L. Agapov and A. P. Sokolov, "Decoupling ionic conductivity from structural relaxation: a way to solid polymer electrolytes?," *Macromolecules*, vol. 44, no. 11, pp. 4410–4414, 2011. 191, 194, 202, 203, 204, 206, 209, 212

[248] J. Bockris and G. Hooper, "Self-diffusion in molten alkali halides," *Discussions of the Faraday Society*, vol. 32, pp. 218–236, 1961. 191, 202, 203, 212

[249] W. Xu, E. I. Cooper, and C. A. Angell, "Ionic liquids: ion mobilities, glass temperatures, and fragilities," *The Journal of Physical Chemistry B*, vol. 107, no. 25, pp. 6170–6178, 2003. 191, 195, 202, 203, 209, 212

[250] O. Mahendran and S. Rajendran, "Ionic conductivity studies in pmma/pvdf polymer blend electrolyte with lithium salts," *Ionics*, vol. 9, no. 3-4, pp. 282–288, 2003. 192, 207

[251] A. Ali, M. Yahya, H. Bahron, R. Subban, M. Harun, and I. Atan, "Impedance studies on plasticized pmma-lix [x: Cf3so3-, n (cf3so2) 2-] polymer electrolytes," *Materials Letters*, vol. 61, no. 10, pp. 2026–2029, 2007.

[252] S. Ramesh and K. Wong, "Conductivity, dielectric behaviour and thermal stability studies of lithium ion dissociation in poly (methyl methacrylate)-based gel polymer electrolytes," *Ionics*, vol. 15, no. 2, pp. 249–254, 2009. 192, 207

[253] D. Golodnitsky, E. Strauss, E. Peled, and S. Greenbaum, "on order and disorder in polymer electrolytes," *Journal of The Electrochemical Society*, vol. 162, no. 14, pp. A2551–A2566, 2015. 192

[254] J. Mattsson, R. Bergman, P. Jacobsson, and L. Börjesson, "Influence of chain length on the α- β bifurcation in oligomeric glass formers," *Physical review letters*, vol. 94, no. 16, p. 165701, 2005. 193, 200

[255] M. Yoshizawa, W. Xu, and C. A. Angell, "Ionic liquids by proton transfer: Vapor pressure, conductivity, and the relevance of δp k a from aqueous solutions," *Journal of the American Chemical Society*, vol. 125, no. 50, pp. 15411–15419, 2003. 195

[256] C. A. Angell, C. T. Imrie, and M. D. Ingram, "From simple electrolyte solutions through polymer electrolytes to superionic rubbers: some fundamental considerations," *Polymer international*, vol. 47, no. 1, pp. 9–15, 1998. 197, 202

[257] F. Stickel, E. W. Fischer, and R. Richert, "Dynamics of glass-forming liquids. ii. detailed comparison of dielectric relaxation, dc-conductivity, and viscosity data," *The Journal of chemical physics*, vol. 104, no. 5, pp. 2043–2055, 1996. 198

[258] J. Mattsson, R. Bergman, P. Jacobsson, and L. Börjesson, "Effects of hydrogen bonding on supercooled liquid dynamics and the implications for supercooled water," *Physical Review B*, vol. 79, no. 17, p. 174205, 2009. 200, 201

[259] D. Engberg, J. Schüller, B. Strube, A. Sokolov, and L. Torell, "Brillouin scattering and dielectric relaxation in ppg of different chain lengths and end groups," *Polymer*, vol. 40, no. 17, pp. 4755–4761, 1999. 200

[260] V. Lubchenko and P. G. Wolynes, "Theory of structural glasses and supercooled liquids," *Annu. Rev. Phys. Chem.*, vol. 58, pp. 235–266, 2007. 204

[261] M. Ediger and P. Harrowell, "Perspective: Supercooled liquids and glasses," *The Journal of Chemical Physics*, vol. 137, no. 8, p. 080901, 2012. 204

[262] H.-B. Yu, K. Samwer, Y. Wu, and W. H. Wang, "Correlation between β relaxation and self-diffusion of the smallest constituting atoms in metallic glasses," *Physical review letters*, vol. 109, no. 9, p. 095508, 2012. 204

[263] H. B. Yu, W. H. Wang, H. Y. Bai, and K. Samwer, "The β-relaxation in metallic glasses," *National Science Review*, vol. 1, no. 3, pp. 429–461, 2014. 204

[264] S. S. Zhang, K. Xu, and T. R. Jow, "Study of libf4 as an electrolyte salt for a li-ion battery," *Journal of The Electrochemical Society*, vol. 149, no. 5, pp. A586–A590, 2002. 207

[265] S. Zhang, K. Xu, and T. Jow, "Low-temperature performance of li-ion cells with a libf 4-based electrolyte," *Journal of Solid State Electrochemistry*, vol. 7, no. 3, pp. 147–151, 2003. 207

[266] W. Wieczorek, D. Raducha, A. Zalewska, and J. R. Stevens, "Effect of salt concentration on the conductivity of peo-based composite polymeric electrolytes," *The Journal of Physical Chemistry B*, vol. 102, no. 44, pp. 8725–8731, 1998. 208

[267] A. Panday, S. Mullin, E. D. Gomez, N. Wanakule, V. L. Chen, A. Hexemer, J. Pople, and N. P. Balsara, "Effect of molecular weight and salt concentration on conductivity of block copolymer electrolytes," *Macromolecules*, vol. 42, no. 13, pp. 4632–4637, 2009. 208

[268] F.-J. Stickel, *Untersuchung der dynamik in niedermolekularen flüssigkeiten mit dielektrischer spektroskopie*. Shaker, 1995. 210

[269] R. J. Larsen and C. F. Zukoski, "Effect of particle size on the glass transition," *Physical Review E*, vol. 83, no. 5, p. 051504, 2011. 210

[270] Q. Qin and G. B. McKenna, "Correlation between dynamic fragility and glass transition temperature for different classes of glass forming liquids," *Journal of Non-Crystalline Solids*, vol. 352, no. 28-29, pp. 2977–2985, 2006. 210